Università degli Studi di Torino

Computer Science Department

Ph.D. Program Technology Driven Sciences: Technologies for Cultural Heritage

Cycle XXXIV

Doctoral Thesis

Enhancing Geomatics Techniques for Cultural Heritage through Multiwavelength Recording and Metric Data Fusion

Efstathios Adamopoulos

* * * * * *

Supervisor	Prof. Liliana Ardissono	
Co-Supervisor	Prof. Fulvio Rinaudo	Dipartimento di Architettura e Design, Politecnico di Torino
Referees/Examines	Prof. Cristiana Achille	Dipertimento di Architettura, Ingegneria delle Construzioni e Ambiente Construito, Politecnico di Milano
	Prof. José Luis Lerma García	Escuela Técnica Superior de Ingeniería Geodésica, Cartográfica y Topográfica, Universitat Politècnica de València
	Prof. Andreas Georgopoulos	School of Rural, Surveying and Geoinformatics Engineering, National Technical University of Athens
Ph.D Program Coordinator	Prof. Stefano De Martino	Dipartimento di Studi Storici, Università degli Studi di Torino

Acknowledgments

The presented research combined several disciplines to propose novel approaches for cultural heritage recording. It is without a doubt a product of multi-disciplinary collaboration, and therefore I have to thank many people of different academic and professional backgrounds who contributed to this work. I also wish to acknowledge all those who, by any means, supported me during the three years of doctoral research leading to the final defense, especially considering the difficulties faced during that time.

I start by thanking prof. Fulvio Rinaudo, my academic supervisor, for all his help, the critical feedback, for believing in me and giving me the freedom to pursue my research interests in the way that I wanted to, and steering, when needed, my research to the right direction by reminding me the place of the surveying and geomatics engineer in the complex process that is heritage documentation. I also thank prof. Liliana Ardissono, who helped me navigate through life in a completely new university environment and assisted with all bureaucratic matters that had to do with my research arrangements, and without whom my research would not have been completed. I extend my deep gratitude to prof. Cristiana Achille, prof. José Luis Lerma García, and prof. Andreas Georgopoulos for helping improve this dissertation through their comments and supporting me in the moments leading to the defense. I am particularly thankful to prof. Georgopoulos for motivating and mentoring me throughout the last years during my journey in the cultural heritage documentation field and to prof. Lerma, whose research on the application of multispectral technologies for archaeology and cultural heritage science, has been a significant inspiration to all my work.

I would like to express my immense gratitude to all members of the Lab of Geomatics for Cultural Heritage (LabG4CH) at the Department of Architecture and Design (DAD)–Politecnico di Torino, for their valuable help regarding the instrumentation and, most of all, for including me in their team and always treating me as one of their own. Giacomo, Alessandra, Giulia, Lorenzo, Filippo, Elisabetta, Alessio, Stefano, Fabio, Filiberto, and Nannina thank you for sharing struggles and achievements, food, arguments, and for always being open for discussion and inspiring me in many ways.

Special thanks to my CIPA emerging professionals team and most of all to Rebecca, Joe, Michelle, and Nour, who journeyed with me during the last three years, navigating the waters of ICOMOS and venturing into new territories. We worked together to consolidate our international presence as a group, organized exciting events, and put an effort to attract a new generation of talented practitioners to help protect our world's cultural heritage, creating wonderful and everlasting

memories along the way. It is also important to mention a few other people I met through CIPA who influenced or supported me in different ways. Thank you Greta, Tugba, Alex, Thomas, Geert, Marina, Ari, Max, Olga, Maria, and Hyeseung.

Thanks to my good friends Abraham, Aïda, Sofiane, Oleh, Symon, and Güncem, with whom I have shared my struggles in academic and personal matters, explored Italy, celebrated, exchanged opinions, and often, cultural perspectives on important and trivial matters.

To Nikiforos, Dimitris, Filippos, Chrysanthi, Kostas, Evi, Lydia, Fanis, Vasilis, Athina, Thomas, Konstantinos, Tania, Panagiotis, Nikos, Kiki, you should know that your support and encouragement was worth more than I can express on paper.

Last but not least, infinite thanks to my parents, Magda and Giorgos, and my sister Despina to whom I dedicate my work– you were always there with a word of encouragement or listening ear.

Contents

List of Tables

List of Figures

Acronyms

2D	Two-Dimensional
3D	Three-Dimensional
BIM	Building Information Modeling
CAD	Computer-Assisted Design
CCD	Charge-Coupled Device
CFA	Color Filter Array
CMOS	Complementary Metal-Oxide-Semiconductor
COTS	Commercial Off-The-Self
DIP	Digital Image Processing
DMVR	Dense Multi-View 3d Reconstruction
DN	Digital Number
DSC	Digital Still Camera
FGR	Fast Global Registration
FN	False Negative
FOSS	Free and Open-Source Software
FP	False Positive
GIS	Geographical Information Systems
GNSS	Global Navigation Satellite System
GPR	Ground-Penetrating Radar
IBM	Image-Based Modeling
LWIR	Long-Wavelength InfraRed
NCC	Normalized Cross-Correlation
NDE	Non-Destructive Evaluation
NIR	Near-InfraRed
NUV	Near-Ultraviolet

PCA	Principal Component Analysis
PS	Phase-Shift
RANSAC	RANdom Sample Consensus
RGB	Red-Green-Blue
RIFT	Radiation-Invariant Feature Transform
ROI	Region of Interest
SfM	Structure-from-Motion
SIFT	Scale-Invariant Feature Transform
SLR	Single-Lens Reflex
SLS	Structured Light Scanning
SSD	Scene Sampling Distance
SWIR	Short-Wavelength InfraRed
TIR	Thermal InfraRed
TLS	Terrestrial Laser Scanning
TN	True Negative
ToF	Time-of-Flight
TP	True Positive
TSR	Thermographic Signal Reconstruction
UVF	UltraViolet Fluorescence
VIS	VISible-spectrum

1 Abstract

The preservation and conservation of cultural heritage assets are elaborate tasks that abound with challenges. Geometrical complexity, multiplicity and degradation of materials, varying historical construction techniques, and a plethora of other intrinsic and extrinsic factors—including environmental pressures and past anthropogenic interventions—induce problems for protecting the historic built environment, archaeological remains, and antiquities. Therefore, extensive knowledge of these parameters is required to ensure the effectiveness of any implemented intervention. Thus, the comprehensive documentation and condition inspection become necessary to holistically address the state of preservation in order to understand the prevailing problems that place cultural heritage assets at risk. Furthermore, monitoring the state of preservation through time is fundamental for effectively interpreting the occurring degradation phenomena and a powerful tool for the decision-making process regarding material heritage protection. Systematic nondestructive acquisition and integrated processing of multisource scientific data play an essential role in surveying the state of preservation of cultural heritage assets. The need for multidisciplinary inspection methodologies has been frequently stressed in literature, mainly in application cases of monumental heritage and objects of outstanding value presenting extensive degradation. Likewise, the non-destructiveness of monitoring methods has often been highlighted as an important factor for safeguarding the condition of significantly deteriorated or already at-risk assets. Hence, active and passive close-range nondestructive sensing techniques and appropriate signal processing methods are regularly used as nondestructive sources of multi-disciplinary data useful for inspection and monitoring applications.

Individual close-range sensing methods, including techniques for reality-based geometric recording of cultural heritage, are often considered separate practices. However, their integration has the potential to improve the documentation of the state of preservation, and to support diagnostics, as many evaluation methods can act complementarily. It should also be highlighted that imparting spatial properties to nondestructive evaluation methods allows for the better interpretation and visualization of the state of preservation, while facilitating the spatial fusion of multi-sensor data. At the same time, monitoring benefits from geometric recording

methods in the sense of acquiring spatial data and utilizing valuable sensing metadata derived from the employed measurement instrumentation.

Recognizing the contribution of implementing multi-sensor approaches for non-destructive documentation of cultural heritage structures and objects as part of the protection practice, this dissertation presents novel applied geomatics methodologies for enhancing the surveying process of cultural heritage, focusing on the metric implementation of state-of-the-art non-destructive recording techniques and the fusion of acquired multiwavelength data. It seeks to validate integrated multi-band recording solutions, which can support the multidisciplinary documentation and condition inspection of critical heritage infrastructure and other objects of historical significance. Following this rationale, close-range sensing techniques are evaluated on their capacity to produce metric, survey-grade results for cultural heritage. The novelty of the conducted research stems from the innovative integration of reality-based digitization and multiwavelength acquisition through 3D scanning, thermography, multispectral imaging, ground-penetrating radar, and the utilization of data sources that are traditionally considered qualitative to obtain metric/quantitative results. Particular emphasis is given to creating reproducible and, as much as possible, practical workflows considering their implementability for heritage science. The dissertation aims to shed light on the problematics of the individual and integrated use of sensing techniques, highlighting metric and radiometric requirements of the data fusion approaches, as well as their usefulness to interpret the condition of heritage assets.

The second chapter of this dissertation delivers a comprehensive overview of the contemporary proximal sensing techniques employed for reality capture and nondestructive evaluation of heritage assets—including their basic operating principles and application scenarios. The third chapter deals with the state of the art on data fusion methodologies encountered in recent literature, outlining the different levels of integration and the challenges faced. The fourth chapter describes a methodology for recording and integrating multispectral terrestrial data and utilizing them in combination with image processing techniques to map the deterioration of heritage assets. Although the presented workflow is mainly evaluated for two-dimensional mapping, an extension to three-dimensional objects is also briefly discussed. The fifth chapter addresses a methodology for full three-dimensional integration of spectral imaging, metric surveying, image-based modeling, scanning, and ground-penetrating radar. The latter methodology is adapted and validated for both historical objects and structures, considering the uniqueness of each case study and the limitations faced. The last chapter of the dissertation discusses the results of the diverse case studies and experimentation scenarios and describes perspectives and outlooks.

2 Introduction and Background

This chapter covers the theoretical background and technical framework associated with the topics of interdisciplinary heritage recording discussed in the thesis. After briefly establishing the facets of cultural heritage documentation's contemporary importance and contribution to preservation, relevant technological developments, and contemporary tendencies are described. Particular attention is given to metrical notions, recording principles, application scenarios, and data treatment methods. Parts of this chapter's contents have been published in Adamopoulos and Rinaudo (2021c) and Adamopoulos, Patrucco, Volinia et al. (2021).

2.1 Theoretical Notions

The significance of documenting tangible cultural heritage, including, but not limited to, movable objects and immovable structures, has been recognized over the recent decades by many international bodies and agencies and is often highlighted by international charters, declarations, resolutions, and other doctrinal texts. Such documents stress the need for detailed collaborative documentation as part of the study, inspection, and monitoring of heritage and acknowledge that protection must consist of a plan of actions based on the fullest possible knowledge of an asset's state of preservation, nature, and history. Producing comprehensive documentation outcomes denotes immediate benefits in terms of project planning, interdisciplinary communication, interpretation, and dissemination of results, but it is also an ethical obligation for posterity (De Vos, 2017; Mezzino et al., 2017).

2.1.1 Heritage Documentation Principles

Acquisition, elaboration, and management of recorded digital data representing material cultural heritage, to be successful, demand interdisciplinary dialogue and collaboration. As cultural heritage studies confront complex 'real world' problems, the implemented recording practices should cross disciplinary boundaries to create new knowledge, achieve a high level of integration and cooperation in order to bridge the different viewpoints, and examine accumulated knowledge from the perspective of neighboring disciplines (Stock & Burton, 2011). However, differences between discrete disciplinary recording practices are existent and

understandable (Boochs et al., 2016). The call for "bridging the gap" between disciplines involved in the cultural heritage documentation domain has been voiced for decades (Letellier, 2001), since appropriate documentation directly reflects on the decision-making for preservation actions. CIPA—the International Scientific Committee of the International Council on Monuments and Sites (ICOMOS) and the International Society of Photogrammetry and Remote Sensing (ISPRS) for Heritage Documentation—plays a key role in this effort by promoting interdisciplinary collaboration. Integrating the recording, analytical, and data management approaches stemming from different disciplines requires collaborative efforts at every documentation stage (Hirsenberger et al., 2019).

Since cultural heritage protection and preservation constitute interdisciplinary activities, documentation should also result from the collaboration of professionals and people from different fields of expertise and interests. As Letellier (2007) describes, heritage data recording and management procedures performed by an interdisciplinary team should be guided by a set of principles. The recorded data allow for an informed condition inspection, routine management, long-term monitoring, and facilitate diagnostic investigation surveys and maintenance. Documentation should occur before, during, and after any conservation or other intervening action, when archaeological or historical evidence is revealed, and when heritage is at risk of being damaged or otherwise irreversibly altered. Everyone involved in the recording process and heritage managers have specific responsibilities for assuring the quality, multiformity, conservation, and continuous updating of the recorded information and for the creation and sharing of permanent records for the heritage assets under threat. Recording heritage information helps ensure that any planned interventions respect heritage assets' defined values, historical qualities, and material characteristics. Thorough documentation provides permanent records of cultural heritage prior to any change, planned or unplanned. Analysis of the recorded information should serve as a tool for learning; archiving and dissemination should be as comprehensive as possible and reflect the heritage asset's significance (Drury & McPherson, 2008).

Heritage records should include metric, quantitative, and qualitative information about the assets, their management, condition, maintenance and repairs, and the threats and risks to their safekeeping. Furthermore, careful consideration should go into the appropriate scope, level, and methods of recording. This entails that the type and workflow of the documentation, as well as the techniques and technologies employed, should be appropriate to the nature and importance of the heritage asset, the project's needs, the record's purpose, the cultural context, and the resources available. Preference should be given to nonintrusive techniques. The rationale for the intended scope and the selection of the recording methods must be clearly stated, and the materials used for compiling final records must be stable. Recording and other heritage information-related activities should be undertaken to an appropriate level of detail to provide

information for sensitive and cost-effective planning, efficient research, restoration work, site management, and creation of permanent records.

2.1.2 Documentation as Part of Heritage Protection

The protection of ancient and historic objects, structures, and their remains poses an intricate task due to the challenges that the presence of a multiplicity of historical materials, adopted construction techniques, and deterioration forms induce. Documentation is a fundamental step toward effectively planning the diagnostic steps that precede the conservation process. The collection and analysis of recorded interdisciplinary information allow for inspecting the state of preservation and monitoring historic assets' properties, including the pressures of the environment and previous interventions.

Within the framework set by contemporary heritage conservation ethics (Viñas, 2002), practical needs arising from sustainable value-based conservation planning (Demas, 2000; Mason & Avrami, 2000; Strange & Whitney, 2003), and experience gained from decades of observing damages caused to material heritage by inappropriate interventions (Palumbo, 2000), derives the stressing need for integrated protection. Thus it becomes necessary to design and implement interdisciplinary methodologies that will allow decision-making for restoration and conservation interventions based on systematic inspection and monitoring (Kioussi et al., 2013). These methodologies should be centered on interdisciplinary recording, processing, management, and visualization of pertinent information that will allow the observation of a monument's characteristics and their change through time (Masciotta et al., 2019), while also enabling better supervision and the strategic planning and promotion on a larger scale (Kioussi et al., 2011). The complexity of collecting and making good use of interdisciplinary information about heritage assets stems from the multifarious protection activities and requires adopting multi-scale and flexible methodologies.

Documentation is a prerequisite for any investigation aiming to reveal information about a heritage asset's state of preservation. The documentation refers to every step of the conservation process (Table 2.1**Error! Reference source not found.**), including the anamnesis, diagnosis, and therapy (the application of conservation interventions) (Fitzner, 2004). Essentially, documentation serves a crucial role in condition inspection and is the first important step towards surveying the causes triggering deterioration. It relies on the geometric recording to provide the spatial reference upon which interdisciplinary information can be integrated, and other metric and quantitative recording techniques to obtain the necessary background for further (potentially intrusive) testing. The integrated documentation may contain a multitude of information, the main categories being historical, archaeological, architectural, geometric, structural, environmental, climatic, and

physicochemical regarding the materials' characteristics and their deterioration (mineralogical, microstructural, hygrothermal information).

As the research presented here mainly concerns multisource documentation for anamnestic purposes, which can also facilitate data collection for diagnosis, a brief analysis on the topic of recording techniques regarding those matters follows in the subsequent sections.

Table 2.1. Approach to material heritage conservation (adapted from Fitzner, 2004)

APPROACH TO INTEGRATED CONSERVATION OF HERITAGE		
↓	↓	↓
ANAMNESIS →	**DIAGNOSIS** →	**THERAPY**
Identification	Materials and properties	Conception, calculation,
Location and description	Preservation state	and test-application of
of the asset	Factors and processes	preservation measures
Art history	of deterioration	Implementation of
Construction history	Progression of	preservation measures
Preservation history	deterioration	Quality control
Case history	Rating of weathering	Monitoring
↑	↑	↑
DOCUMENTATION		

2.1.2.1 *Documentation within the Scope of Anamnesis*

Anamnesis addresses the compilation, evaluation, and presentation of documents, photographs, information, and data for locating, identifying, and describing heritage assets and portraying their history.

The on-site visual identification of materials, deterioration, and earlier preservation interventions is a valuable method associated with the anamnesis. Observation of visible characteristics on the surfaces of heritage assets related to materials, construction techniques, weathering, and physical damage is crucial for distinguishing impending risks and planning diagnostic surveys. Certain types of weathering and damage can be more common for specific historic materials or under specific environmental conditions. Regardless, the visual inspection can provide extensive information that can help draw some first conclusions about the state of preservation and support configuring the plan of the diagnostical workflow (Kapsalas et al., 2007). The resulting information should be recorded systematically

and in detail, supported and cross-correlated with information from historical and contemporary sources.

Geometric documentation also has a vital role in the anamnesis, as evident from United Nations Educational, Scientific and Cultural Organization (UNESCO, 1972) which defines it as:

- "the action of acquiring, processing, presenting and recording the necessary data for the determination of the position and the actual existing form, shape, and size of a monument in the three-dimensional space at a particular given moment in time;

- the geometric documentation records the present of the monuments, as this has been shaped in the course of time and is the necessary background for the studies of their past, as well as the care of their future."

Traditionally, the scope of the geometric recording is to provide conservation specialists with measurements in the form of vector plans, sections or outlines plotted on hard copy that let direct use on site. However, the development of new approaches, algorithms, and digital techniques in the field of three-dimensional (3D) data acquisition, along with robust computational systems and affordable costs of the respective sensors, have allowed the efficient usage and dissemination of both imagery products and 3D data, usually in the form of 3D models. In addition, these advancements have enabled automation, higher speeds, and increased fidelity. However, their most important contribution is the possibility of producing alternative digital documentation products, like the ones referred to above (Georgopoulos, 2018). The choice of suitable recording methods highly depends on dimensions, risk of damage or collapse, accessibility, and specified accuracy requirements (Böhler, 2006). The difficulty of choosing between geometric recording methodologies also lies in the vastly dissimilar characteristics among tangible heritage assets (even of the same typology) and their complexity which is often a result of significant weathering. Besides, complexity may be one of the most critical challenges of heritage documentation, which demands drastically different approaches to be adopted depending on the object of study. Furthermore, the object can often be strongly associated with the surrounding environment, and thus, documentation for anamnesis should also include it.

The anamnestic stage that precedes diagnosis includes data collection with on-site methods, apart from the geometric documentation, and takes into account scale and complexity. At this stage, documentation should lead to an exhaustive description of the characteristics of the cultural heritage asset. For this purpose, various non-destructive evaluation (NDE) methods are employed, such as digital imaging, endoscopy, thermography, ground-penetrating radar, and ultrasonic tomography (Moropoulou et al., 2005).

2.1.2.2   Documentation within the Scope of Diagnosis

The diagnostical study utilizes interdisciplinary information supplied by the anamnesis and constitutes the basis for the conception, calculation, and planning of conservation interventions. The diagnosis's overall aim is to characterize, quantify, interpret, and rate degradation on the historical asset by considering all the documented characteristics, the material properties, the factors and mechanisms of weathering (Fitzner, 2002).

The diagnosis's methodological approach includes the analysis of the data collected on-site, as well as laboratory tests after minor sampling, and considers the different scales of degradation. At this stage, the anamnestic information supports the interpretation of analytical investigation results, which leads to the localization and detailed description of historic material properties and their alterations, characterization, and quantification of weathering characteristics and forms, drawing conclusions regarding the alteration inducing factors, thorough assessment of previous conservation measures and their compatibility, qualitative evaluation of the state of preservation, damage and risk prognosis, and drafting recommendations about appropriate measures including their urgency (Genovese, 2005). The diagnosis monitors endogenous, environmental, and anthropogenic factors of deterioration.

2.2 Fundamentals of Recording Techniques

Digital recording for cultural heritage documentation considers many active and passive nonintrusive sensing techniques and image processing methods (Tobiasz et al., 2019). Despite the commonly practiced separation between geometric recording and NDE—due to restrictions imposed by the vastly different instrumentation and signal processing methods involved—the data and metadata acquired through geometric recording methods can more often than not support non-destructive inspection (Chiabrando et al., 2017; Lo Turco et al., 2017). Furthermore, NDE techniques can be performed in a metric way as well. Thus, documentation techniques should not be separated, as they can both provide rich multipurpose anamnestic information if properly implemented. However, this repurposing of recorded information requires technical knowledge of the involved sensing techniques, from both a spatial and a radiometric aspect, or at least a sense of their capabilities and limitations. Therefore it is important to discuss the fundamental characteristics of both the reality-capturing and non-destructive evaluation technologies before evaluating their alternative uses or integration scenarios.

Rapid advances in sensor technologies and digital recording techniques have provided powerful geometric recording tools in recent years. These technological solutions include equipment for data acquisition, such as Global Navigation Satellite System (GNSS) receivers, total stations, digital cameras, scanners, etc., the

software for processing and managing the recorded data, and, of course, computer hardware, for running the software, storing information and presenting them in various data types (Georgopoulos & Stathopoulou, 2017). The technological developments in image-based and scanning-based 3D reality capturing have allowed for affordable, easy-to-use techniques, automatized and accurate software solutions (Remondino, 2011). However, the quality check of captured data and deriving metric products should always be prioritized during geometric heritage surveys to ensure the validity and suitability of results. Furthermore, the combination of digitization methods should always be considered as it can often support the results' optimization (Grussenmeyer et al., 2008; Remondino & Rizzi, 2010). The application of different geomatics techniques interrelates with the complexity and size of the heritage asset but actually is determined by numerous factors such as portability of available instrumentation, personnel experience, budget, accuracy specifications, and the integrability of recording methods (Evgenikou & Georgopoulos, 2015; Frisky et al., 2020; Teza et al., 2016). It should be mentioned that accuracy specifications vary depending on the stage of recording (reconnaissance, preliminary, detailed recording), the scale that records such as plans, cross-sections, orthophotos, and maps of materials/deterioration are being presented, and the level of detail (LoD) required for spatial information management in Geographical Information Systems (GIS) and Building Information Modeling (BIM) environments.

Alongside the advancements in reality capturing, significant technological developments have taken place in the field of (historic) materials NDE. Non-destructive inspection techniques operating at the visible, infrared, gigahertz, and terahertz ranges of the electromagnetic spectrum have become versatile and cost-effective and have been increasingly used in many fields, with innovation and development mainly being driven by industry. NDE sensors have different advantages and limitations depending on their operating principles and spectral range, but nevertheless, the continuous innovation and development of portable and compact devices will have a major role for future NDE instruments as these can increasingly facilitate the decision making process through agile on-site inspections (Wang et al., 2020). Figure 2.1 presents an overview of the investigated recording techniques and their operating wavelengths.
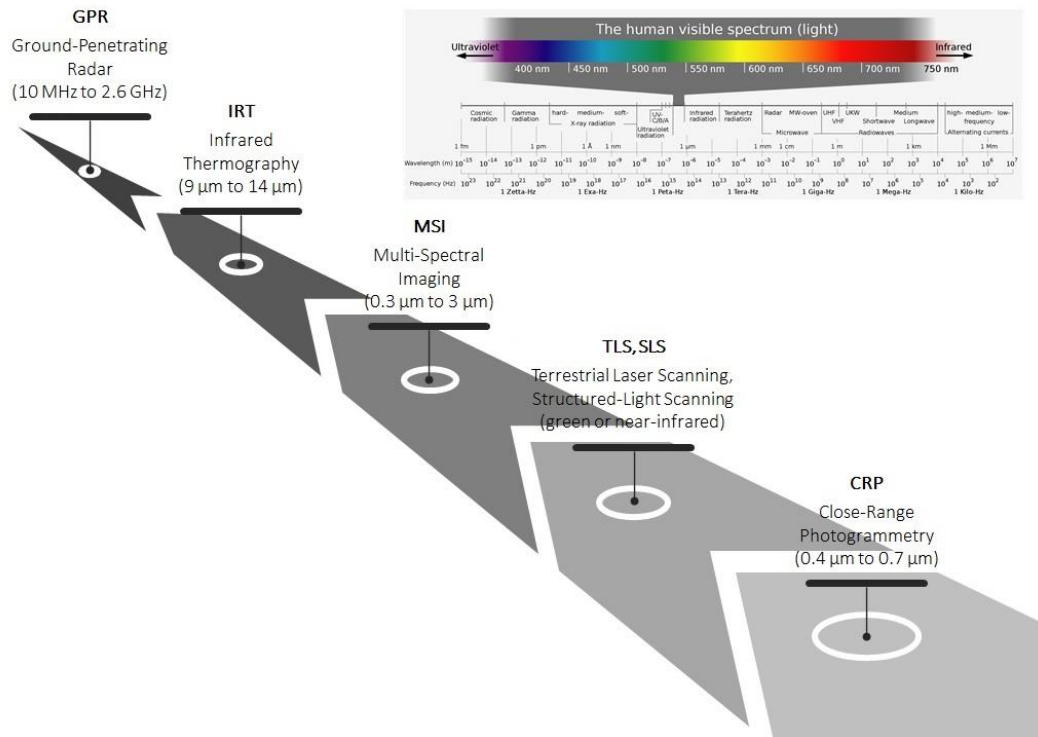
Figure 2.1. Recording techniques and operating wavelengths.

2.2.1 Scanning

Scanning techniques are based on active recording methods; they emit radiation through their own source and record the backscatter instead of sensing the reflected radiation originating from other sources (Grussenmeyer et al., 2016). Scanning sensors are also referred to as range sensors because they can estimate the range or depth of points in the 3D space. Depending on their scanning principles, which vary significantly, scanning techniques pose different advantages and disadvantages (Van Genechten, 2008). They generally enable recording in an accurate and fast manner and are relatively easy to use. Terrestrial Laser Scanning (TLS) and structured-light scanning (SLS) are the most common active sensing techniques for close-range recording heritage applications.

2.2.1.1 Terrestrial Laser Scanning

Terrestrial laser scanning describes a variety of range measuring techniques for surface scanning based on laser technology. TLS allows the analysis of real-world objects through a sampled or dense collection of data about their surfaces (XYZ coordinates of numerous points) and possibly about their appearance (color or intensity of backscattered energy). In a conventional laser scanning instrument, the scanner measures stepwise the surrounding scene with a fast vertical mirror rotation, and a slower horizontal instrument rotation. More specifics on the scanning mechanism and measuring techniques of TLS can be found in Fröhlich

and Mettenleiter (2004), Beraldin et al. (2010), and Petrie and Toth (2018). The advantage of TLS stems from the capacity to accurately record large datasets in short times, in comparison with other recording techniques. The collected 3D data (point clouds) are being used to reconstruct elevation models, 3D models, or to produce sections and drawings. TLS sensors are line-of-sight, and therefore multiple scans may be required to cover objects, structures, or their remains fully. The implementation of TLS means that the captured point clouds do not need to be scaled like photogrammetric models. There are three typologies of TLS instrumentation more widely used for cultural heritage documentation, operating on different recording principles:

(a) Time-of-Flight (ToF) scanners measure distances by recording the time difference between the emitted laser pulse and the received backscatter. These devices are characterized by lower acquisition speed and accuracy (5–6 mm) but are mainly suited for long-range acquisition.

(b) Phase Shift (PS) scanners estimate the difference of phase between the emitted and backscattered signal (sinusoidal wave patterns) of continuous laser pulses. These devices are characterized by short ranges (up to 300 m), better accuracy than ToF scanners (2–3 mm), and are thus suited for documentation at large scales.

(c) Triangulation scanners consist of a laser pulse emitting source and an optical sensor, which respectively transmit and record laser pulses from two different angles and determine the reflection points' positions by solving the triangles formed. These devices can be extremely precise, reaching accuracies up to fractions of a millimeter, while at the same time, the point clouds they produce can be very dense (i.e., up to 0.05 mm). However, their range is limited, not exceeding a couple of meters. Although there are such triangulation scanners that require to be mounted on a tripod, most of these devices are handheld, thus allowing detailed recording of small-sized complex objects, such as sculptures.

Table 2.2 presents a brief comparison between TLS devices available in 2021 (riegl.com/uploads/tx_pxpriegldownloads/RIEGL_VZ-400i_Datasheet_2020-10-06.pdf; leica-geosystems.com/datasheet/Leica_ScanStation_P30-P40_Plant_DS_en.pdf; media.faro.com/Tech-Sheet-FARO-Focus-Laser-Scanners-ENG.pdf; zf-laser.com/Z-F-IMAGER-R-5016.pdf; konicaminolta.com/vivid-910_vi-910_instruction_eng.pdf).

Table 2.2. Laser scanners.

	RIEGL VZ-400i	Leica ScanStation P30	FARO Focus^S 150	Z+F IMAGER 5016	Konica Minolta VIVID 910
Type	ToF	ToF	PS	PS	Triangulation
Range	1.5–800 m	0.4–270 m	0.6–150 m	0.3–365 m	0.6–2.5 m
Accuracy	5 mm	6 mm	3.5 mm	2 mm	0.3–1.8 mm
Precision	3 mm	2 mm	1 mm	1 mm	8–32 μm
Weight	9.7 kg	12.25* kg	4.2 kg	7.8 kg	11 kg

Note: *w/o batteries

Recording in 3D with TLS presupposes planning the data acquisition campaign in terms of identifying the surfaces to be covered, determining the optimal number and location of scanning positions and targets, and the management process of the point clouds (Barsanti et al., 2014). Optimally placed scanning positions should be selected to maximize cover and incidence angles, achieve the required resolution specifications while decreasing occlusions, and, if possible, the number of scans/scanning time (Metawie & Marzouk, 2020). Targets are positioned in overlapping areas to facilitate registration between scans. It is essential to maintain a good spatial distribution of scan targets not only on the *x-y* plane but also at the *z*-direction, to avoid multiplicity of solutions when solving the orientation between scans. Depending on the registration method between point clouds from different scanning positions, at least four correctly distributed targets at *xyz* should be positioned (Barber et al., 2003). Registration is usually performed through a coarse transformation based on common, often artificial, targets followed by a fine cloud-to-cloud closest neighbor-based registration (Bouaziz et al., 2013; Fabado et al., 2013; Lachat et al., 2018).

Regarding cultural heritage documentation, PS scanning devices have successfully been used for high-fidelity modeling of numerous geometrically complex monuments (Dorninger et al., 2013; Pritchard et al., 2017; Vacca et al.,

2012). The use of ToF scanning devices has become less frequent, although it is preferred for long-range applications such as geoarchaeological investigation of historical mines (Kincey et al., 2017), and is also used in applications that require acquisition from varying ranges in combination with PS scanners (Guarnieri et al., 2017; M. Monego et al., 2017, 2019). Nevertheless, the possibility of directly geo-referencing point clouds through the integration of ToF scanners and GNNS measurement systems provides a powerful 3D recording solution (Li et al., 2019). Both ToF and PS scanners have been extensively used for deformation monitoring of historical structures (Batur et al., 2020; Georgopoulos et al., 2016; Jaafar et al., 2017; Pesci et al., 2011, 2013). Triangulation scanning has been mainly employed in the detailed digitalization of sculptures (Balletti & Ballarin, 2019; Guidi et al., 2006; Levoy et al., 2000).

Laser scanning can also be a source of important radiometric data exploitable to facilitate non-destructive condition surveying further. Reflectivity values recorded by TLS—which express the intensity of the backscattered laser energy—have been recently explored for mapping the alterations of historical surfaces (Armesto-González et al., 2010; González-Jorge et al., 2012; Li & Cheng, 2018; Pozo-Antonio et al., 2019; Sánchez-Aparicio et al., 2018; Suchocki, 2020) as well as for surface moisture detection (Lerones et al., 2016; Suchocki et al., 2020; Suchocki & Katzer, 2018).

2.2.1.2 *Structured-Light Scanning*

Structured-light scanning instrumentation's operating principle is based on the projection of particular coded light patterns on the surface of an object and the computation of depth information by recording the projected pattern' deformations. This technique is based on triangulation but does not require the utilization of a laser source. The projected pattern covers either the entire surface of an object or a part of it which is captured either by a digital single-lens reflex (SLR) camera or an optical machine vision camera. The recorded scene is processed to retrieve the position of 3D points. The light patterns can consist of multiple fringes of different colors or complex patterns with curves, either time-encoded or space-encoded. SLS devices usually have a narrow Field-Of-View (FOV) that ranges from a few centimeters to a couple of meters, based on the components of the system and the calibration process. Depending on the complexity of the object's surface, its size, and the required density or final required accuracy, a considerable number of individual scans from various viewing angles may be necessary to completely cover the object area and acquire a complete and detailed visual representation. This technique may be accompanied by the collection of texture information and can lead to impressive results in terms of accuracy and productivity (Pavlidis et al., 2007). Table 2.3 presents a brief comparison between SLS devices available in the market in 2021 (artec3d.com/portable-3d-scanners/specifications; mantis-vision.com/handheld-3d-scanners; einscan.com/handheld-3d-scanner/einscan-pro-

hd/einscan-pro-hd-specs; creaform3d.com/handyscan-3d-silver-series-professional-3d/technical-specifications).

Table 2.3. Structured-light scanners.

	Artec3D Space Spider	Artec3D Eva	Mantis Vision F6 SMART	SHINNING 3D EinScan Pro HD	AMETEK HandySCAN 3D Silver
Accuracy	0.05 mm	0.1 mm	0.045 mm	0.04	0.04 mm
Resolution	0.1 mm	0.2 mm	0.2 - 3 mm	0.24	0.1 mm
Range	0.2 – 0.3 m	0.4 – 1 m	0.5 – 4 m	0.51 – 0.61 m	0.1 – 4 m
Color	Yes	Yes	Yes	Yes	No
Retail price	19,700	13,700	15,000	7,700	19,990

SLS solutions custom-made from off-the-shelf hardware components require calibration before every acquisition to determine the extrinsic and intrinsic parameters of the projector and the camera in order to achieve optimal metric results (Yamazoe et al., 2018). Commercially available SLS systems are often compact, easy to deploy, affordable, and easy to calibrate, and for these reasons, they are instrumental in dense resolution and high accuracy 3D photorealistic representation of archaeological finds on-site or while under restoration (García Molina et al., 2021; Graciano et al., 2017; McPherron et al., 2009). Comprehensive comparisons between widely available SLS handheld systems can be found in Kersten et al. (2016), Kersten et al. (2018), and Morena et al. (2018).

2.2.2 Digital Imaging

2.2.2.1 *Digital Reflex Cameras (Visible Region 400–700 nm)*

The digital still camera (DSC) consists of imaging optics, an image sensor, and a signal-processor that receives a signal from the image sensor and generates digital data that are compressed and stored on a memory device (Toyoda, 2006). Optical

radiation is detected in a DSC by converting the incoming radiation into an electrical output signal which is ultimately digitized. The image sensor consists of optical photodetectors that can detect incoming electromagnetic radiation. Two main focal plane array imaging sensors are used in DSCs: charge-coupled device (CCD) and complementary metal-oxide-semiconductor (CMOS). Their spectral response is situated from near-ultraviolet (NUV), around 320–370 nm, to about 1100 nm—the limit of near-infrared (NIR). Regardless of the type, all DSC image sensors consist of a 2D-photosite array to generate a digital photograph. The radiation-sensitive area of every photosite, in most cases a photodiode or photogate, collects the photons during the exposure time. On top of the sensor and below the array of micro-lenses that enable the collimation of the incident radiation to the photodiode (Holst, 1998; Theuwissen, 1995), manufacturers place a color filter array (CFA): a mosaic pattern of thin optical filters that are colored red, green or blue (Holst, 1998; Nakamura, 2006). As every pixel will initially have one color component (red or green or blue – Figure 2.2. A Bayer color filter array acquires Photosite-specific spectral information.), the other two components get interpolated from neighboring pixels to create a triplet of integer DNs (Digital Numbers) for every pixel. Generally, DSCs use a red-green-blue (RGB) pattern with a repeating group of four photodiodes. This arrangement is called a Bayer pattern. Bayer patterns typically feature two green filters per group of four enlarging the perceived sharpness of the digitally recorded scene (Bayer, 1975; Hunt, 2004). When obtaining an off-the-self DSC, the imaging sensor is moreover covered with a NUV–NIR blocking/cut-off filter (also called hot-mirror) that allows only visible light to pass. By applying this filter, the DSC manufacturer ensures that the sensor's array of photosensitive detectors will generate a photographic signal by mainly taking the visible EM radiation into account.
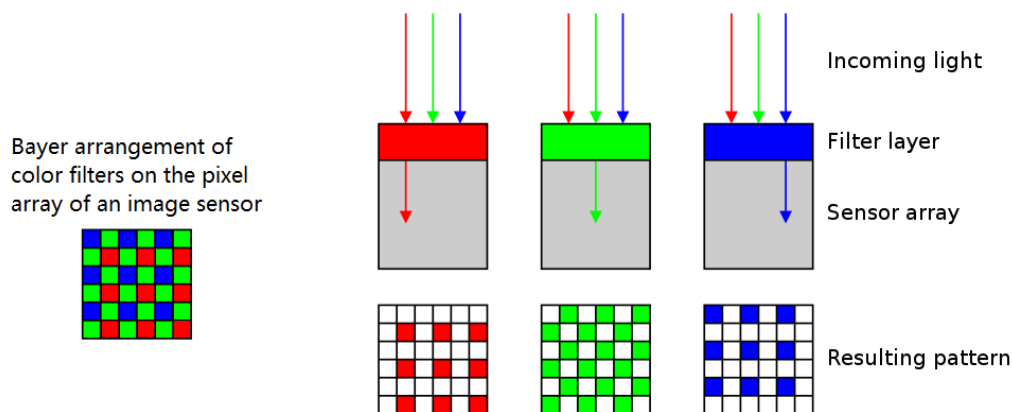
Figure 2.2. A Bayer color filter array acquires Photosite-specific spectral information.

The detector pitch is a fixed property of a sensor. It is the distance from the center of one photosite to the center of the neighboring photosite. Scene sampling distance (SSD) is the corresponding distance projected in object space, stating the horizontally or vertically measured scene distance between two consecutive sample

locations. The detector pitch can generate images with various SSDs. Amongst other factors, the SSD is determined by the scene's local topography, the distance of the camera to the scene (object distance), and the focal length f of the lens (Verhoeven, 2016). Table 2.4 presents a brief comparison of full-frame digital cameras available in the market in 2021.

Table 2.4. Full-frame digital cameras.

	Canon EOS R5	Canon EOS R6	Nikon Z7 II	Nikon D780	Sony a7 III
Body type	mirrorless	mirrorless	mirrorless	SLR	mirrorless
Resolution	8192×5464 max	5472×3648 max	8256×5504 max	6048×4024 max	6000×4000 max
Pixels	45 megapixels	20 megapixels	46 megapixels	25 megapixels	24 megapixels
Sensor size	36×24 mm	36×24 mm	35.9×23.9 mm	35.9×23.9 mm	35.8×23.8 mm
Pixel pitch	4.39 μm	6.58 μm	4.35 μm	5.94 μm	5.97 μm
Weight*	738 g	680 g	705 g	840 g	650 g

Note: *body weight including batteries; SLR: single lens-reflex

2.2.2.2 Multispectral Cameras (Near-ultraviolet to short-wave infrared region 350–3000 nm)

Multispectral sensors are passive systems that are able to record data in a small number of bands of the electromagnetic spectrum concurrently (Sabins & Ellis, 2020). The primary problem of these sensors is achieving multispectrality and accurate synchronization of all involved elements. Various configurations can be utilized to accomplish this (Del Pozo et al., 2017)—on the one hand, implementing a single device integrating several lenses (photodetector plus optical filter), where each lens records data for the spectral band permitted by its filter. On the other, there are single detector instruments utilizing a ring of band-specific filters that fixes the required input filter by means of small, rapid rotation. The advantage of the latter cameras over the former is the absence of eccentricity between the different captures; in this case, the multispectral image is conformed almost immediately with no need for parallax correction (distance between the lenses). Furthermore, in this case, the geometric corrections and the correction of systematic errors are made only for the existing lens, such that time can be saved. By contrast,

they have the important drawback of not being able to capture the multispectral dataset at the exact same moment of time.

Multispectral recording for heritage science and archaeology has been usually associated with single-detector instruments capable of recording radiance at multiple narrow spectral bands. Multispectral NIR/short-wave infrared (SWIR) imaging of antiquities and historical artwork has been explored with sensors that employ complementary metal-oxide-semiconductors (CMOS) based on InGaAs (indium gallium arsenide, 750–1700 nm) or PtSi (platinum silicide, 750–5000 nm) detectors, and NUV imaging with AlGaN (aluminum gallium nitride)-based developed since the 1990s (Bendada et al., 2015; Delaney et al., 2016; Fischer & Kakoulli, 2006; Liang, 2012).

Miniaturized multispectral instruments, initially designed for low-altitude aerial applications, are the ones recently employed for built heritage inspection. These instruments, usually operating at the wavelength range between 400–1100 nm, involve multi-camera configurations—multiple narrowband detectors (lenses) recording at 4–12 different spectral channels. Table 2.5 presents the characteristics of some miniaturized multispectral camera options that have been implemented for terrestrial applications.

Table 2.5. Multispectral cameras.

Make and Model	Configuration	Spectral Bands	Resolution
Buzzard Six Band	6-camera	Blue, Green, Red, NIR1, NIR2, NIR3	1280 × 1024 pixels
MicaSense RedEdge	5-camera	Blue, Green, Red, Red Edge, NIR	1280 × 960 pixels
Sal MAIA	9-camera	VIS, Violet, Blue, Green, Red, Red Edge, NIR1, NIR 2	1280 × 960 pixels
Tetracam ADC-Micro	single 3-band camera	Green, Red, NIR	2048 × 1536 pixels
Tetracam μ-MCA	4, 6 or 12-camera	user-selectable	1280 × 1024 pixels

Building materials have specific spectral signatures at different areas of the electromagnetic spectrum, which can be obtained under controlled laboratory conditions. Defects, deterioration, temperature variations, and moisture content

alter their normal and homogeneous spectral behavior. Therefore, recording spectral anomalies with multispectral imaging sensors facilitates the identification of these characteristics (Del Pozo et al., 2016). However, acquiring useful data of these surface alterations on heritage objects and structures poses considerable challenges, such as selecting the proper multispectral instruments, radiometrically and geometrically calibrating them (Del Pozo, et al., 2014; Guo et al., 2019), and identifying those environmental factors that affect the captured reflectance data, which makes the use of these technologies not frequent. Notably, Del Pozo et al. (2015) report using a Tetracam Mini-MCA6 to obtain multispectral ortho-mosaics to map a historical church's altered and unaltered materials and moisture. Furthermore, Kolokoussis et al., (2021) report implementing a system combining a visual and very near-infrared multispectral camera to map biodeterioration and corrosion on four medieval masonry heritage buildings.

The complementarity of RGB and NIR reflectance photography is often considered essential for inspecting damage on historic assets. However, the cost-to-resolution ratio of multispectral camera systems and the complex processing required for the collected data are often considered prohibitive in the heritage sector. Thus, the recording of multispectral reflectance data is sometimes simulated via modified commercial cameras (Falco, 2009; Verhoeven, 2008). Lerma et al. (2012), and Meroño et al. (2015), have used this method to obtain color and very near-visible images to identify alterations on historical stone monuments.

2.2.3 Photogrammetric Techniques

Modern close-range photogrammetry has evolved from metric cameras to more agile and cost-effective solutions. Photogrammetric techniques have substantially changed, incorporating high-resolution digital sensor technologies, new computing capabilities, multi-image processing techniques (coming from the field of computer vision), and even oblique-imagery acquisition (Chiabrando et al., 2015). Close-range photogrammetry has many uses: visualization, dissemination, preparation of models and 3D scenes for virtual and augmented reality applications, definition and obtainment of plans and measurements, support of excavation and restoration work, facilitation of numerical modeling and condition monitoring (Yilmaz et al., 2007; Marín-Buzon et al., 2021).

2.2.3.1   Digital Close-Range Photogrammetry 2D Applications

Digital close-range photogrammetry involves many methods whose application usually depends on the surface complexity and dimensions of the surveyed object. For relatively simple geometries, digital image rectification provides a non-expensive solution for orthoimage generation. A projective transformation-based rectification can be chosen for nearly planar surfaces, while polynomial and differential rectification methods can be helpful for more complex surfaces

(Hemmleb & Wiedemann, 1997). If the surface can be described as a parametric volume, such as a polyhedron, a cylinder, or a cone, the digital rectification can be realized with unwrapping techniques (Georgopoulos et al., 2020).

2.2.3.2 *Image-Based 3D Modeling and Rendering*

Ortho-rectification and surface developments are, in most cases, not sufficient for the complete geometric recording and photorealistic representation of a heritage asset. For this reason, a large number of images have to be simultaneously processed to cover it completely, producing homogeneous 3D geometric results and ortho-textures. The advancements in dense image matching (Remondino et al., 2014) and the improvements in camera sensor manufacturing (Markiewicz et al., 2019) have drastically improved image-based modeling (IBM) and 3D rendering solutions. The current approaches are based on computer vision algorithms and are generally robust, affordable, and agile, both in terms of implementation and the flexibility of scene-sampling distances and other parameters that can be adjusted according to requirements (Westoby et al., 2012). These approaches allow the use of non-metric and even lower-end sensors, and have widened the scope of 3D modeling and rendering applications for cultural heritage because of their increased automatization.

Multi-view IBM refers to digitization approaches for the generation of 3D point clouds and models from overlapping images using robust automated algorithms (Fonstad et al., 2013). Standard multi-view 3D reconstruction pipelines start with the detection and description of features on every image of an image dataset. Then follow Structure-from-Motion (SfM) implementations to estimate the camera positions and 3D point coordinates in a local coordinate system without a real scale, producing a sparse cloud. Subsequently, the 3D point cloud is further densified by employing dense image matching algorithms, and most pixels of the scene are reconstructed in a procedure typically called Dense Multi-View 3D Reconstruction (DMVR). Later the dense point cloud is meshed into a 3D model, usually using Delaunay triangulation algorithms, and textured by interpolating color information from the imagery dataset. Multi-view IBM approaches do not require implementing control points with known coordinates to function. However, the use of control points with known coordinates during the orientation improves the accuracy of the final results and is mandatory for acquiring measurements or for geo-referencing. For applications that do not demand high-accuracy metric products, the 3D models can be scaled based on measured reference lengths instead of using measured control point networks.

Multi-view SfM/DMVR-based recording techniques are cost-effective and can effectively involve oblique imagery from consumer-grade cameras to produce accurate and high-resolution spatial results (Hassani, 2015; Aicardi, 2018). In addition, they require low levels of supervision and user expertise. As a result, these

techniques have become widely used in heritage science and archaeology. Typical applications involve the documentation of archaeological remains (Douglass et al., 2015; López et al., 2016; McCarthy, 2014; Toprak et al., 2019), architecture (Adami et al., 2018; Columbu & Verdiani, 2014; Koutsoudis et al., 2014; Lo Brutto et al., 2017; Russo et al., 2019; Tucci et al., 2015) and other historical structures (Kouimtzoglou et al., 2017; Martínez et al., 2013; Peña-Villasenín et al., 2017), sculptures and monuments (Apollonio et al., 2014; Cardaci et al., 2019; Koehl & Fuchs, 2019; Girelli et al., 2019; Malik & Guidi, 2018), artifacts (Adamopoulos & Rinaudo, 2019; Gil-Melitón & Lerma, 2019; Kingsland, 2020; Santos et al., 2017), and virtual restorations or reconstructions (Chen et al., 2018; Fazio & Lo Brutto, 2020; Stampouloglou et al., 2020; Tsiafaki et al., 2016; Tucci et al., 2017).

2.2.4 Infrared Thermography

Infrared thermography is a close-range sensing technique well-established for inspection, testing, and monitoring. Infrared thermography is a noncontact and noninvasive technique that allows repeatability, prolonged use, and makes possible the comparison between areas of the target, and multitemporal application, thus presenting many advantages over other NDE technologies (Rosina & Grinzato, 2001; Moropoulou et al., 2018). Through thermal detectors, it measures levels of emitted infrared radiation at the long-wavelength infrared (LWIR) portion (7 μm – 14 μm) of the electromagnetic spectrum (Modest, 2013). Infrared radiation is emitted from all materials, at temperatures above absolute zero (i.e., T > -273.15 °C), due to their molecules' mobility. This infrared motion increases at higher material temperatures and reduces at lower temperatures. The intensity, frequency, and wavelength of infrared radiation depend on the temperature and magnitude of the source and the material's emissivity (Vollmer & Möllmann, 2018).
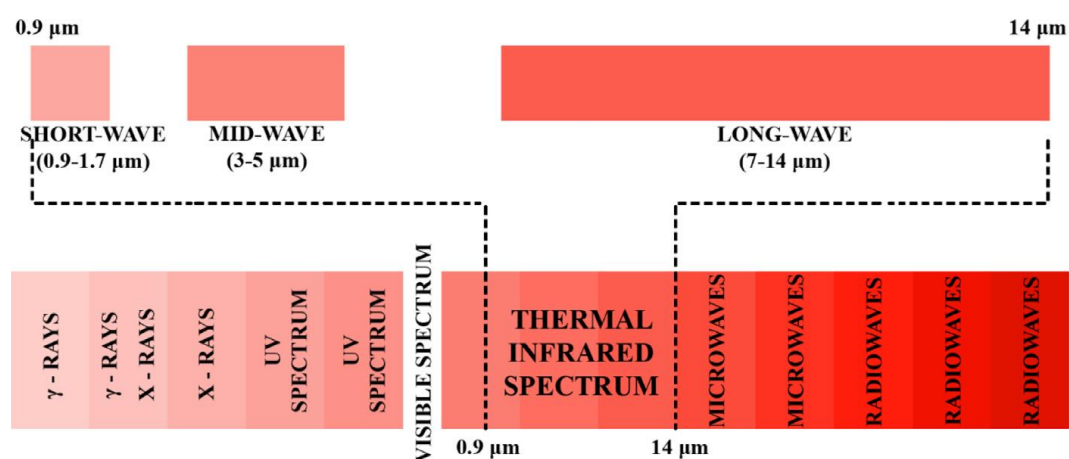
Figure 2.3. Detailed representation of the thermal infrared spectrum (Kirimtat & Krejcar, 2018).

A thermal camera is a device employing a thermal-infrared detector that records the radiant energy at the LWIR range, which falls onto the camera lens and converts

it to a measurable form (Figure 2.3). Using the radiation detector, the thermal camera displays a target's temperature, creating a visual representation, a two-dimensional thermal image from the detected average of incoming radiative energy intensities (Corsi, 2010). There are a few fundamental parameters that affect the performance of the thermal camera's sensor and subsequently image quality. They are sensor spectral range, or spectral response; spatial resolution, or pixel pitch; thermal sensitivity, or equivalent random noise level; intensity resolution, or number of intensity levels; scan speed, or update rate of the scanning mechanism (Kirimtat & Krejcar, 2018). The spectral range refers to the portion of the infrared spectrum in which the camera will be operationally active. Sensitivity is measured in Celsius degrees and reflects the minimum detectable temperature difference. Inspection-purposed temperature sensors with good sensitivity recognize temperature differences of even 0.040 °C (uncooled cameras). The intensity resolution is proportional to the number of hues or shades on the thermal camera screen. The higher the resolution, the more smoothly temperature changes will occur. If a target has sudden temperature changes, it will be due to the target itself and not to the camera. Most contemporary thermal imaging devices employ 12–17 μm pixel-pitch arrays. The spatial resolution of the thermal sensor depends on the number of pixels. This is similar to optical digital photography and defines the number of independent measurement points (Venkataraman & Raj, 2003). The resolution of the thermography cameras is considerably lower than that of the visible spectrum cameras, mostly only 160 x 120, 240 x 180, 320 x 240, 464 x 348, and up to 1280 x 1024 pixels for high-end instruments (field of view varies from 6° to 58°), and their cost is generally higher (Gade & Moeslund, 2014). Recently, more affordable thermal camera models have come into the market, including smartphone-adjustable low-resolution instruments. However, these inexpensive cameras provide lower accuracy, which makes them unusable for some applications. Table 2.6 presents some common thermal cameras purposed for infrastructure inspection available in the market in 2021 (flir.eu/products/t1020; flir.eu/products/t840; flir.eu/products/t540; fluke.com/product/thermal-cameras/tix580; thermal.com/seek_shotpro_specsheet-1.pdf).

Table 2.6. Thermal cameras for building inspections.

	FLIR T1020	FLIR T840	FLIR T540	Fluke TiX580	Seek ShotTPRO
Resolution	1024×768	640×480	464×348	640×480	320×240
FOV[1]	12 °/28 °/45 °/7	14 °/24 °/42 °	14 °/24 °/42 °	12 °/34 °/48 °	52 °
NETD[2]	< 20 mK	< 30 mK	< 50 mK	< 50 mK	< 70 mK
Accuracy	2%	2%	2%	2%	
Range	7.5–14 μm	7.5–14 μm	7.5–14 μm	7.5–14 μm	7.5–14 μm

Note: [1] Field-Of-View, [2] Noise Equivalent Temperature Difference (thermal sensitivity).

The typical way of displaying thermal images through a device or computer is generally either a black-and-white image or a colored image, where each color correlates with a temperature range (Figure 2.4). Thermal images are essentially a mapping of the distribution of infrared radiation, which originates from the different parts of the object. It is also possible to depict isothermal curves, which are lines at the boundary between two colors that reflect points with the same temperature. The thermal image processing software can provide heat profiles, temperature frequency histograms in each area, temperature differences from different images, points with maximum and minimum temperatures, as well as magnifications and filtering. Nevertheless, thermal infrared images can be difficult to interpret; in general, specific training is necessary.
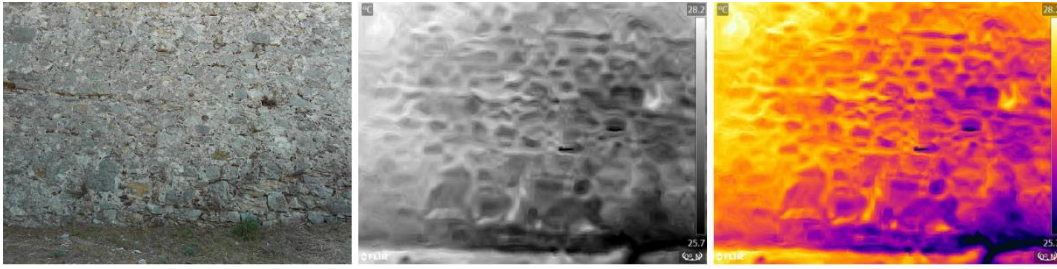
Figure 2.4. Image and corresponding thermogram (grey and iron color pallet) of an external façade at the Fort of Karababa in Chalkida, Greece.

To obtain high quality and useful thermographic data, it is usually necessary to take into account the prevailing conditions (ambient temperature, relative humidity, recording distance, materials emissivity factor) to adjust the camera, eliminating the noise errors they cause in measuring the temperature changes of a target's surface (Avdelidis & Moropoulou, 2003; Barreira et al., 2021). For this reason, infrared thermography should be used in controlled environments. Furthermore, the infrared thermal images are, in general, noisy and suffer from a low signal-to-noise ratio. Hence, various digital image processing (DIP) techniques are used to enhance acquired thermal images. For image enhancement purposes, various point operation algorithms like contrast stretching, histogram equalization, etc., can be used (Bagavathiappan et al., 2013). The objective of these algorithms is to stretch the histogram of an image, which will, in turn, increase the dynamical range of the image, thereby enhancing the contrast. Using advanced signal analysis techniques like thermographic signal reconstruction (TSR) and principal component analysis (PCA), defects of greater depths can be detected with higher thermal contrast. The texture analysis-based feature extraction of thermal images has been found to be helpful in image classification (Figure 2.5). For detection of hot spots, image segmentation and image thresholding are performed. Several segmentation and thresholding algorithms are used, and their choices depend on the nature of the image and the users' objective (Panella et al., 2020).
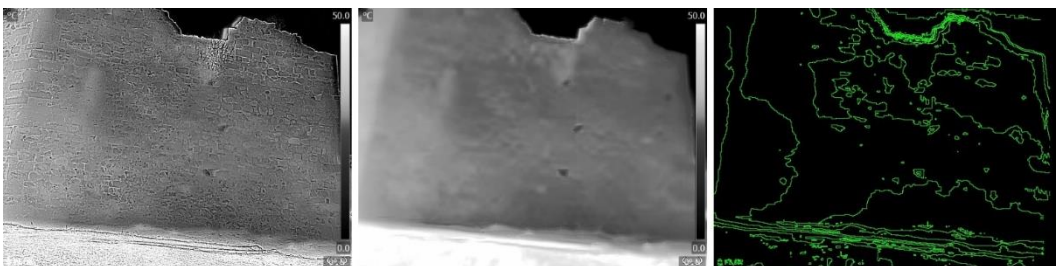
Figure 2.5. Thermogram elaboration for an external façade at the Fort of Karababa in Chalkida, Greece; (a) Multi-Spectral Dynamic image, (b) first Principal Component, and (c) thermal contours.

Infrared thermography records the emitted thermal radiation from a surface and enables the analysis of surface temperature patterns, revealing existing anomalies. In other terms, thermography aims to identify surface and near-surface areas of interest by observing local temperature differences using thermal sensors (Bogue,

2013). In infrared thermography, two different approaches are employed: active and passive (Usamentiaga et al., 2014). In active thermography, the target is subjected to thermal stimulation by an external radiation source. The heat propagation depends on the materials' thermal properties but also on subsurface irregularities, which result in temperature differences on the target's surface. In this scenario, measured thermal radiation comes from the thermal response of the target to the external excitation. This technique is applied in cases where the target is in thermal equilibrium and does not show surface temperature differences or if they are so small that they cannot be detected with passive testing (Shepard, 1997). Given the ability to control the intensity of the external energy source, the artificial thermal excitation can reach deeper into the object, and therefore information can be obtained from more internal layers. Active thermography has been implemented for the detection of cracks and defects of historic metallic objects and archaeological findings (De Capua et al., 2018; Mercuri et al., 2011; Mercuri et al., 2015; Morello & De Capua, 2016; Zhang et al., 2016), evaluation of conservation state and monitoring of wooden panel paintings (Sfarra et al., 2011, 2012; Yao, 2018), marqueterie (Chulkov et al., 2021) and mixed materials objects (Di Tuccio et al., 2015, Yousefi et al., 2019), frescoes (Bodnar et al., 2012; Cadelano et al., 2015; Grinzato, 2012; Sfarra et al., 2014; Yousefi et al., 2019), and mural paintings (Kordatos et al., 2013). Successful application of active thermography requires that the targeted surface is more or less homogeneous (has a defined high emissivity and thus low reflectivity) and that a good knowledge exists about the radiation coming from additional sources—direct or indirect (reflected)—and other environmental factors which may affect the measurements (Maierhofer et al., 2010; Tavukçuoğlu et al., 2010). This suggests inherent difficulties in applying active thermography for historic structures, especially for cases of highly deteriorated architectural elements, and thus less frequent use.

Passive thermography measures the thermal radiation emitted from the target's surface without external heat stimulation. Passive thermography is a technique often employed for building inspections when the measurement of temperature differences is a parameter for evaluating the existing structure's state of preservation or energy performance (Balaras & Argiriou, 2002). The documentation of irregular temperature distributions on a building's façade or structural element may help detect potential problems or damages by evaluating surface temperature changes compared with assigned reference values (Avdelidis & Moropoulou, 2004; Bisegna et al., 2014; Maldague, 2001). Recent critical developments in thermal sensor technology, in combination with other advantages stemming from its non-destructive nature, have led to extensive application in structural surveys of historic architecture (Brooke, 2018; Finco et al., 2019; Grinzato et al., 2002; Esteve, 2016; Kylili et al., 2014). Applications of passive infrared thermography regarding the investigation of historic buildings include identification of the distribution of original and replacement materials (Delegou et al., 2019; Lerma et al., 2018; Moropoulou et al., 2013), evaluation of the plaster conditions (de Freitas et al.,

2014; Moral Ruiz et al., 2018; Torres-González et al., 2021; Volinia, 2000), assessment of cracks (Briceño et al., 2019; Paoletti et al., 2013), characterization of material loss-induced features and other alterations on architectural surfaces (Danese et al., 2009; Delegou et al., 2019; Gomes-Heras et al., 2010; İnce et al., 2018), detection of moisture (Garrido et al., 2019; Grinzato et al., 2010; Lerma et al., 2011; Martínez-Garrido et al., 2018), location of hidden defects and subsurface construction (Glavaš et al., 2019; Ibarra-Castanedo et al., 2017; Spodek & Rosina, 2009), as well as evaluation of restoration and consolidation interventions (Alexakis et al., 2018; Avdelidis et al., 2003).

Built heritage passive thermographic applications are frequently implemented with independence of geometry in such a way that only the qualitative localization of the thermal phenomena is possible, using 2D thermograms. However, the importance of geometry in the field of NDE of existing structures is high when accurate quantification of investigated alteration-caused thermal anomalies or energy audit is required (Cho, 2015; Lagüela et al., 2016). Additionally, the acquisition of metric thermal information is a prerequisite for integrating with other proximally sensed data. In thermographic surveys, the geometric, and subsequently, the topological information is generally neglected for two main reasons: low spatial resolution of thermograms and difficulty of thermal sensors' calibration procedures. Thermal infrared metric recording of heritage structures has been explored with different approaches during the last two decades of research. The implementation of photogrammetric techniques has proven to be efficient in providing survey-grade thermal data, although at varied costs and complexity of methods involved.

2.2.4.1 *Thermogram Rectification*

Thermographic cameras, such as those used for building inspections (built on solid-state sensors), can be treated, in principle, as standard photogrammetric cameras. As in optical photography, a thermal image is subject to distortion effects (Hess et al., 2015). Thus, a correction to the original image is required (rectification) to absolve the optical aberrations introduced by the lens of the camera and the perspective distortions (González-Jorge et al., 2012; Luhmann et al., 2013; Rodríguez-Martín et al., 2016). After the rectification process, distances and areas can be measured with a constant scale on the thermal orthoimage (Franzen et al., 2013). The algorithm of the rectification process is the projective plane transformation.

$$X = \frac{a_0 + a_1 x' + a_2 y'}{c_1 x' + c_2 y' + 1}$$

$$Y = \frac{b_0 + b_1 x' + b_2 y'}{c_1 x' + c_2 y' + 1}$$

Where X, Y are the rectified (real) coordinates of a planar element, x′ and y′ are the pixel coordinates in the image, and a_0, a_1, a_2, b_0, b_1, b_2, c_1, c_2 are the mathematical coefficients of the projective matrix that encloses rotation, scale, translation, and perspective. In order to solve the system of equations, the knowledge of the coordinates of 4 points on the object is the only requirement for the determination of this projective matrix, as well as the calibration parameters of the camera. The geometric calibration for infrared cameras can be achieved with calibration targets made with burning lamps, materials of different emissivity, or printed patterns and can be more accurately calculated when repeating patterns are involved in calculating the distortion errors, instead of the calibration targets' corners or edges (Usamentiaga et al., 2017, 2018).

If the camera position and interior orientation (calibrated focal length, position of principal point, coefficients of lens distortion polynomial) are unknown, knowledge of the real (X, Y, Z) coordinates of at least 3 points on the object is necessary to compute the exterior orientation—the spatial resection of the camera position (Hanke & Grussenmeyer, 2002).

2.2.4.2 *Photogrammetry and Infrared Thermography*

The recent research in IBM and the availability of higher resolution thermographic cameras have allowed for improvements in 3D modeling and rendering with the use of thermal infrared images through the automation of the photogrammetric processes of image matching, orientation, dense points' reconstruction, and ortho-thermography generation. Lagüela et al. (2016) highlighted that certain specifications have to be met for the successful generation of 3D point clouds directly from thermograms, such as the acquisition of orthogonal and oblique images, which will be used for the accurate implementation of the photogrammetric principles, maintaining a robust geometry for the reconstruction, and exploitation of only the orthogonal images for texturing the 3D results, to avoid the inclination and convergence effect.

2.2.5 Ground-Penetrating Radar

Ground-penetrating radar (GPR) is a geophysical prospection technique widely used for NDE applications. GPR is a noninvasive measurement method that utilizes high-frequency (10 – 10,000 MHz) low-power electromagnetic pulse sequences to locate subsurface targets and interfaces between materials with different electrical and magnetic properties. The possibility of distinguishing between materials and mapping interfaces within visually opaque substances or earth material depends mainly on the propagation speed of electromagnetic waves and the difference in electrical conductivity and permeability between different materials (Daniels, 2005; Persico, 2014). GPR's operating principle is based on the generation of short-duration radio wave pulses by a transmitter, transmitted as wide beams at a speed

that depends on the electromagnetic properties of the medium. The electromagnetic signal propagates in a medium (such as masonry structures, stone, fresco, or subsoil) and, when it encounters an interface between materials with different electrical properties, then some of its energy is reflected or diffused back to the surface, some is refracted, and the residual energy of the pulse passes through the interface to deeper horizons, where this process can be repeated. The part of the wave reflected from an interface returns to the surface, where it is detected and recorded by the receiver (Daniels, 2004).

The duration and the waveform of the source pulse generated by the transmitter depend on the frequency of the antenna (Annan, 2003). The transmission frequency of the antenna affects the spatial resolution both at the longitudinal sense, as well as the lateral sense, which depends on the wavelength of the electromagnetic signal. Additionally, the operating depth is also affected by the transmission frequency and is inversely proportional to the spatial resolution. Specifically, the higher the center operating frequency used by the antenna, the shorter and narrower the pulse providing higher detection resolution between two points of the medium. However, since the attenuation of the electromagnetic signal increases with the frequency, the high-frequency waves cannot penetrate to great depths, resulting in a smaller operating depth. The opposite happens when a lower center frequency antenna is used, where in this case, the penetration depth is greater but with a clear reduction in the resolution achieved. Since radars can only measure in fractions of their wavelength, an object (or material alteration, or other anomalies) that is smaller than a minimum size will simply remain undetected (and undetectable). To be detectable, a target should be at least approximately 10%, or greater, of the dominant wavelength—a value that presents an estimation of GPR surveying accuracy. However, if the target's size is below 10% of the wavelength is may not detectable by a low-frequency antenna even though the radar may be capable of achieving the required depth, and it may also remain undetected by a high-frequency antenna if it lies far from the GPR system (Daniels, 2005; Utsi, 2017, pp. 13-26). Based on the above, it is understood that the selection of the appropriate operating frequency of the antenna depends on the purpose of the investigation and the requirements of the respective application of geo-radar inspection (**Table 2.7**).

Table 2.7. Depth range of penetration and resolution for different frequencies, in addition to their most common applications (Solla et al., 2016).

Central frequency	Depth (m)	Resolution (m)	Applications
2 GHz	0.5	0.0125	Concrete, rebar, pavement, cracking, voids
1 GHz	1.5	0.025	Concrete, rebar, pavement, cracking, voids
800 MHz	2.5	0.03	Concrete, voids, archaeology
500 MHz	5	0.05	Voids, archaeology, environmental
250 MHz	10	0.125	Archaeology, geological, environmental

| 100 MHz | 25 | 0.25 | Geological, mining |
| 50-25 MHz | 50 | 0.5–1 | Geological |

The resolution of a GPR system expresses its capacity to distinguish between two radar returns that are closely spaced (**Figure 2.6**). Longitudinal (range or depth) resolution is defined as the minimum vertical demarcation that two distinct reflective surfaces (or reflectors, or targets) must have in order to be detectable by a given antenna, and which is usually considered to be equal to 1/4 of the wavelength λ corresponding to the center frequency of the antenna. Specifically, the time difference between the two surfaces must be greater than half the pulse width W. The range resolution length is expressed as follows:

$$\Delta r \geq \frac{Wv}{4} \tag{2.1}$$

Lateral (angular or sideways displacement) resolution is a function of the signal propagation speed, the distance of the reflective surfaces from the transmitter and receiver antennas, and the pulse width. The lateral resolution length is as follows:

$$\Delta R \geq \sqrt{\frac{vrW}{2}} \tag{2.2}$$

where r is the distance to the reflective surface (Annan, 2009; Everett, 2013; pp. 239-278). Transect spacing, or the distance between adjacent radar survey lines, defines the resolution of the GPR survey at the direction perpendicular to the moving direction of the antenna and to the retrieved traces and varies from one GPR application to another. Even though for some applications, one or two survey lines may provide adequate, complex GPR application scenarios such as historic building inspections and archaeometry usually require more survey lines to reduce the potential of non-detection and to draw detailed conclusions (Pérez-Gracia et al., 2010). A helpful rule of thumb for GPR surveys is to allow a spacing between successive lines of no more than the width of the antenna being used (Utsi, 2017, pp. 73-82).
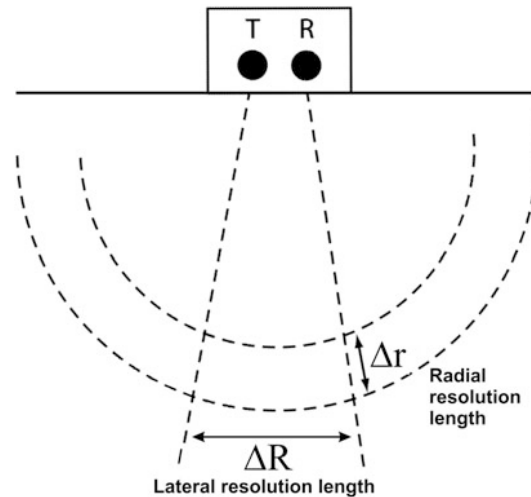
Figure 2.6. The two aspects to GPR resolution (Nobes & Deng, 2019).

As the, crucial for maintenance and damage repairing, inspection of historic buildings and structures must, in many cases, be minimally invasive, making some common and useful techniques' application not favorable, GPR has acquired great importance as a technique for revealing both historical and structural information about monumental heritage (Binda et al., 2003; Deiana, 2019; Işık et al., 2020; Lachowicz & Rucka, 2019; Lampropoulos et al., 2017; Leucci et al., 2012; Ludeno et al., 2020; Masini et al., 2007; Orlando & Slob, 2009; Pérez-Gracia et al., 2013; Pérez-Gracia et al., 2008; Ranalli et al., 2004; Solla et al., 2010). In particular, some issues of structural interest are the probable presence of fractures (Labropoulos & Moropoulou, 2013; Leucci et al., 2007), voids (Johnston et al., 2018), infiltrations of humidity (Leucci et al., 2006), or metallic bars (Masini et al., 2010) due to previous restoration works, often not adequately documented. These investigations are well-advised, especially if new restoration works are planned (Kanli et al., 2015; Rucka et al., 2016). In particular, the nondestructive investigations can provide information for addressing the restorations properly and enable one to check the success of the restoration works by means of post-intervention monitoring. Some issues of historical interest are the presence of tombs, walled rooms, and hidden pictures, mosaics, and floors (Pieraccini et al. 2006). In particular, the changes that a historic building or structure has undergone through the centuries have not been documented in many cases, or, in others, the documents have been lost. In some cases, the significance of a retrieved buried target can be both historical and structural, as, for example, in the case of a hidden crypt under a church. It is worth mentioning that GPR, in combination with other techniques, has also been applied for the condition assessment of stone sculptures. However, their geometry, which is usually more complex than building elements, imposes considerable challenges for geophysical surveying (Kadioglu & Kadioglu, 2010; Sambuelli et al., 2011; Dimitriadis et al., 2017; Cozzolino et al., 2020).

As can be seen from the above, a primary challenge of GPR is the interpretation of the collected data, which highly depends on the quality of performed

measurements, knowledge of the prospected medium dielectric properties, layering of the materials, and suitability of signal processing techniques (Martinho & Dionísio, 2014; Nobes & Deng, 2019). An equally important issue for retrieving useful information from GPR measurements is the dimensionality of presenting the results, with two-dimensional sections and three-dimensional representations being the most frequent visualization scenarios for historical building and sculpture state of preservation assessment.
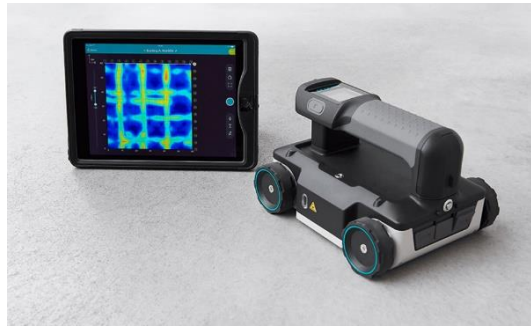
Figure 2.7. The portable Ground Penetrating Radar Proceq GP8000 (proceq.com/fr/produit/radar-a-penetration-de-sol-portable-proceq-gp8000).

2.2.5.1 *Two-Dimensional GPR Sections*

By performing a horizontal GPR scan along a linear profile on the *x*-axis, the recording of 2D data is obtained, which results from the successive individual one-dimensional traces retrieved along the path of the antenna. The retrieved data can be displayed as a two-dimensional image using a predefined color scale or palette (usually grayscale), matching the strength (range) of the recorded signal with a specific hue (brightness) of the selected palette (**Figure 2.7**). This image, also referred to as a 2D scan profile or radargram, represents a vertical section in the ground or structure where the horizontal axis corresponds to the position of the antenna along with the scan, and the vertical axis to the time of the electromagnetic wave's dual-path which corresponds to depth. Retrieving this type of result requires mechanical equipment with a built-in position encoder, which records the distance the antenna traverses along the scan line and the retrieval location of each individual trace (Blake, 1995).

Reflections from small or point scatterers below the ground, building elements, or other surfaces appear on the radargram as diffraction hyperbolas (**Figure 2.8**). This is because the electromagnetic waves are transmitted by the monostatic antenna in the form of a wide conical beam so that the receiver records the reflected signals from an undersurface target, not only when it passes just above the position where the target is located but also in multiple scans before and after this position. The shape of the retrieved hyperbola depends on the antenna layout, the depth at which the point scatterer is located, the speed at which the electromagnetic waves propagate, and the scan spacing selected by the operator. At greater depths, the

hyperbolae are larger because they consist of more scans. In addition, higher electromagnetic wave velocities (lower relative dielectric constant) produce wider hyperbolae and vice versa. Finally, the shorter the selected interval between scans (equivalent to a larger number of scans per unit of horizontal distance), the wider the hyperbolae recorded by point scatterers. The reflection always comes from the top of the point target, and the maximum (peak) of the recorded hyperbola curve corresponds precisely to the position where the target is. Usually, the larger the size (diameter) of a point scatterer, the stronger (wider) the hyperbolic reflection produced. The brightness or power of a hyperbolic reflection depends on the difference in electrical conductivity (and therefore, relative dielectric constant) between the medium and the target. As a general rule, the brightness of a reflection produced by an interface between two materials with different dielectric properties is proportional to the dielectric contrast between the two materials, which means that the higher the contrast, the stronger is the reflection produced (Annan, 2009; Solla et al., 2016).
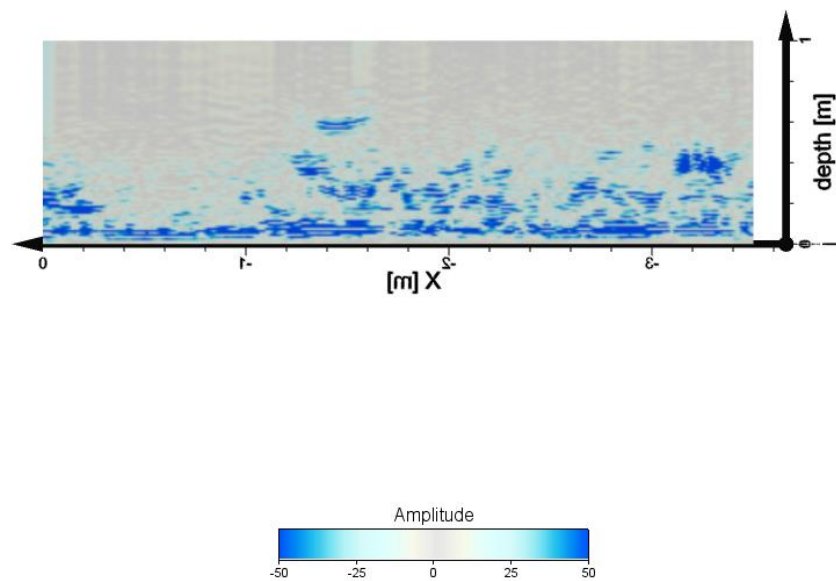
Figure 2.8. Two-dimensional visualization of GPR data: lower riverside façade of Castello del Valentino in Turin, Italy.

When scanning with GPR over a continuous boundary layer, the antenna receives consecutive reflections from the parts of said boundary, which in the retrieved 2D radargram appear in the form of a continuous reflecting layer that resembles the boundary layer. When the antenna crosses over an undersurface linear target of tubular shape transversely, i.e., perpendicular to the longitudinal axis of the target, then the recorded reflection will be hyperbolic, similar to the case of diffraction by point scatterers described above. If the antenna moves in parallel, i.e., along the target, then the reflection will appear as a continuous straight line, as long as the distance of the antenna from the subsurface target remains constant. Various subsurface inhomogeneities such as gaps (with air or water) produce strong

reflections without a specific shape. Reflection polarity can also provide important information when interpreting GPR results. The presence of various subsurface discontinuities, such as large air-filled voids or cracks, is detected in the form of strong inverted phase reflections with a black-and-white sequence of colors and an indeterminate shape. In the case of disintegrated areas with high levels of moisture or water-filled voids, then the generated reflections will be strong but will show the normal polarity sequence (white-black-white), which is very important for the identification and differentiation between specific types of deterioration when interpreting radargrams. In addition, these reflections are usually stronger and more visible than those mentioned above. This is due to the fact that, for example, if we consider a stone or concrete structure, the dielectric contrast between the diffuser and water is much higher than the dielectric contrast between concrete and air (Linford, 2006; Morris et al., 2019).

2.2.5.2 *Three-Dimensional Visualization of GPR Data*

By collecting multiple parallel 2D sections (time-slice method) or, in other words, by performing multiple horizontal scans on a *xy* axial plane of grid coordinates, a three-dimensional data set can be recorded that can be used to construct subsurface models (**Figure 2.9**), thus improving the efficiency and quality of the signal interpretation (Nuzzo et al., 2002). 3D data retrieval requires the use of a properly designed measurement grid; the dimensions and distance between successive scan lines on each axis are user-defined. The way in which scans are performed on the grid is usually towards one direction starting from the same straight line ("normal" way of scanning), although there may be the possibility of zig-zag measurements, in which the direction of the profiles changes alternately. Essentially, with this type of GPR scanning, the mapping of a subsurface area of interest is achieved, providing information about the location, depth, and orientation of the internal reflectors. Today most of the processing software with which the geo-radar systems are equipped with provides the possibility of displaying the 3D data in various ways, such as in the form of horizontal sections at defined time ranges that correspond to depths parallel to the recording level, or isosurfaces—interpolated surfaces that represent subsurface points with a constant reflection coefficient or amplitude (Leucci, 2019; Lualdi et al., 2003; Novo, 2013; Utsi, 2017, pp. 105-116).
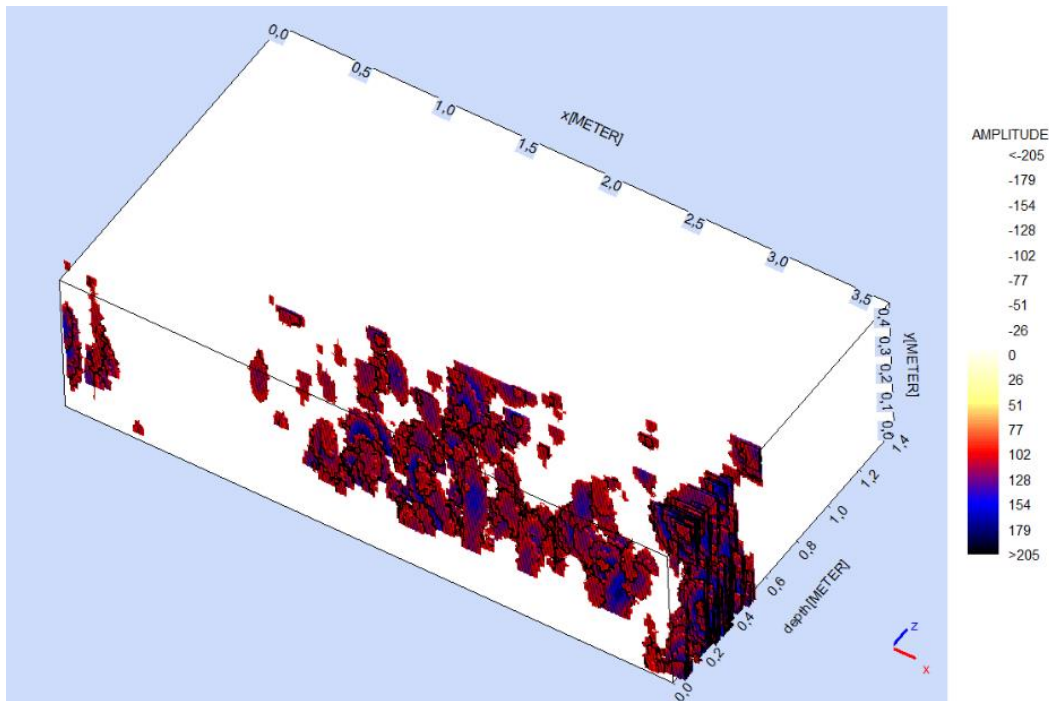
Figure 2.9. Three-dimensional visualization of GPR data: lower riverside façade of Castello del Valentino in Turin, Italy.

2.2.6 Mapping of Deterioration

Mapping does not constitute a sensing technique but can support the application of close-range sensing techniques for the condition inspection of heritage assets and depends on data recorded with various sensing techniques. Mapping is nevertheless recognized widely as a valuable non-destructive method useful for supporting preservation work, as it can be applied to all historic materials at different scales. It registers information about the surface patterns of structures and objects that can be later analyzed through computational systems. Mapping the materials and alterations of cultural heritage assets is frequently performed as a manual process that uses as background color photos.

Mapping stone antiquities and, in general, historical objects has seldom been performed digitally. Recently, after the introduction of laser scanning and multi-view dense reconstruction, direct mapping of sculptures' deterioration on high-resolution 3D models has been explored with specialized software (Ansel et al., 2016; Kozub & Kozub, 2016; Siedler & Vetter, 2015) and programs for editing 3D models (Pfeuffer et al., 2018) through the segmentation of areas showing different damage levels.

Mapping of architectural façades and other elements of historic structures is a common practice for cleaning and restoration works. It facilitates the description, registration, and quantification of the, often overlapping, multitude of surface patterns on historic structures. When performed in a digital, computerized manner,

it produces spatial information, entities with geometric attributes that can be correlated, compared, used to produce statistical information, and allow for the annotation of semantic data about the characteristics of materials and their decay. Traditionally, surface mapping is a technique manually performed inside computer-aided design (CAD) or GIS environments by describing the shape of surface patterns and organizing them into thematic layers (Brunetaud et al., 2012; Fitzner & Heinrichs, 2001; Inkpen et al., 2008; Janvier-Badosa et al., 2013, 2016; Mileto et al., 2015). An alternative way of mapping deterioration is the visualization of damage levels/indexes, which can be either accomplished directly or indirectly by analyzing the mapped deterioration patterns (Delgado Rodrigues, 2015; Fitzner et al., 2003; Franković et al., 2015; Germinario et al., 2020; Gizzi et al., 2016; Heinrichs, 2008; Heinrichs & Fitzner, 2011; Puy-Alquiza et al., 2021; Randazzo et al., 2020). The additional spatial annotation of lithotypes facilitates the association between materials and alteration (Adamopoulos et al., 2017; Delegou et al., 2013; Franković et al., 2015; Germinario et al., 2020; Gizzi et al., 2016; Gulotta & Toniolo, 2019; Hatir et al., 2019; Iandelli et al., 2021; İnce et al., 2018; Martínez-Martínez et al., 2017; McCabe et al., 2007; Puy-Alquiza et al., 2021). Mapping supports the interpretation of weathering phenomena when combined with data from non-destructive testing (Adamopoulos et al., 2017; Delegou et al., 2013; Fitzner et al., 2003; Heinrichs & Fitzner, 2011; İnce et al., 2018; Kilic, 2015; Martínez-Martínez et al., 2017; Silveira da Costa et al., 2021), laboratory mineralogical, chemical and physical characterization (Adamopoulos et al., 2017; Iandelli et al, 2021; Lazzerini et al., 2016; Martínez-Martínez et al., 2017; Puy-Alquiza et al., 2021), and environmental measurements (Adamopoulos et al., 2017; Gizzi et al., 2016; Gutiérrez-Carrillo; Heinrichs, 2008; Martínez-Martínez et al., 2017; Silveira da Costa et al., 2021). Mapping is typically a photo-based approach where a color photo, an orthorectified image, or an orthoimage-mosaic is used as a base map for designing the geometrical shape of surface patterns. The metric (accuracy, scale-dependent spatial resolution) and chromatic quality of this background are essential for identifying deterioration (Silveira da Costa et al., 2021; Thornbush & Viles, 2007). Thus, acquiring suitable images is crucial for successful deterioration mapping. However, not only true color images have been considered as base maps, but also images captured at portions of the electromagnetic spectrum beyond the visible.

References

Böhler, W. (2006). Comparison of 3D laser scanning and other 3D measurement techniques. In E. Baltsavias, A. Gruen, L. Van Gool, M. Pateraki (Eds.), Recording, Modeling and Visualization of Cultural Heritage (1st edition, pp. 89–99). Taylor & Francis.

Adami, A., Fassi, F., Fregonese, L., & Piana, M. (2018). Image-based techniques for the survey of mosaics in the St Mark's Basilica in Venice. Virtual Archaeology Review, 9(19), 1–20. https://doi.org/10.4995/var.2018.9087

Adamopoulos, E., & Rinaudo, F. (2019). An Updated Comparison on Contemporary Approaches for Digitization of Heritage Objects. Proceedings of the 2019 IMEKO TC-4 International Conference on Metrology for Archaeology and Cultural Heritage (2019 MetroArchaeo), 1–6. https://www.imeko.org/publications/tc4-Archaeo-2019/IMEKO-TC4-METROARCHAEO-2019-1.pdf

Adamopoulos, E., Tsilimantou, E., Keramidas, V., Apostolopoulou, M., Karoglou, M., Tapinaki, S., Ioannidis, C., Georgopoulos, A., & Moropoulou, A. (2017). Multi-Sensor Documentation of Metric and Qualitative Information of Historic Stone Structures. ISPRS Annals of Photogrammetry, Remote Sensing and Spatial Information Sciences, IV-2/W2, 1–8. https://doi.org/10.5194/isprs-annals-IV-2-W2-1-2017

Aicardi, I., Chiabrando, F., Maria Lingua, A., & Noardo, F. (2018). Recent trends in cultural heritage 3D survey: The photogrammetric computer vision approach. Journal of Cultural Heritage, 32, 257–266. https://doi.org/10.1016/j.culher.2017.11.006

Alexakis, Emm., Delegou, E. T., Lampropoulos, K. C., Apostolopoulou, M., Ntoutsi, I., & Moropoulou, A. (2018). NDT as a monitoring tool of the works progress and the assessment of materials and rehabilitation interventions at the Holy Aedicule of the Holy Sepulchre. Construction and Building Materials, 189, 512–526. https://doi.org/10.1016/j.conbuildmat.2018.09.007

Annan, A. P. (2003). Ground Penetrating Radar Principles, Procedures & Applications. Sensors & Software Inc.

Annan, A. P. (2009). Electromagnetic Principles of Ground Penetrating Radar. In H. M. Jol (Ed.), Ground penetrating radar: Theory and applications (1st edition, pp. 3–40). Elsevier Science.

Ansel, J., Gerling, C., Hofmeister, S., & Schick, S. (2016). Zwei Heiligenfiguren aus der katholischen Marienkirche in Bad Mergentheim: Ein außergewöhnliches Restaurierungsprojekt und der Testlauf für eine 3-D-Dokumentation. Denkmalpflege in Baden-Württemberg–Nachrichtenblatt der Landesdenkmalpflege, 45(3), 157–163. https://journals.ub.uni-heidelberg.de/index.php/nbdpfbw/article/view/32981/26674

Apollonio, F. I., Ballabeni, M., & Gaiani, M. (2014). Fuentes de color mejoradas para el modelado tridimensional de artefactos arqueológicos de tamaño medio localizados in situ. Virtual Archaeology Review, 5(10), 59–76. https://doi.org/10.4995/var.2014.4218

Armesto-González, J., Riveiro-Rodríguez, B., González-Aguilera, D., & Rivas-Brea, M. T. (2010). Terrestrial laser scanning intensity data applied to damage detection for historical buildings. Journal of Archaeological Science, 37(12), 3037–3047. https://doi.org/10.1016/j.jas.2010.06.031

Avdelidis, N. P., & Moropoulou, A. (2003). Emissivity considerations in building thermography. Energy and Buildings, 35(7), 663–667. https://doi.org/10.1016/S0378-7788(02)00210-4

Avdelidis, N. P., & Moropoulou, A. (2004). Applications of infrared thermography for the investigation of historic structures. Journal of Cultural Heritage, 5(1), 119–127. https://doi.org/10.1016/j.culher.2003.07.002

Avdelidis, N. P., Moropoulou, A., & Theoulakis, P. (2003). Detection of water deposits and movement in porous materials by infrared imaging. Infrared Physics & Technology, 44(3), 183–190. https://doi.org/10.1016/S1350-4495(02)00212-8

Bagavathiappan, S., Lahiri, B. B., Saravanan, T., Philip, J., & Jayakumar, T. (2013). Infrared thermography for condition monitoring – A review. Infrared Physics & Technology, 60, 35–55. https://doi.org/10.1016/j.infrared.2013.03.006

Balaras, C. A., & Argiriou, A. A. (2002). Infrared thermography for building diagnostics. Energy and Buildings, 34(2), 171–183. https://doi.org/10.1016/S0378-7788(01)00105-0

Balletti & Ballarin. (2019). An Application of Integrated 3D Technologies for Replicas in Cultural Heritage. ISPRS International Journal of Geo-Information, 8(6), 285. https://doi.org/10.3390/ijgi8060285

Barber, D., Mills, J., & Bryan, P. (2003). Towards a Standard Specification for Terrestrial Laser Scanning of Cultural Heritage. ISPRS - International Archives of the Photogrammetry, Remote Sensing and Spatial Information Sciences, XXXIV-5/C15. https://www.isprs.org/proceedings/xxxv/congress/comm5/papers/187.pdf

Barreira, E., Almeida, R. M. S. F., & Simões, M. L. (2021). Emissivity of Building Materials for Infrared Measurements. Sensors, 21(6), 1961. https://doi.org/10.3390/s21061961

Barsanti, S. G., Remondino, F., Fenández-Palacios, B. J., & Visintini, D. (2014). Critical Factors and Guidelines for 3D Surveying and Modelling in Cultural Heritage. International Journal of Heritage in the Digital Era, 3(1), 141–158. https://doi.org/10.1260/2047-4970.3.1.141

Batur, M., Yilmaz, O., & Ozener, H. (2020). A Case Study of Deformation Measurements of Istanbul Land Walls via Terrestrial Laser Scanning. IEEE Journal of Selected Topics in Applied Earth Observations and Remote Sensing, 13, 6362–6371. https://doi.org/10.1109/JSTARS.2020.3031675

Bayer, B. E. (1975). Color imaging array (Patent No. US3971065A). https://www.freepatentsonline.com/3971065.pdf

Bendada, A., Sfarra, S., Ibarra, C., Akhloufi, M., Caumes, P., Pradere, C., Batsale, C., & Maldague, X. (2015). Subsurface imaging for panel paintings inspection: A comparative study of the ultraviolet, the visible, the infrared and the terahertz spectra. Opto-Electronics Review, 23(1), 88–99. https://doi.org/10.1515/oere−2015−0013

Beraldin, J.-A., Blais, F., & Lohr, U. (2010). Laser Scanning Technology. In G. Vosselman & H.-G. Maas (Eds.), Airborne and Terrestrial Laser Scanning (pp. 1–42). Whittles Publishing.

Bertani, D., & Consolandi, L. (2006). High Resolution Imaging in the Near Infrared. In L. MacDonald (Ed.), Digital heritage: Applying digital imaging to cultural heritage (1st Edition, pp. 211–238). Elsevier (Butterworth-Heinemann).

Binda, L., Saisi, A., Tiraboschi, C., Valle, S., Colla, C., & Forde, M. (2003). Application of sonic and radar tests on the piers and walls of the Cathedral of Noto. Construction and Building Materials, 17(8), 613–627. https://doi.org/10.1016/S0950-0618(03)00056-4

Bisegna, F., Ambrosini, D., Paoletti, D., Sfarra, S., & Gugliermetti, F. (2014). A qualitative method for combining thermal imprints to emerging weak points of ancient wall structures by passive infrared thermography – A case study. Journal of Cultural Heritage, 15(2), 199–202. https://doi.org/10.1016/j.culher.2013.03.006

Blake, V. S. (1995). Image processing and interpretation of ground penetrating radar data. 600, 175–180.

Bodnar, J. L., Candoré, J. C., Nicolas, J. L., Szatanik, G., Detalle, V., & Vallet, J. M. (2012). Stimulated infrared thermography applied to help restoring mural paintings. NDT & E International, 49, 40–46. https://doi.org/10.1016/j.ndteint.2012.03.007

Bogue, R. (2013). Sensors for condition monitoring: A review of technologies and applications. Sensor Review, 33(4), 295–299. https://doi.org/10.1108/SR-05-2013-675

Boochs, F., Bentkowska-Kafel, A., & Wefers, S. (2016). Interdisciplinary Dialogue Towards an Enhanced Understanding of Optical Techniques for Recording Material Cultural Heritage—

Results of a COST Action. In C. E. Catalano & L. De Luca (Eds.), Proceedings of the 2016 EUROGRAPHICS Workshop on Graphics and Cultural Heritage (pp. 119–122). Eurographics Association. https://doi.org/10.2312/GCH.20161412

Bouaziz, S., Tagliasacchi, A., & Pauly, M. (2013). Sparse Iterative Closest Point. Computer Graphics Forum, 32(5), 113–123. https://doi.org/10.1111/cgf.12178

Briceño, C., Gonzales, M., Yaya, C., Moreira, S., & Aguilar, R. (2019). Preliminary Structural Diagnosis of the Sacsamarca Church in Peru Using Photogrammetry and IR Thermography. In R. Aguilar, S. Moreira, M. A. Pando, L. F. Ramos, & D. Torrealva (Eds.), Structural Analysis of Historical Constructions: An Interdisciplinary Approach (1st Edition, pp. 2431–2438). Springer International Publishing: Imprint: Springer. https://doi.org/10.1007/978-3-319-99441-3

Brooke, C. (2018). Thermal Imaging for the Archaeological Investigation of Historic Buildings. Remote Sensing, 10(9), 1401. https://doi.org/10.3390/rs10091401

Brunetaud, X., Luca, L. D., Janvier-Badosa, S., Beck, K., & Al-Mukhtar, M. (2012). Application of digital techniques in monument preservation. European Journal of Environmental and Civil Engineering, 16(5), 543–556. https://doi.org/10.1080/19648189.2012.676365

Cadelano, G., Bison, P., Bortolin, A., Ferrarini, G., Peron, F., Girotto, M., & Volinia, M. (2015). Monitoring of historical frescoes by timed infrared imaging analysis. Opto-Electronics Review, 23(1), 100–106. https://doi.org/10.1515/oere−2015−0012

Cardaci, A., Versaci, A., & Azzola, P. (2019). 3D Low-Cost Acquisition for the Knowledge of Cultural Heritage: The case Study of the Bust of San Nicola da Tolentino. The International Archives of the Photogrammetry, Remote Sensing and Spatial Information Sciences, XLII-2/W17, 93–100. https://doi.org/10.5194/isprs-archives-XLII-2-W17-93-2019

Chen, S., Yang, H., Wang, S., & Hu, Q. (2018). Surveying and Digital Restoration of Towering Architectural Heritage in Harsh Environments: A Case Study of the Millennium Ancient Watchtower in Tibet. Sustainability, 10(9), 3138. https://doi.org/10.3390/su10093138

Chiabrando, F., Donadio, E., & Rinaudo, F. (2015). SfM for Orthophoto to Generation: A Winning Approach for Cultural Heritage Knowledge. ISPRS - International Archives of the Photogrammetry, Remote Sensing and Spatial Information Sciences, XL-5/W7, 91–98. https://doi.org/10.5194/isprsarchives-XL-5-W7-91-2015

Chiabrando, F., Lo Turco, M., & Rinaudo, F. (2017). Modeling the Decay in an HBIM Starting from 3D Point Clouds. A Followed Approach for Cultural Heritage Knowledge. ISPRS - International Archives of the Photogrammetry, Remote Sensing and Spatial Information Sciences, XLII-2/W5, 605–612. https://doi.org/10.5194/isprs-archives-XLII-2-W5-605-2017

Cho, Y. K. (2015). 3D as-is building energy modeling and diagnostics: A review of the state-of-the-art. Advanced Engineering Informatics, 29, 184–195. https://doi.org/10.1016/j.aei.2015.03.004

Chulkov, A. O., Sfarra, S., Saeed, N., Peeters, J., Ibarra-Castanedo, C., Gargiulo, G., Steenackers, G., Maldague, X., Omar, M. A., & Vavilov. (2021). Evaluating quality of marquetries by applying active IR thermography and advanced signal processing. Journal of Thermal Analysis and Calorimetry, 143, 3835–3848. https://doi.org/10.1007/s10973-020-09326-2

Columbu, S., & Verdiani, G. (2014). Digital Survey and Material Analysis Strategies for Documenting, Monitoring and Study the Romanesque Churches in Sardinia, Italy. In M. Ioannides, N. Magnenat-Thalmann, E. Fink, R. Žarnić, A.-Y. Yen, & E. Quak (Eds.), Digital Heritage. Progress in Cultural Heritage: Documentation, Preservation, and Protection (Vol. 8740, pp. 446–453). Springer International Publishing. https://doi.org/10.1007/978-3-319-13695-0_43

Corsi, C. (2010). History highlights and future trends of infrared sensors. Journal of Modern Optics, 57(18), 1663–1686. https://doi.org/10.1080/09500341003693011

Cozzolino, M., Di Meo, A., Gentile, V., Mauriello, P., & Zullo, E. (2020). Combined Use of 3D Metric Survey and GPR for the Diagnosis of the Trapezophoros with Two Griffins Attacking a Doe of Ascoli Satriano (Foggia, Italy). Geosciences, 10(8), 307. https://doi.org/10.3390/geosciences10080307

Danese, M., Demšar, U., Masini, N., & Charlton, M. (2009). Investigating Material Decay of Historic Buidlings Using Visual Analytics with Multi-Temporal Infrared Thermographic Data. Archaeometry, 52(3), 482–501. https://doi.org/10.1111/j.1475-4754.2009.00485.x

Daniels, D. J. (2005). Ground Penetrating Radar. In K. Chang (Ed.), Encyclopedia of RF and Microwave Engineering (pp. 1833–1846). John Wiley & Sons, Inc. https://doi.org/10.1002/0471654507.eme152

Daniels, D. J. (Ed.). (2004). Ground Penetrating Radar. Institution of Engineering and Technology. https://doi.org/10.1049/PBRA015E

De Capua, C., Morello, R., & Jablonski, I. (2018). Active and eddy current pulsed thermography to detect surface crack and defect in historical and archaeological discoveries. Measurement, 116, 676–684. https://doi.org/10.1016/j.measurement.2017.10.035

de Freitas, S. S., de Freitas, V. P., & Barreira, E. (2014). Detection of façade plaster detachments using infrared thermography – A nondestructive technique. Construction and Building Materials, 70, 80–87. https://doi.org/10.1016/j.conbuildmat.2014.07.094

De Vos, P. J. (2017). Documenting for Posterity: Advocating the Use of Advanced Recording Techniques for Documentation in the Field of Building Archaeology. ISPRS Annals of Photogrammetry, Remote Sensing and Spatial Information Sciences, IV-2/W2, 59–65. https://doi.org/10.5194/isprs-annals-IV-2-W2-59-2017

Deiana, R. (2019). The contribution of geophysical prospecting to the multidisciplinary study of the Sarno Baths, Pompeii. Journal of Cultural Heritage, 40, 274–279. https://doi.org/10.1016/j.culher.2019.04.018

Delegou, E. T., Tsilimantou, E., Oikonomopoulou, E., Sayas, J., Ioannidis, C., & Moropoulou, A. (2013). Mapping of Building Materials and Consevation Interventions Using GIS: The Case of Sarantapicho Acropolis and Erimokastro Acropolis in Rhodes. International Journal of Heritage in the Digital Era, 2(4), 631–653. https://doi.org/10.1260/2047-4970.2.4.631

Delgado Rodrigues, J. (2015). Defining, mapping and assessing deterioration patterns in stone conservation projects. Journal of Cultural Heritage, 16, 267–275. https://doi.org/10.1016/j.culher.2014.06.007

Del Pozo, S., Herrero-Pascual, J., Felipe-García, B., Hernández-López, D., Rodríguez-Gonzálvez, P., & González-Aguilera, D. (2015). Multi-Sensor Radiometric Study to Detect Pathologies in Historical Buildings. ISPRS - International Archives of the Photogrammetry, Remote Sensing and Spatial Information Sciences, XL-5/W4, 193–200. https://doi.org/10.5194/isprsarchives-XL-5-W4-193-2015

Del Pozo, S., Rodríguez-Gonzálvez, P., Hernández-López, D., & Felipe-García, B. (2014). Vicarious Radiometric Calibration of a Multispectral Camera on Board an Unmanned Aerial System. Remote Sensing, 6(3), 1918–1937. https://doi.org/10.3390/rs6031918

Del Pozo, S., Rodríguez-Gonzálvez, P., Sánchez-Aparicio, L. J., Muñoz-Nieto, A., Hernández-López, D., Felipe-García, B., & González-Aguilera, D. (2017). Multispectral Imaging in Cultural Heritage Conservation. The International Archives of the Photogrammetry, Remote

Sensing and Spatial Information Sciences, XLII-2/W5, 155–162. https://doi.org/10.5194/isprs-archives-XLII-2-W5-155-2017

Del Pozo, S., Sánchez-Aparicio, L. J., Rodriguez-Gonzalvez, P., Herrero-Pascual, J., Muñoz-Nieto, A., & Gonzalez-Aguilera, D. (2016). Multispectral Imaging: Fundamentals, Principles and Methods of Damage Assessment in Constructions. In B. Riveiro & M. Solla (Eds.), Non-Destructive Techniques for the Evaluation of Structures and Infrastructure (1st Edition, pp. 139–166). CRC Press. https://doi.org/10.1201/b19024

Delaney, J. K., Thoury, M., Zeibel, J. G., Ricciardi, P., Morales, K. M., & Dooley, K. A. (2016). Visible and infrared imaging spectroscopy of paintings and improved reflectography. Heritage Science, 4(1), 6. https://doi.org/10.1186/s40494-016-0075-4

Delegou, E. T., Mourgi, G., Tsilimantou, E., Ioannidis, C., & Moropoulou, A. (2019). A Multidisciplinary Approach for Historic Buildings Diagnosis: The Case Study of the Kaisariani Monastery. Heritage, 2(2), 1211–1232. https://doi.org/10.3390/heritage2020079

Demas, M. (2000). Planning for Conservation and Management of Archaeological Sites: A Value-Based Approach. In Management Planning for Archaeological Sites (pp. 27–54). The Getty Conservation Institute.

Di Tuccio, M. C., Ludwig, N., Gargano, M., & Bernardi, A. (2015). Thermographic inspection of cracks in the mixed materials statue: Ratto delle Sabine. Heritage Science, 3(1), 10. https://doi.org/10.1186/s40494-015-0041-6

Dimitriadis, K., Moraitou, G., Styllas, M., Panagakos, I., Konstantakis, I., & Avlonitou, S. (2017). Ground-Penetrating Radar for Nondestructive Structural Imaging of Ancient Sculptures. In Nondestructive Techniques for the Assessment and Preservation of Historic Structures (1st Edition, pp. 249–255). CRC Press.

Dorninger, P., Nothegger, C., & Rasztovits, S. (2013). Efficient 3D Documentation of Neptune Fountain in The Park of Schönbrunn Palace at Millimeter Scale. ISPRS Annals of Photogrammetry, Remote Sensing and Spatial Information Sciences, II-5/W1, 103–108. https://doi.org/10.5194/isprsannals-II-5-W1-103-2013

Douglass, M., Lin, S., & Chodoronek, M. (2015). The Application of 3D Photogrammetry for In-Field Documentation of Archaeological Features. Advances in Archaeological Practice, 3(2), 136–152. https://doi.org/10.7183/2326-3768.3.2.136

Drury, P., & McPherson, A. (2008). Conservation Principles: Policies and Guidance for the Sustainable Management of the Historic Environment. English Heritage.

Esteve, S. T. (2016). Aplicación de la Termografía Infrarroja como ensayo no destructivo (END) en la restauración del patrimonio arquitectónico. Papeles del Partal: revista de restauración monumental, 8, 69–82.

Everett, M. E. (2013). Near-Surface Applied Geophysics. Cambridge University Press. https://doi.org/10.1017/CBO9781139088435

Evgenikou, V., & Georgopoulos, A. (2015). Investigating 3D Reconstruction Methods for Small Artifacts. ISPRS - International Archives of the Photogrammetry, Remote Sensing and Spatial Information Sciences, XL-5/W4, 101–108. https://doi.org/10.5194/isprsarchives-XL-5-W4-101-2015

Fabado, S., Seguí, A. E., Cabrelles, M., Navarro, S., García-De-San-Miguel, D., & Lerma, J. L. (2013). 3DVEM Software Modules for Efficient Management of Point Clouds and Photorealistic 3D Models. ISPRS - International Archives of the Photogrammetry, Remote Sensing and Spatial Information Sciences, XL-5/W2, 255–260. https://doi.org/10.5194/isprsarchives-XL-5-W2-255-2013

Falco, C. M. (2009). Invited Article: High resolution digital camera for infrared reflectography. Review of Scientific Instruments, 80(7), 071301. https://doi.org/10.1063/1.3174431

Fazio, L., & Lo Brutto, M. (2020). 3D survey for the archaeological study and virtual reconstruction of the "Sanctuary of Isis" in the ancient Lilybaeum (Italy). Virtual Archaeology Review, 11(22), 1–14. https://doi.org/10.4995/var.2020.11928

Finco, L., Girotto, M., Gomez Serito, M., & Volinia, M. (2019). Un contributo per la conoscenza della chiesa maggiore di Santa Giulitta: La termografia all'infrarosso per la lettura delle tessiture murarie e l'interpretazione delle fasi costruttive. In Un paesaggio medievale tra Piemonte e Liguria: Il sito di Santa Giulitta e l'Alta Val Tanaro / a cura di Paolo Demeglio (pp. 364–373). Insegna del Giglio. https://doi.org/10.36153/heredium01-045

Fischer, C., & Kakoulli, I. (2006). Multispectral and hyperspectral imaging technologies in conservation: Current research and potential applications. Studies in Conservation, 51(sup1), 3–16. https://doi.org/10.1179/sic.2006.51.Supplement-1.3

Fitzner, B. (2002). Damage diagnosis on stone monuments—In situ investigation and laboratory studies. Proceedings of the International Symposium of the Conservation of the Bangudae Petroglyph, 29–71.

Fitzner, B. (2004). Documentation and evaluation of stone damage on monuments. Proceedings of the 10th International Congress on Deterioration and Conservation of Stone, 2, 677–690.

Fitzner, B., & Heinrichs, K. (2001). Damage diagnosis on stone monuments – weathering forms, damage categories and damage indices. Acta Universitatis Carolinae, Geologica, 45(1), 12–13.

Fitzner, B., Heinrichs, K., & Bouchardiere, D. L. (2003). Weathering damage on Pharaonic sandstone monuments in Luxor-Egypt. Building and Environment, 38(9–10), 1089–1103. https://doi.org/10.1016/S0360-1323(03)00086-6

Franković, M., Novaković, N., & Matović, V. (2015). Damage quantification of built stone on Dark Gate (Belgrade, Serbia): Sample of damage index application for decay rate evaluation. Environmental Earth Sciences, 73(10), 6181–6193. https://doi.org/10.1007/s12665-014-3843-z

Franzen, C., Siedler, G., Franzen, C., & Vetter, S. (2013). Orthogonal IRT imaging. In A. C. Addison, G. Guidi, L. De Luca, S. pescarin (Eds.), Proceeding of the 2013 Digital Heritage International Congress (DigitalHeritage) (pp. 633–636), Institute of Electrical and Electronics Engineers. https://doi.org/10.1109/DigitalHeritage.2013.6743805

Frisky, A., Fajri, A., Brenner, S., & Sablatnig, R. (2020). Acquisition Evaluation on Outdoor Scanning for Archaeological Artifact Digitalization: Proceedings of the 15th International Joint Conference on Computer Vision, Imaging and Computer Graphics Theory and Applications, 792–799. https://doi.org/10.5220/0008964907920799

Fröhlich, C., & Mettenleiter, M. (2004). Terrestrial Laser Scanning – New Pesrpectives in 3D Surveying. ISPRS - International Archives of the Photogrammetry, Remote Sensing and Spatial Information Sciences, XXXVI-8/W2, 7–13.

Gade, R., & Moeslund, T. B. (2014). Thermal cameras and applications: A survey. Machine Vision and Applications, 25(1), 245–262. https://doi.org/10.1007/s00138-013-0570-5

Garrido, I., Lagüela, S., Sfarra, S., & Solla, M. (2019). Algorithms for the automatic detection and characterization of pathologies in heritage elements from thermographic images. ISPRS - International Archives of the Photogrammetry, Remote Sensing and Spatial Information Sciences, XLII-2/W15, 497–501. https://doi.org/10.5194/isprs-archives-XLII-2-W15-497-2019

Genovese, R. A. (2005). Architectural, archaeologic and environmental restoration planning methodology historic researches and techniques of survey aiming to conservation. Proceedings of the XX CIPA Symposium, 5.

Georgopoulos, A. (2018). Contemporary Digital Technologies at the Service of Cultural Heritage. In B. Chanda, S. Chaudhuri, & S. Chaudhury (Eds.), Heritage Preservation (pp. 1–20). Springer Singapore. https://doi.org/10.1007/978-981-10-7221-5_1

Georgopoulos, A., & Stathopoulou, E. K. (2017). Data Acquisition for 3D Geometric Recording: State of the Art and Recent Innovations. In M. L. Vincent, V. M. López-Menchero Bendicho, M. Ioannides, & T. E. Levy (Eds.), Heritage and Archaeology in the DigitalAge (pp. 1–26). Springer International Publishing. https://doi.org/10.1007/978-3-319-65370-9_1

Georgopoulos, A., Skamantzari, M., & Tapinaki, S. (2020). Digitally Developing Medieval Fortifications. Defensive Architecture of the Mediterranean Vol. X (FORTMED2020), 317–324. https://doi.org/10.4995/FORTMED2020.2020.11468

Georgopoulos, G. D., Telioni, E. C., & Tsontzou, A. (2016). The contribution of laser scanning technology in the estimation of ancient Greek monuments' deformations. Survey Review, 48(349), 303–308. https://doi.org/10.1179/1752270615Y.0000000035

Germinario, C., Gorrasi, M., Izzo, F., Langella, A., Limongiello, M., Mercurio, M., Musmeci, D., Santoriello, A., & Grifa, C. (2020). Damage Diagnosis of Ponte Rotto, a Roman Bridge Along the Ancient Appia. International Journal of Conservation Science, 11(Special Issue 1), 277–290.

Gil-Melitón, M., & Lerma, J. L. (2019). Patrimonio histórico militar: Digitalización 3D de la espada nazarí atribuida a Ali Atar. Virtual Archaeology Review, 10(20), 52–69. https://doi.org/10.4995/var.2019.10028

Girelli, V. A., Tini, M. A., Dellapasqua, M., & Bitelli, G. (2019). High resolution 3D acquisition and modelling in cultural heritage knowledge and restoration projects: The survey of the Fountain of Neptune in Bologna. ISPRS - International Archives of the Photogrammetry, Remote Sensing and Spatial Information Sciences, XLII-2/W11, 573–578. https://doi.org/10.5194/isprs-archives-XLII-2-W11-573-2019

Gizzi, F. T., Sileo, M., Biscione, M., Danese, M., & Alvarez de Buergo, M. (2016). The conservation state of the Sassi of Matera site (Southern Italy) and its correlation with the environmental conditions analysed through spatial analysis techniques. Journal of Cultural Heritage, 17, 61–74. https://doi.org/10.1016/j.culher.2015.05.002

Glavaš, H., Hadzima-Nyarko, M., Buljan, I. H., & Barić, T. (2019). Locating Hidden Elements in Walls of Cultural Heritage Buildings by Using Infrared Thermography. Buildings, 9(2), 32. https://doi.org/10.3390/buildings9020032

Gomes-Heras, M., Martinez-Perez, L., Fort, R., & Alvarez de Buergo, M. (2010). Decay assessment through thermographic analysis in architectural and archaeological heritage. Geophysical Research Abstracts Vol. 12, EGU2010-8596. EGU General Assembly 2010, Vienna. https://meetingorganizer.copernicus.org/EGU2010/EGU2010-8596.pdf

González-Jorge, H., Gonzalez-Aguilera, D., Rodriguez-Gonzalvez, P., & Arias, P. (2012). Monitoring biological crusts in civil engineering structures using intensity data from terrestrial laser scanners. Construction and Building Materials, 31, 119–128. https://doi.org/10.1016/j.conbuildmat.2011.12.053

González-Jorge, H., Lagüela, S., Krelling, P., Armesto, J., & Martínez-Sánchez, J. (2012). Single image rectification of thermal images for geometric studies in façade inspections. Infrared Physics & Technology, 55(5), 421–426. https://doi.org/10.1016/j.infrared.2012.05.003

Graciano, A., Ortega, L., Segura, R. J., & Feito, F. R. (2017). Digitization of religious artifacts with a structured light scanner. Virtual Archaeology Review, 8(17), 49. https://doi.org/10.4995/var.2016.4650

Grinzato, E. (2012). IR Thermography Applied to the Cultural Heritage Conservation. Proceedings of the 18th World Conference on Non-Destructive Testing, 46–49. https://www.ndt.net/article/wcndt2012/papers/598_wcndtfinal00597.pdf

Grinzato, E., Bison, P. G., & Marinetti, S. (2002). Monitoring of ancient buildings by the thermal method. Journal of Cultural Heritage, 3(1), 21–29. https://doi.org/10.1016/S1296-2074(02)01159-7

Grinzato, E., Cadelano, G., & Bison, P. (2010). Moisture map by IR thermography. Journal of Modern Optics, 57(18), 1770–1778. https://doi.org/10.1080/09500341003731597

Grussenmeyer, P., Landes, T., Doneus, M., & Lerma, J. L. (2016). Basics of Range-Based Modelling Techniques in Cultural Heritage 3D Recording. In E. Stylianidis & F. Remondino (Eds.), 3D Recording, Documentation and Management of Cultural Heritage (pp. 305–368). Whittles Publishing.

Grussenmeyer, P., Landes, T., Voegtle, T., & Ringle, K. (2008). Comparison Methods of Terrestrial Laser Scanning, Photogrammetry and Tacheometry Data for Recording of Cultural Heritage Buildings. The International Archives of the Photogrammetry, Remote Sensing and Spatial Information Sciences, XXXVI-5/C53, 213–218.

Guarnieri, A., Fissore, F., Masiero, A., & Vettore, A. (2017). From TLS Survey to 3D Solid Modeling for Documentation of Built Heritage: The Case Study of Porta Savonarola in Padua. ISPRS - International Archives of the Photogrammetry, Remote Sensing and Spatial Information Sciences, XLII-2/W5, 303–308. https://doi.org/10.5194/isprs-archives-XLII-2-W5-303-2017

Guidi, G., Frischer, B., Russo, M., Spinetti, A., Carosso, L., & Micoli, L. L. (2006). Three-dimensional acquisition of large and detailed cultural heritage objects. Machine Vision and Applications, 17(6), 349–360. https://doi.org/10.1007/s00138-006-0029-z

Gulotta, D., & Toniolo, L. (2019). Conservation of the Built Heritage: Pilot Site Approach to Design a Sustainable Process. Heritage, 2(1), 797–812. https://doi.org/10.3390/heritage2010052

Guo, Y., Senthilnath, J., Wu, W., Zhang, X., Zeng, Z., & Huang, H. (2019). Radiometric Calibration for Multispectral Camera of Different Imaging Conditions Mounted on a UAV Platform. Sustainability, 11(4), 978. https://doi.org/10.3390/su11040978

Gutiérrez-Carrillo, M. L., Bestué Cardiel, I., Molero Melgarejo, E., & Marcos Cobaleda, M. (2020). Pathologic and Risk Analysis of the Lojuela Castle (Granada-Spain): Methodology and Preventive Conservation for Medieval Earthen Fortifications. Applied Sciences, 10(18), 6491. https://doi.org/10.3390/app10186491

Hanke, K., & Grussenmeyer, P. (2002). Architectural Photogrammetry. In M. Kasser & Y. Egels (Eds.), Digital photogrammetry (pp. 300–339). Taylor & Francis. https://www.routledge.com/Digital-Photogrammetry/Egels-Kasser/p/book/9780748409457#

Hassani, F. (2015). Documentation of cultural heritage; techniques, potentials, and constraints. ISPRS - International Archives of the Photogrammetry, Remote Sensing and Spatial Information Sciences, XL-5/W7, 207–214. https://doi.org/10.5194/isprsarchives-XL-5-W7-207-2015

Hatır, M. E., Korkanç, M., & Başar, M. E. (2019). Evaluating the deterioration effects of building stones using NDT: The Küçükköy Church, Cappadocia Region, central Turkey. Bulletin of

Engineering Geology and the Environment, 78(5), 3465–3478. https://doi.org/10.1007/s10064-018-1339-x

Heinrichs, K. (2008). Diagnosis of weathering damage on rock-cut monuments in Petra, Jordan. Environmental Geology, 56(3–4), 643–675. https://doi.org/10.1007/s00254-008-1358-1

Heinrichs, K., & Fitzner, B. (2011). Assessment of weathering damage on the Petroglyphs of Cheonjeon-ri, Ulsan, Republic of Korea. Environmental Earth Sciences, 63(7–8), 1741–1761. https://doi.org/10.1007/s12665-010-0828-4

Hemmleb, M., & Wiedemann, A. (1997). Digital Rectification and Generation of Orthoimages in Architectural Photogrammetry. ISPRS - International Archives of the Photogrammetry, Remote Sensing and Spatial Information Sciences, XXXII-5/C1B, 261–267.

Hess, M., Vanoni, D., Petrovic, V., & Kuester, F. (2015). High-resolution thermal imaging methodology for non-destructive evaluation of historic structures. Infrared Physics & Technology, 73, 219–225. https://doi.org/10.1016/j.infrared.2015.09.020

Hirsenberger, H., Ranogajec, J., Vucetic, S., Lalic, B., & Gracanin, D. (2019). Collaborative projects in cultural heritage conservation – management challenges and risks. Journal of Cultural Heritage, 37, 215–224. https://doi.org/10.1016/j.culher.2018.10.006

Holst, G. C. (1999). CCD Arrays, Cameras and Displays (2nd Edition). SPIE Press.

Hunt, R. W. G. (2004). The reproduction of colour (6th Edition). Wiley. https://onlinelibrary.wiley.com/doi/book/10.1002/0470024275

Iandelli, N., Coli, M., Donigaglia, T., & Ciuffreda, A. L. (2021). An Unconventional Field Mapping Application: A Complete Opensource Workflow Solution Applied to Lithological Mapping of the Coatings of Cultural Heritage. ISPRS International Journal of Geo-Information, 10(6), 357. https://doi.org/10.3390/ijgi10060357

Ibarra-Castanedo, C., Sfarra, S., Klein, M., & Maldague, X. (2017). Solar loading thermography: Time-lapsed thermographic survey and advanced thermographic signal processing for the inspection of civil engineering and cultural heritage structures. Infrared Physics & Technology, 82, 56–74. https://doi.org/10.1016/j.infrared.2017.02.014

İnce, İ., Bozdağ, A., Tosunlar, M. B., Hatır, M. E., & Korkanç, M. (2018). Determination of deterioration of the main facade of the Ferit Paşa Cistern by non-destructive techniques (Konya, Turkey). Environmental Earth Sciences, 77, 420. https://doi.org/10.1007/s12665-018-7595-z

Inkpen, R., Duane, B., Burdett, J., & Yates, T. (2008). Assessing stone degradation using an integrated database and geographical information system (GIS). Environmental Geology, 56, 789–801. https://doi.org/10.1007/s00254-008-1309-x

Ioannidis, C., & Georgopoulos, A. (n.d.). Innovative Techniques for the Acquisition and Processing of Multisource Data for the Geometric Documentation of Monuments. 19.

Işık, N., Halifeoğlu, F. M., & İpek, S. (2020). Nondestructive testing techniques to evaluate the structural damage of historical city walls. Construction and Building Materials, 253, 119228. https://doi.org/10.1016/j.conbuildmat.2020.119228

Jaafar, H. A., Meng, X., Sowter, A., & Bryan, P. (2017). New approach for monitoring historic and heritage buildings: Using terrestrial laser scanning and generalised Procrustes analysis. Structural Control and Health Monitoring, 24(11), e1987. https://doi.org/10.1002/stc.1987

Janvier-Badosa, S., Beck, K., Brunetaud, X., & Al-Mukhtar, M. (2013). Historical Study of Chambord Castle: Basis for Establishing the Monument Health Record. International Journal of Architectural Heritage, 7(3), 247–260. https://doi.org/10.1080/15583058.2011.634959

Johnston, B., Ruffell, A., McKinley, J., & Warke, P. (2018). Detecting voids within a historical building façade: A comparative study of three high frequency GPR antenna. Journal of Cultural Heritage, 32, 117–123. https://doi.org/10.1016/j.culher.2018.02.003

Kadioglu, S., & Kadioglu, Y. K. (2010). Picturing internal fractures of historical statues using ground penetrating radar method. Advances in Geosciences, 24, 23–34. https://doi.org/10.5194/adgeo-24-23-2010

Kanli, A. I., Taller, G., Nagy, P., Tildy, P., Pronay, Z., & Toros, E. (2015). GPR survey for reinforcement of historical heritage construction at fire tower of Sopron. Journal of Applied Geophysics, 112, 79–90. https://doi.org/10.1016/j.jappgeo.2014.11.005

Kapsalas, P., Maravelaki-Kalaitzaki, P., Zervakis, M., Delegou, E. T., & Moropoulou, A. (2007). Optical inspection for quantification of decay on stone surfaces. NDT & E International, 40(1), 2–11. https://doi.org/10.1016/j.ndteint.2006.07.012

Kersten, T. P., Lindstaedt, M., & Starosta, D. (2018). Comparative Geometrical Accuracy Investigations of Hand-Held 3D Scanning Systems: An Update. ISPRS - International Archives of the Photogrammetry, Remote Sensing and Spatial Information Sciences, XLII–2, 487–494. https://doi.org/10.5194/isprs-archives-XLII-2-487-2018

Kersten, T. P., Przybilla, H.-J., & Lindstaedt, M. (2016). Investigations of the Geometrical Accuracy of Handheld 3D Scanning Systems. Photogrammetrie - Fernerkundung - Geoinformation, 2016(5–6), 271–283. https://doi.org/10.1127/pfg/2016/0305

Kilic, G. (2015). Using advanced NDT for historic buildings: Towards an integrated multidisciplinary health assessment strategy. Journal of Cultural Heritage, 16(4), 526–535. https://doi.org/10.1016/j.culher.2014.09.010

Kincey, M., Gerrard, C., & Warburton, J. (2017). Quantifying erosion of 'at risk' archaeological sites using repeat terrestrial laser scanning. Journal of Archaeological Science: Reports, 12, 405–424. https://doi.org/10.1016/j.jasrep.2017.02.003

Kingsland, K. (2020). Comparative analysis of digital photogrammetry software for cultural heritage. Digital Applications in Archaeology and Cultural Heritage, 18, e00157. https://doi.org/10.1016/j.daach.2020.e00157

Kioussi, A., Labropoulos, K., Karoglou, M., Moropoulou, A., & Zarnic, R. (2011). Recommendations and Strategies for the Establishment of a Guideline for Monument Documentation Harmonized with the Existing European Standards and Codes. Geoinformatics FCE CTU, 6, 178–184. https://doi.org/10.14311/gi.6.23

Kirimtat, A., & Krejcar, O. (2018). A review of infrared thermography for the investigation of building envelopes: Advances and prospects. Energy and Buildings, 176, 390–406. https://doi.org/10.1016/j.enbuild.2018.07.052

Koehl, M., & Fuchs, M. (2019). 3D Modelling of architectural blocks and antique sculptures for the conservation and the promotion of archaeological heritage – Experiments in Alsace. ISPRS - International Archives of the Photogrammetry, Remote Sensing and Spatial Information Sciences, XLII-2/W15, 625–632. https://doi.org/10.5194/isprs-archives-XLII-2-W15-625-2019

Kolokoussis, P., Skamantzari, M., Tapinaki, S., Karathanassi, V., & Georgopoulos, A. (2021). 3D and Hyperspectral Data Integration for Acessing Material Degradation in Medieval Masonry Heritage Buildings. The International Archives of the Photogrammetry, Remote Sensing and Spatial Information Sciences, XLIII-B2-2021, 583–590. https://doi.org/10.5194/isprs-archives-XLIII-B2-2021-583-2021

Kordatos, E. Z., Exarchos, D. A., Stavrakos, C., Moropoulou, A., & Matikas, T. E. (2013). Infrared thermographic inspection of murals and characterization of degradation in historic monuments. Construction and Building Materials, 48, 1261–1265. https://doi.org/10.1016/j.conbuildmat.2012.06.062

Kouimtzoglou, T., Stathopoulou, E. K., Agrafiotis, P., & Georgopoulos, A. (2017). Image-Based 3D Reconstruction Data as an Analysis and Documentation Tool for Architects: The case of Plaka Bridge in Greece. ISPRS - International Archives of the Photogrammetry, Remote Sensing and Spatial Information Sciences, XLII-2/W3, 391–397. https://doi.org/10.5194/isprs-archives-XLII-2-W3-391-2017

Koutsoudis, A., Vidmar, B., Ioannakis, G., Arnaoutoglou, F., Pavlidis, G., & Chamzas, C. (2014). Multi-image 3D reconstruction data evaluation. Journal of Cultural Heritage, 15(1), 73–79. https://doi.org/10.1016/j.culher.2012.12.003

Kozub, B., & Kozub, P. (2016). 3D photo monitoring as a long-term monument mapping method for stone sculptures. Science and art: a future for stone: Proceedings of the 13th International Congress on the Deterioration and Conservation of Stone Volume 2, 1031–1040.

Kylili, A., Fokaides, P. A., Christou, P., & Kalogirou, S. A. (2014). Infrared thermography (IRT) applications for building diagnostics: A review. Applied Energy, 134, 531–549. https://doi.org/10.1016/j.apenergy.2014.08.005

Labropoulos, K., & Moropoulou, A. (2013). Ground penetrating radar investigation of the bell tower of the church of the Holy Sepulchre. Construction and Building Materials, 47, 689–700. https://doi.org/10.1016/j.conbuildmat.2013.05.036

Lachat, E., Landes, T., & Grussenmeyer, P. (2018). Comparison of Point Cloud Registration Algorithms for Better Result Assessment – Towards an Open-Source Solution. ISPRS - International Archives of the Photogrammetry, Remote Sensing and Spatial Information Sciences, XLII–2, 551–558. https://doi.org/10.5194/isprs-archives-XLII-2-551-2018

Lachowicz, J., & Rucka, M. (2019). Diagnostics of pillars in St. Mary's Church (Gdańsk, Poland) using the GPR method. International Journal of Architectural Heritage, 13(8), 1223–1233. https://doi.org/10.1080/15583058.2018.1501117

Lagüela, S., Díaz-Vilariño, L., Roca, D., & Filgueira, A. (2016). Thermographic 3D Modeling of Existing Constructions. In B. Riveiro & M. Solla (Eds.), Non-Destructive Techniques for the Evaluation of Structures and Infrastructure (1st edition, pp. 233–252). CRC Press. https://www.routledge.com/Non-Destructive-Techniques-for-the-Evaluation-of-Structures-and-Infrastructure/Riveiro-Solla/p/book/9781138028104

Lampropoulos, K. C., Moropoulou, A., & Korres, M. (2017). Ground penetrating radar prospection of the construction phases of the Holy Aedicula of the Holy Sepulchre in correlation with architectural analysis. Construction and Building Materials, 155, 307–322. https://doi.org/10.1016/j.conbuildmat.2017.08.044

Lerma, C., Mas, Á., Gil, E., Vercher, J., & Torner, M. E. (2018). Quantitative Analysis Procedure for Building Materials in Historic Buildings by Applying Infrared Thermography. Russian Journal of Nondestructive Testing, 54(8), 601–609. https://doi.org/10.1134/S1061830918080065

Lerma, J. L. (Ed.). (2008). Theory and practice on Terrestrial Laser Scanning: Training material based on practical applications. Universidad Politecnica de Valencia Editorial. https://lirias.kuleuven.be/retrieve/122640

Lerma, J. L., Cabrelles, M., & Portalés, C. (2011). Multitemporal thermal analysis to detect moisture on a building façade. Construction and Building Materials, 25(5), 2190–2197. https://doi.org/10.1016/j.conbuildmat.2010.10.007

Lerma, J. L., Cabrelles, M., Akasheh, T. S., & Haddad, N. A. (2012). Documentation of Weathered Architectural Heritage with Visible, near Infrared, Thermal and Laser Scanning Data. International Journal of Heritage in the Digital Era, 1(2), 251–275. https://doi.org/10.1260/2047-4970.1.2.251

Lerones, P. M., Vélez, D. O., Rojo, F. G., Gómez-García-Bermejo, J., & Casanova, E. Z. (2016). Moisture detection in heritage buildings by 3D laser scanning. Studies in Conservation, 61(sup1), 46–54. https://doi.org/10.1179/2047058415Y.0000000017

Letellier, R. (2001). 'Bridging the Gap' Between the Information User and the Information Provider. The International Archives of the Photogrammetry, Remote Sensing and Spatial Information Sciences, XXXIV-5/C7, 18–22.

Letellier, R. (2015). Recording, Documentation and Information Management for the Conservation of Heritage Places (1st Edition). Routledge. https://doi.org/10.4324/9781315793917

Leucci, G. (2019). Nondestructive Testing Technologies for Cultural Heritage: Overview. In G. Leucci, Nondestructive Testing for Archaeology and Cultural Heritage (pp. 15–73). Springer International Publishing. https://doi.org/10.1007/978-3-030-01899-3_3

Leucci, G., Cataldo, R., & De Nunzio, G. (2006). Subsurface water-content identification in a crypt using GPR and comparison with microclimatic conditions. Near Surface Geophysics, 4(4), 207–213. https://doi.org/10.3997/1873-0604.2005045

Leucci, G., Cataldo, R., & De Nunzio, G. (2007). Assessment of fractures in some columns inside the crypt of the Cattedrale di Otranto using integrated geophysical methods. Journal of Archaeological Science, 34(2), 222–232. https://doi.org/10.1016/j.jas.2006.04.012

Leucci, G., Masini, N., & Persico, R. (2012). Time–frequency analysis of GPR data to investigate the damage of monumental buildings. Journal of Geophysics and Engineering, 9(4), S81–S91. https://doi.org/10.1088/1742-2132/9/4/S81

Levoy, M., Rusinkiewicz, S., Ginzton, M., Ginsberg, J., Pulli, K., Koller, D., Anderson, S., Shade, J., Curless, B., Pereira, L., Davis, J., & Fulk, D. (2000). The Digital Michelangelo Project: 3D Scanning of Large Statues. SIGGRAPH '00: Proceedings of the 27th Annual Conference on Computer Graphics and Interactive, 131–144. https://doi.org/10.1145/344779.344849

Lezzerini, M., Antonelli, F., Columbu, S., Gadducci, R., Marradi, A., Miriello, D., Parodi, L., Secchiari, L., & Lazzeri, A. (2016). Cultural Heritage Documentation and Conservation: Three-Dimensional (3D) Laser Scanning and Geographical Information System (GIS) Techniques for Thematic Mapping of Facade Stonework of St. Nicholas Church (Pisa, Italy). International Journal of Architectural Heritage, 10(1), 9–19. https://doi.org/10.1080/15583058.2014.924605

Li, L., Cao, X., He, Q., Sun, J., Jia, B., & Dong, X. (2019). A new 3D laser-scanning and GPS combined measurement system. Comptes Rendus Geoscience, 351(7), 508–516. https://doi.org/10.1016/j.crte.2019.09.004

Li, Q., & Cheng, X. (2018). Damage Detection for Historical Architectures Based on TLS Intensity Data. ISPRS - International Archives of the Photogrammetry, Remote Sensing and Spatial Information Sciences, XLII–3, 915–921. https://doi.org/10.5194/isprs-archives-XLII-3-915-2018

Liang, H. (2012). Advances in multispectral and hyperspectral imaging for archaeology and art conservation. Applied Physics A, 106(2), 309–323. https://doi.org/10.1007/s00339-011-6689-1

Linder, W. (2006). Digital photogrammetry: A practical course (2nd Edition). Springer.

Linford, N. (2006). The application of geophysical methods to archaeological prospection. Reports on Progress in Physics, 69(7), 2205–2257. https://doi.org/10.1088/0034-4885/69/7/R04

Lo Brutto, M., Dardanelli, G., Ebolese, D., Milazzo, G., Pipitone, C., & Sciortino, R. (2017). The Main Portal of the Cathedral of Monreale: First Geometric Analysis and Interpretive Assessment of Architectural Features. ISPRS - International Archives of the Photogrammetry, Remote Sensing and Spatial Information Sciences, XLII-5/W1, 381–387. https://doi.org/10.5194/isprs-archives-XLII-5-W1-381-2017

Lo Turco, M., Mattone, M., & Rinaudo, F. (2017). Metric Surveys and BIM Technologies to Record Decay Conditions. ISPRS - International Archives of the Photogrammetry, Remote Sensing and Spatial Information Sciences, XLII-5/W1, 261–268. https://doi.org/10.5194/isprs-archives-XLII-5-W1-261-2017

López, J. A. B., Jiménez, G. A., Romero, M. S., García, E. A., Martín, S. F., Medina, A. L., & Guerrero, J. A. E. (2016). 3D modelling in archaeology: The application of Structure from Motion methods to the study of the megalithic necropolis of Panoria (Granada, Spain). Journal of Archaeological Science: Reports, 10, 495–506. https://doi.org/10.1016/j.jasrep.2016.11.022

Lualdi, M., Zanzi, L., & Binda, L. (2003). Acquisition and processing requirements for high quality 3D reconstructions from GPR investigations. Non-Destructive Testing in Civil Engineering 2003. International Symposium on Non-Destructive Testing in Civil Engineering NDT-CE 2003, Berlin. http://citeseerx.ist.psu.edu/viewdoc/download?doi=10.1.1.508.5225&rep=rep1&type=pdf

Ludeno, G., Cavalagli, N., Ubertini, F., Soldovieri, F., & Catapano, I. (2020). On the Combined Use of Ground Penetrating Radar and Crack Meter Sensors for Structural Monitoring: Application to the Historical Consoli Palace in Gubbio, Italy. Surveys in Geophysics, 41(3), 647–667. https://doi.org/10.1007/s10712-019-09526-y

Luhmann, T., Piechel, J., & Roelfs, T. (2013). Geometric Calibration of Thermographic Cameras. In C. Kuenzer & S. Dech (Eds.), Thermal Infrared Remote Sensing (Vol. 17, pp. 27–42). Springer Netherlands. https://doi.org/10.1007/978-94-007-6639-6_2

Maierhofer, C., Röllig, M., & Krankenhagen, R. (2010). Integration of active thermography into the assessment of cultural heritage buildings. Journal of Modern Optics, 57(18), 1790–1802. https://doi.org/10.1080/09500341003703497

Maldague, X. (2001). Theory and practice of infrared technology for nondestructive testing. Wiley.

Malik, U. S., & Guidi, G. (2018). Massive 3D digitization of sculptures: Methodological approaches for improving efficiency. IOP Conference Series: Materials Science and Engineering, 364, 012015. https://doi.org/10.1088/1757-899X/364/1/012015

Marín-Buzón, C., Pérez-Romero, A., López-Castro, J. L., Ben Jerbania, I., & Manzano-Agugliaro, F. (2021). Photogrammetry as a New Scientific Tool in Archaeology: Worldwide Research Trends. Sustainability, 13(9), 5319. https://doi.org/10.3390/su13095319

Markiewicz, J., Pilarska, M., Łapiński, S., Kaliszewska, A., Bieńkowski, R., & Cena, A. (2019). Quality assessment of the use of a medium format camera in the investigation of wall paintings: An image-based approach. Measurement, 132, 224–237. https://doi.org/10.1016/j.measurement.2018.07.001

Martínez, S., Ortiz, J., Gil, M. L., & Rego, M. T. (2013). Recording Complex Structures Using Close Range Photogrammetry: The Cathedral of Santiago De Compostela. The Photogrammetric Record, 28(144), 375–395. https://doi.org/10.1111/phor.12040

Martínez-Garrido, M. I., Fort, R., Gómez-Heras, M., Valles-Iriso, J., & Varas-Muriel, M. J. (2018). A comprehensive study for moisture control in cultural heritage using non-destructive

techniques. Journal of Applied Geophysics, 155, 36–52. https://doi.org/10.1016/j.jappgeo.2018.03.008

Martínez-Martínez, J., Benavente, D., Jiménez Gutiérrez, S., García-del-Cura, M. A., & Ordóñez, S. (2017). Stone weathering under Mediterranean semiarid climate in the fortress of Nueva Tabarca island (Spain). Building and Environment, 121, 262–276. https://doi.org/10.1016/j.buildenv.2017.05.034

Martinho, E., & Dionísio, A. (2014). Main geophysical techniques used for non-destructive evaluation in cultural built heritage: A review. Journal of Geophysics and Engineering, 11(5), 053001. https://doi.org/10.1088/1742-2132/11/5/053001

Masciotta, M. G., Morais, M. J., Ramos, L. F., Oliveira, D. V., Sánchez-Aparicio, L. J., & González-Aguilera, D. (2019). A Digital-based Integrated Methodology for the Preventive Conservation of Cultural Heritage: The Experience of HeritageCare Project. International Journal of Architectural Heritage, 1–20. https://doi.org/10.1080/15583058.2019.1668985

Masini, N., Nuzzo, L., & Rizzo, E. (2007). GPR investigations for the study and the restoration of the rose window of Troia Cathedral (southern Italy). Near Surface Geophysics, 5(5), 287–300. https://doi.org/10.3997/1873-0604.2007010

Masini, N., Persico, R., & Rizzo, E. (2010). Some examples of GPR prospecting for monitoring of the monumental heritage. Journal of Geophysics and Engineering, 7(2), 190–199. https://doi.org/10.1088/1742-2132/7/2/S05

Mason, R., & Avrami, E. (2000). Heritage Values and Challeneges of Conservation Planning. In Management Planning for Archaeological Sites (pp. 13–26). The Getty Conservation Institute.

McCabe, S., Smith, B. J., & Warke, P. A. (2007). An holistic approach to the assessment of stone decay: Bonamargy Friary, Northern Ireland. Geological Society, London, Special Publications, 271, 77–86. https://doi.org/10.1144/GSL.SP.2007.271.01.09

McCarthy, J. (2014). Multi-image photogrammetry as a practical tool for cultural heritage survey and community engagement. Journal of Archaeological Science, 43, 175–185. https://doi.org/10.1016/j.jas.2014.01.010

McPherron, S. P., Gernat, T., & Hublin, J.-J. (2009). Structured light scanning for high-resolution documentation of in situ archaeological finds. Journal of Archaeological Science, 36(1), 19–24. https://doi.org/10.1016/j.jas.2008.06.028

Mercuri, F., Cicero, C., Orazi, N., Paoloni, S., Marinelli, M., & Zammit, U. (2015). Infrared Thermography Applied to the Study of Cultural Heritage. International Journal of Thermophysics, 36(5–6), 1189–1194. https://doi.org/10.1007/s10765-014-1645-x

Mercuri, F., Zammit, U., Orazi, N., Paoloni, S., Marinelli, M., & Scudieri, F. (2011). Active infrared thermography applied to the investigation of art and historic artefacts. Journal of Thermal Analysis and Calorimetry, 104(2), 475–485. https://doi.org/10.1007/s10973-011-1450-8

Meroño, J. E., Perea, A. J., Aguilera, M. J., & Laguna, A. M. (2015). Recognition of materials and damage on historical buildings using digital image classification. South African Journal of Science, 111(1/2), 1–9. https://doi.org/10.17159/sajs.2015/20140001

Metawie, M., & Marzouk, M. (2020). Optimizing Laser Scanning Positions in Buildings Exteriors: Heritage Building Applications. Journal of Civil Engineering and Management, 26(3), 304–314. https://doi.org/10.3846/jcem.2020.12006

Mezzino, D., Barazzetti, L., Santana Quintero, M., & El-Habashi, A. (2017). Digital Tools for Documenting and Conserving Bahrain's Built Heritage For Posterity. ISPRS - International Archives of the Photogrammetry, Remote Sensing and Spatial Information Sciences, XLII-2/W5, 513–519. https://doi.org/10.5194/isprs-archives-XLII-2-W5-513-2017

Mileto, C., Vegas, F., & Lerma, J. L. (2015). Multidisciplinary Studies, Crossreading and Transversal Use of Thermography: The Castle of Monzón (Huesca) as a case study. In P. Rodríguez-Navarro (Ed.), Defensive Architecture of the Mediterranean: Volume 2 (pp. 405–412). Universitat Politècnica de València. https://doi.org/10.4995/FORTMED2015.2015.1786

Modest, M. F. (2013). Radiative heat transfer (Third Edition). Academic Press.

Monego, M., Fabris, M., Menin, A., & Achilli, V. (2017). 3-D Survey Applied to Industrial Archaeology by TLS Methodology. ISPRS - International Archives of the Photogrammetry, Remote Sensing and Spatial Information Sciences, XLII-5/W1, 449–455. https://doi.org/10.5194/isprs-archives-XLII-5-W1-449-2017

Monego, M., Menin, A., Fabris, M., & Achilli, V. (2019). 3D survey of Sarno Baths (Pompeii) by integrated geomatic methodologies. Journal of Cultural Heritage, 40, 240–246. https://doi.org/10.1016/j.culher.2019.04.013

Moral Ruiz, C., García Bueno, A., Cultrone, G., & Almagro Gorbea, A. (2018). Análisis de alteraciones murarias y modificaciones relacionales en dos áreas del palacio de Pedro I del Alcázar de Sevilla mediante estudio documental y verificación termográfica. Arqueología de la Arquitectura, 15, 068. https://doi.org/10.3989/arq.arqt.2018.002

Morello, R., & De Capua, C. (2016). Thermography for non-invasive diagnosis of conservation state of archaeological discoveries. Proceedings of 6th EnvImeko - IMEKO TC19 Symposium on Environmental Instrumentation and Measurements, 26–29. https://www.imeko.org/publications/tc19-2016/IMEKO-TC19-2016-010.pdf

Morena, S., Barba, S., & Álvaro-Tordesillas, A. (2019). Shining 3D EinScan-Pro, Application and Validation in the Field of Cultural Heritage, from the Chillida-Leku Museum to the Archaeological Museum of Sarno. ISPRS - International Archives of the Photogrammetry, Remote Sensing and Spatial Information Sciences, XLII-2/W18, 135–142. https://doi.org/10.5194/isprs-archives-XLII-2-W18-135-2019

Moropoulou, A., Avdelidis, N., Karoglou, M., Delegou, E., Alexakis, E., & Keramidas, V. (2018). Multispectral Applications of Infrared Thermography in the Diagnosis and Protection of Built Cultural Heritage. Applied Sciences, 8(2), 284. https://doi.org/10.3390/app8020284

Moropoulou, A., Delegou, E. T., Avdelidis, N. P., & Athanasiadou, A. (2005). Integrated diagnostics using advanced in situ measuring technology. Cultural Heritage Conservation and Environmental Impact Assessment by Non-Destructive Testing and Micro-Analysis, 1116–1123. https://www.irbnet.de/daten/iconda/CIB_DC24683.pdf

Moropoulou, A., Labropoulos, K. C., Delegou, E. T., Karoglou, M., & Bakolas, A. (2013). Non-destructive techniques as a tool for the protection of built cultural heritage. Construction and Building Materials, 48, 1222–1239. https://doi.org/10.1016/j.conbuildmat.2013.03.044

Morris, I., Abdel-Jaber, H., & Glisic, B. (2019). Quantitative Attribute Analyses with Ground Penetrating Radar for Infrastructure Assessments and Structural Health Monitoring. Sensors, 19(7), 1637. https://doi.org/10.3390/s19071637

Nakamura, J. (2006). Basics of Image Sensors. In J. Nakamura (Ed.), Image Sensors and Signal Processing for Digital Still Cameras (1st Edition, pp. 53–94). CRC Press. https://doi.org/10.1201/9781420026856

Nobes, D. C., & Deng, J. (2019). Ground Penetrating Radar Resolution in Archaeological Geophysics. In G. El-Qady & M. Metwaly (Eds.), Archaeogeophysics (pp. 183–204). Springer International Publishing. https://doi.org/10.1007/978-3-319-78861-6_9

Novo, A. (2013). Ground-Penetrating Radar (GPR). In C. Corsi, B. Slapšak, & F. Vermeulen (Eds.), Good Practice in Archaeological Diagnostics (pp. 165–176). Springer International Publishing. https://doi.org/10.1007/978-3-319-01784-6_9

Nuzzo, L., Leucci, G., Negri, S., Carrozzo, M. T., & Quarta, T. (2002). Application of 3D visualization techniques in the analysis of GPR data for archaeology. Annals of Geophysics, 45(2), 321–337. https://doi.org/10.4401/ag-3517

Orlando, L., & Slob, E. (2009). Using multicomponent GPR to monitor cracks in a historical building. Journal of Applied Geophysics, 67(4), 327–334. https://doi.org/10.1016/j.jappgeo.2008.09.003

Palumbo, G. (2000). Threats and Challenges to the Architectural Heritage in the Mediterranean. In Management Planning for Archaeological Sites (pp. 3–12). The Getty Conservation Institute.

Panella, F. W., Pirinu, A., & Dattoma, V. (2020). A Brief Review and Advances of Thermographic Image - Processing Methods for IRT Inspection: A Case of Study on GFRP Plate. Experimental Techniques. https://doi.org/10.1007/s40799-020-00414-4

Paoletti, D., Ambrosini, D., Sfarra, S., & Bisegna, F. (2013). Preventive thermographic diagnosis of historical buildings for consolidation. Journal of Cultural Heritage, 14(2), 116–121. https://doi.org/10.1016/j.culher.2012.05.005

Pavlidis, G., Koutsoudis, A., Arnaoutoglou, F., Tsioukas, V., & Chamzas, C. (2007). Methods for 3D digitization of Cultural Heritage. Journal of Cultural Heritage, 8(1), 93–98. https://doi.org/10.1016/j.culher.2006.10.007

Peña-Villasenín, S., Gil-Docampo, M., & Ortiz-Sanz, J. (2017). 3-D Modeling of Historic Façades Using SFM Photogrammetry Metric Documentation of Different Building Types of a Historic Center. International Journal of Architectural Heritage, 11(6), 871–890. https://doi.org/10.1080/15583058.2017.1317884

Pérez-Gracia, V., Caselles, J. O., Clapés, J., Martinez, G., & Osorio, R. (2013). Non-destructive analysis in cultural heritage buildings: Evaluating the Mallorca cathedral supporting structures. NDT & E International, 59, 40–47. https://doi.org/10.1016/j.ndteint.2013.04.014

Pérez-Gracia, V., Di Capua, D., Gonzalez-Drigo, R., Caselles, O., Pujades, L. G., & Salinas, V. (2010). GPR resolution in cultural heritage applications. Proceedings of the XIII Internarional Conference on Ground Penetrating Radar, 1–5. https://doi.org/10.1109/ICGPR.2010.5550199

Pérez-Gracia, V., García, F., Pujades, L. G., González Drigo, R., & Di Capua, D. (2008). GPR survey to study the restoration of a Roman monument. Journal of Cultural Heritage, 9(1), 89–96. https://doi.org/10.1016/j.culher.2007.09.003

Persico, R. (2014). Introduction to ground penetrating radar: Inverse scattering and data processing. Wiley-IEEE Press. https://ieeexplore.ieee.org/book/6836128

Pesci, A., Casula, G., & Boschi, E. (2011). Laser scanning the Garisenda and Asinelli towers in Bologna (Italy): Detailed deformation patterns of two ancient leaning buildings. Journal of Cultural Heritage, 12(2), 117–127. https://doi.org/10.1016/j.culher.2011.01.002

Pesci, A., Teza, G., Bonali, E., Casula, G., & Boschi, E. (2013). A laser scanning-based method for fast estimation of seismic-induced building deformations. ISPRS Journal of Photogrammetry and Remote Sensing, 79, 185–198. https://doi.org/10.1016/j.isprsjprs.2013.02.021

Petrie, G., & Toth, C. K. (2018). Terrestrial Laser Scanners. In J. Shan & C. K. Toth (Eds.), Topographic Laser Ranging and Scanning: Principles and Processing (2nd ed., pp. 87–128). CRC Press.

Pfeuffer, C., Rahrig, M., Snethlage, R., & Drewello, R. (2018). 3D mapping as a tool for the planning of preservation measures on sculptures made of natural stone. Environmental Earth Sciences, 77(8), 312. https://doi.org/10.1007/s12665-018-7479-2

Pieraccini, M., Noferini, L., Mecatti, D., Luzi, G., Atzeni, C., Persico, R., & Soldovieri, F. (2006). Advanced Processing Techniques for Step-Frequency Continuous-Wave Penetrating Radar: The Case Study of "Palazzo Vecchio" Walls (Firenze, Italy). Research in Nondestructive Evaluation, 17(2), 71–83. https://doi.org/10.1080/09349840600689475

Pozo-Antonio, J. S., Puente, I., Pereira, M. F. C., & Rocha, C. S. A. (2019). Quantification and mapping of deterioration patterns on granite surfaces by means of mobile LiDAR data. Measurement, 140, 227–236. https://doi.org/10.1016/j.measurement.2019.03.066

Pritchard, D., Sperner, J., Hoepner, S., & Tenschert, R. (2017). Terrestrial laser scanning for heritage conservation:the Cologne Cathedral documentation project. ISPRS Annals of Photogrammetry, Remote Sensing and Spatial Information Sciences, IV-2/W2, 213–220. https://doi.org/10.5194/isprs-annals-IV-2-W2-213-2017

Puy-Alquiza, M. J., Ordaz Zubia, V. Y., Aviles, R. M., & Salazar-Hernández, Ma. D. C. (2021). Damage detection historical building using mapping method in music school of the University of Guanajuato, Mexico. Mechanics of Advanced Materials and Structures, 28(10), 1049–1060. https://doi.org/10.1080/15376494.2019.1629049

Ranalli, D., Scozzafava, M., & Tallini, M. (2004). Ground penetrating radar investigations for the restoration of historic buildings: The case study of the Collemaggio Basilica (L'Aquila, Italy). Journal of Cultural Heritage, 5(1), 91–99. https://doi.org/10.1016/j.culher.2003.05.001

Randazzo, L., Collina, M., Ricca, M., Barbieri, L., Bruno, F., Arcudi, A., & La Russa, M. F. (2020). Damage Indices and Photogrammetry for Decay Assessment of Stone-Built Cultural Heritage: The Case Study of the San Domenico Church Main Entrance Portal (South Calabria, Italy). Sustainability, 12(12), 5198. https://doi.org/10.3390/su12125198

Remondino, F. (2011). Heritage Recording and 3D Modeling with Photogrammetry and 3D Scanning. Remote Sensing, 3(6), 1104–1138. https://doi.org/10.3390/rs3061104

Remondino, F., & Rizzi, A. (2010). Reality-based 3D documentation of natural and cultural heritage sites—Techniques, problems, and examples. Applied Geomatics, 2(3), 85–100. https://doi.org/10.1007/s12518-010-0025-x

Remondino, F., Spera, M. G., Nocerino, E., Menna, F., & Nex, F. (2014). State of the art in high density image matching. The Photogrammetric Record, 29(146), 144–166. https://doi.org/10.1111/phor.12063

Rodríguez-Martín, M., Lagüela, S., González-Aguilera, D., & Martínez, J. (2016). Thermographic test for the geometric characterization of cracks in welding using IR image rectification. Automation in Construction, 61, 58–65. https://doi.org/10.1016/j.autcon.2015.10.012

Rosina, E., & Grinzato, E. (2001). Infrared and Thermal Testing for Conservation of Historic Buildings. Materials Evaluation, 59(8), 942–954.

Rucka, M., Lachowicz, J., & Zielińska, M. (2016). GPR investigation of the strengthening system of a historic masonry tower. Journal of Applied Geophysics, 131, 94–102. https://doi.org/10.1016/j.jappgeo.2016.05.014

Rudolf, P. (2006). Principles and Evolution of Digital Cameras. In L. MacDonald (Ed.), Digital heritage: Applying digital imaging to cultural heritage (1st Edition, pp. 177–210). Elsevier (Butterworth-Heinemann).

Russo, M., Carnevali, L., Russo, V., Savastano, D., & Taddia, Y. (2019). Modeling and deterioration mapping of façades in historical urban context by close-range ultra-lightweight UAVs

photogrammetry. International Journal of Architectural Heritage, 13(4), 549–568. https://doi.org/10.1080/15583058.2018.1440030

Sabins, F. F. J., & Ellis, J. M. (2020). Remote sensing: Principles, Interpretation, and Applications (4th Edition). Waveland Press.

Sambuelli, L., Bohm, G., Capizzi, P., Cardarelli, E., & Cosentino, P. (2011). Comparison between GPR measurements and ultrasonic tomography with different inversion algorithms: An application to the base of an ancient Egyptian sculpture. Journal of Geophysics and Engineering, 8(3), S106–S116. https://doi.org/10.1088/1742-2132/8/3/S10

Sánchez-Aparicio, L. J., Del Pozo, S., Ramos, L. F., Arce, A., & Fernandes, F. M. (2018). Heritage site preservation with combined radiometric and geometric analysis of TLS data. Automation in Construction, 85, 24–39. https://doi.org/10.1016/j.autcon.2017.09.023

Santos, P., Ritz, M., Fuhrmann, C., & Fellner, D. (2017). 3D mass digitization: A milestone for archeological documentation. Virtual Archaeology Review, 8(16), 1–11. https://doi.org/10.4995/var.2017.6321

Sfarra, S., Ibarra-Castanedo, C., Ambrosini, D., Paoletti, D., Bendada, A., & Maldague, X. (2011). Integrated Approach between Pulsed Thermography, Near Infrared Reflectography and Sandwich Holography for Wooden Panel Paintings Advanced Monitoring. Russian Journal of Nondestructive Testing, 47(4), 284–293. https://doi.org/10.1134/S1061830911040097

Sfarra, S., Ibarra-Castanedo, C., Ambrosini, D., Paoletti, D., Bendada, A., & Maldague, X. (2014). Non-Destructive Testing Techniques to Help the Restoration of Frescoes. Arabian Journal for Science and Engineering, 39(5), 3461–3480. https://doi.org/10.1007/s13369-014-0992-z

Shepard, S. M. (1997). Introduction to active thermography for non-destructive evaluation. Anti-Corrosion Methods and Materials, 44(4), 236–239. https://doi.org/10.1108/00035599710183199

Siedler, G., & Vetter, S. (2015). Modern methods of documentation for conservation—Digital mapping in metigo® MAP, Software for documentation, mapping and quantity survey and analysis. Geophysical Research Abstracts, 17, EGU2015-10588.

Silveira da Costa, V., Montagna da Silveira, A., & da Silva Torres, A. (2021). Evaluation of Degradation State of Historic Building Facades through Qualitative and Quantitative Indicators: Case Study in Pelotas, Brazil. International Journal of Architectural Heritage, 1–24. https://doi.org/10.1080/15583058.2021.1901161

Solla, M., Lorenzo, H., & Pérez-Gracia, V. (2016). Ground Penetrating Radar: Fundamentals, Methodologies and Applications in Structures and Infrastructure. In B. Riveiro & M. Solla (Eds.), Non-Destructive Techniques for the Evaluation of Structures and Infrastructure (1st Edition, pp. 89–111). CRC Press. http://dx.doi.org/10.1201/b19024-7

Solla, M., Lorenzo, H., Novo, A., & Rial, F. I. (2010). Ground-penetrating radar assessment of the medieval arch bridge of San Antón, Galicia, Spain. Archaeological Prospection, 17(4), 223–232. https://doi.org/10.1002/arp.390

Spodek, J., & Rosina, E. (2009). Application of Infrared Thermography to Historic Building Investigation. Journal of Architectural Conservation, 15(1), 65–81. https://doi.org/10.1080/13556207.2009.10785040

Stampouloglou, M., Toska, O., Tapinaki, S., Kontogianni, G., Skamantzari, M., & Georgopoulos, A. (2020). Archaeological anastylosis of two Macedonian tombs in a 3D virtual environment. Virtual Archaeology Review, 11(22), 26–40. https://doi.org/10.4995/var.2020.11877

Stanco, F., Battiato, S., Gallo, G., Bianco, S., Colombo, A., Gasparini, F., & Chettini, R. (2012). Applications of Spectral Imaging and Reproduction to Cultural Heritage. In Digital imaging

for cultural heritage preservation analysis, restoration, and reconstruction of ancient artworks (1st Edition, pp. 183–213). CRC Press.

Stock, P., & Burton, R. J. F. (2011). Defining Terms for Integrated (Multi-Inter-Trans-Disciplinary) Sustainability Research. Sustainability, 3(8), 1090–1113. https://doi.org/10.3390/su3081090

Strange, I., & Whitney, D. (2003). The changing roles and purposes of heritage conservation in the UK. Planning Practice and Research, 18(2–3), 219–229. https://doi.org/10.1080/0269745032000168278

Suchocki, C. (2020). Comparison of Time-of-Flight and Phase-Shift TLS Intensity Data for the Diagnostics Measurements of Buildings. Materials, 13(2), 353. https://doi.org/10.3390/ma13020353

Suchocki, C., & Katzer, J. (2018). Terrestrial laser scanning harnessed for moisture detection in building materials – Problems and limitations. Automation in Construction, 94, 127–134. https://doi.org/10.1016/j.autcon.2018.06.010

Suchocki, C., Damięcka-Suchocka, M., Katzer, J., Janicka, J., Rapiński, J., & Stałowska, P. (2020). Remote Detection of Moisture and Bio-Deterioration of Building Walls by Time-Of-Flight and Phase-Shift Terrestrial Laser Scanners. Remote Sensing, 12(11), 1708. https://doi.org/10.3390/rs12111708

Tapinaki, S., Skamantzari, M., Chliverou, R., Evgenikou, V., Konidi, A. M., Ioannatou, E., Mylonas, A., & Georgopoulos, A. (2019). 3D Image Based Geometric Documentation of a Medieval Fortress. The International Archives of the Photogrammetry, Remote Sensing and Spatial Information Sciences, XLII-2/W9, 699–705. https://doi.org/10.5194/isprs-archives-XLII-2-W9-699-2019

Tavukçuoğlu, A., Akevren, S., & Grinzato, E. (2010). In situ examination of structural cracks at historic masonry structures by quantitative infrared thermography and ultrasonic testing. Journal of Modern Optics, 57(18), 1779–1789. https://doi.org/10.1080/09500340.2010.484553

Teza, G., Pesci, A., & Ninfo, A. (2016). Morphological Analysis for Architectural Applications: Comparison between Laser Scanning and Structure-from-Motion Photogrammetry. Journal of Surveying Engineering, 142(3), 04016004. https://doi.org/10.1061/(ASCE)SU.1943-5428.0000172

Theuwissen, A. J. (2002). Solid-State Imaging with Charge-Coupled Devices (Vol. 1). Kluwer Academic Publishers. https://doi.org/10.1007/0-306-47119-1

Thornbush, M. J., & Viles, H. A. (2007). Photo-based decay mapping of replaced stone blocks on the boundary wall of Worcester College, Oxford. Geological Society, London, Special Publications, 271(1), 69–75. https://doi.org/10.1144/GSL.SP.2007.271.01.08

Tobiasz, Markiewicz, Łapiński, Nikel, Kot, & Muradov. (2019). Review of Methods for Documentation, Management, and Sustainability of Cultural Heritage. Case Study: Museum of King Jan III's Palace at Wilanów. Sustainability, 11(24), 7046. https://doi.org/10.3390/su11247046

Toprak, A. S., Polat, N., & Uysal, M. (2019). 3D modeling of lion tombstones with UAV photogrammetry: A case study in ancient Phrygia (Turkey). Archaeological and Anthropological Sciences, 11(5), 1973–1976. https://doi.org/10.1007/s12520-018-0649-z

Torres-González, M., Alejandre, F. J., Flores-Alés, V., Calero-Castillo, A. I., & Blasco-López, F. J. (2021). Analysis of the state of conservation of historical plasterwork through visual inspection and non-destructive tests. The case of the upper frieze of the Toledanos Room (The Royal Alcázar of Seville, Spain). Journal of Building Engineering, 40, 102314. https://doi.org/10.1016/j.jobe.2021.102314

Toyoda, K. (2006). Digital Still Cameras at a Glance. In J. Nakamura (Ed.), Image Sensors and Signal Processing for Digital Still Cameras (1st Edition, pp. 1–19). CRC Press. https://doi.org/10.1201/9781420026856

Trussell, J., & Vrhel, M. (2008). Fundamentals of Digital Imaging. Cambridge University Press.

Tsiafaki, D., Koutsoudis, A., Arnaoutoglou, F., & Michailidou, N. (2016). Virtual reassembly and completion of a fragmentary drinking vessel. Virtual Archaeology Review, 7(15), 67–76. https://doi.org/10.4995/var.2016.5910

Tucci, G., Bonora, V., Conti, A., & Fiorini, L. (2015). Benchmarking Range-Based and Image-Based Techniques for Digitizing a Glazed Earthenware Frieze. ISPRS Annals of Photogrammetry, Remote Sensing and Spatial Information Sciences, II-5/W3, 315–322. https://doi.org/10.5194/isprsannals-II-5-W3-315-2015

Tucci, G., Bonora, V., Conti, A., & Fiorini, L. (2017). High-quality 3D models and their use in a cultural heritage conservation project. ISPRS - International Archives of the Photogrammetry, Remote Sensing and Spatial Information Sciences, XLII-2/W5, 687–693. https://doi.org/10.5194/isprs-archives-XLII-2-W5-687-2017

UNESCO. (1972). Photogrammetry applied to the survey of Historic Monuments, of Sites and to Archaeology. UNESCO editions.

Usamentiaga, R., Garcia, D. F., Ibarra-Castanedo, C., & Maldague, X. (2017). Highly accurate geometric calibration for infrared cameras using inexpensive calibration targets. Measurement, 112, 105–116. https://doi.org/10.1016/j.measurement.2017.08.027

Usamentiaga, R., Ibarra-Castanedo, C., & Maldague, X. (2018). Comparison and evaluation of geometric calibration methods for infrared cameras to perform metric measurements on a plane. Applied Optics, 57(18), D1. https://doi.org/10.1364/AO.57.0000D1

Usamentiaga, R., Venegas, P., Guerediaga, J., Vega, L., Molleda, J., & Bulnes, F. (2014). Infrared Thermography for Temperature Measurement and Non-Destructive Testing. Sensors, 14(7), 12305–12348. https://doi.org/10.3390/s140712305

Utsi, E. C. (2017). Ground penetrating radar (1st Edition). Elsevier.

Vacca, G., Deidda, M., Dessi, A., & Marras, M. (2012). Laser Scanner Survey to Cultural Heritage Conservation and Restoration. ISPRS - International Archives of the Photogrammetry, Remote Sensing and Spatial Information Sciences, XXXIX-B5, 589–594. https://doi.org/10.5194/isprsarchives-XXXIX-B5-589-2012

Venkataraman, B., & Raj, B. (2003). Performance parameters for thermal imaging systems. Insight - Non-Destructive Testing and Condition Monitoring, 45(8), 531–535. https://doi.org/10.1784/insi.45.8.531.52914

Verhoeven, G. (2008). Imaging the invisible using modified digital still cameras for straightforward and low-cost archaeological near-infrared photography. Journal of Archaeological Science, 35(12), 3087–3100. https://doi.org/10.1016/j.jas.2008.06.012

Verhoeven, G. (2016). Basics of Photography for Cultural Heritage Imaging. In E. Stylianidis & F. Remondino (Eds.), 3D Recording, documentation and management of cultural heritage (pp. 127–252). Whittles Publishing.

Viñas, S. M. (2002). Contemporary theory of conservation. Studies in Conservation, 47(Supplement-1), 25–34. https://doi.org/10.1179/sic.2002.47.Supplement-1.25

Volinia, M. (2000). Integration of qualitative and quantitative infrared surveys to study the plaster conditions of Valentino Castle. In R. B. Dinwiddie & D. H. LeMieux (Eds.), Proc. SPIE 4020 (pp. 324–334). SPIE. https://doi.org/10.1117/12.381566

Vollmer, M., & Möllmann, K.-P. (2018). Infrared thermal imaging: Fundamentals, research and applications (2nd Edition). Wiley-VCH Verlag GmbH & Co. KGaA.

Wang, B., Zhong, S., Lee, T.-L., Fancey, K. S., & Mi, J. (2020). Non-destructive testing and evaluation of composite materials/structures: A state-of-the-art review. Advances in Mechanical Engineering, 12(4), 1–28. https://doi.org/10.1177/1687814020913761

Westoby, M. J., Brasington, J., Glasser, N. F., Hambrey, M. J., & Reynolds, J. M. (2012). 'Structure-from-Motion' photogrammetry: A low-cost, effective tool for geoscience applications. Geomorphology, 179, 300–314. https://doi.org/10.1016/j.geomorph.2012.08.021

Yamazoe, H., Habe, H., Mitsugami, I., & Yagi, Y. (2018). Depth error correction for projector-camera based consumer depth cameras. Computational Visual Media, 4(2), 103–111. https://doi.org/10.1007/s41095-017-0103-7

Yao, Y., Sfarra, S., Lagüela, S., Ibarra-Castanedo, C., Wu, J.-Y., Maldague, X., & Ambrosini, D. (2018). Active thermography testing and data analysis for the state of conservation of panel paintings. International Journal of Thermal Sciences, 126, 143–151. https://doi.org/10.1016/j.ijthermalsci.2017.12.036

Yilmaz, H. M., Yakar, M., Gulec, S. A., & Dulgerler, O. N. (2007). Importance of digital close-range photogrammetry in documentation of cultural heritage. Journal of Cultural Heritage, 8(4), 428–433. https://doi.org/10.1016/j.culher.2007.07.004

Yousefi, B., Sfarra, S., Ibarra-Castanedo, C., Avdelidis, N. P., & Maldague, X. P. V. (2019). Thermography data fusion and nonnegative matrix factorization for the evaluation of cultural heritage objects and buildings. Journal of Thermal Analysis and Calorimetry, 136(2), 943–955. https://doi.org/10.1007/s10973-018-7644-6

Zawieska, D., & Markiewicz, J. (2016). Development of Photogrammetric Documentation of the Borough at Biskupin Based on Archival Photographs—First Results. In M. Ioannides, E. Fink, A. Moropoulou, M. Hagedorn-Saupe, A. Fresa, G. Liestøl, V. Rajcic, & P. Grussenmeyer (Eds.), Digital Heritage. Progress in Cultural Heritage: Documentation, Preservation, and Protection (Vol. 10059, pp. 3–9). Springer International Publishing. https://doi.org/10.1007/978-3-319-48974-2_1

Zhang, H.-N., Zhang, Z.-W., Lei, Y., Qu, L., Gao, F., & Feng, L.-C. (2016). Infrared thermal wave non-destructive detection for the internal structure of metal Buddha head. In W. Bao & Y. Lv (Eds.), Selected Proceedings of the Chinese Society for Optical Engineering Conferences held November 2015: Vol. Proc. of SPIE Vol. 9796 (97960A). https://doi.org/10.1117/12.2228854

3 Related Work

This chapter delivers an overview of recent developments and contemporary trends in close-range sensing data fusion techniques regarding heritage documentation applications. The discussed data types refer to multi-wavelength 2D and 3D information sourced through the non-destructive recording techniques described in the previous chapter. Different levels and techniques of data fusion are being reviewed. Particularly, the implications of integrating heterogeneous cultural heritage sensed data (oriented towards inspection and condition monitoring) and their complementarity are highlighted to identify topics of interest, noteworthy application scenarios, and research gaps. Particular emphasis is given to integrating data from metric surveying and recording techniques that are traditionally non-metric. In addition, the state-of-the-art of automated/semi-automated methods for extracting thematic information about the surface condition of tangible cultural heritage from integrated multisource data is also discussed. The readers should note that the majority of this chapter's contents have been published in Adamopoulos (2021), Adamopoulos, Patrucco et al. (2021), Adamopoulos and Rinaudo (2019; 2021c), and Adamopoulos, Volinia et al. (2020).

3.1 Data Fusion

As a general multidisciplinary approach, the term *data fusion* implies integrating data from different sources to enhance their potential value and interpretability and allow the generation of high-quality visual representations. Sensor fusion, data integration, and information fusion are similar terms often referring to the same concept. However, in the framework of this thesis, sensor fusion methods are referred to only as those employing simultaneous data acquisition with multi-sensor configurations, to distinguish them from data fusion approaches performed at a post-acquisition processing stage. Data fusion methods are referred to as those integrating non-simultaneously acquired data from one or multiple sources, including active, passive, and mixed sensor recording techniques.

Data fusion approaches are notably beneficial for inspecting and monitoring cultural heritage assets' condition. They significantly improve multidisciplinary holistic documentation, enhance the properties of recorded data, enable integrated analysis, and help minimize the misinterpretations caused by cross-examining

multisource information, which may lead to a false understanding of the state of preservation. Data fusion approaches are most often categorized depending on the data processing stage at which fusion occurs (Klein, 2004). Ramos & Remondino (2015) proposed an expanded classification of data fusion processes considering aspects such as purpose, data format, and dimensionality.

The task of integrating heterogeneous sensing data depends on aspects such as spatial resolution, spectral resolution, and positional accuracy. Integrative geometric recording approaches and especially those involving ranging and photogrammetric data, are a widely discussed topic of data fusion for both historical architectures (Bevilacqua et al., 2018; Klapa et al., 2017; Murtiyoso et al., 2018) and antiquities (Akca et al., 2006; Serna et al., 2015). However, fusion procedures with data traditionally considered as non-metric or information recorded at beyond-visible wavelengths are less frequently discussed. The near-visible spectral images' similarities with color images allow for the high-resolution texturing of historical assets' 3D representations and the direct implementation of IBM-driven processing, thus facilitating integration with other data sources. The problematics of integrating thermograms with metric data come from their inherent differences compared with visible-spectrum images and concern both spatial (low-resolution) and radiometric (different observable features) characteristics. Methodologies for thermal and geometric data fusion often depend on sensor registration (optical and thermal camera or laser scanner and thermal camera), product registration (thermogram and point cloud or thermogram and 3D mesh), or hybrid photogrammetric techniques. Implementing one of these data fusion techniques largely depends on the scale of the survey and the available equipment and can produce thermal-textured 3D point clouds or meshes. Data collected with non-destructive methods using microwave and ultrasound radiation-based methods can also be integrated when the position of utilized antennae is estimated or tracked, thus allowing the referencing into a given coordinate system; however, this type of fusion refers mainly to information visualization and not integrated use.

3.1.1 Integration between Photogrammetric and Ranging Techniques

The primary goal of heritage geometric recording is the generation of complete, accurate, and photorealistic 3D representations and 2D metric derivatives, such as orthoimage-mosaics and vector drawings. As discussed in Chapter 2, there is a wide range of active and passive sensors and advanced techniques for geometric recording, producing different data types. Integrative IBM and TLS approaches are the standard procedure for modeling ancient and historical structures (and their remains) and ensure that predefined density, accuracy, and texture-resolution specifications are met (Alshawabkeh, 2020; Chiabrando et al., 2019; Fassi et al., 2011; Nex & Rinaudo, 2011). Fusion approaches introduced for multisource point

cloud (3D-to-3D) integration include manual registration via annotation of common features (Muñumer & Lerma, 2015), spatial information system-based registration (von Schwerin et al., 2013), ICP-based registration (Altuntas at al., 2016; Jo & Hong, 2019; Shanoer & Abed, 2018), feature-based registration (Bastonero et al., 2014; Tombari & Remondino, 2013), registration based on intensity image and range image matching (Altuntas, 2014), and georeferencing-based registration (Murtiyoso et al., 2018; Scaioni, 2005). With the rapid increase in the implementation of unmanned aerial systems (UAS) for cultural heritage, IBM has recently introduced fascinating integrative approaches on the convergence of TLS and low-altitude aerial photogrammetry (Jo & Hong, 2019; Liang et al., 2018; Ulvi, 2021; Xu et al., 2014). Fusion between photogrammetric and (triangulation or structured-light) scanning data is also applicable for sculptures and small objects and can facilitate replication and inspection (Hayes et al., 2015; Liu et al., 2012; Serna et al., 2015).

3.1.2 Multispectral Data

For multi-sensor recording (and for some designs of integrated devices), it is expected that the images from different spectral channels need to be shifted or spatially re-scaled to be registered (2D-to-2D fusion) in order to form an aligned image cube (Liang, 2012). Several algorithms exist associated with image registration (Zitová & Flusser, 2003). Image registration involving only linear shifts is relatively simple and can be calculated by performing cross-correlation. Spatial image scaling involving re-sampling could result in some loss of information; therefore, it is best to design the system's optics to avoid scaling of the images. High-resolution imaging of large objects inevitably involves mosaicking of images. Therefore, adjacent images must be taken with sufficient overlap to allow automatic image registration. When the shifts are linear, a simple cross-correlation algorithm can be used for image registration. As regards architectural heritage applications, the issue of registering images collected in different spectra has often been addressed through the manual identification of common features (Lerma et al., 2011, 2012).

One prevalent form of multispectral data fusion for built heritage monitoring involves multi-sensor acquisition. IBM and TLS-produced ortho-mosaics referenced at the same coordinate system can be treated as multispectral images. Conde et al. (2016), Del Pozo et al. (2016), and Sánchez-Aparicio et al. (2016) experimented with fusing data from terrestrial scanners operating at different wavelengths, multispectral and commercial digital cameras to produce multispectral ortho-mosaics for detecting pathologies on constructions.

Three-dimensional digitization is seldom used in combination with single-band, multiband, and multispectral recording in the near-visible spectra (NUV, NIR, and SWIR), despite the proven advantages of such integration for

conservation and archaeology (Simon Chane, Mansouri, et al., 2013). Registration between near-visible and 3D data has been performed with different methods. A few 3D/near-visible integrated recording devices have been reported for applications regarding cultural heritage objects over the past years, but not solely. A popular approach has been the coupling of a structured light projector and a monochromatic CCD-based camera to capture both reflectance and geometrical information, employing multiple narrow-band interference filters (Haladová et al., 2015; Mączkowski et al., 2016; Mansouri et al., 2007; Sitnik et al., 2010; Zhang et al., 2016). Rosenberg et al. (2020) has proposed an alternative approach by developing a multimodal system combining multiple band-specific light projectors and imaging sensors. Brusko et al. (2006) has developed a prototype instrument integrating a commercial image spectrograph and a time-of-flight range-finder to study planar objects. Surroundings are scanned horizontally and vertically using a rotating stage and a rotating mirror, respectively. The calibration is performed by calculating the correspondence parameters between projected spots from the laser device and their multispectral image datasets.

Selecting different sensors for the 3D digitization and the multispectral recording is often the preferred approach for cultural heritage because it absolves the user from complicated calibration procedures. However, when performing 2D-to-3D registration, the relative orientation of the camera to the 3D data becomes a trivial issue and has to be performed for every view. The traditional approach of identifying homologous points to retrieve the unknown intrinsic and extrinsic camera parameters is very much dependent on their number and distribution and may prove problematic for non-planar surfaces (Kedzierski et al., 2017). Pelagotti et al. (2009) proposed the generation of depth maps from 3D models, producing intrinsic mapping between their pixels and corresponding vertices of the models, and registered those depth maps with texture from spectral images based on the mutual information. Simon Chane, Schütze, et al. (2013) have performed photogrammetric tracking of a pre-calibrated multispectral camera and a fringe projection system used on the same scene for 3D digitization to calculate their relative position and project the multispectral data on the 3D, achieving an accuracy of better than half an image pixel. Nocerino et al. (2018) and Zainuddin et al. (2019) have used photogrammetrically oriented multispectral and ultraviolet datasets, respectively, for texturing scanning-produced models.

It should be emphasized that the decreasing cost of multispectral cameras for terrestrial applications, and the availability of high-resolution modified consumer-grade cameras, have widened the application of SfM/DMVR-based software to automatically generate 3D models with beyond-visible texture (Grifoni et al., 2018; Mathys et al., 2019; Webb et al., 2018). The applications combining technical photography with shape reconstruction approaches range currently from enhancing surface features to condition diagnostics. These approaches expunge the need for employing additional sensors (to capture the 3D shape), texture registration

algorithms, and calibration procedures. However, the automatization and, therefore, simplification of the near-visible IBM process has also led to studies that do not report on the spatial or radiometric quality of the results (Grifoni et al., 2020; Lanteri et al., 2019; Lanteri & Agresti, 2017; Pamart et al., 2017).

3.1.3 Thermographic Data

The registration between orthorectified infrared thermal and visible-spectrum images/image-mosaics is usually performed for cultural heritage applications through manual identification of common points distinguishable in both spectra (characteristic points or, more commonly, carefully placed special targets with different reflectance characteristics) to define the necessary transformative relation (Bitelli et al., 2021; Rizzi et al., 2007). Furthermore, the most frequently applied approach for the fusion of thermal and metric data of historic architecture has been the integration of thermograms and metric 3D products, collected with individual proximal sensing techniques. This process often refers to the co-registration of point clouds (or derivative 3D products) captured by TLS—which contain metric spatial information—and thermograms, and has been considered the most cost-effective approach, especially when the complete thermographic mapping of a historic structure or building element is required. Estimating the geometric relation between a metric entity and a thermogram (the relative position and orientation matrix) is realized by defining common features, which allows for the accurate projection of the thermal intensities onto the point cloud/model to create a thermal texture.

Due to the inherently different characteristics between thermal and visible-spectrum images and limitations imposed by low spatial resolution (Mizginov & Kniaz, 2019), research on thermographic mapping for cultural heritage assets has mainly concentrated on workflows reconstructing the 3D shape from RGB images and applying the texture from registered thermal infrared images, and hybrid workflows which apply the photogrammetric principles on both RGB and thermal infrared images and use only the latter for texturing. González-Aguilera et al. (2013), Dlesk et al. (2018), and Patrucco et al. (2020) performed image-based modeling using thermal infrared images captured with NEC TH9260, FLIR E95, and FLIR SC660 thermal cameras, respectively, to reconstruct digitally and to inspect built heritage. Other approaches have taken advantage of both the optical and thermal sensors integrated into the thermographic cameras. Macher et al. (2019) used the RGB images from a thermal camera to create an internal space's point cloud and superimposed the thermal images on the RGB images for the purpose of coloring the point cloud with thermal data. Then they used the thermal product to transfer the information of the thermal intensities to a laser-scanned point cloud with BIM enrichment purposes. Previtali et al. (2013) developed a hybrid approach to compute photogrammetrically the orientation of both thermal and RGB images together in a combined bundle adjustment, improving the reconstruction accuracies

and mapped the infrared images on 3D models of building façades. More complex thermal modeling methodologies have included the reconstruction of 3D point clouds from RGB images and precise registration of the thermal image sequences using geometric constraints and feature matching. Hoegner and Stilla (2018) included a priori knowledge of the existing mesh into the estimation of the camera orientations and then extracted the thermal 3D point cloud directly from the thermal images. Dino et al. (2020) used a cascade method to identify potential matches between thermal and RGB images and removed those incorrect using a RANdom Sample Consensus (RANSAC) version. After a multi-view image-based reconstruction, they performed plane fitting to define the reconstructed walls' geometry to apply the thermal texture.

The first approaches for thermal texturing via 2D-to-3D registration were developed on a manual basis. This method was implemented by Spanò et al. (2005) to study the surfaces of the Church of the Beata Vergine dei dolori in Villastellone (Italy), Zalama et al. (2011) to perform an analysis of humidity, microorganisms, and stained-glass window breaks for the Church of Santa Maria in Palencia (Spain), Costanzo et al. (2015) to detect thermal anomalies and to improve the knowledge on the health state of a masonry building at the St. Augustine Monumental Compound in Cosenza (Italy), and Mileto et al. (2015), to localize stone deterioration and humidity at the Castle of Monzón in Huesca (Spain). Manual product registration has the significant drawback that enough feature correspondences may not be visible on the thermal imagery to perform the necessary matching. More advanced approaches have been devised to perform automatic registration by identifying correspondences between features on the 2D thermal images and features on 3D metric products. Lagüela et al. (2013) performed Line Segment Detection on thermal images and then classified and intersected the detected horizontal and vertical lines to compute intersection points, corresponding primarily to corners. They used curvature analysis to extract 3D features from a TLS point cloud and computed each image's orientation with respect to the point cloud through an iterative process using RANSAC and the collinearity equations. González-Aguilera et al. (2012) generated and radiometrically improved range images from a TLS point cloud. Using the Harris operator for feature extraction and subsequently hierarchical image matching between thermal and visible range images with constraints based on epipolar geometry, they performed the spatial resection of the thermographic cameras, supported by statistical tests. After the thermographic images' robust orientation, they obtained a thermographic dense surface model by a pair-wise matching process supported by the semi-global matching technique and applying a projective equation.

Methodologies for simultaneous measurement of high-density thermal and 3D metric data have also been recently developed to facilitate massive and more agile thermographic modeling. Commercial integrated or custom-made multi-sensor instrumentation has been employed in this direction, requiring co-registration

between different sensors used during the acquisition. Sensor co-registration parameters consist of the vector of differences in the sensors' position and the rotation angles between them and are necessary to transform and integrate measurements into the same coordinate system. In general, sensor co-registration that includes thermal cameras is not common due to thermal infrared measurements' requirements regarding the angle and distance of acquisition (Coret et al., 2004). Alba et al. (2011) set up a bi-camera system coupling an AVIO thermocamera and a Nikon RGB camera and used the latter imaging sensor to create a photogrammetric network for multi-view image-based 3D recording, strengthened with additional camera stations. Then the photogrammetric and TLS-produced point clouds were registered, and the thermal intensities were mapped on building models. Borrmann et al. (2013) used a pre-calibrated robotic moving system combining an Optris PI 160 thermocamera, a Riegl VZ-400 laser scanner, and a Logitech QuickCam Pro 9000 webcam mounted on a modified VolksBot RT 3 platform to perform simultaneous metric and thermal acquisition. Merchán et al. (2018) developed a hybrid scanning system employing a Riegl VZ-400 scanner, a Nikon D90 RGB camera, and a FLIR AX5 thermal camera. The hybrid sensor was calibrated with the help of targets incorporating both optical and thermal reflectance discriminants, distributed over a wide area of the scene, and tested in Adán et al. (2021). Yang et al. (2018) used two iPhone SE smartphones and a FLIR ONE camera for iOS sturdily placed on a tripod. They utilized the Normalized Cross-Correlation (NCC) technique to register the optical images of the thermographic camera attached to one smartphone, with the optical images captured with the other smartphone, in order to project the thermal images on the 3D model produced with a multi-view stereo-based approach. Finally, Lin et al. (2019) used independent datasets of RGB and thermal images to generate point clouds. They utilized the Fast Point Feature Histogram feature as initial correspondence between the point clouds, reciprocity test to find the mutual nearest correspondences, tuple test to verify the compatibility of the correspondences to remove the outliers from the correspondence set, and Fast Global Registration (FGR) and RANSAC to estimate the coarse alignment. After determining the best thermal-RGB image pairs based on the lowest Euclidean distance, they used radiation-invariant feature transform (RIFT), normalized barycentric coordinate system, and RANSAC to extract reliable matches. Afterward, they performed a fine registration by mono-plotting the RGB images, followed by image resectioning of the thermal images. Finally, they proposed a global image pose refinement approach to minimize temperature disagreements from different images of the same points eliminating blur effects.

3.1.4 Penetrating Radar Data

Not unlike thermograms, GPR data are more challenging to interpret and have lower resolution compared with TLS and close-range photogrammetry, and thus are

usually acquired and used independently (Cozzolino et al., 2019; Pérez et al., 2018). The expected level of integration between geometric and geophysical data for architectural heritage non-destructive investigations is frequently the registration of GPR slices or surfaces interpolated from 3D grid-organized GPR measurements and metric products computed with methods for reality capturing (Biscarini et al., 2020; De Giorgi et al., 2021). When historical structures' surfaces with relatively flat geometries are investigated, the integration in 3D space is, according to the bibliography, achieved through measuring the 3D positioning of control points (usually the start and end-point) of the scan lines (Agrafiotis et al., 2017; Ercoli et al., 2016; Puente et al., 2015; Solla et al., 2020). Apart from registration, the availability of a dense geometric 3D model or point cloud can also assist the spatial correction of GRP data collected for structures with more complex geometries, the most common example being historic bridges (Arias et al., 2007; Fauchard et al., 2013; Lubowiecka et al., 2009, 2011; Mills & Chandler, 2007; Pérez-Gracia et al., 2011; Riveiro et al., 2012; Solla, Caamaño, et al., 2012; Solla, Lorenzo, et al., 2012; Stavroulaki et al., 2016). Geophysical exploration of columns may require only a simplified knowledge of the geometrical shapes ((Santos-Asssunçao, Pérez-Gracia, Caselles, et al., 2014; Santos-Assunçao, Pérez-Gracia, Gonzalez, et al., 2014)). The integration of positioning systems, laser scanning, and GPR presents exciting potential for integrated surface and subsurface mapping but is subject to significant limitations (Merkle et al., 2020).

3.2 Integrated Processing and Pixel-Level Fusion of Multi-Sensor Data

As previously described, cohesive condition inspection and state-of-preservation monitoring require extensive knowledge of the advantages and limitations of each individual close-range sensing technique. However, the complementarity of multisource data and the challenges occurring from their integrated use for cultural heritage applications should also be considered.

Scanning and IBM can satisfy the 3D reality-based modeling needs for inspection, multitemporal monitoring, and additionally building information modeling (BIM) in the case of structures (Rocha et al., 2019; Alshawabkeh et al., 2021). These techniques employ mobile instrumentation, which makes them easily adaptable for complicated acquisition scenarios, and can reach millimetric accuracy of extracted features; however, they cannot provide any subsurface information. Conditionally, TLS can be applied for surface defect and moisture detection, subject to sensor calibration and knowledge of the material's emissivity at the laser instrument's operating band. Furthermore, the integration between scanning and image-based methods emphasizes the complementarity of geometric and color information (Tucci et al., 2017a; Liu et al., 2012; Percy et al., 2015; Lerma et al.,

2015; Tucci et al., 2017b; Sahin & Mengüç, 2019), enabling surface feature extraction regarding deterioration and physical defects.

Thermographic evaluation is appropriate for surface and very near-surface detection and feature extraction of defects or moisture but is less mobile than IBM/TLS and requires knowledge of the ambient and material influence on LWIR radiance measurements. However, the integration of thermography with metric surveying allows the quantification of extracted thermal features and their correlation in 3D space to address potential sources of moisture or subsurface radiant sources and to calculate envelopes for sustainable conservation in the case of historic buildings. In addition, the resolution of thermographic results can be significantly improved through pan-sharpening, super-resolution enhancement, or hybrid color-thermal IBM.

Multispectral imaging offers solutions for pattern extraction concerning the surface alteration of historical materials and moisture—especially the combination with learning-based digital image segmentation results in the rapid mapping of the surface conditions. However, challenges occur in implementing multi-sensor instrumentation due to increased cost, reduced mobility, calibration needs, and sensor fusion requirements.

GPR introduces one of the most promising monitoring technologies due to its ability to identify the material depth and locate discontinuities between materials due to their different dielectric properties. The fusion of GPR measurements with geometric data enables spatial correction for structures of complex geometry but simultaneously facilitates better 3D visualization of the prospection results and increases the accuracy of locating material discontinuities defects in 3D. Furthermore, 3D modeling and GPR integration support truthful numerical modeling and parametrization for structural health analysis.

In the sense of pixel-level fusion, data fusion for built heritage is scarcely being applied through the quantization of multitemporal or multispectral images to increase interpretation by utilizing clustering classification or principal component analysis (Lerma et al., 2011). On the other hand, integrated management of non-destructively recorded data through Geographic Information Systems (GIS) is a more common approach that allows geo-processing analysis for thematic pathology representation.

The reciprocity of mapping and infrared spectral imaging, especially thermography, has often been considered essential for detecting weathering on historic structures (Barbosa et al., 2021; İnce et al., 2018; Jo & Lee, 2014; Kilic, 2015; Mileto et al., 2015; Napolitano et al., 2020). The additional inclusion of NIR reflectance images enhances the identifiability of deterioration, mainly when there is a presence of vegetation and biogenic crusts, which pathology exhibits vastly different near-infrared reflectance characteristics compared to healthy historical

construction materials (Armesto-González et al., 2010; Lerma et al., 2012). However, the decision to include recorded data from multiple spectral bands comes with the realization that suitable sensing techniques have to be selected.

3.3 Automated Mapping of Deterioration

The progress in automated mapping for cultural heritage is directed on condition inspection of historic structures and has primarily concentrated on identifying and classifying the building elements, materials, and additionally deterioration as a binary concept—considering the presence and absence of deterioration solely on images. The segmentation algorithms that have been considered are mainly based on dimensionality reduction, unsupervised clustering, and deep learning approaches, occasionally considering spectral bands in the infrared range. The need for more efficient inspection (Dias et al., 2021) and intelligent identification of conservation needs (Marzouk et al., 2020) has led to the adoption of image processing approaches to generate the thematic data needed for deterioration mapping. Digital image processing (DIP) refers to the manipulation of the digital images to extract features and recognize patterns, which, after having acquired the suitable base maps, can be performed with techniques as simple as thresholding, edge detection, or information reduction to obtain the required results (Cossu & Chiappini, 2004; Moropoulou et al., 2013; Vázquez et al., 2011). However, these approaches still largely depend on the human factor since many parameters have to be tuned differently for each application, and deterioration patterns often have to be identified and extracted one at a time.

The current rise of deep learning-based pattern recognition has delivered powerful tools for fully automated detection of deterioration (often through convolutional neural networks), even when a plethora of surface patterns can be observed (Hatir et al., 2020; Hatir & İnce, 2021; Mansuri & Patel, 2021; Pathak, 2021). Nevertheless, deep-learning implementations require large image datasets to be efficiently trained, which is often impractical for conservation applications. They may also underperform considering the uniqueness of each heritage asset, many of which present a unique mixture of historical materials. Therefore, other more easily executed supervised learning-based approaches are sometimes considered for deterioration detection through classification and regression.

Multiband image segmentation for heritage conservation purposes has been applied via a range of clustering algorithms, some of the most common being maximum-likelihood, minimum-distance, and k-means (Del Pozo et al., 2016; Grilli & Remondino, 2019; Lerma, 2001, 2005; Sánchez & Quirós, 2017). However, the relevant works aim at segmenting the materials and elements of historical façades, and when deterioration is considered, it is determined as present or absent. Specifically, most identified relevant works consider the altered and unaltered areas

of a historical material as two categories rather than identifying the different deterioration typologies.

References

Adán, A., Pérez, V., Vivancos, J.-L., Aparicio-Fernández, C., & Prieto, S. A. (2021). Proposing 3D Thermal Technology for Heritage Building Energy Monitoring. Remote Sensing, 13(8), 1537. https://doi.org/10.3390/rs13081537

Agrafiotis, P., Lampropoulos, K., Georgopoulos, A., & Moropoulou, A. (2017). 3D Modelling the Invisible Using Ground Penetrating Radar. ISPRS - International Archives of the Photogrammetry, Remote Sensing and Spatial Information Sciences, XLII-2/W3, 33–37. https://doi.org/10.5194/isprs-archives-XLII-2-W3-33-2017

Akca, D., Grün, A., Alkis, Z., Demir, N., Breuckmann, B., Erduyan, I., & Nadir, E. (2006). 3D modeling of the Weary Herakles statue with a coded structured light system [Application/pdf,Online-Datei]. ISPRS - International Archives of the Photogrammetry, Remote Sensing and Spatial Information Sciences, XXXVI(5), 14–19. https://doi.org/10.3929/ETHZ-A-005746782

Alba, M. I., Barazzetti, L., Scaioni, M., Rosina, E., & Previtali, M. (2011). Mapping Infrared Data on Terrestrial Laser Scanning 3D Models of Buildings. Remote Sensing, 3(9), 1847–1870. https://doi.org/10.3390/rs3091847

Alshawabkeh, Y. (2020). Color and Laser Data as a Complementary Approach for Heritage Documentation. Remote Sensing, 12(20), 3465. https://doi.org/10.3390/rs12203465

Alshawabkeh, Y., Baik, A., & Miky, Y. (2021). Integration of Laser Scanner and Photogrammetry for Heritage BIM Enhancement. ISPRS International Journal of Geo-Information, 10(5), 316. https://doi.org/10.3390/ijgi10050316

Altuntas, C. (2014). Pair-wise automatic registration of three-dimensional laser scanning data from historical building by created two-dimensional images. Optical Engineering, 53(5), 053108. https://doi.org/10.1117/1.OE.53.5.053108

Altuntas, C., Yildiz, F., & Scaioni, M. (2016). Laser Scanning and Data Integration for Three-Dimensional Digital Recording of Complex Historical Structures: The Case of Mevlana Museum. ISPRS International Journal of Geo-Information, 5(2), 18. https://doi.org/10.3390/ijgi5020018

Arias, P., Armesto, J., Di-Capua, D., González-Drigo, R., Lorenzo, H., & Pérez-Gracia, V. (2007). Digital photogrammetry, GPR and computational analysis of structural damages in a mediaeval bridge. Engineering Failure Analysis, 14(8), 1444–1457. https://doi.org/10.1016/j.engfailanal.2007.02.001

Armesto-González, J., Riveiro-Rodríguez, B., González-Aguilera, D., & Rivas-Brea, M. T. (2010). Terrestrial laser scanning intensity data applied to damage detection for historical buildings. Journal of Archaeological Science, 37(12), 3037–3047. https://doi.org/10.1016/j.jas.2010.06.031

Barbosa, M. T., Rosse, V. J., & Laurindo, N. G. (2021). Thermography evaluation strategy proposal due moisture damage on building facades. Journal of Building Engineering, 43, 102555. https://doi.org/10.1016/j.jobe.2021.102555

Bastonero, P., Donadio, E., Chiabrando, F., & Spanò, A. (2014). Fusion of 3D models derived from TLS and image-based techniques for CH enhanced documentation. ISPRS Annals of

Photogrammetry, Remote Sensing and Spatial Information Sciences, II–5, 73–80. https://doi.org/10.5194/isprsannals-II-5-73-2014

Bevilacqua, M. G., Caroti, G., Piemonte, A., & Terranova, A. A. (2018). Digital Technology and Mechatronic Systems for the Architectural 3D Metric Survey. In E. Ottaviano, A. Pelliccio, & V. Gattulli (Eds.), Mechatronics for Cultural Heritage and Civil Engineering (Vol. 92, pp. 161–180). Springer International Publishing. https://doi.org/10.1007/978-3-319-68646-2_7

Biscarini, C., Catapano, I., Cavalagli, N., Ludeno, G., Pepe, F. A., & Ubertini, F. (2020). UAV photogrammetry, infrared thermography and GPR for enhancing structural and material degradation evaluation of the Roman masonry bridge of Ponte Lucano in Italy. NDT & E International, 115, 102287. https://doi.org/10.1016/j.ndteint.2020.102287

Bitelli, G., Barbieri, E., Girelli, V. A., Lambertini, A., Mandanici, E., Melandri, E., Roggio, D. S., Santangelo, A., Tini, M. A., Tondelli, S., & Ugolini, A. (2021). The Complex of Santa Croce in Ravenna as a Case Study: Integration of 3D Techniques for Surveying and Monitoring of a Historical Site. Proceedings ARQUEOLÓGICA 2.0 - 9th International Congress & 3rd GEORES - GEOmatics and PREServation, 408–413. https://doi.org/10.4995/arqueologica9.2021.12164

Borrmann, D., Elseberg, J., & Nüchter, A. (2013). Thermal 3D Mapping of Building Façades. In S. Lee, H. Cho, K.-J. Yoon, & J. Lee (Eds.), Intelligent Autonomous Systems 12 (Vol. 193, pp. 173–182). Springer Berlin Heidelberg. https://doi.org/10.1007/978-3-642-33926-4_16

Brusco, N., Capeleto, S., Fedel, M., Paviotti, A., Poletto, L., Cortelazzo, G. M., & Tondello, G. (2006). A System for 3D Modeling Frescoed Historical Buildings with Multispectral Texture Information. Machine Vision and Applications, 17(6), 373–393. https://doi.org/10.1007/s00138-006-0026-2

Chiabrando, F., Sammartano, G., Spanò, A., & Spreafico, A. (2019). Hybrid 3D Models: When Geomatics Innovations Meet Extensive Built Heritage Complexes. ISPRS International Journal of Geo-Information, 8(3), 124. https://doi.org/10.3390/ijgi8030124

Conde, B., Del Pozo, S., Riveiro, B., & González-Aguilera, D. (2016). Automatic mapping of moisture affectation in exposed concrete structures by fusing different wavelength remote sensors: Automatic Mapping of Moisture Affectation in Concrete Structures. Structural Control and Health Monitoring, 23(6), 923–937. https://doi.org/10.1002/stc.1814

Coret, L., Briottet, X., Kerr, Y. H., & Chehbouni, A. (2004). Simulation Study of View Angle Effects on Thermal Infrared Measurements Over Heterogeneous Surfaces. IEEE Transactions on Geoscience and Remote Sensing, 42(3), 664–672. https://doi.org/10.1109/TGRS.2003.819443

Cossu, R., & Chiappini, L. (2004). A color image segmentation method as used in the study of ancient monument decay. Journal of Cultural Heritage, 5(4), 385–391. https://doi.org/10.1016/j.culher.2004.03.005

Costanzo, A., Minasi, M., Casula, G., Musacchio, M., & Buongiorno, M. (2014). Combined Use of Terrestrial Laser Scanning and IR Thermography Applied to a Historical Building. Sensors, 15(1), 194–213. https://doi.org/10.3390/s150100194

Cozzolino, M., Di Meo, A., & Gentile, V. (2019). The contribution of indirect topographic surveys (photogrammetry and laser scanner) and GPR investigations in the study of the vulnerability of the Abbey of Santa Maria a Mare, Tremiti Islands (Italy). Annals of Geophysics, 62(3), SE343. https://doi.org/10.4401/ag-7987

De Giorgi, L., Ferrari, I., Giuri, F., Leucci, G., & Scardozzi, G. (2021). Integrated Geoscientific Surveys at the Church of Santa Maria della Lizza (Alezio, Italy). Sensors, 21(6), 2205. https://doi.org/10.3390/s21062205

Del Pozo, S., Herrero-Pascual, J., Felipe-García, B., Hernández-López, D., Rodríguez-Gonzálvez, P., & González-Aguilera, D. (2016). Multispectral Radiometric Analysis of Façades to Detect Pathologies from Active and Passive Remote Sensing. Remote Sensing, 8(1), 80. https://doi.org/10.3390/rs8010080

Dias, I. S., Flores-Colen, I., & Silva, A. (2021). Critical Analysis about Emerging Technologies for Building's Façade Inspection. Buildings, 11(2), 53. https://doi.org/10.3390/buildings11020053

Dino, I. G., Sari, A. E., Iseri, O. K., Akin, S., Kalfaoglu, E., Erdogan, B., Kalkan, S., & Alatan, A. A. (2020). Image-based construction of building energy models using computer vision. Automation in Construction, 116, 103231. https://doi.org/10.1016/j.autcon.2020.103231

Dlesk, A., Vach, K., & Holubec, P. (2018). Usage of Photogrammetric Processing of Thermal Images for Civil Engineers. ISPRS - International Archives of the Photogrammetry, Remote Sensing and Spatial Information Sciences, XLII–5, 99–103. https://doi.org/10.5194/isprs-archives-XLII-5-99-2018

Ercoli, M., Brigante, R., Radicioni, F., Pauselli, C., Mazzocca, M., Centi, G., & Stoppini, A. (2016). Inside the polygonal walls of Amelia (Central Italy): A multidisciplinary data integration, encompassing geodetic monitoring and geophysical prospections. Journal of Applied Geophysics, 127, 31–44. https://doi.org/10.1016/j.jappgeo.2016.02.003

Fassi, F., Achille, C., & Fregonese, L. (2011). Surveying and modelling the main spire of Milan Cathedral using multiple data sources: Surveying and modelling the main spire of Milan Cathedral using multiple data sources. The Photogrammetric Record, 26(136), 462–487. https://doi.org/10.1111/j.1477-9730.2011.00658.x

Fauchard, C., Antoine, R., Bretar, F., Lacogne, J., Fargier, Y., Maisonnave, C., Guilbert, V., Marjerie, P., Thérain, P.-F., Dupont, J.-P., & Pierrot-Deseilligny, M. (2013). Assessment of an ancient bridge combining geophysical and advanced photogrammetric methods: Application to the Pont De Coq, France. Journal of Applied Geophysics, 98, 100–112. https://doi.org/10.1016/j.jappgeo.2013.08.009

García-Molina, D.F.; López-Lago, S.; Hidalgo-Fernandez, R.E.; Triviño-Tarradas, P. Digitalization and 3D Documentation Techniques Applied to Two Pieces of Visigothic Sculptural Heritage in Merida Through Structured Light Scanning. J. Comput. Cult. Herit. 2021, 14, 1–19, doi:10.1145/3427381.

González-Aguilera, D., Lagüela, S., Rodríguez-Gonzálvez, P., & Hernández-López, D. (2013). Image-based thermographic modeling for assessing energy efficiency of buildings façades. Energy and Buildings, 65, 29–36. https://doi.org/10.1016/j.enbuild.2013.05.040

González-Aguilera, D., Rodriguez-Gonzalvez, P., Armesto, J., & Lagüela, S. (2012). Novel approach to 3D thermography and energy efficiency evaluation. Energy and Buildings, 54, 436–443. https://doi.org/10.1016/j.enbuild.2012.07.023

Grifoni, E., Bonizzoni, L., Gargano, M., Melada, J., Mignani, I., & Ludwig, N. (2020). Multianalytical investigation and 3D Multiband modeling: An integrated survey of the Garnier Valletti pomological collection. Proceedings of the 2020 IMEKO TC-4 International Conference on Metrology for Archaeology and Cultural Heritage (2020 MetroArchaeo), 251–256. https://www.imeko.org/publications/tc4-Archaeo-2020/IMEKO-TC4-MetroArchaeo2020-048.pdf

Grifoni, E., Legnaioli, S., Nieri, P., Campanella, B., Lorenzetti, G., Pagnotta, S., Poggialini, F., & Palleschi, V. (2018). Construction and comparison of 3D multi-source multi-band models for cultural heritage applications. Journal of Cultural Heritage, 34, 261–267. https://doi.org/10.1016/j.culher.2018.04.014

Grilli, E., & Remondino, F. (2019). Classification of 3D Digital Heritage. Remote Sensing, 11(7), 847. https://doi.org/10.3390/rs11070847

Haladová, Z. B., Szemzö, R., Kovačovský, T., & Žižka, J. (2015). Utilizing Multispectral Scanning and Augmented Reality for Enhancement and Visualization of the Wooden Sculpture Restoration Process. Procedia Computer Science, 67, 340–347. https://doi.org/10.1016/j.procs.2015.09.278

Hatir, M. E., Barstuğan, M., & İnce, İ. (2020). Deep learning-based weathering type recognition in historical stone monuments. Journal of Cultural Heritage, 45, 193–203. https://doi.org/10.1016/j.culher.2020.04.008

Hatır, M. E., İnce, İ., & Korkanç, M. (2021). Intelligent detection of deterioration in cultural stone heritage. Journal of Building Engineering, 44, 102690. https://doi.org/10.1016/j.jobe.2021.102690

Hayes, J., Fai, S., Kretz, S., Ouimet, C., & White, P. (2015). Digitally-Assisted Stone Carving of a Relief Sculpture for the Parliament Buildings National Historic Site of Canada. ISPRS Annals of Photogrammetry, Remote Sensing and Spatial Information Sciences, II-5/W3, 97–103. https://doi.org/10.5194/isprsannals-II-5-W3-97-2015

Hoegner, L., & Stilla, U. (2018). Mobile thermal mapping for matching of infrared images with 3D building models and 3D point clouds. Quantitative InfraRed Thermography Journal, 1–19. https://doi.org/10.1080/17686733.2018.1455129

İnce, İ., Bozdağ, A., Tosunlar, M. B., Hatır, M. E., & Korkanç, M. (2018). Determination of deterioration of the main facade of the Ferit Paşa Cistern by non-destructive techniques (Konya, Turkey). Environmental Earth Sciences, 77(11), 420. https://doi.org/10.1007/s12665-018-7595-z

Jo, Y. H., & Lee, C. H. (2014). Quantitative modeling and mapping of blistering zone of the Magoksa Temple stone pagoda (13th century, Republic of Korea) by graduated heating thermography. Infrared Physics & Technology, 65, 43–50. https://doi.org/10.1016/j.infrared.2014.02.011

Jo, Y., & Hong, S. (2019). Three-Dimensional Digital Documentation of Cultural Heritage Site Based on the Convergence of Terrestrial Laser Scanning and Unmanned Aerial Vehicle Photogrammetry. ISPRS International Journal of Geo-Information, 8(2), 53. https://doi.org/10.3390/ijgi8020053

Kedzierski, M., Walczykowski, P., Wojtkowska, M., & Fryskowska, A. (2017). Integration of Point Clouds and Images Acquired from a Low-Cost NIR Camera Sensor for Cultural Heritage Purposes. ISPRS - International Archives of the Photogrammetry, Remote Sensing and Spatial Information Sciences, XLII-2/W5, 407–414. https://doi.org/10.5194/isprs-archives-XLII-2-W5-407-2017

Kilic, G. (2015). Using advanced NDT for historic buildings: Towards an integrated multidisciplinary health assessment strategy. Journal of Cultural Heritage, 16(4), 526–535. https://doi.org/10.1016/j.culher.2014.09.010

Klapa, P., Mitka, B., & Zygmunt, M. (2017). Application of Integrated Photogrammetric and Terrestrial Laser Scanning Data to Cultural Heritage Surveying. IOP Conference Series: Earth and Environmental Science, 95, 032007. https://doi.org/10.1088/1755-1315/95/3/032007

Klein, L. A. (2004). Sensor and Data Fusion: A Tool for Information Assessment and Decision Making. SPIE. https://doi.org/10.1117/3.563340

Lagüela, S., Díaz-Vilariño, L., Martínez, J., & Armesto, J. (2013). Automatic thermographic and RGB texture of as-built BIM for energy rehabilitation purposes. Automation in Construction, 31, 230–240. https://doi.org/10.1016/j.autcon.2012.12.013

Lanteri, L., & Agresti, G. (2017). Ultraviolet Fluorescence 3D Models for Diagnostics of Cultural Heritage. European Journal of Science and Theology, 13(2), 35–40.

Lanteri, L., Agresti, G., & Pelosi, C. (2019). A New Practical Approach for 3D Documentation in Ultraviolet Fluorescence and Infrared Reflectography of Polychromatic Sculptures as Fundamental Step in Restoration. Heritage, 2(1), 207–215. https://doi.org/10.3390/heritage2010015

Lerma, J. L. (2001). Multiband Versus Multispectral Supervised Classification of Architectural Images. The Photogrammetric Record, 17(97), 89–101. https://doi.org/10.1111/0031-868X.00169

Lerma, J. L. (2005). Automatic Plotting of Architectural Facades with Multispectral Images. Journal of Surveying Engineering, 131(3), 73–77. https://doi.org/10.1061/(ASCE)0733-9453(2005)131:3(73)

Lerma, J. L., Akasheh, T. S., Haddad, N. A., & Cabrelles, M. (2011). Multispectral sensors in combination with recording tools for cultural heritage documentation. Change Over Time, 1(2), 236–250.

Lerma, J. L., Cabrelles, M., & Navarro, S. (2015). Fusion of range-based data and image-based datasets for efficient documentation of cultural heritage objects and sites. The International Archives of the Photogrammetry, Remote Sensing and Spatial Information Sciences, XL-5/W7, 277–281. https://doi.org/10.5194/isprsarchives-XL-5-W7-277-2015

Lerma, J. L., Cabrelles, M., & Portalés, C. (2011). Multitemporal thermal analysis to detect moisture on a building façade. Construction and Building Materials, 25(5), 2190–2197. https://doi.org/10.1016/j.conbuildmat.2010.10.007

Lerma, J. L., Cabrelles, M., Akasheh, T. S., & Haddad, N. A. (2012). Documentation of Weathered Architectural Heritage with Visible, near Infrared, Thermal and Laser Scanning Data. International Journal of Heritage in the Digital Era, 1(2), 251–275. https://doi.org/10.1260/2047-4970.1.2.251

Liang, H. (2012). Advances in multispectral and hyperspectral imaging for archaeology and art conservation. Applied Physics A, 106(2), 309–323. https://doi.org/10.1007/s00339-011-6689-1

Liang, H., Li, W., Lai, S., Zhu, L., Jiang, W., & Zhang, Q. (2018). The integration of terrestrial laser scanning and terrestrial and unmanned aerial vehicle digital photogrammetry for the documentation of Chinese classical gardens—A case study of Huanxiu Shanzhuang, Suzhou, China. Journal of Cultural Heritage, 33, 222–230. https://doi.org/10.1016/j.culher.2018.03.004

Lin, D., Jarzabek-Rychard, M., Tong, X., & Maas, H.-G. (2019). Fusion of thermal imagery with point clouds for building façade thermal attribute mapping. ISPRS Journal of Photogrammetry and Remote Sensing, 151, 162–175. https://doi.org/10.1016/j.isprsjprs.2019.03.010

Liu, J. W., Jiang, Z. Q., Sun, X., & Hu, H. (2012). Integration of close Range Photogrammetry and Structured Light Scanner for Cultural Heritage Documentation. Advanced Materials Research, 468–471, 1966–1969. https://doi.org/10.4028/www.scientific.net/AMR.468-471.1966

Lubowiecka, I., Arias, P., Riveiro, B., & Solla, M. (2011). Multidisciplinary approach to the assessment of historic structures based on the case of a masonry bridge in Galicia (Spain). Computers & Structures, 89(17–18), 1615–1627. https://doi.org/10.1016/j.compstruc.2011.04.016

Lubowiecka, I., Armesto, J., Arias, P., & Lorenzo, H. (2009). Historic bridge modelling using laser scanning, ground penetrating radar and finite element methods in the context of structural dynamics. Engineering Structures, 31(11), 2667–2676. https://doi.org/10.1016/j.engstruct.2009.06.018

Macher, H., Boudhaim, M., Grussenmeyer, P., Siroux, M., & Landes, T. (2019). Combination of Thermal and Geometric Information for BIM Enrichment. ISPRS - International Archives of the Photogrammetry, Remote Sensing and Spatial Information Sciences, XLII-2/W15, 719–725. https://doi.org/10.5194/isprs-archives-XLII-2-W15-719-2019

Mączkowski, G., Lech, K., & Sitnik, R. (2016). Low-cost Solution for Spectral Reflectance Estimation of 3D Surface. Journal of Imaging Science and Technology, 60(5), 504011–504017. https://doi.org/10.2352/J.ImagingSci.Technol.2016.60.5.050401

Mansouri, A., Lathuiliere, A., Marzani, F., Voisin, Y., & Gouton, P. (2007). Toward a 3D Multispectral Scanner: An Application to Multimedia. IEEE Multimedia, 14(1), 40–47. https://doi.org/10.1109/MMUL.2007.22

Mansuri, L. E., & Patel, D. A. (2021). Artificial intelligence-based automatic visual inspection system for built heritage. Smart and Sustainable Built Environment, ahead-of-print(ahead-of-print). https://doi.org/10.1108/SASBE-09-2020-0139

Marzouk, M., & Zaher, M. (2020). Artificial intelligence exploitation in facility management using deep learning. Construction Innovation, 20(4), 609–624. https://doi.org/10.1108/CI-12-2019-0138

Mateus, L., Fernández, J., Ferreira, V., Oliveira, C., Aguiar, J., Gago, A. S., Pacheco, P., & Pernão, J. (2019). Terrestrial Laser Scanning and Digital Photogrammetry for Heritage Conservation: Case Study of the Historical Walls of Lagos, Portugal. The International Archives of the Photogrammetry, Remote Sensing and Spatial Information Sciences, XLII-2/W11, 843–847. https://doi.org/10.5194/isprs-archives-XLII-2-W11-843-2019

Mathys, A., Jadinon, R., & Hallot, P. (2019). Exploiting 3D Multispectral Texture for a Better Feature Identification for Cultural Heritage. ISPRS Annals of Photogrammetry, Remote Sensing and Spatial Information Sciences, IV-2/W6, 91–97. https://doi.org/10.5194/isprs-annals-IV-2-W6-91-2019

Merchán, P., Merchán, M. J., Salamanca, S., & Adán, A. (2018). Application of Multisensory Technology for Resolution of Problems in the Field of Research and Preservation of Cultural Heritage. In M. Ioannides, J. Martins, R. Žarnić, & V. Lim (Eds.), Advances in Digital Cultural Heritage (Vol. 10754, pp. 32–47). Springer International Publishing. https://doi.org/10.1007/978-3-319-75789-6_3

Merkle, D., Frey, C., & Reiterer, A. (2021). Fusion of ground penetrating radar and laser scanning for infrastructure mapping. Journal of Applied Geodesy, 15(1), 31–45. https://doi.org/10.1515/jag-2020-0004

Mileto, C., Vegas, F., & Lerma, J. L. (2015). Multidisciplinary Studies, Crossreading and Transversal Use of Thermography: The Castle of Monzón (Huesca) as a case study. In Editorial Universitat Politècnica de València (Ed.), MODERN AGE FORTIFICATIONS of the MEDITERRANEAN COAST - DEFENSIVE ARCHITECTURE OF THE MEDITERRANEAN (FORTMED2015). Editorial Universitat Politècnica de València. https://doi.org/10.4995/FORTMED2015.2015.1786

Mills, J. P., & Chandler, J. H. (2007). Digital Photogrammetry, GPR and Finite Elements in Heritage Documentation: Geometry and Structural Damages. The Photogrammetric Record, 22(117), 94–96. https://doi.org/10.1111/j.1477-9730.2007.00418.x

Mizginov, V. A., & Kniaz, V. V. (2019). Evaluating the Accuracy of 3D Object Reconstruction from Thermal Images. ISPRS - International Archives of the Photogrammetry, Remote Sensing and Spatial Information Sciences, XLII-2/W18, 129–134. https://doi.org/10.5194/isprs-archives-XLII-2-W18-129-2019

Moropoulou, A., Labropoulos, K. C., Delegou, E. T., Karoglou, M., & Bakolas, A. (2013). Non-destructive techniques as a tool for the protection of built cultural heritage. Construction and Building Materials, 48, 1222–1239. https://doi.org/10.1016/j.conbuildmat.2013.03.044

Muñumer, E., & Lerma, J. L. (2015). Fusion of 3D data from different image-based and range-based sources for efficient heritage recording. 2015 Digital Heritage, 83–86. https://doi.org/10.1109/DigitalHeritage.2015.7413840

Murtiyoso, A., Grussenmeyer, P., Suwardhi, D., & Awalludin, R. (2018). Multi-Scale and Multi-Sensor 3D Documentation of Heritage Complexes in Urban Areas. ISPRS International Journal of Geo-Information, 7(12), 483. https://doi.org/10.3390/ijgi7120483

Napolitano, R., Hess, M., & Glisic, B. (2020). Quantifying the Differences in Documentation and Modeling Levels for Building Pathology and Diagnostics. Archives of Computational Methods in Engineering, 27(4), 1135–1152. https://doi.org/10.1007/s11831-019-09350-y

Nex, F., & Rinaudo, F. (2011). LiDAR or Photogrammetry? Integration is the answer. Italian Journal of Remote Sensing, 107–121. https://doi.org/10.5721/ItJRS20114328

Nocerino, E., Rieke-Zapp, D. H., Trinkl, E., Rosenbauer, R., Farella, E. M., Morabito, D., & Remondino, F. (2018). Mapping VIS and UVL Imagery on 3D Geometry for Non-Invasive, Non-Contact Analysis of a Vase. ISPRS - International Archives of the Photogrammetry, Remote Sensing and Spatial Information Sciences, XLII–2, 773–780. https://doi.org/10.5194/isprs-archives-XLII-2-773-2018

Pamart, A., Guillon, O., Faraci, S., Gattet, E., Genevois, M., Vallet, J. M., & De Luca, L. (2017). Multispectral Photogrammetric Data Acquisition and Processing for Wall Paintings Studies. ISPRS - International Archives of the Photogrammetry, Remote Sensing and Spatial Information Sciences, XLII-2/W3, 559–566. https://doi.org/10.5194/isprs-archives-XLII-2-W3-559-2017

Patrucco, G., Cortese, G., Giulio Tonolo, F., & Spanò, A. (2020). Thermal and Optical Data Fusion Supporting Built Heritage Analyses. ISPRS - International Archives of the Photogrammetry, Remote Sensing and Spatial Information Sciences, XLIII-B3-2020, 619–626. https://doi.org/10.5194/isprs-archives-XLIII-B3-2020-619-2020

Pelagotti, A., Mastio, A. D., Uccheddu, F., & Remondino, F. (2009). Automated Multispectral Texture Mapping of 3D Models. Proceedings of the 2009 17th European Signal Processing Conference, 1215–1219. https://ieeexplore.ieee.org/document/7077788

Percy, K., Ward, S., Santana Quintero, M., & Morrison, T. (2015). Integrated Digital Technologies for the Architectural Rehabilitation & Conservation of Beinn Bhreagh Hall & Surrounding Site, Nova Scotia, Canada. ISPRS Annals of the Photogrammetry, Remote Sensing and Spatial Information Sciences, II-5/W3, 235–241. https://doi.org/10.5194/isprsannals-II-5-W3-235-2015

Pérez, J., de Sanjosé Blasco, J., Atkinson, A., & del Río Pérez, L. (2018). Assessment of the Structural Integrity of the Roman Bridge of Alcántara (Spain) Using TLS and GPR. Remote Sensing, 10(3), 387. https://doi.org/10.3390/rs10030387

Pérez-Gracia, V., Di Capua, D., Caselles, O., Rial, F., Lorenzo, H., González-Drigo, R., & Armesto, J. (2011). Characterization of a Romanesque Bridge in Galicia (Spain). International Journal of Architectural Heritage, 5(3), 251–263. https://doi.org/10.1080/15583050903560249

Previtali, M., Barazzetti, L., Redaelli, V., Scaioni, M., & Rosina, E. (2013). Rigorous procedure for mapping thermal infrared images on three-dimensional models of building façades. Journal of Applied Remote Sensing, 7(1), 073503. https://doi.org/10.1117/1.JRS.7.073503

Puente, I., Solla, M., González-Jorge, H., & Arias, P. (2015). NDT Documentation and Evaluation of the Roman Bridge of Lugo Using GPR and Mobile and Static LiDAR. Journal of Performance of Constructed Facilities, 29(1), 06014004. https://doi.org/10.1061/(ASCE)CF.1943-5509.0000531

Ramos, M. M., & Remondino, F. (2015). Data fusion in Cultural Heritage – A Review. ISPRS - International Archives of the Photogrammetry, Remote Sensing and Spatial Information Sciences, XL-5/W7, 359–363. https://doi.org/10.5194/isprsarchives-XL-5-W7-359-2015

Riveiro, B., Arias, P., Armesto, J., Caamaño, J. C., & Solla, M. (2012). From Geometry to Diagnosis: Experiences of Geomatics in Structural Engineering. ISPRS - International Archives of the Photogrammetry, Remote Sensing and Spatial Information Sciences, XXXIX-B5, 291–296. https://doi.org/10.5194/isprsarchives-XXXIX-B5-291-2012

Rizzi, A., Voltolini, F., Girardi, S., Gonzo, L., & Remondino, F. (2007). Digital Presentation, Documentation and Analysis of Paintings, Monuments and Large Cultural Heritage with Infrared Technology, Digital Cameras and Range Sensors. ISPRS - International Archives of the Photogrammetry, Remote Sensing and Spatial Information Sciences, XXXVI-5/C53, 3–8.

Rocha, Mateus, Fernández, & Ferreira. (2020). A Scan-to-BIM Methodology Applied to Heritage Buildings. Heritage, 3(1), 47–67. https://doi.org/10.3390/heritage3010004

Rosenberger, M., Zhang, C., Zhang, Y., & Notni, G. (2020). 3D High-resolution multimodal imaging system for real-time applications. In S. Zhang & K. G. Harding (Eds.), Proc. SPIE 11397 (p. 1139704). SPIE. https://doi.org/10.1117/12.2558413

Sahin, C. D., & Mengüç, M. P. (2019). Image registration method for mobile-device-based multispectral optical diagnostics for buildings. Applied Optics, 58(26), 7165. https://doi.org/10.1364/AO.58.007165

Sánchez, J., & Quirós, E. (2017). Semiautomatic detection and classification of materials in historic buildings with low-cost photogrammetric equipment. Journal of Cultural Heritage, 25, 21–30. https://doi.org/10.1016/j.culher.2016.11.017

Sánchez-Aparicio, L. J., Del Pozo, S., Rodriguez-Gonzalvez, P., Herrero-Pascual, J., Muñoz-Nieto, A., & Gonzalez-Aguilera, D. (2016). Practical use of multispectral techniques for the detection of pathologies in constructions. In B. Riveiro & M. Solla (Eds.), Non-Destructive Techniques for the Evaluation of Structures and Infrastructure (1st Edition, pp. 253–271). CRC Press. https://doi.org/10.1201/b19024

Santos-Asssunçao, S., Pérez-Gracia, V., Gonzalez, R., Caselles, O., Clapes, J., & Salinas, V. (2014). Geophysical exploration of columns in historical heritage buildings. Proceedings of the 15th International Conference on Ground Penetrating Radar, 97–102. https://doi.org/10.1109/ICGPR.2014.6970393

Santos-Assunçao, S., Pérez-Gracia, V., Caselles, O., Clapes, J., & Salinas, V. (2014). Assessment of Complex Masonry Structures with GPR Compared to Other Non-Destructive Testing Studies. Remote Sensing, 6(9), 8220–8237. https://doi.org/10.3390/rs6098220

Scaioni, M. (2005). Direct Georeferencing of TLS in Surveying of Complex Sites. ISPRS - International Archives of the Photogrammetry, Remote Sensing and Spatial Information Sciences, XXXVI-5/W17. https://www.isprs.org/proceedings/XXXVI/5-W17/pdf/23.pdf

Serna, C. G., Pillay, R., & Trémeau, A. (2015). Data Fusion of Objects Using Techniques Such as Laser Scanning, Structured Light and Photogrammetry for Cultural Heritage Applications. In

A. Trémeau, R. Schettini, & S. Tominaga (Eds.), Computational Color Imaging (Vol. 9016, pp. 208–224). Springer International Publishing. https://doi.org/10.1007/978-3-319-15979-9_20

Shanoer, M. M., & Abed, F. M. (2018). Evaluate 3D laser point clouds registration for cultural heritage documentation. The Egyptian Journal of Remote Sensing and Space Science, 21(3), 295–304. https://doi.org/10.1016/j.ejrs.2017.11.007

Simon Chane, C., Mansouri, A., Marzani, F. S., & Boochs, F. (2013). Integration of 3D and multispectral data for cultural heritage applications: Survey and perspectives. Image and Vision Computing, 31(1), 91–102. https://doi.org/10.1016/j.imavis.2012.10.006

Simon Chane, C., Schütze, R., Boochs, F., & Marzani, F. (2013). Registration of 3D and Multispectral Data for the Study of Cultural Heritage Surfaces. Sensors, 13(1), 1004–1020. https://doi.org/10.3390/s130101004

Sitnik, R., Mączkowski, G., & Krzesłowski, J. (2010). Integrated shape, color, and reflectivity measurement method for 3D digitization of cultural heritage objects. In A. M. Baskurt (Ed.), Proc. SPIE 7526 (p. 75260Q). SPIE. https://doi.org/10.1117/12.839166

Solla, M., Caamaño, J. C., Riveiro, B., & Arias, P. (2012). A novel methodology for the structural assessment of stone arches based on geometric data by integration of photogrammetry and ground-penetrating radar. Engineering Structures, 35, 296–306. https://doi.org/10.1016/j.engstruct.2011.11.004

Solla, M., Gonçalves, L. M. S., Gonçalves, G., Francisco, C., Puente, I., Providência, P., Gaspar, F., & Rodrigues, H. (2020). A Building Information Modeling Approach to Integrate Geomatic Data for the Documentation and Preservation of Cultural Heritage. Remote Sensing, 12(24), 4028. https://doi.org/10.3390/rs12244028

Solla, M., Lorenzo, H., Novo, A., & Caamaño, J. C. (2012). Structural analysis of the Roman Bibei bridge (Spain) based on GPR data and numerical modelling. Automation in Construction, 22, 334–339. https://doi.org/10.1016/j.autcon.2011.09.010

Spanò, A., Volinia, M., & Girotto, M. (2005). Spatial Data and Temperature: Relationship to Deepen. Integrated Methods for Advanced Architectural Diagnosis and Metric Documentation. In M. Marabelli, C. Parisi, G. Buzzanca, & A. Paradisi (Eds.), Proceedings of the art '05. Eightth Internation Conference on Non'Destructive Investigations and Microanalysis for the Diagnostics and Conservation of the Cultural and Environmental Heritage. Italian Society of Non-Destructive Testing Monitoring Diagnostics AIPnD.

Stavroulaki, M. E., Riveiro, B., Drosopoulos, G. A., Solla, M., Koutsianitis, P., & Stavroulakis, G. E. (2016). Modelling and strength evaluation of masonry bridges using terrestrial photogrammetry and finite elements. Advances in Engineering Software, 101, 136–148. https://doi.o rg/10.1016/j.advengsoft.2015.12.007

Tombari, F., & Remondino, F. (2013). Feature-based automatic 3D registration for cultural heritage applications. 55–62. https://doi.org/10.1109/DigitalHeritage.2013.6743713

Tucci, G., Bonora, V., Conti, A., & Fiorini, L. (2017a). Digital Workflow for the Acquisition and Elaboration of 3D Data in a Monumental Complex: The Fortress of Saint John the Baptist in Florence. The International Archives of the Photogrammetry, Remote Sensing and Spatial Information Sciences, XLII-2/W5, 679–686. https://doi.org/10.5194/isprs-archives-XLII-2-W5-679-2017

Tucci, G., Bonora, V., Conti, A., & Fiorini, L. (2017b). High-Quality 3D Models and their Use in a Cultural Heritage Conservation Project. The International Archives of the Photogrammetry, Remote Sensing and Spatial Information Sciences, XLII-2/W5, 687–693. https://doi.org/10.5194/isprs-archives-XLII-2-W5-687-2017

Ulvi, A. (2021). Documentation, three-dimensional (3D) modelling and visualization of cultural heritage by using unmanned aerial vehicle (UAV) photogrammetry and terrestrial laser scanners. International Journal of Remote Sensing, 42(6), 1994–2021. https://doi.org/10.1080/01431161.2020.1834164

Vázquez, M. A., Galán, E., Guerrero, M. A., & Ortiz, P. (2011). Digital image processing of weathered stone caused by efflorescences: A tool for mapping and evaluation of stone decay. Construction and Building Materials, 25(4), 1603–1611. https://doi.org/10.1016/j.conbuildmat.2010.10.003

von Schwerin, J., Richards-Rissetto, H., Remondino, F., Agugiaro, G., & Girardi, G. (2013). The MayaArch3D project: A 3D WebGIS for analyzing ancient architecture and landscapes. Literary and Linguistic Computing, 28(4), 736–753. https://doi.org/10.1093/llc/fqt059

Webb, E. K., Robson, S., MacDonald, L., Garside, D., & Evans, R. (2018). Spectral and 3D Cultural Heritage Documentation Using a Modified Camera. ISPRS - International Archives of the Photogrammetry, Remote Sensing and Spatial Information Sciences, XLII–2, 1183–1190. https://doi.org/10.5194/isprs-archives-XLII-2-1183-2018

Xu, Z., Wu, L., Shen, Y., Li, F., Wang, Q., & Wang, R. (2014). Tridimensional reconstruction applied to cultural heritage with the use of camera-equipped UAV and terrestrial laser scanner. Remote Sensing, 6(11), 10413–10434. https://doi.org/10.3390/rs61110413

Yang, M.-D., Su, T.-C., & Lin, H.-Y. (2018). Fusion of Infrared Thermal Image and Visible Image for 3D Thermal Model Reconstruction Using Smartphone Sensors. Sensors, 18(7), 2003. https://doi.org/10.3390/s18072003

Zainuddin, K., Majid, Z., Ariff, M. F. M., Idris, K. M., Abbas, M. A., & Darwin, N. (2019). 3D Modeling for Rock Art Documentation using Lightweight Multispectral Camera. ISPRS - International Archives of the Photogrammetry, Remote Sensing and Spatial Information Sciences, XLII-2/W9, 787–793. https://doi.org/10.5194/isprs-archives-XLII-2-W9-787-2019

Zalama, E., Gómez-García-Bermejo, J., Llamas, J., & Medina, R. (2011). An Effective Texture Mapping Approach for 3D Models Obtained from Laser Scanner Data to Building Documentation: An effective texture mapping approach. Computer-Aided Civil and Infrastructure Engineering, 26(5), 381–392. https://doi.org/10.1111/j.1467-8667.2010.00699.x

Zhang, C., Rosenberger, M., Breitbarth, A., & Notni, G. (2016). A novel 3D multispectral vision system based on filter wheel cameras. Proceedings of the 2016 IEEE International Conference on Imaging Systems and Techniques (IST), 267–272. https://doi.org/10.1109/IST.2016.7738235

Zitová, B., & Flusser, J. (2003). Image registration methods: A survey. Image and Vision Computing, 21(11), 977–1000. https://doi.org/10.1016/S0262-8856(03)00137-9

4 Semi-Automated Deterioration Mapping using Close-Range Multispectral Data

The methodology described in this section has been developed with the aim to automate the process of documenting the existing conditions of historic surfaces subject to deterioration. The developed mapping procedure delves into the fields of sensing, imaging science, and pattern recognition to deliver an accurate approach for efficiently classifying surface deterioration patterns (identified through other techniques), applicable for both historic structures and antiquities. Hence, this section explains in detail the research design for a mapping methodology based on multispectral data recording and processing, including the techniques followed for close-range reflectance data acquisition, preliminary treatment, fusion, and supervised classification. Furthermore, in this section, significant emphasis is given to evaluating various multispectral image composites to improve the thematic accuracy of the segmentation, simultaneously considering—for the first time—reflectance images captured at the visible, NIR, LWIR, and NUV spectra. The outlined procedure intends to address heritage assets of varying complexity and multiplicity of deterioration patterns but mainly confronts the mapping problem as a 2D approach because of the inherent usefulness of 2D thematic mapping products for actions pertinent to support heritage protection and their more straightforward translation to semantic entities.

The novelty of the proposed methodology lies in the implementation of a single-sensor low-cost approach for recording the multispectral data at the near-visible spectra differentiating from most relevant work, which applies multi-camera recording or uses different LiDAR instruments to acquire narrowband reflectance data. It is evident that these multi-sensor approaches induce high costs, while the proposed methodology is considerably more affordable and flexible. Additionally, there is a crucial advantage over the employment of miniaturized multispectral sensors in terms of spatial resolution and ease of application. Another innovative aspect of the proposed methodology is the implementation of learning-based supervised algorithms to automate the supervised segmentation process. Moreover, the application case studies considered for this methodology concerned historical

surfaces presenting multiple decay patterns (often heavily deteriorated), in contrast with other relevant image-based application scenarios found in recent literature, which mainly consider the alteration or not of the historical materials, and not the multiplicity of decay forms. The design and application of the described methods used for semi-automated deterioration mapping have been previously outlined in Adamopoulos (2021), Adamopoulos & Rinaudo (2021a), Adamopoulos & Rinaudo (2021b), and Adamopoulos, Rinaudo, & Adamopoulou (2021).

4.1 Methodological Approach

The designing of the methodological workflow considered the potential usefulness of the complementarity of multispectral data, passively captured at and near the visible spectrum, for the digital mapping of historic surfaces' preservation state. Its rationale was set on the identified lack of practical image-based methods for automatic condition mapping, especially regarding severely degraded historical surfaces. The proposed workflow aims to be flexible in terms of adopting easy-to-implement close-range sensing technologies for data recording and free and open-sourced software (FOSS) tools for image processing. DIP techniques are adopted for the classification of deterioration patterns. The process of mapping the significantly weathered historic surfaces is carried out through supervised-learning-based models, which use as input representative patches of the already identified deterioration categories. Unsupervised data reduction methods, such as clustering, are also considered to tackle problems encountered due to overlap between multiple deterioration forms. This methodological workflow primarily addresses historical surfaces that are relatively planar or that can be sufficiently described as an assortment of parallel two-dimensional planes. Different multispectral image compositions are involved in line with the scope of this research.

Figure 4.1 depicts the overall research design for the 2D deterioration mapping approach. An essential parameter for ensuring the accuracy and interpretability of the surface classification is the quality of input spectral intensity data, meaning the acquired raw images, which are later used for semi-automated pattern recognition. Therefore, the workflow starts with capturing appropriate radiance images and then continues with their radiometric correction and integration. The multispectral composites are digitally synthesized from the band-specific data and then segmented into deterioration categories after visual identification on-site. The output maps of the deterioration classification procedure can be transferred to an environment appropriate for spatial information management, semantic annotation, and further processing. The principle of using low-cost instrumentation and software is followed during every step of the process, as it is a crucial factor for heritage non-destructive inspection.

DATA ACQUISITION		PRE-PROCESSING		PATTERN ANALYSIS
Sensors	**Raw Data**	**Data Correction**	**Image Composition**	**Supervised Classification**
	Red-Green-Blue True Color images	Raw data extraction		Training areas definition
Modified digital camera with external filters	Ultraviolet Reflectance images	Radiometric correction	Registration	Decision tree/ Ensemble learning/ Regression
	Near-Infrared Reflectance image	Spatial correction	Bands selection	**Unsupervised Classification**
Thermal camera	Thermal-Infrared Reflectance images	High-resolution TIR image generation	Synthesis of multiband image composites	Clustering/ Data reduction

Figure 4.1. Semi-automated deterioration mapping methodology.

4.1.1 Multispectral Data Acquisition

The proposed workflow propounds—as an alternative to the use of multispectral sensors—implementing modified CMOS-based digital SLR cameras in order to allow the acquisition of high-resolution spectral radiance images. This decision comes with the drawbacks of sacrificing the narrowness of spectral sensitivity and reducing the number of spectral channels, but nevertheless grants higher versatility and decreases the cost of the required instrumentation (Verhoeven, 2008; Webb et al., 2018).

As previously mentioned in subchapter 2.2.2.2, multispectral imaging in the 350–1100 nm range can be simulated via modified commercial cameras (and frequently with multi-sensor approaches). Commercial off-the-shelf (COTS) digital camera detectors are generally sensitive in a portion of the electromagnetic range up to 1100 nm, which is partially cut off by an internal blocking filter. By removing the internal near-infrared cut-off filter, a charge-coupled device (CCD) or a complementary metal-oxide-semiconductor (CMOS)-based camera can be used as an affordable and easy-to-acquire alternative for multispectral capturing. In such a way, narrowband or wideband externally placed filters capture radiance data at the very near-ultraviolet, visible, and near-infrared range. At the same time, the camera retains user-friendly features and interfaces to a wide variety of photographic accessories and software interfaces. The acquisition with a modified digital camera follows different approaches depending on the use of the radiance images. For example, suppose the object of study is investigated with a single-multispectral rectified image approach. In that case, the spectral images should be acquired as parallel as possible to the architectural surfaces to avoid occlusions and with large focal lengths to avoid significant distortions that can affect image quality during the resampling phase of distortion correction. Furthermore, the images should be acquired under homogeneous illumination to improve their radiometric potential and with a steady tripod, thus preventing image blur. Either the measurement of a

network of control points well distributed over the investigated historical surface or the placement of calibrated scales should take place before image acquisition.

The use of thermal cameras, common for building inspections, is additionally considered for recording radiance data at the LWIR range, providing an additional spectral band for the produced multispectral composites. Emphasis is yet again given to lower-end instruments, which reduce the cost and the complexity of implementation. Nevertheless, this introduces additional processing steps, as the significantly low spatial resolution of mobile, low-cost thermal cameras necessitates the resolution enhancement of acquired thermograms to match the spatial resolution of other spectral bands.

4.1.2 Multispectral Data Pre-Processing

Preliminary treatment of the images acquired with a modified digital SLR camera at multiple electromagnetic spectrum bands involves adjusting recorded radiance values, geometric correction, and preparation of the multispectral image composites for automated pattern segmentation. First, the acquired raw images are radiometrically corrected because various noise sources influence the actual reflectance values. The noise model of the imaging sensor (Tsin et al., 2001; Liu et al., 2008; Zheng et al., 2009) can be estimated as:

$$I = f(L + N_v) + N_b \tag{1}$$

where *I* are the recorded values of the raw digital images, *L* is the digital level of the radiance component, N_v is the digital level of the vignetting noise, N_b is the digital level of the optical system's background noise, and $f(\cdot)$ is the radiometric function carried out to obtain the full resolution image that depends on the Bayer filter. The digital files acquired with the camera are downloaded in the RawDigger 1.4.4 (LibRaw, LLC) software where, after having been corrected by the sensor's background noise (N_b), the color filter array (debayering) conversion is reversed, to acquire raw digital images. The raw images are then corrected from the vignetting effect (N_v). An automatic flat field correction may also be applied to remove any remaining ambiental effects. The next step of pre-processing is transforming the *L* values of the raw radiance images into reflectance values. The transformation equation (Del Pozo et al., 2016), which can occur after calibrating the camera with a vicarious radiance-based method, is:

$$\rho = \frac{c0_\lambda + c1_\lambda + L/Fv_\lambda}{E_\lambda} \cdot \pi \tag{2}$$

where $c0_\lambda$ and $c1_\lambda$, offset and gain, are the calibration coefficients of each camera band, Fv^λ is the shutter opening time factor, and E_λ is the solar irradiance at the ground level.

The spectral reflectance images are undistorted in the Fiji image processing package—a distribution of ImageJ2 (Rueden et al., 2017)—and then each image is orthorectified with an affine transform in the HyperCube image analysis software (https://www.erdc.usace.army.mil/Media/Fact-Sheets/Fact-Sheet-Article-View/Article/610433/hypercube) depending on available measured coordinates. Figure 4.2 showcases a schematic representation of the pre-processing stages taking place prior to any multispectral composition and segmentation of the deterioration patterns.

The addition of a thermal-infrared image into the data stack consisting of the corrected reflectance images to simulate a multispectral image cube presupposes that the thermal-infrared image should be of the same spatial resolution as the other reflectance images. Therefore, pre-processing of the low-resolution thermal data involves the creation of a high-resolution image from a set of low-resolution burst mode images. For this purpose, the inverse distance weighting method (Shepard, 1968) is used, predicting the high-resolution pixel values from sets of pixels in the low-resolution burst mode thermal-infrared images.

In order to form a multispectral image cube, registration of multiple single-band reflectance images is also performed in HyperCube. Alternatively, non-rectified images are registered using a projective transformation, nearest-neighbor interpolation, and resampled with the same scene sampling distance. The synthesis of the multispectral composites considers the same principle of using low-cost equipment, and thus all considered composites consist of a number of bands (3 channels) that will allow segmentation to be performed in the Fiji image processing package or other freeware—avoiding the use of commercial specialized spatial analysis software.

Background noise removal
+ reverse debayering conversion

Vignetting correction

Flat-field correction

Radiance-to-reflectance
transformation

Rectification
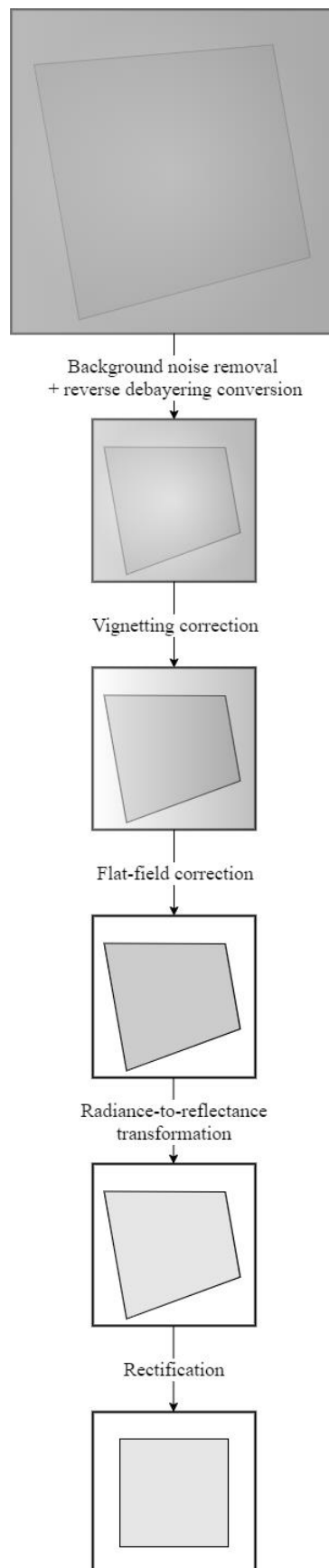
Figure 4.2. Schematic representation of pre-processing procedures for the spectral images.

4.1.3 Segmentation of Deterioration Patterns

The methodology tested for semi-automated thematic deterioration mapping considers that different approaches could be followed to classify surface patterns, depending on the complexity of observable surface deterioration. Thus, a choice of distinct digital image processing tools is considered depending on the multiplicity of deterioration forms. The ICOMOS ISCS: Illustrated glossary on stone deterioration patterns (2008) has been followed as a guide to identifying individual degradation patterns during visual inspection. Historic surfaces presenting few and easily distinguishable patterns can be mapped with unsupervised segmentation techniques (such as thresholding and clustering). Nevertheless, a supervised machine learning-based approach is proposed as it can use as input the areas-regions of interest (ROIs) detected through visual inspection or analytical testing of the historical materials and their alteration.

The proposed supervised segmentation procedure for classifying the deterioration patterns is performed via the Trainable WeKa Segmentation 3D plugin (Arganda-Carreras et al., 2017) of ImageJ2. The machine learning-based image segmentation techniques follow decision tree (Quinlan, 1993), ensemble learning (Breiman, 2001), and regression approaches. Specifically, the Random Tree, Random Forest, Fast Random Forest, LogitBoost, and j48 classifiers are employed. The supervised approach presupposes the annotation of image regions of interest (ROIs), corresponding to each semantic deterioration category to be segmented, which will train the algorithmic model to provide a semantic classification of the entire image.

The decision tree model is a machine learning algorithm that can be used for both supervised classification and regression problems. A decision tree simply consists of a series of sequential decisions made to reach a specific result of distinct data classes. The classes are mutually exclusive and represented by specific attributes. The learning input, which consists of sets of pixels belonging to known classes, assists the accurate classification of annotated pixels and not annotated pixels. Each node of the decision tree decides an outcome based on the attribute values and leads either to another node, using an appropriate subtree, or to a leaf, which gives the predicted class of the pixel (Quinlan, 1996). The Random Tree classifier is based on a decision tree learning method. Single decision trees are easy to conceptualize but usually suffer from high variance, making them not competitive in terms of accuracy.

A random forest classifier combines ensemble classification machine learning algorithms and decision trees. Each tree classifier is independently generated from the input training data using a random sample like in bagging. When growing a tree, the best possible split is computed for a random subset, instead of always computing the best split for each node. In this way, tree diversity is generated using two ways

of randomization. Aggregating predictions make the class prediction of the ensemble. Random forest generally overcomes the accuracy limitations of single decision trees (Breiman, 2001; Zhao & Zhang, 2008).

LogitBoost is a boosting algorithm that performs classification using a regression scheme as the base learner and can handle multi-class problems. It can be seen as a convex optimization; it applies the cost function of logistic regression on a generalized additive model. This classifier determines the appropriate number of iterations by performing efficient internal cross-validation (Friedman et al., 2000).

The J48 is another classifier that produces a decision tree generated by the C4.5 algorithm by Quinlan (1993). It is also known as a statistical classifier.

4.1.4 Accuracy Metrics-Segmentation Evaluation

The performance of the machine learning classification implementations and different multispectral combinations is quantitatively evaluated using manually produced degradation maps as the ground truth. Different parameters are used to assess the classification efficiency of the intelligent feature extraction techniques based on accuracy metrics common for thematic mapping. More specifically, the evaluation relies on the precision (fraction of appropriate classification among the classified instances) and F1-score (harmonic mean of precision and sensitivity) calculated for each class (Equations 3,4) and on the overall accuracy (Equation 5)—useful to estimate the overall performance of the classifiers.

$$Precision \ = \ \frac{TP}{TP + FP} \tag{3}$$

$$F1 \ Score = \frac{2TP}{2TP + FP + FN} \tag{4}$$

$$Overall \ Accuracy = \frac{TP + TN}{(TP + TN) + (FP + FN)} \tag{5}$$

where, for each class, the *TP* (true positive), *FP* (false positive), and *FN* (false negative) come from an error matrix (**Table 4.1**), a square array of numbers which express the number of pixels assigned to a particular class in one classification relative to the number of pixels assigned to a particular class in the reference data (Congalton & Green, 2019; Das, 2021).

Table 4.1. The Error matrix.

PREDICTED VALUES

POSITIVE   NEGATIVE

	POSITIVE	NEGATIVE
POSITIVE	TP	FN
NEGATIVE	FP	TN

ACTUAL VALUES

Note: *TP* True Positive; *FP* False Positive; *FN* False Negative; *TN* True Negative.

4.2 Experimental Results

The experimental part of this chapter reports on the implementation of the methodology presented in 4.1, demonstrating how it was adapted for different scenarios of cultural heritage documentation and inspection. The description of the multispectral recording and deterioration mapping precedes a brief mention of the instrumentation used. Detailed accuracy statistics for produced thematic maps could be calculated for the case studies where reference maps were available.

Close-range multispectral datasets, purposed for deterioration mapping, were taken with an EOS Rebel SL1 (Canon Inc., Tokyo, Japan) digital SLR camera with an EF-S 18-55mm f/3.5-5.6 IS II lens. The internal hot mirror filter of the SL1 camera had been removed. Low-cost external filters were employed with the camera to allow radiance imaging at different spectral bands of the 400–1100 nm range. Additionally, the FLIR ONE Pro (Teledyne FLIR LLC, Wilsonville, OR, USA) thermographic camera (attached to a smartphone) was employed for a few case studies to evaluate the proposed methodology's performance when including data acquired at the LWIR band.

4.2.1 Historical Structures

4.2.1.1 Karababa Fortress

This first historical structure (Figure 4.3), selected as a case study for the application of the semi-automated deterioration mapping workflow, due to its current state of

preservation, was a masonry fortification in Chalcis (Euboea, Greece). The Fort of Karababa is an Ottoman fortress constructed in 1684 on the homonymous hill which dominates the Boeotian coast across the city of Chalcis. The construction of the fortress was part of the effort to protect the city of Chalcis from impending Venetian attacks (Mamaloukos, 2020). The architectural style of the fortress is more European than Turkish. It is oblong in plan, with a rampart on the north side, three bastions, and a large tower.

Map data: Google, 2021 @ CNES / Airbus, Maxar Technologies

Figure 4.3. Fort of Karababa, bird's-eye view.

Several parts of the fortification walls have ancient spolia built-in, while some parts are preserved in poor condition. The weathered masonry surfaces selected for evaluating the methodology are presented in Figure 4.4. They are on the north side, and for abbreviation purposes, they have been named A, B, C, and D, starting with the westernmost (on the west bastion).

Spectral radiance images were acquired as parallel as possible to the architectural surfaces to avoid occlusions and with large focal lengths to avoid large distortions that could affect image quality during the resampling phase of distortion correction. Three filters were employed to allow RGB, UV, and NIR photo shooting. Furthermore, the images were acquired under homogeneous illumination conditions and without shadows. The thermographic images were acquired in sets of burst images to increase their spatial resolution digitally.

Figure 4.4. Fort of Karababa north side, façades selected for evaluating the mapping methodology; from upper left, clockwise: A (westernmost), B, C and D (eastermost).

The captured raw NIR and UV images were converted to radiance and then to reflectance images, based on the pixel values of a reference surface collected with a spectroradiometer. Visible-spectrum images were RGB calibrated based on the pixel values of a reference photographic color-balance target. The resulting band-specific reflectance images were then undistorted.

Multispectral image composites were constructed by performing combinations between different spectra, a procedure presented in Table 4.2. The corrected spectral reflectance images were resampled to match the resolution of all bands, and the sky and ground were trimmed from all multispectral composites to reduce the chance of potential misclassifications.

Table 4.2. Composition of multispectral images-Karababa Fortress.

Multispectral image	Red band	Green band	Blue band
G-B-NUV	green	blue	ultraviolet
R-G-B	red	green	blue
NIR-R-G	near infra-red	red	green
TIR-NIR-R	thermal infra-red	near infra-red	red
NIR-M-UV	near infra-red	RGB monochromatic	ultraviolet
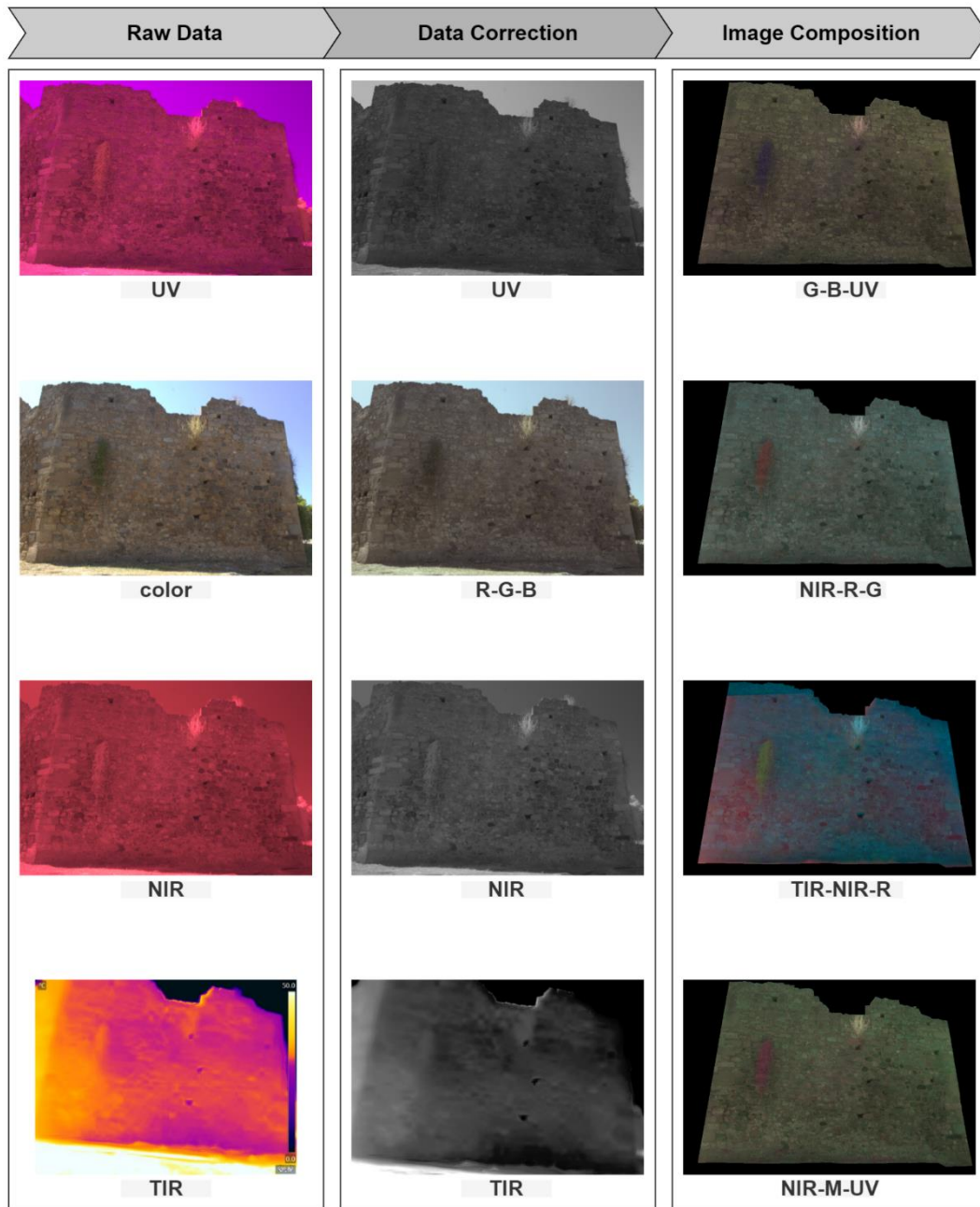
Figure 4.5. Multispectral data preparation for façade D, Fort of Karababa. Note: *UV* Ultraviolet; *R* Red; *B* Blue; *G* Green; *NIR* Near Infra-Red; *TIR* Thermal Infra-Red; *M* Monochromatic color image.

After the composition of multispectral images was completed (Figure 4.5), 80 classifications were performed. The observed categories of deterioration were vegetation, moss, black crusts, lichens, missing material (including loss of components, large cracks, and windows), and dampness. These constituted all the categories of surface pathology that altered the surface reflectance characteristics of the masonry façades. The classification results are presented in Figures 4.6–4.9.
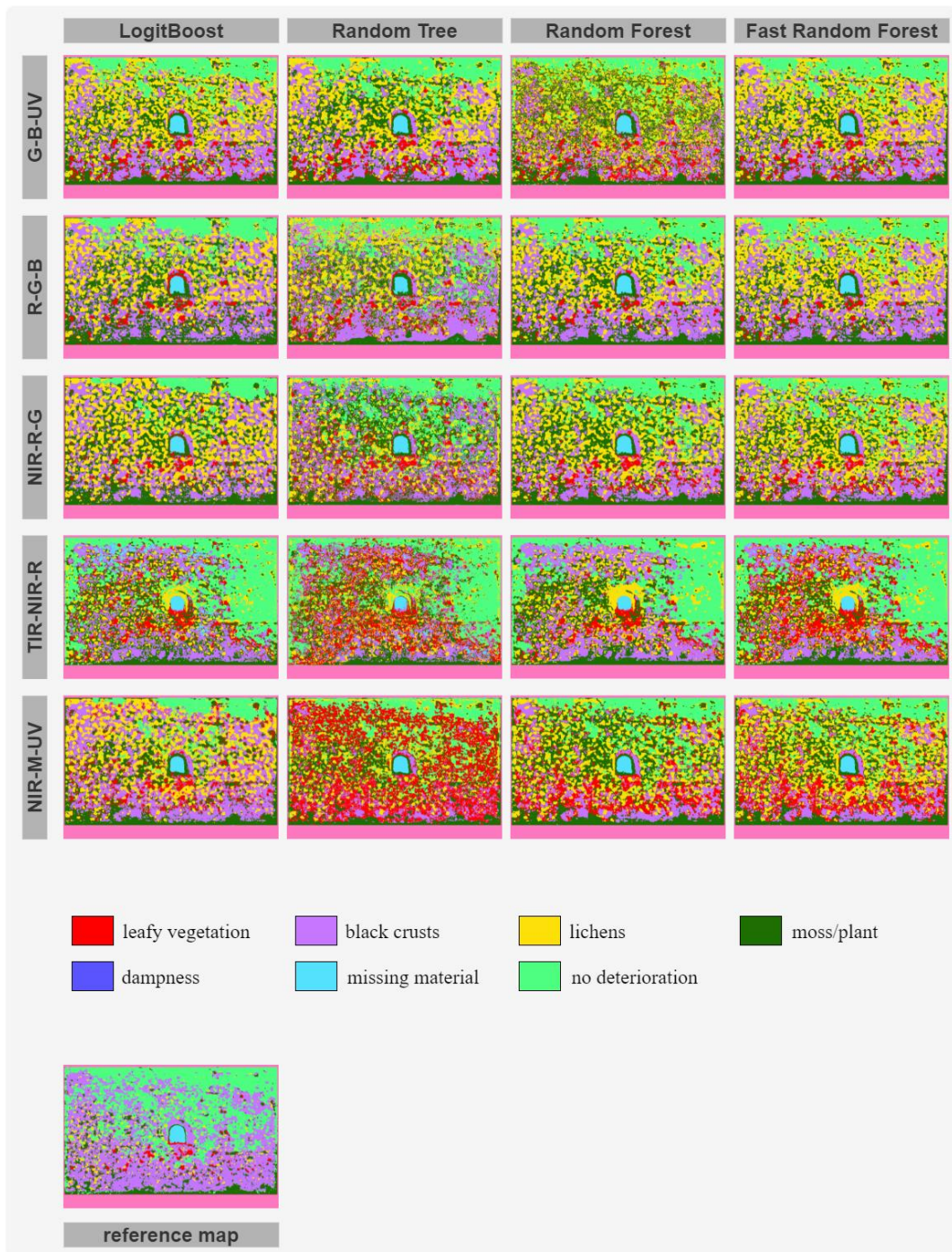
Figure 4.6. Thematic deterioration mapping of façade A, Fort of Karababa.
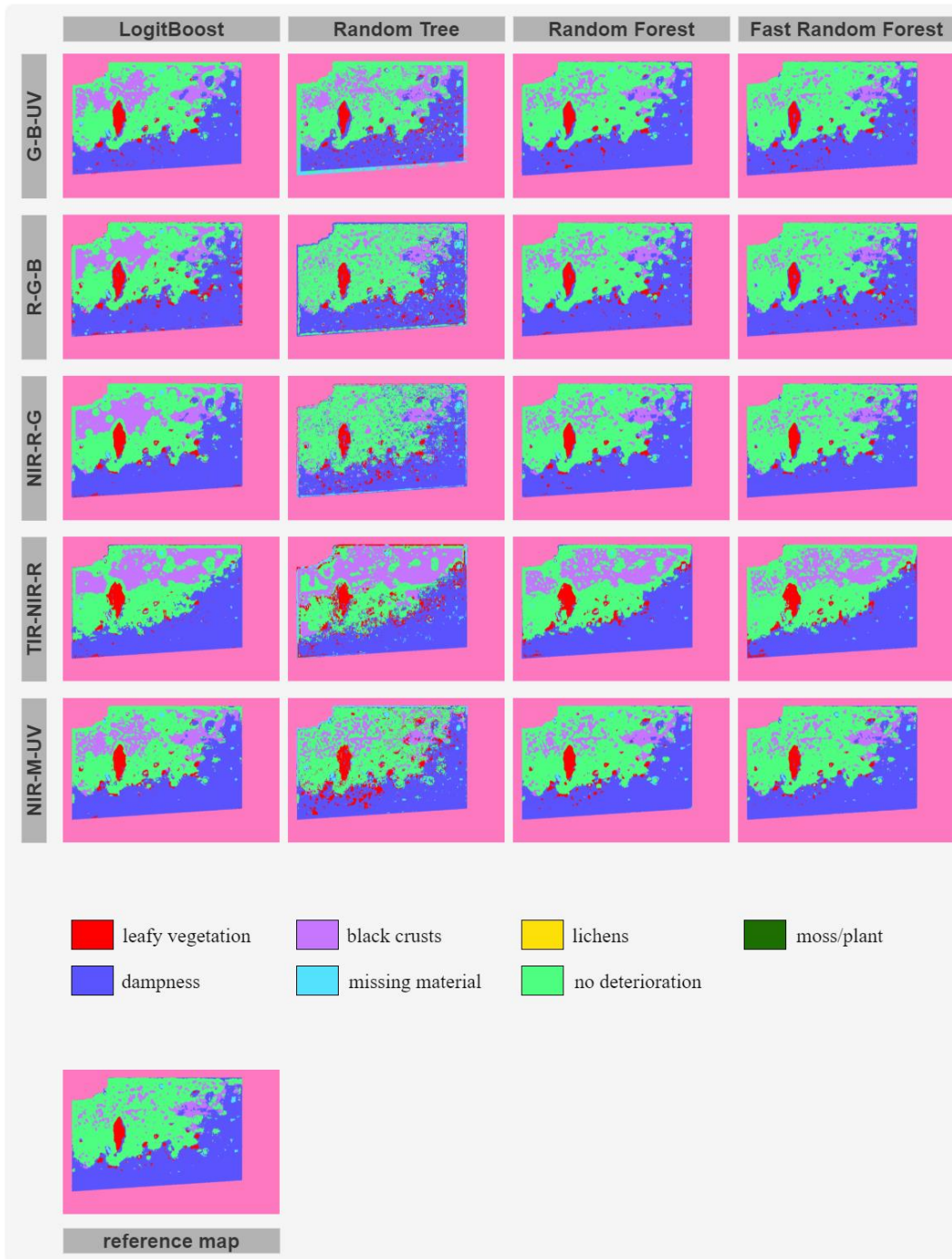
Figure 4.7. Thematic deterioration mapping of façade B, Fort of Karababa.
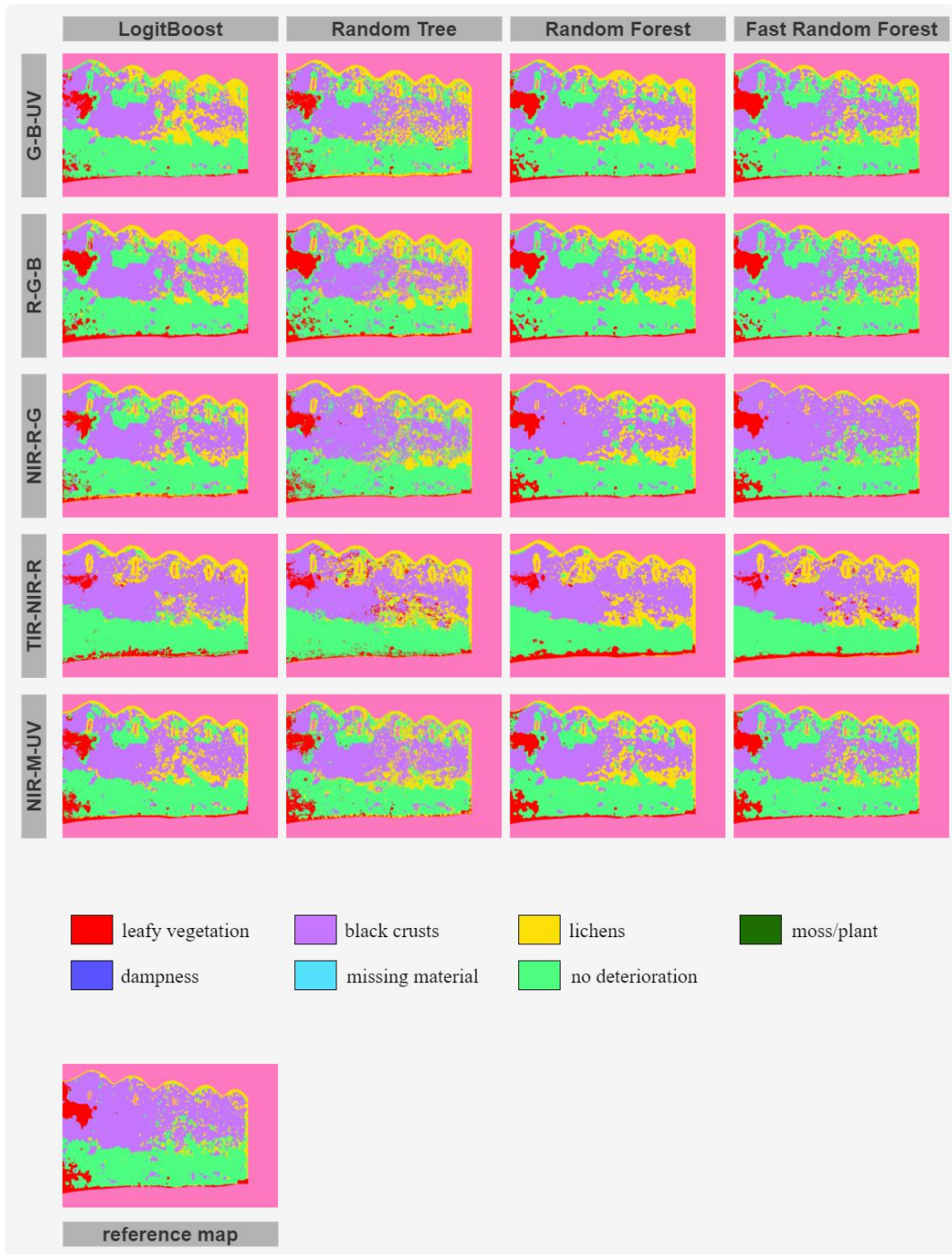
Figure 4.8. Thematic deterioration mapping of façade C, Fort of Karababa.
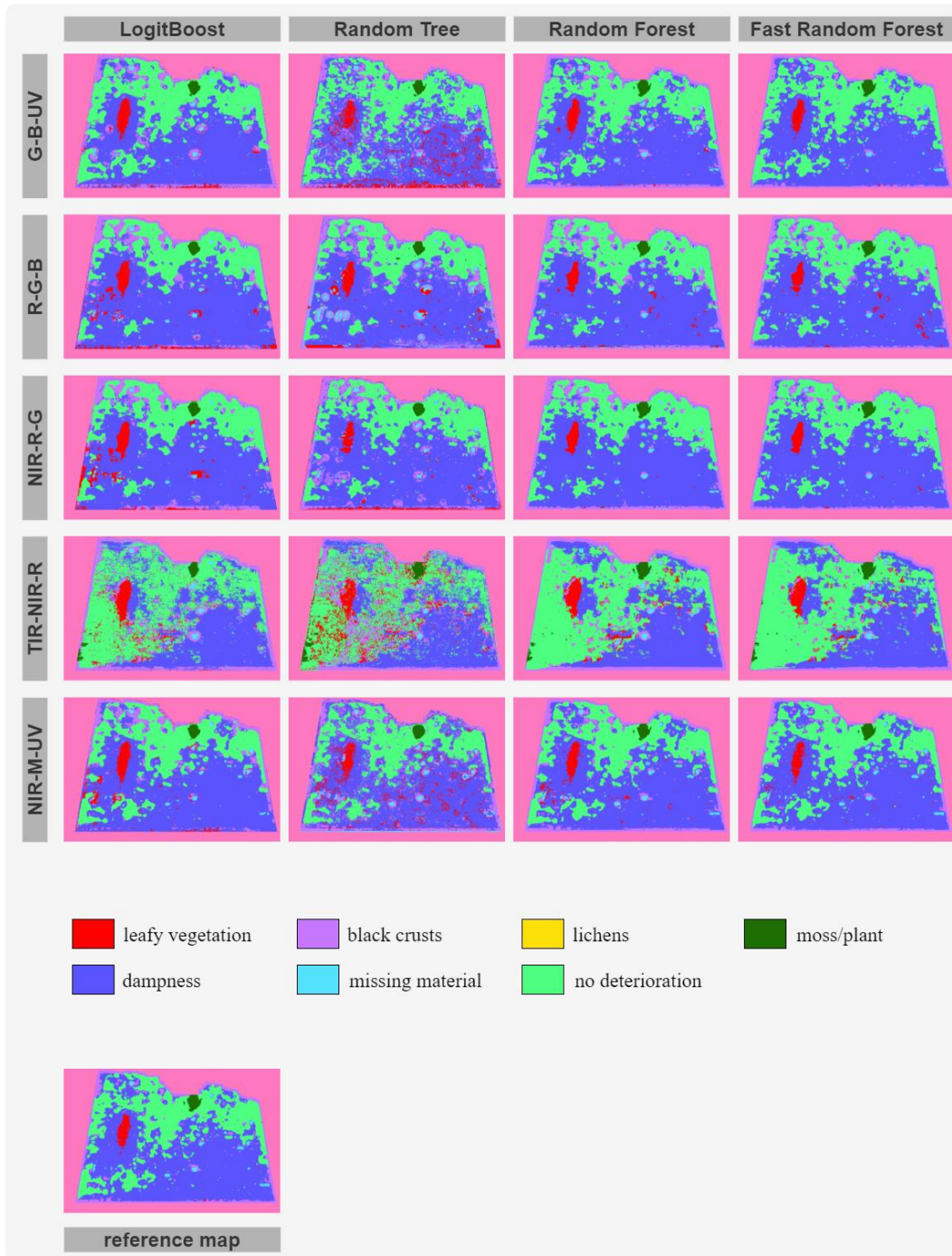
Figure 4.9. Thematic deterioration mapping of façade D, Fort of Karababa.

The comparisons aiming to evaluate thematic mapping accuracy were performed using manually produced full reference maps and not sampled patch areas. Overall accuracy statistics calculated from the confusion matrixes are presented in Table 4.3. The precision and F1-score results are presented in detail in Tables 4.4–4.7.

Based on the calculated statistics, the results for façade A were deemed of low classification accuracy. However, deterioration maps produced for the rest of the

studied historical architectural surfaces were of generally high thematic accuracy, especially for classifications performed via ensemble learning algorithmic implementations. Furthermore, the inclusion of different spectral bands improved the classification potential (subject to different present categories of deterioration). The low-quality classification ($38 <$ overall accuracy% < 56) of multispectral image composites for façade A can be attributed to the poor preservation condition, high level of biogenic deterioration characterizing almost the entire architectural surface, and extensive overlap among different surface patterns—particularly between moss and other deterioration. The thematic reference maps consider only one type of deterioration category for each image pixel, the most dominant one in the area that this pixel represents, which is clearly observable by visual inspection. Considering an equal scale of representation, the semi-automated classification depends on the reflectance values (at the employed spectra) for that same area. When a pixel represents a real-life area of the historical surface where multiple deterioration forms are present, the perceived radiometric signature is altered and consists of a combination of the radiometric signatures of the different deterioration forms, which hinders categorization into a single class. Therefore, the categorization of pixels into different classes through DIP can only be accurate when each of them presents a distinct radiometric reflectance value, characteristic of one specific deterioration form. However, this façade presented in many areas overlaps between moss and lichens, meaning pixels with multiple radiometric signatures combined, which explains the low precision and F1-score values for these categories of deterioration, despite the high values observed for the rest of the deterioration categories. Misclassifications could also be observed between the healthy materials' surfaces and patterns caused by lichens. Additionally, dampness at varying levels was present throughout the façade's surface, which complicated the process. Nevertheless, classifications performed for the other three façades, where the segregation among different deterioration forms was more clearly distinguishable, were of significantly higher quality (up to 86.8 overall accuracy%). Therefore, the mapping results of façade A were not considered to extract further conclusions.

Table 4.3. Overall accuracy statistics by image and classifier.

	A	B	C	D
	Overall Accuracy (%)			
G-B-UV				
LogitBoost	51.9	82.1	66.9	76.8
Random Tree	41.6	71.0	66.3	66.7
Random Forest	51.7	84.9	69.9	78.1
Fast Random Forest	51.4	84.6	70.2	79.8
R-G-B				
LogitBoost	50.7	77.3	67.9	78.5
Random Tree	52.5	73.7	63.7	74.3
Random Forest	56.0	84.4	69.8	81.9
Fast Random Forest	55.6	84.4	69.9	83.1
NIR-R-G				
LogitBoost	44.8	80.4	71.3	80.1
Random Tree	49.6	72.6	71.0	77.4
Random Forest	50.5	85.4	75.8	83.8
Fast Random Forest	51.5	86.3	79.0	84.6
TIR-NIR-R				
LogitBoost	48.8	74.6	76.3	58.4
Random Tree	38.4	64.9	71.3	50.9
Random Forest	49.8	76.8	76.3	57.3
Fast Random Forest	46.3	78.5	77.7	58.4
NIR-M-UV				
LogitBoost	49.0	83.2	71.6	75.3
Random Tree	37.5	75.4	66.8	66.6
Random Forest	44.1	85.5	69.3	77.0
Fast Random Forest	44.4	86.8	69.8	78.2

Note: *UV* Ultraviolet; *R* Red; *B* Blue; *G* Green; *NIR* Near Infra-Red; *TIR* Thermal Infra-Red; *M* Monochromatic color image.

Table 4.4. Accuracy statistics calculated for façade A, Fort of Karababa.

	leafy vegetation		no deterioration		black crusts		lichens		missing material		moss	
G-B-UV												
LB	25.4	37.1	96.0	53.2	93.3	66.2	17.3	29.4	98.8	95.8	98.8	95.8
RT	13.2	21.8	96.2	53.9	91.4	49.6	15.0	25.3	94.0	94.9	94.0	94.9
RF	23.2	35.2	96.4	56.9	93.9	64.1	18.1	30.4	98.5	95.9	98.5	95.9
FRF	26.5	38.4	95.5	53.3	93.6	65.1	16.5	28.2	99.1	95.1	99.1	95.1
R-G-B												
LB	29.5	38.4	94.5	48.5	83.7	65.5	17.7	29.2	96.8	91.9	96.8	91.9
RT	18.7	28.3	90.7	57.4	87.5	67.7	15.2	24.9	92.9	85.3	92.9	85.3
RF	41.6	49.3	90.3	61.4	93.0	67.2	19.2	31.8	97.6	96.7	97.6	96.7
FRF	38.0	46.1	93.4	57.9	92.8	69.1	17.6	29.8	97.2	96.6	97.2	96.6
NIR-R-G												
LB	35.8	48.7	97.1	37.6	84.9	59.8	15.5	26.5	99.1	92.8	99.1	92.8
RT	15.1	25.2	87.5	61.5	82.0	56.6	21.4	32.7	97.7	95.9	97.7	95.9
RF	29.6	43.6	97.8	58.4	94.4	59.5	18.3	30.6	99.5	97.3	99.5	97.3
FRF	29.4	43.6	95.7	57.8	95.1	61.2	17.2	29.3	99.8	97.3	99.8	97.3
TIR-NIR-R												
LB	16.9	27.7	64.0	58.8	78.1	47.8	30.7	45.2	20.4	31.5	20.4	31.5
RT	6.7	12.0	61.8	53.9	69.5	38.5	16.6	24.5	37.8	45.2	37.8	45.2
RF	19.6	31.5	64.4	58.3	75.2	50.3	25.8	39.2	73.4	71.1	73.4	71.1
FRF	9.9	17.6	63.2	58.1	77.4	43.2	29.3	43.5	33.9	45.0	33.9	45.0
NIR-M-UV												
LB	16.1	27.0	97.4	41.5	83.8	66.4	16.9	28.4	99.6	90.7	99.6	90.7
RT	3.6	6.9	95.3	61.5	87.9	31.1	24.6	36.8	99.1	94.4	99.1	94.4
RF	10.6	18.9	96.7	59.9	93.2	45.1	20.6	33.8	99.7	94.9	99.7	94.9
FRF	9.9	17.8	96.5	57.1	93.4	45.3	18.3	30.8	99.8	94.1	99.8	94.1
	precision	F1-score	precision	F1-score	precision	F1-score	precision	F1-score	precision	F1-score	precision	F1-score

Note: *LB* LogitBoost; *RT* Random Tree; *RF* Random Forest; *FRF* Fast Random Forest.

Table 4.5. Accuracy statistics calculated for façade B, Fort of Karababa.

	leafy vegetation		no deterioration		black crusts		missing material		dampness	
G-B-UV										
LB	44.4	60.3	87.5	82.1	56.7	60.4	39.0	53.4	91.7	90.4
RT	28.7	42.6	80.1	77.0	46.1	48.3	6.8	12.3	86.0	79.1
RF	46.3	61.4	86.3	87.0	75.5	64.1	37.8	53.2	89.8	91.7
FRF	41.8	55.8	85.3	87.7	81.8	60.2	45.4	60.5	88.5	91.0
R-G-B										
LB	27.7	42.6	85.8	80.4	49.9	51.2	26.0	39.5	87.6	88.5
RT	27.9	42.0	77.7	78.6	57.0	53.0	13.8	23.5	85.4	81.3
RF	39.0	54.6	87.4	87.5	74.7	64.3	40.8	56.0	89.2	90.3
FRF	40.5	55.0	85.5	88.0	83.0	58.6	45.7	60.7	87.8	90.0
NIR-R-G										
LB	41.4	57.5	87.0	81.2	51.4	56.6	31.4	45.0	91.4	92.1
RT	26.6	40.1	79.0	77.4	50.8	45.7	11.6	20.2	83.4	81.5
RF	48.6	63.9	88.0	87.3	76.7	67.9	28.6	43.2	89.8	91.6
FRF	54.3	68.0	86.4	88.3	84.6	64.8	43.1	58.0	89.6	92.2
TIR-NIR-R										
LB	38.9	55.0	77.5	71.4	45.4	52.3	34.5	48.4	90.5	89.6
RT	16.2	27.3	77.2	59.3	39.5	51.2	10.0	17.7	91.8	85.7
RF	31.1	46.5	80.4	75.1	51.0	58.4	39.9	52.9	92.5	90.0
FRF	32.2	47.6	79.8	77.6	56.0	61.0	43.8	55.4	93.4	89.6
NIR-M-UV										
LB	40.5	56.5	88.9	83.9	59.3	63.8	35.1	48.4	92.6	92.5
RT	17.6	29.4	82.9	78.6	59.8	59.1	15.9	26.8	90.0	86.5
RF	38.9	55.0	87.6	87.5	76.3	70.2	26.6	41.0	92.9	92.2
FRF	44.5	59.3	87.3	88.6	84.5	69.4	43.0	58.1	90.9	92.4
	precision	F1-score	precision	F1-score	precision	F1-score	precision	F1-score	precision	F1-score

Note: *LB* LogitBoost; *RT* Random Tree; *RF* Random Forest; *FRF* Fast Random Forest.

Table 4.6. Accuracy statistics calculated for façade C, Fort of Karababa.

	leafy vegetation		no deterioration		black crusts		lichens	
G-B-UV								
LB	52.2	62.0	66.4	75.7	92.8	69.0	30.0	41.9
RT	47.7	60.2	66.2	70.8	90.3	72.0	30.5	43.0
RF	47.4	61.6	66.8	75.0	93.5	73.6	38.2	50.8
FRF	47.2	61.0	62.5	72.5	93.4	73.9	46.3	56.0
R-G-B								
LB	42.1	56.4	64.2	72.5	91.4	72.4	36.1	46.3
RT	39.6	54.8	64.2	69.5	89.6	68.5	29.9	42.1
RF	47.7	62.0	64.3	73.5	92.9	73.5	41.2	52.1
FRF	50.4	63.8	59.1	70.2	92.8	73.2	51.0	57.1
NIR-R-G								
LB	55.3	65.1	65.3	72.7	92.1	77.2	40.2	51.5
RT	47.9	60.8	70.5	74.2	88.3	77.0	36.4	47.7
RF	43.3	58.0	75.4	78.7	92.4	82.1	43.4	54.6
FRF	43.5	57.9	74.7	78.3	89.9	85.9	63.3	62.0
TIR-NIR-R								
LB	37.1	45.5	80.3	82.5	92.6	83.5	36.2	47.3
RT	32.8	43.8	83.3	84.7	91.0	75.8	28.8	41.0
RF	37.6	49.8	90.0	84.9	93.5	83.8	33.1	46.9
FRF	37.2	47.2	89.2	86.6	92.8	84.1	35.8	49.3
NIR-M-UV								
LB	49.3	55.6	68.2	74.5	92.7	77.6	40.5	51.7
RT	36.4	48.3	66.7	70.2	89.8	74.7	29.2	39.4
RF	39.6	54.1	65.5	72.4	93.9	74.9	39.3	51.8
FRF	42.0	55.8	59.3	69.2	93.7	75.5	53.0	58.9
	precision	F1-score	precision	F1-score	precision	F1-score	precision	F1-score

Note: *LB* LogitBoost; *RT* Random Tree; *RF* Random Forest; *FRF* Fast Random Forest.

Table 4.7. Accuracy statistics calculated for façade D, Fort of Karababa.

	leafy vegetation		no deterioration		black crusts		missing material		plant		dampness	
G-B-UV												
LB	21.1	34.9	90.1	78.6	32.1	43.3	31.7	47.0	68.5	38.0	89.2	88.7
RT	26.6	40.8	88.7	78.3	23.0	33.8	25.9	40.1	70.1	37.4	89.4	86.6
RF	64.4	78.4	89.2	79.3	38.9	54.4	28.5	43.8	53.8	36.7	91.9	91.5
FRF	67.7	80.7	88.1	80.2	44.0	58.7	31.1	46.9	54.7	36.8	91.5	91.6
R-G-B												
LB	29.5	45.3	78.8	77.8	29.3	41.7	29.9	45.2	67.4	37.8	90.6	83.9
RT	11.4	19.9	76.7	73.1	19.8	29.9	22.2	35.5	63.8	38.2	84.1	74.1
RF	52.6	68.2	79.6	76.3	34.7	50.2	27.7	42.6	57.1	37.3	90.0	85.1
FRF	61.4	74.6	78.3	76.0	44.6	58.2	27.0	42.0	53.4	36.5	88.4	86.0
NIR-R-G												
LB	21.6	35.4	91.8	75.2	26.8	37.1	30.7	46.1	72.4	38.3	87.3	88.4
RT	24.1	38.7	92.3	74.5	23.9	36.0	8.1	14.7	67.7	38.4	88.4	84.7
RF	47.3	63.7	89.9	78.1	32.1	46.7	25.2	39.7	63.4	38.2	92.1	91.1
FRF	47.3	63.1	88.5	78.9	37.2	51.8	29.4	45.1	57.3	37.4	91.9	91.3
TIR-NIR-R												
LB	18.6	31.3	54.9	61.1	25.6	38.8	25.2	39.3	49.9	34.6	83.3	62.9
RT	8.5	15.5	53.8	56.2	18.2	28.7	24.6	37.8	28.4	28.6	80.2	57.1
RF	21.4	35.0	50.7	57.9	31.3	45.7	31.4	46.8	38.5	32.7	80.9	61.1
FRF	23.8	37.9	48.8	56.2	40.7	54.2	33.4	49.3	37.4	32.3	78.7	62.6
NIR-M-UV												
LB	24.0	38.5	80.7	72.6	23.5	32.0	26.9	41.2	68.8	38.0	86.5	85.1
RT	13.1	22.7	78.9	70.6	20.2	30.5	13.2	22.8	56.6	35.6	82.2	75.2
RF	36.0	52.4	80.1	73.8	36.7	52.1	25.1	39.7	59.4	37.7	87.4	84.5
FRF	43.9	59.3	78.9	73.8	42.4	56.4	25.7	40.5	54.1	36.7	86.7	85.1
	precision	F1-score	precision	F1-score	precision	F1-score	precision	F1-score	precision	F1-score	precision	F1-score

Note: *LB* LogitBoost; *RT* Random Tree; *RF* Random Forest; *FRF* Fast Random Forest.

The inclusion of the NIR spectral band in the multispectral composites fairly improved the classification results for all deterioration forms. The segmentation of a NIR-R-G multispectral image and the Fast Random Forest classifier proved to be the most consistent solution overall (79.8 < overall accuracy%). Figure 4.10 presents a side-by-side comparison between the reference maps and the NIR-R-G composites segmented with the Fast Random Forest classifier. Using the UV reflectance data generally did not provide significant improvement to the quality of

the classifications. Including the TIR band also did not improve the deterioration patterns' classification. Furthermore, the fusion of visible with thermal data significantly decreased the accuracy of detecting deterioration when dampness was present, even though the thermograms can help distinguish the areas of dampness as shown in Figure 4.11.
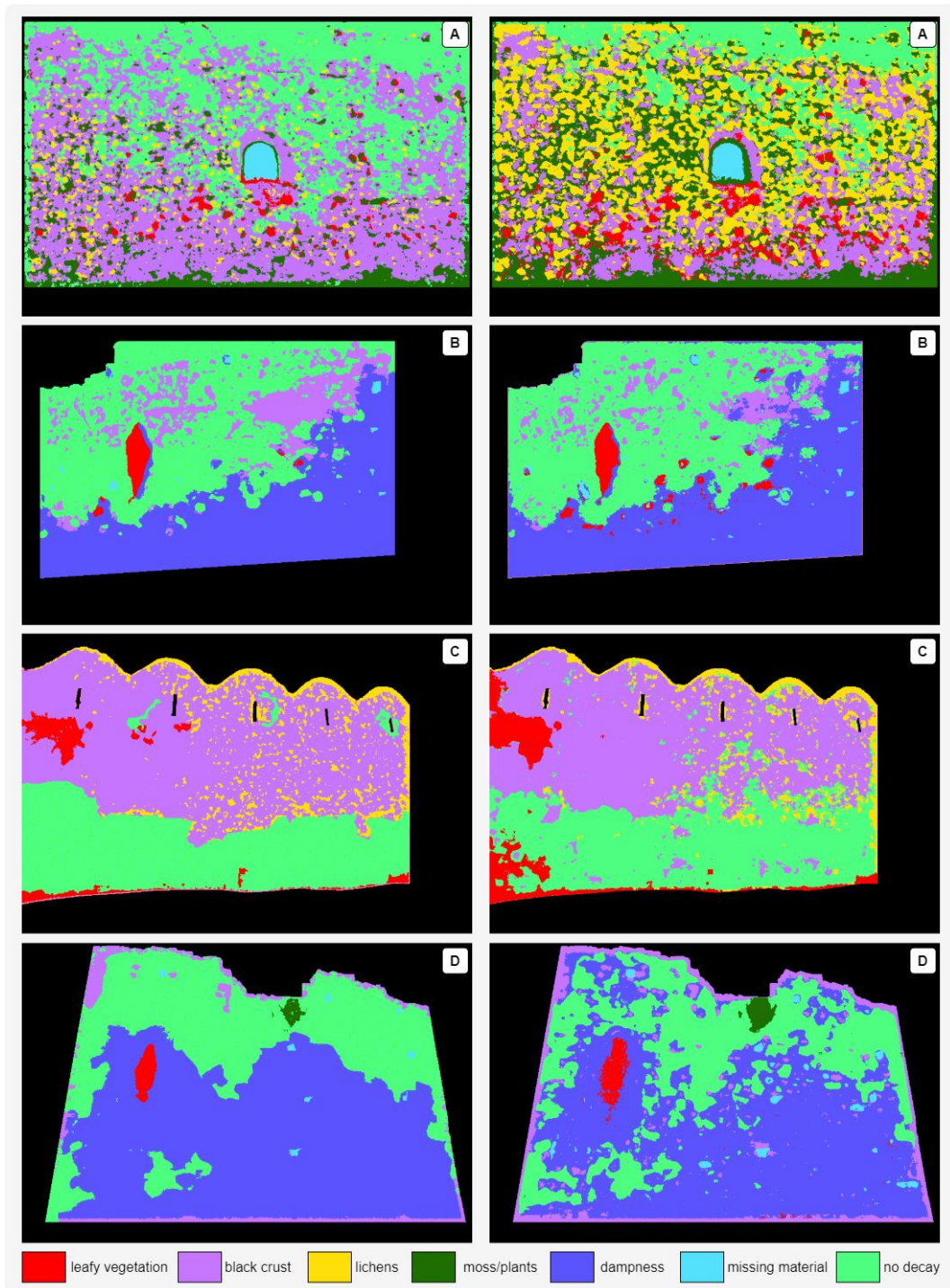
Figure 4.10. Reference deterioration maps (left) and corresponding deterioration maps produced with a NIR-R-G multispectral image using the Fast Random Forest classifier (right).
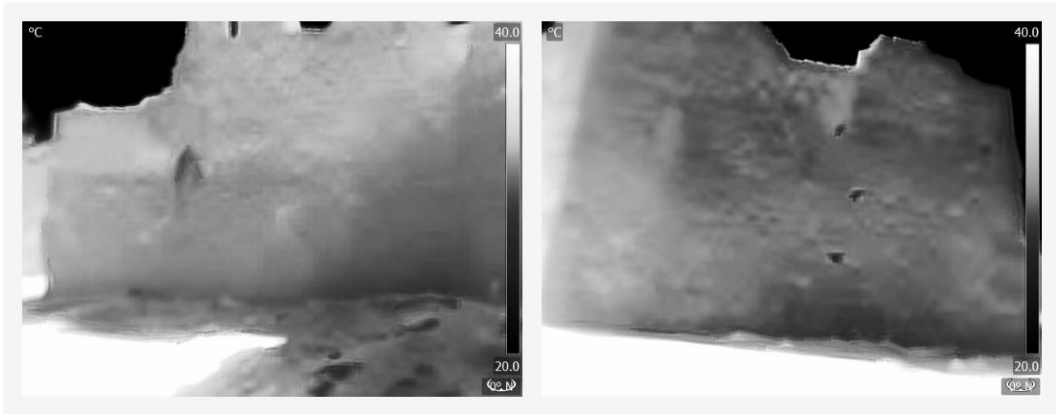
Figure 4.11. Thermograms of façades B (left) and D (right).

According to the overall accuracy results, the Fast Random Forest classifier was the most accurate learning-based method for deterioration classification for all multispectral images, not including the TIR band (69.9% < overall accuracy < 86.8%).On the other hand, implementing the Random Tree classifier resulted in more inconsistent and less accurate classifications (63.7% < overall accuracy < 77.4%). Furthermore, LogitBoost outperformed the Random Tree classifier.

According to the precision and F1-score values, moss and lichens were the most misclassified of the surface patterns, even though both random forest approaches improved their classification. The results prove that the distinction among non-deteriorated material, dampness, and black crusts/discoloration and plants is much more easily detectable (and therefore classifiable) than biogenic colonization of any form. Therefore, surface alterations of the historical materials—which alter the reflectance characteristics—can be more accurately mapped using multispectral images in comparison with the deterioration forms that completely cover them as an additional layer. The segmentation of multispectral composites (synthesized with visible and NIR spectrum images), with classifiers combining random trees and ensemble learning, performed exceptionally well even where a high number of surface patterns were present. It should be highlighted that the accuracy evaluation considered some level of bias since the manually produced reference thematic maps cannot consider the overlapping surface patterns.

The investigated semi-automated methodology has the limitation that it can map only the pathologies that have been previously recognized through visual inspection (or analytical techniques) because appropriate regions of interest have to be annotated to train the intelligent algorithms. However, a crucial advantage is that it produces easily interpretable mapping results, contrary to unsupervised methods where each mapped pattern class has to be a posteriori assigned to a deterioration category. Furthermore, there is a clear advantage over deep learning-based methods that require large image datasets for rapid monitoring purposes of monumental heritage structures.

4.2.1.2   Temple of Apollo Epikourios

This second historical structure selected as a case study for applying the semi-automated deterioration mapping workflow, the Temple of Apollo Epikourios (Figure 4.12), is one of the best-preserved monuments of classical antiquity, an imposing monument of ancient Greek architecture. The temple is positioned at the archaeological site of Bassae (Messenia, Greece) and has been inscribed on the UNESCO World Heritage List since 1986. It was constructed toward the end of the 5th century BC in the rocky heights of the Arcadian mountains, mostly of local limestone. The classical temple was founded on bedrock, on a specially built terrace. It is the only known temple that combines elements of all three architectural orders of antiquity. The temple is Doric, peripteral, and distyle in antis, with pronaos, cella, adyton, and opisthodomos. A Doric frieze of undecorated metopes and triglyphs ran along the outer facades. Parts of the temple were excavated and restored in 1902–1906. The Ministry of Culture has overseen the conservation of the monument since 1982. A temporary shelter, erected in 1987, is covering the monument to protect it against the region's harsh weather conditions and against acid rain (Vikatou, 2021; Papadopoulos & Savvatianou, 2014).

Figure 4.12. The Temple of Apollo Epikourios at Bassae.

For this case study, spectral images at the visible and NIR spectra were acquired for a few architectural surfaces characteristic of the observable deterioration patterns. After the radiometric adjustment and rectification of the collected raw data, the corrected spectral reflectance images were resampled to match the

resolution of all bands, and the unwanted areas were trimmed from all multispectral composites to reduce the chance of potential misclassifications. Two composite images were synthesized, an R-G-B and a NIR-R-G image, which were evaluated together with a NIR reflectance monochromatic image. The semi-automated thematic mapping of deterioration was assessed for patches of images, producing higher accuracy results for the NIR images than the two multispectral composites. This could be justified by the more homogeneous radiometry of the NIR reflectance images since the original historical materials and previous restoration materials presented similar reflectance characteristics at the near-infrared spectrum (Figure 4.13). Additionally, the image segmentation procedure based on the supervised learning-based approach could not produce representations of the overlapping deterioration patterns observed. Therefore, it was decided to apply unsupervised classification based on multiple data reduction techniques on the rectified NIR reflectance image of each investigated architectural surface, in order to avoid misclassification of decay forms and to produce a different thematic mapping for each type of decay.
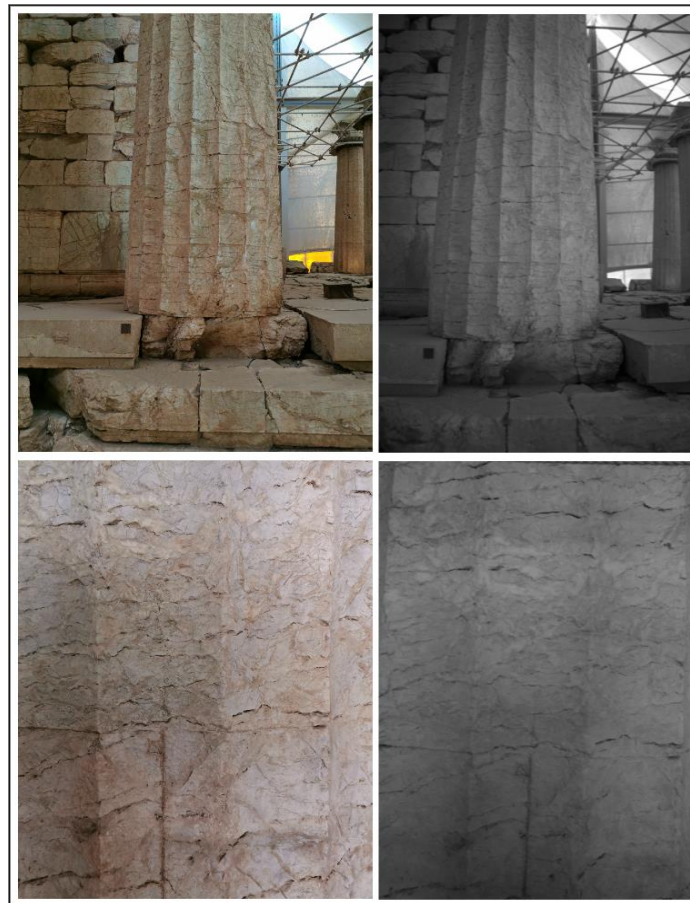
Figure 4.13. Color (left) and near-infrared reflectance (right) images of the same column captured at the Temple of Apollo Epikourios at Bassae, from further and closer range.

The architectural surfaces of the monument had been mostly cleaned, and therefore, the observable categories of degradation were only loss of material,

cracks, and discoloration. After generating the NIR reflectance orthoimages, binary images representing these different deterioration categories were produced. Thresholding was applied for identifying discoloration after flat-field correction, which eliminated any remaining inhomogeneous illumination problems. Edge detection and afterward binarization was performed on the first principal component of the images to detect cracks. Finally, histogram equalization and thresholding were performed to identify the loss of material. The visualization and management of the overlapping thematic mapping results were performed in the FOSS GIS environment QGIS Desktop 3.18.2. Figure 4.14 presents the generation of the binarized category-specific deterioration results for an architectural surface and the production of thematic layers in the FOSS GIS environment. The thematic maps produced for investigated characteristic surfaces are presented in Figure 4.15 and Figure 4.16.
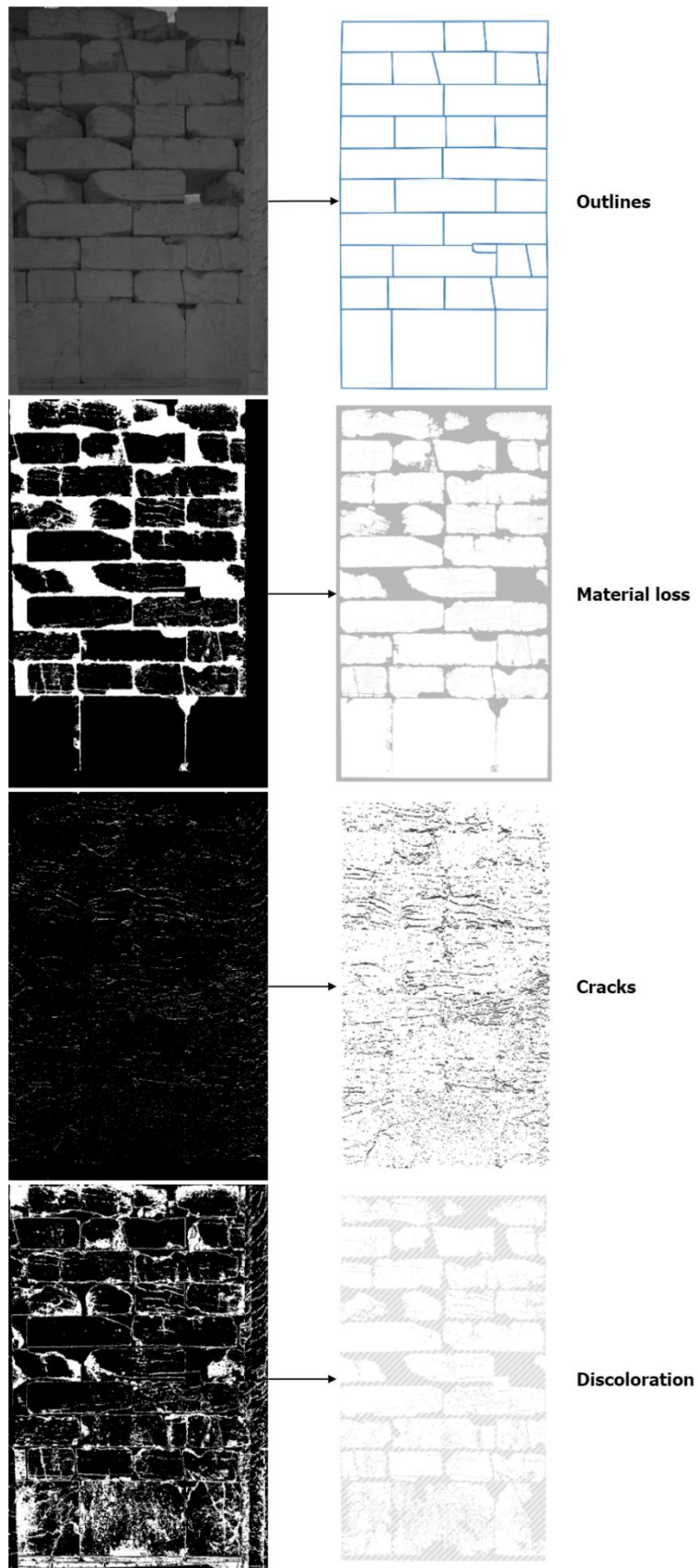
Figure 4.14. Generation of thematic map layers (right) in QGIS using features extracted from rectified near-infrared reflectance images (left) for the Temple of Apollo Epikourios.
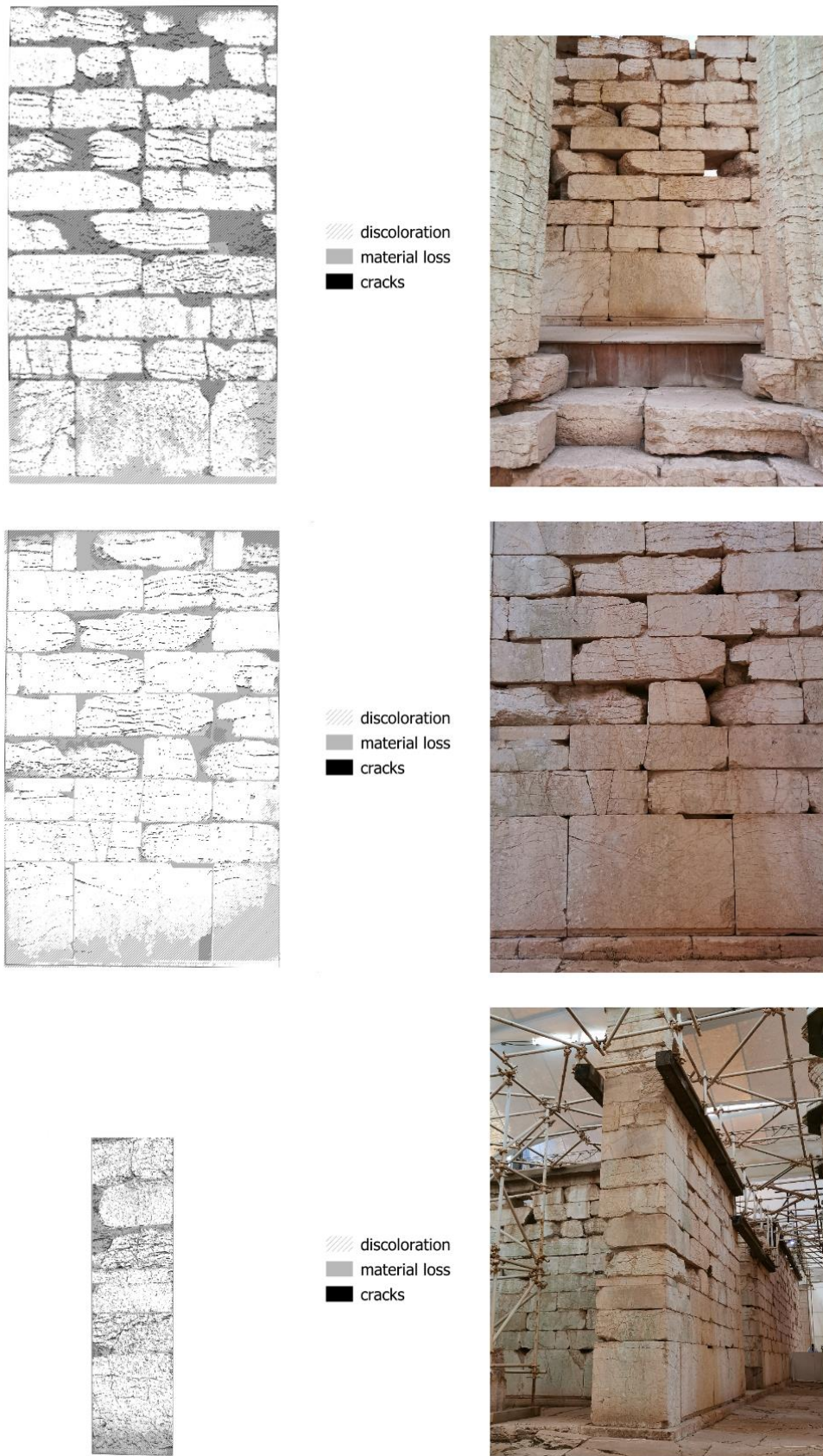
Figure 4.15. Degradation maps and corresponding images for characteristic areas of walls at the Temple of Apollo Epikourios.
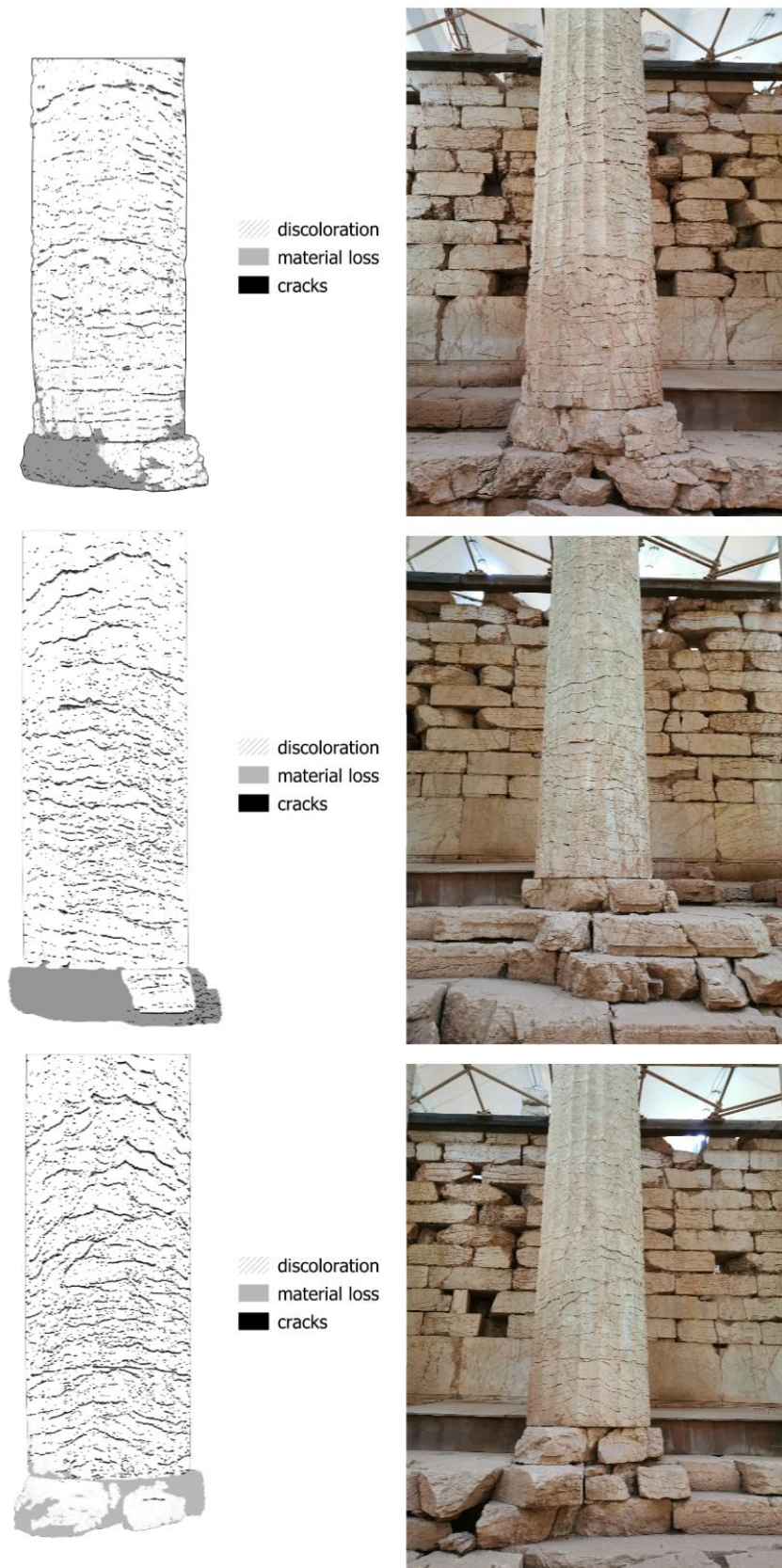
Figure 4.16. Degradation maps and corresponding images for characteristic areas of columns at the Temple of Apollo Epikourios.

4.2.1.3   Temple of Athena and Zeus Soter

The Temple of Athena and Zeus Soter is the most notable excavated monument of the ancient city of Phigalia (Ilia, Greece). It is located on the hill "Kourdoumbouli" at the southwest end of the Agora of the ancient city. It is a rectangular temple with pronaos and cella. The life of the temple spans from the 4th century BC until the Roman Era, while there must also have been an Archaic phase. It was constructed of large stone blocks according to the irregular isodomic system and is preserved up to a height of three building blocks (Figure 4.17). The stone cubic pedestal of the worshiping statue was found in the cella, while there was a table for offerings in front of it. The large number of inscriptions found inside the temple testifies to its political significance for the city of Phigalia (Sgouropoulou, 2021).

For this case study, the use of both visible and NIR-spectrum images was opted due to the existence of biological colonization (moss, lichens, biogenic crusts, vegetation), benefiting from the dissimilar reflectance characteristics that it presents at different wavelengths (Figure 4.18). Orthoimage mosaics were generated using an SfM/DMVR approach for parts of the cella and the cubic stone pedestal with the RGB and NIR-reflectance images. Then, they were blended to create pseudo-color orthoimage mosaics (using the Green, Red, and NIR bands) in the HyperCube software. Next, the resulting base maps were segmented to the areas presenting different degradation forms following a *k*-means unsupervised clustering approach with centroids initialized using the *k*-means++ algorithm. Finally, the classified images were digitized, and the degradation was semantically annotated in QGIS to the corresponding thematic layers (Figures 4.19–4.23). A map of damage categories regarding the Temple of Athena and Zeus Soter remains could also be produced. Figure 4.24 additionally provides statistics on the coverage of the historical stone surfaces by various degradation forms. Both investigated surfaces were, in their entirety, covered by biogenic material or discolored.
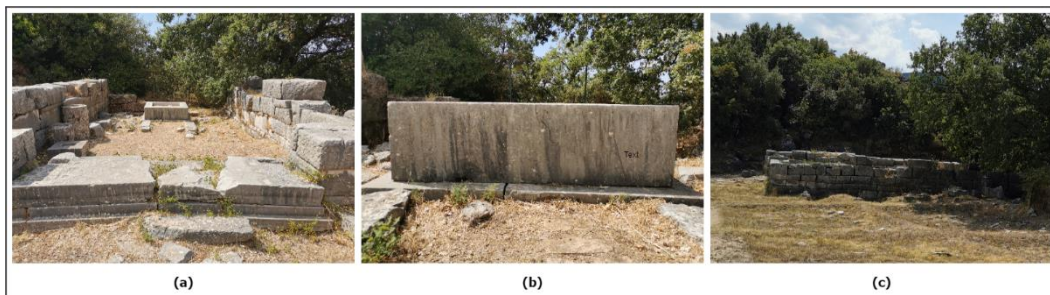
Figure 4.17. Remains of the ancient Temple of Athena and Zeus Sotiros; (**b**) the investigated (west) side of the stone cubic pedestal of the worshiping statue; (**c**) the investigated (north) side of the cella wall.

Figure 4.18. Color and near-infrared images captured at the Temple of Athena and Zeus Sotiros.

Figure 4.19. Orthoimage mosaic, cella wall remains at the Temple of Athena and Zeus Sotiros.
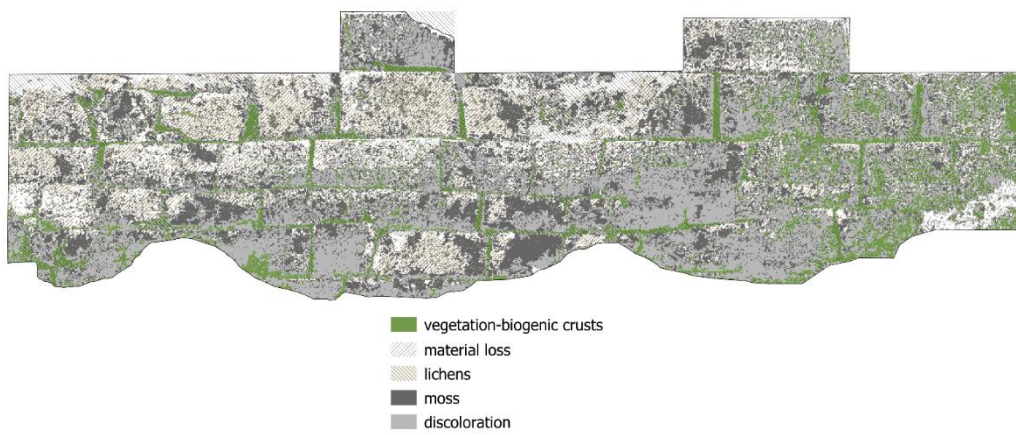
Figure 4.20. Degradation map, cella wall remains at the Temple of Athena and Zeus Sotiros.
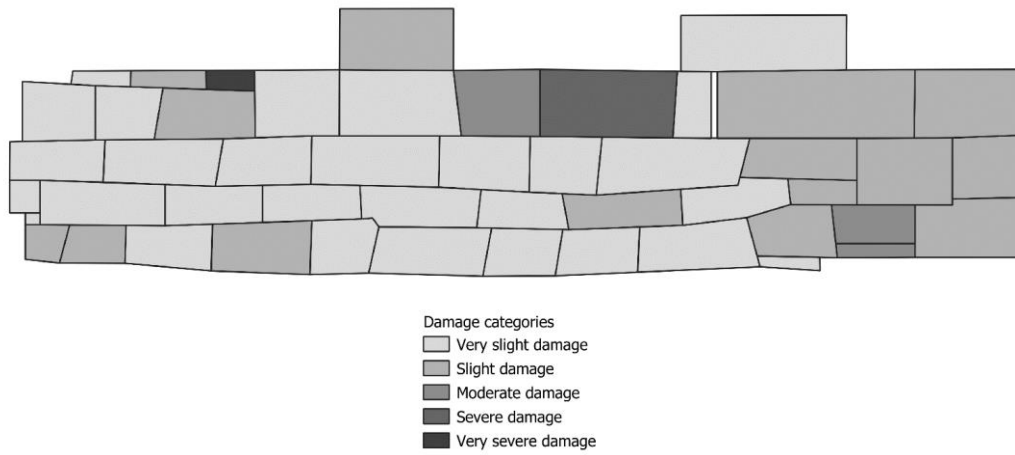
Figure 4.21. Damage index map, cella wall remains at the Temple of Athena and Zeus Sotiros.

Figure 4.22. Orthoimage mosaic, cubic stone pedestal at the Temple of Athena and Zeus Sotiros.

Figure 4.23. Degradation map, cubic stone pedestal at the Temple of Athena and Zeus Sotiros.
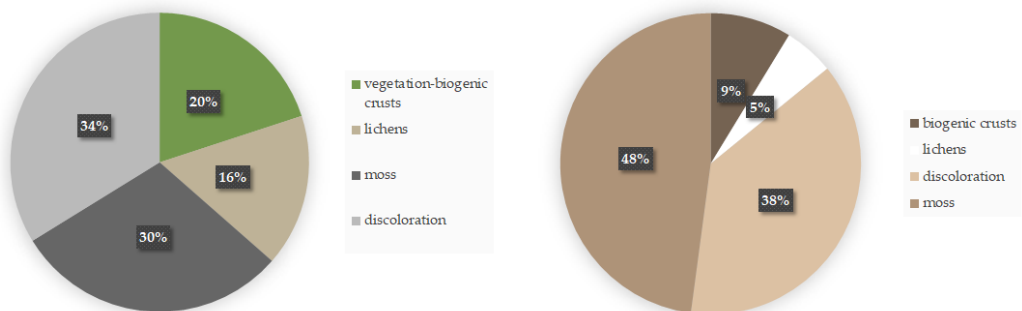
Figure 4.24. Degradation pattern statistics for the investigated surfaces at the remains of the Temple of Athena and Zeus Sotiros; cella wall (**left**) and cubic stone pedestal (**right**).

4.2.1.4   Archaeological Site of Lepreum

The ancient Lepreum constituted one of the most important cities of Elis's Trifylia. Lepreum had two citadels, the prehistoric acropolis on the naturally fortified hill of Agios Dimitrios, east of the modern village, and the acropolis of the historical period to its north. The peripteral temple of Demeter is the most important monument in the Classical acropolis. The historical city extended up to the prehistoric acropolis. The remains of the Classical and Hellenistic acropolis (Figure 4.25), particularly the well-preserved enceinte of isodomic and polygonal masonry with its square towers, show that the city thrived during these periods. Inside the enceinte are several buildings, including the Classical Doric peripteral temple of Demeter, mentioned by Pausanias (Antonopoulos, 2021).

Figure 4.25. Ancient walls at the archaeological site of Lepreum.

For this case study, photogrammetric approaches were followed using multiband datasets (examples of reflectance images shown in Figure 17), as described in Figure 4.26, to generate the necessary base maps for the mapping process. The thermal orthoimage mosaic was produced following a hybrid approach exploiting both the visible and thermal images captured by the FLIR One Pro camera (Figure 4.27). The false-color multiband image mosaic composed of three single-band mosaics (RGB, NIR, and TIR) was classified to create the thematic map (true-color image shown in Figure 4.28 and final degradation pam inFigure 4.29). Statistics were again calculated for the coverage of the historic surface by various degradation forms (Figure 4.30), while the damage map (Figure 4.31) considered the presence of vegetation, moss, and bio-colonization. Additionally, the historical surface was almost entirely covered by biogenic material or discolored in this case study.

Figure 4.26. Reflectance images captured at the archaeological site of Lepreum: (from left to right) true color, near-infrared, and thermal infrared.
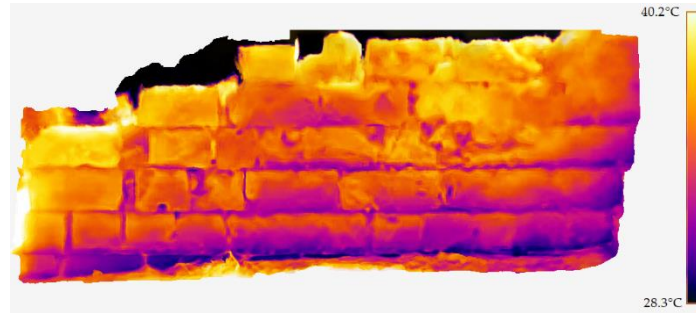
Figure 4.27. Thermal orthoimage mosaic of an ancient wall at the archaeological site of Lepreum.

Figure 4.28. Orthomosaic of an ancient wall at the archaeological site of Lepreum.
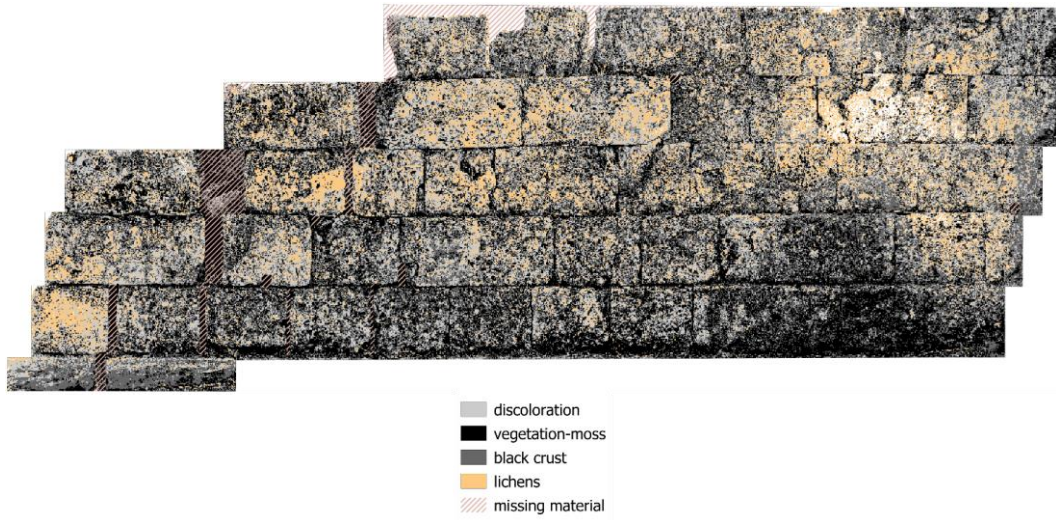
Figure 4.29. Degradation map of an ancient wall at the archaeological site of Lepreum.
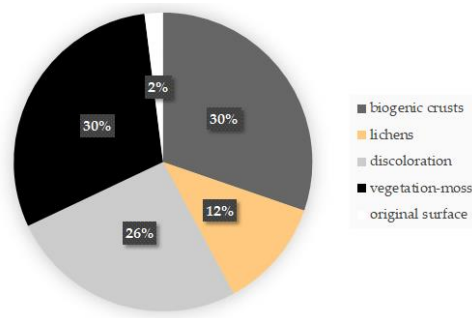
Figure 4.30. Degradation pattern statistics for the investigated surface of the wall at the archaeological site of Lepreum.
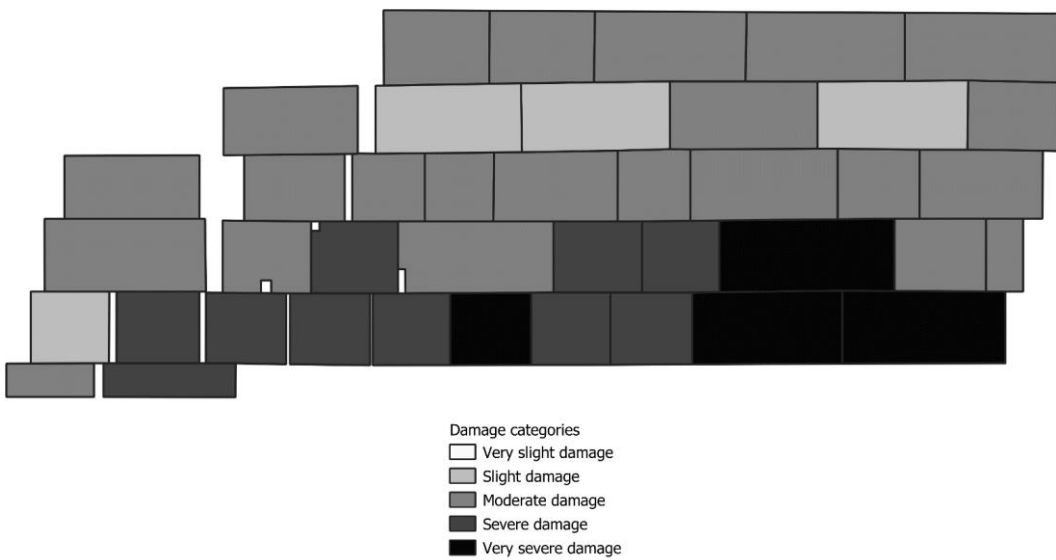
Figure 4.31. Damage index map, of an ancient wall at the archaeological site of Lepreum.

4.2.2 Historical Objects

4.2.2.1   Stone Stelae

The antiquities involved in this study were eight inscribed and uninscribed stone stelae from the Archaeological Museum of Eretria (Euboea, Greece). The instrumentation used for the dual-band image acquisition included the modified Canon Rebel-SL1 digital camera (with a resolution of 5184×3456 pixels) with an external NIR-pass filter and a smartphone employing a Sony IMX600 sensor (with a resolution of 3648×2736 pixels, at RAW capturing mode) with LEICA optics for color imaging. The NIR and VIS images were recorded, exported, and pre-processed as described in section 4.1.2, considering a 1:2 scale, and a NIR-R-G multispectral image composite was generated.

The main identified categories of deterioration on the stelae were moss-lichens, discoloration, crusts, and black crusts (Figure 4.32) and were therefore selected as classes for the DIP-based classification, along with an additional class for relatively healthy marble surfaces. Given the manual nature of selecting the classification classes and annotating the sample regions for training the classifiers, four different classifiers were trained to allow comparisons. All classifiers used for deterioration mapping were based on a decision tree learning method. The evaluated in ImageJ classifiers were the Random Tree, Random Forrest, Fast Random Forrest, and j48. The machine learning techniques were tested for four stelae, and then the trained classifiers were applied to the other four, which presented similar deterioration patterns.

To evaluate the classification results, reference maps were constructed. R-G-B images were also involved in the evaluation to estimate the contribution of introducing near infrared-spectrum data for improving the classification. Error matrixes were calculated as an accuracy metric to compare performances. Table 4.8 reports the accuracy performance of the tested classifiers run on R-G-B and NIR-R-G images.

Table 4.8. Accuracy results for different classifiers.

	M.E. 18084	M.E. 980	M.E. 1357	M.E. 1131	
	0.73	0.78	0.83	0.90	j48
RGB	0.71	0.77	0.82	0.95	RT
	0.75	0.81	0.84	0.94	RF
	0.76	0.82	0.84	0.97	FRF
	0.74	0.79	0.84	0.94	j48
NIRRG	0.81	0.85	0.86	0.94	RT
	0.79	0.81	0.85	0.95	RF
	0.78	0.85	0.86	0.98	FRF

Note: *RT* Random Tree; *RF* Random Forest; *FRF* Fast Random Forest.

Figure 4.32. Stelae at the Archaeological Museum of Eretria.

All experimentations generated results with over 70% overall accuracy. Among them, consistently high accuracy results were achieved with the Random Tree implementation for the more decayed stelae and with the Fast Random Forest for the less decayed stelae. Figures 4.33 and 4.34 present the comparison between reference maps and generated results. The ability of the random forest method to tackle problems in decision tree learning, such as learning unusual irregular patterns and overfitting training data, by assigning random subsets of the training and from them random input feature subsets, facilitated better accuracies when the distinction between pathologies and cleaned/cleaner surface was clearer. However, when there was overlap between degradation forms or small enclaves of moss-lichens pixels were present inside discolored areas, the decision tree method, which uses all features of interest for the training, proved more efficient.

It should be highlighted that the complexity of the stelae's surface degradation can contribute to the misclassification of pixels. This becomes apparent from the higher accuracy values observed for Stelae M.E. 980 and M.E. 1131. The reference data consider the predominant form of degradation present at each part of the marbles' surface, but, in fact, the different degradation forms can be overlapping, which means that these data are not perfect. Therefore, classifiers assume the reference data correct, but there is an uncertainty present, which rises as the number of degradation categories increases. This reflects on the misclassified pixels, which may not always be assigned to an incorrect class, but on a lesser dominant degradation category at a particular region of interest.

Additionally, inhomogeneous reflectance caused by features induced due to material loss—on the micro and macro scale (i.e., erosion, pitting, missing parts)—can affect the performance of the classification and can usually not be mapped as they are overlapping and often caused by weathering phenomena such as biological colonization (Urzi, 2004).

It is evident from error matrixes Table 4.9 and Table 4.10, that when multiple degradation forms were present, the most common misclassification was between moss-lichens and discoloration, but also clean surface and discoloration when discoloration was not very intense (considering the dual-band Random Tree approach as the most accurate for stelae 18084 and 1357).

Including the near-infrared data generally improved accuracy slightly, and particularly for the more decayed stelae, which can be explained by the vastly different reflectance characteristics of the biodegraded areas at the NIR spectrum.

Table 4.9. Error Matrix; degradation mapping of stela M.E. 18084 through the Random Tree-based ML approach.

0.76	0.05	0.03	0.24	🟩
0.21	0.92	0.34	0.00	🟪
0.02	0.03	0.64	0.00	🟨
0.00	0.00	0.00	0.75	🟦
🟩	🟪	🟨	🟦	

Table 4.10. Error Matrix; degradation mapping of stela M.E. 1357 through the Random Tree-based ML approach.

0.88	0.14	0.00	0.08	🟩
0.10	0.80	0.23	0.11	🟪
0.00	0.06	0.76	0.00	🟨
0.01	0.00	0.01	0.80	🟦
🟩	🟪	🟨	🟦	
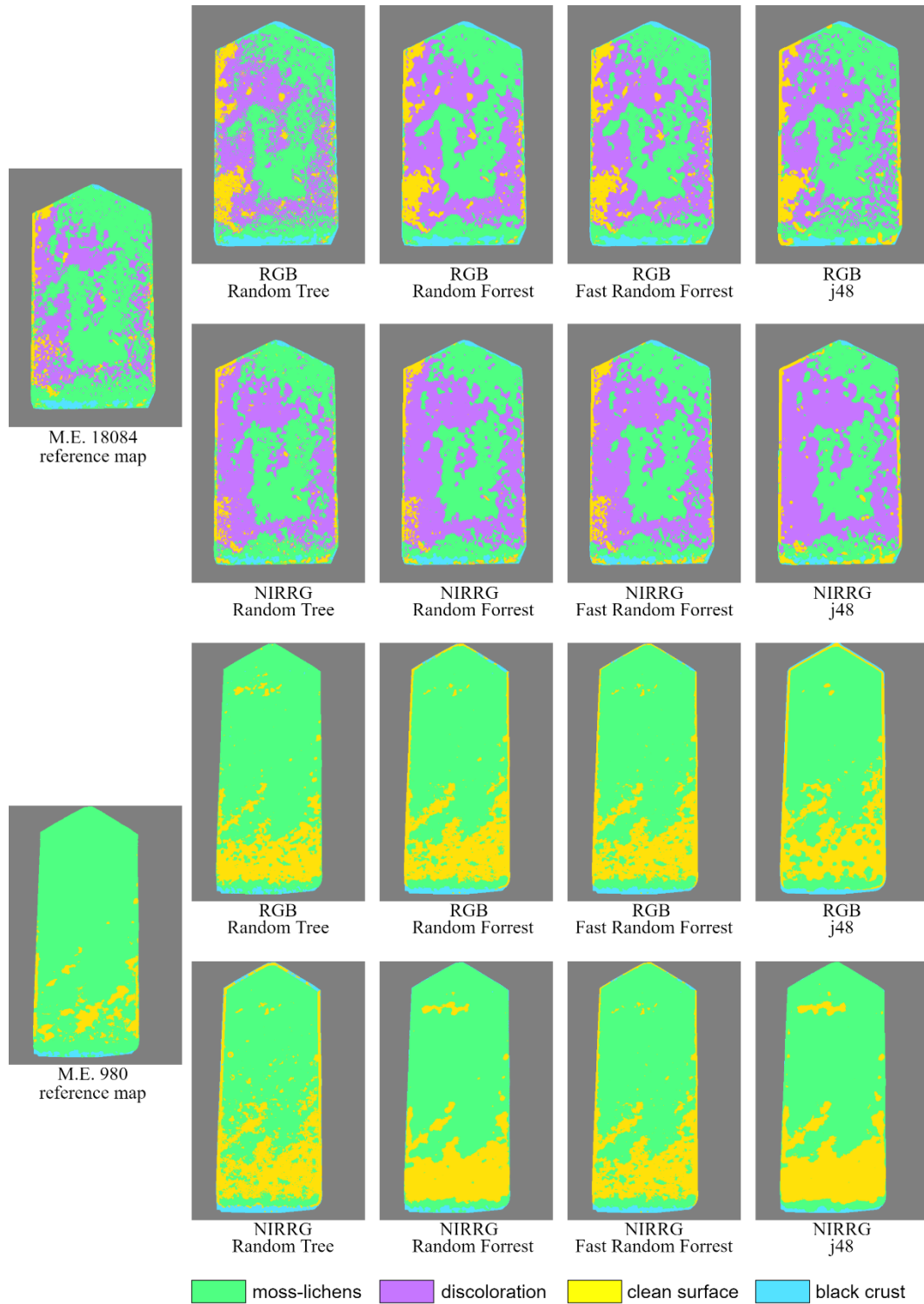
Figure 4.33. Classification results stelae M.E. 18084 and M.E. 980
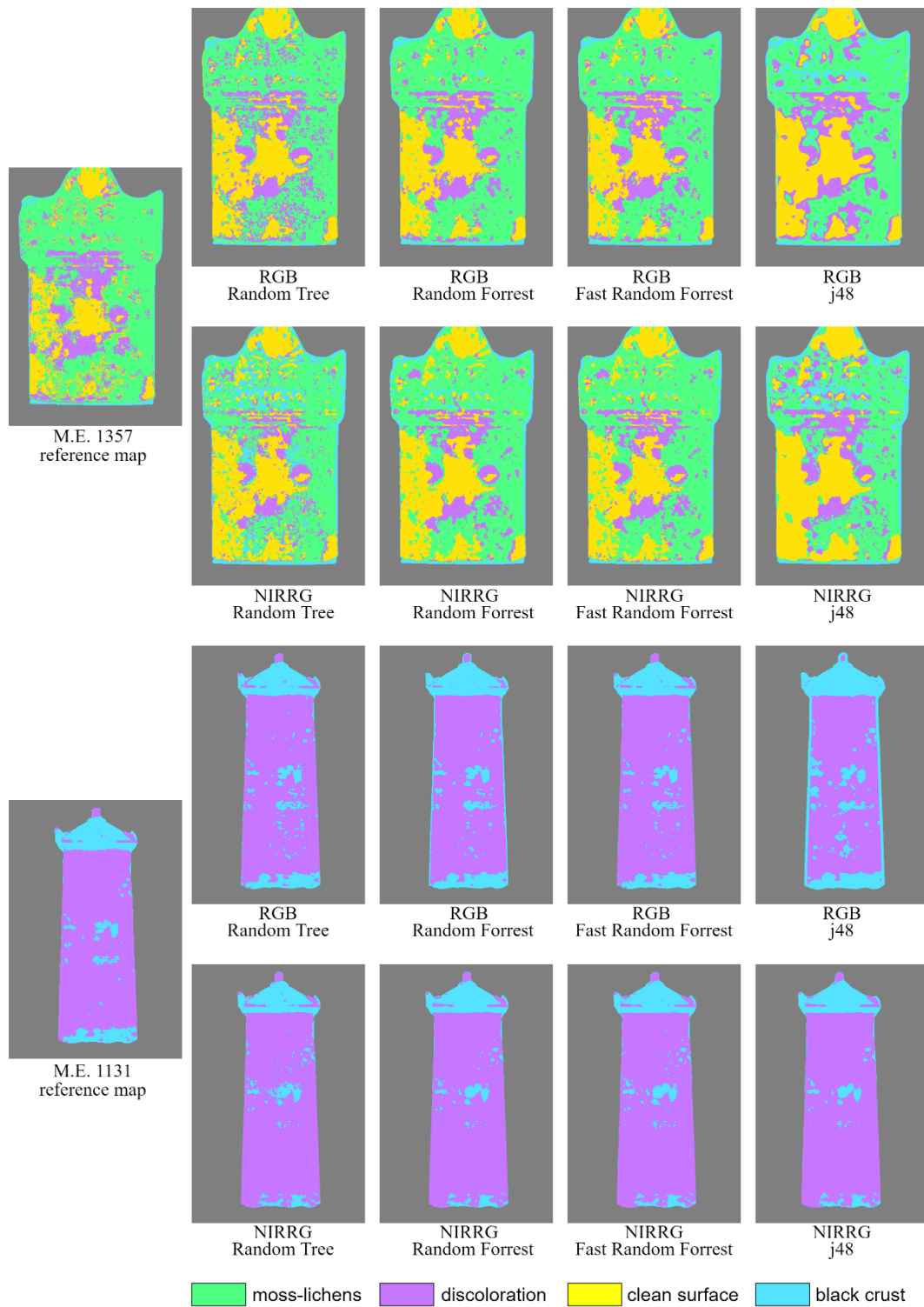
Figure 4.34. Classification results stelae M.E. 1357 and M.E. 1131

The trained and tested classifiers were applied to the image composites of the other four stelae to complete the degradation mapping (Figure 4.35).
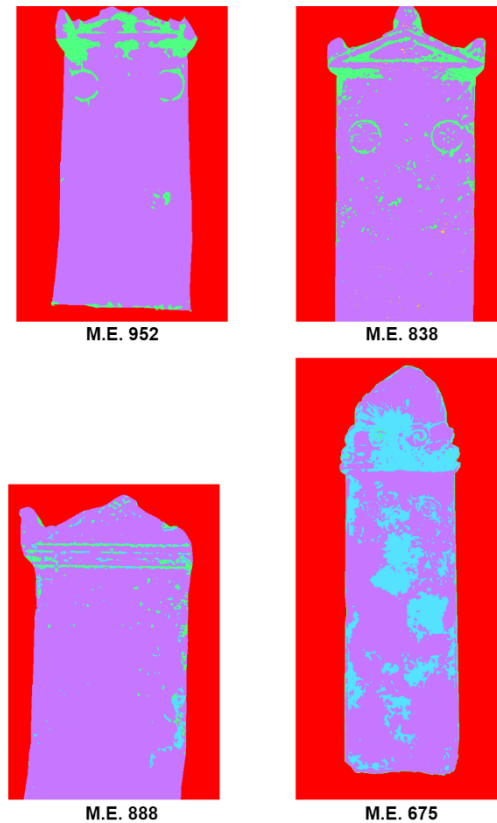
Figure 4.35. Degradation mapping of stelae using the trained classifiers and the NIRRG composites.

The investigated semi-automated mapping workflow proved to performed well for different case studies of stone stelae that presented dissimilar surface pathology. For practical reasons, some of the steps followed in this case study may be skipped. If, for example, the camera sensor cannot be geometrically or radiometrically calibrated, the proposed approach can still produce degradation maps useful for conservation purposes. Including NIR images in the approach proved to increase the accuracy of the results for some cases, especially when biodeterioration was present; however, including only the true color images still provided high-accuracy results. Therefore, an unmodified camera can also be used to provide the necessary input for ML-based segmentation.

A critical issue observed in this case study stems from the complexity of the mapped surfaces. Overlapping of degradation forms can cause some misclassifications, while more easily definable deterioration patterns can produce higher accuracy results. The subjective visual identification between less and more degraded surfaces that present the same pathology can also affect the approach's performance. Features causes by material loss cannot be easily detected if they are not the cause for other degradation patterns (such as moss caused by concentrated moisture in the created cavities).

4.2.2.2   Stone Sculptures—Extension to 3D Geometry

This case study discusses applying the semi-automatic mapping workflow for 3D digitization and visualization of the state of preservation of heavily degraded stone objects, through the case study of a bust of Franz Joseph I of Austria from the *Accademia Carrara di Bergamo* (Figure 4.36).

The object's geometric recording was performed with a structured-light system and digital photogrammetric approaches to obtain diverse data types. Imagery for SfM/DMVR approach-based reconstruction was robustly captured with the modified Rebel SL1 camera. A UV-NIR-cut external filter was used for the color images, and a NIR-pass filter (700–1400 nm) was used to capture near-infrared reflectance images.

Post-processing of the produced 3D point clouds, application of different visualization techniques, and segmentation of the 3D models based on RGB and near-infrared textures were performed in CloudCompare, as well as the metric validation of the photogrammetric results. The classification of images and models' textures was implemented in MATLAB through K-means clustering-based image segmentation, using k-means++ algorithm for cluster center initialization. The number of clusters was chosen by roughly identifying the number of present deterioration patterns, according to the 'Illustrated glossary on stone deterioration patterns' and by considering that at least one cluster should correspond to the healthy materials' surface.

Figure 4.36. A view of the bust of Franz Joseph I.

The 3D models generated with image-based approaches from RGB and NIR imagery were metrically validated by comparing them to the ground-truth model

produced with SLS. In both cases, mean Hausdorff distances estimated with the appropriate measurement tool in CloudCompare ranged below 1 mm. Furthermore, the two models had remarkably similar density and surface characteristics, and the distances calculated between the two surfaces were, on average, less than 0.5 mm.

Shading of meshes' surfaces was based on approximate normal rendering with the Eye-Dome Lighting (EDL) shader, approximate ambient occlusion rendering with the Screen space ambient occlusion (SSAO) shader, and applying Sobel filtering over anisotropic diffusion filtered images to obtain gradient maps of the surface. The results, shown in Figure 4.37, and particularly rendering according to SSAO and gradient vectors gave more interpretable visualizations of the surface's characteristics.

Figure 4.37. Visualizations of digital model in CloudCompare with approximated normal rendering using SSAO shader (left) and Sobel filter-based solution (right).

Photogrammetrically-produced models are illustrated in Figure 4.38. After transferring the NIR intensities from the texture mosaic image file to the model's surface triangles, a direct segmentation of the weathering stages was achieved by directly segmenting in 3D according to the grayscale values. This segmentation had good correspondence with the real-life situation of degradation, as seen in Figure 4.39. Furthermore, the segmented surfaces area could be measured, which has significant value for the conservation interventions' efficient planning.

Figure 4.38. Digital models produced with image-based techniques: untextured (left), textured with RGB imagery (center), and with NIR imagery (right).
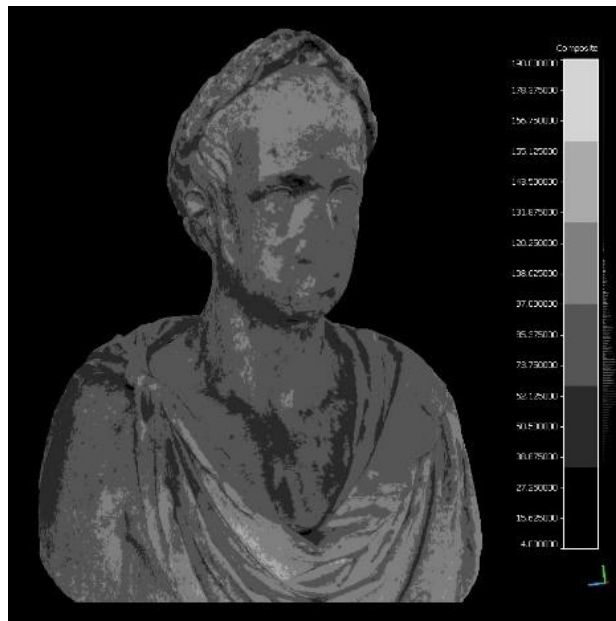
Figure 4.39. Direct 3D segmentation of the model based on NIR texture to visualize stone weathering stages (darkest tone translates to a higher level of weathering).

The detailed classification of the deterioration patterns in 3D was implemented with two different techniques. The first included exporting RGB and NIR 2D ortho-mosaics of the bust's surface, blending them to create a multispectral pseudo-colored image, then classifying it with an unsupervised method, and finally back-projecting the 2D classification results onto the 3D object. The second technique was based on the NIR texture's direct unsupervised classification (Figure 4.40). Results from the first implementation were more easily interpretable as specific segmented areas had an apparent correspondence to a particular type of deterioration. However, the projection of the classified ortho-mosaic onto the model created few gaps in the textured product due to the occlusions caused by complex

geometry. Multiple partial classified ortho-mosaics on convenient planes would be needed to cover the full object and avoid the occlusions as much as possible. The second technique provided a classification covering the complete object without occlusion problems. However, in this case, results were not as easily interpretable because of errors created during the classification—due to areas that presented the same decay patterns but were unconnected on the texture image.
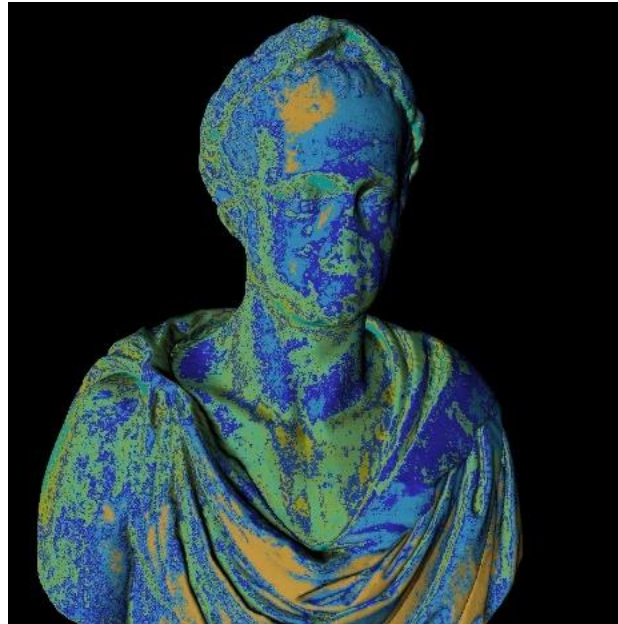
Figure 4.40. 3D classification of deterioration using the near-infrared texture. Blue-colored areas correspond to healthier material, while green corresponds to biodeterioration and black crusts, and orange to stone patina.

References

Antonopoulos, K. B. (2021). Ancient Phigalia. ODYSSEUS Portal. http://odysseus.culture.gr/h/3/gh351.jsp?obj_id=19880

Arganda-Carreras, I., Kaynig, V., Rueden, C., Eliceiri, K. W., Schindelin, J., Cardona, A., & Sebastian Seung, H. (2017). Trainable Weka Segmentation: A machine learning tool for microscopy pixel classification. *Bioinformatics*, *33*(15), 2424–2426. https://doi.org/10.1093/bioinformatics/btx180

Barszcz, M., Montusiewicz, J., Paśnikowska-Łukaszuk, M., & Sałamacha, A. (2021). Comparative Analysis of Digital Models of Objects of Cultural Heritage Obtained by the "3D SLS" and "SfM" Methods. *Applied Sciences*, *11*(12), 5321. https://doi.org/10.3390/app11125321

Breiman, L. (2001). Random Forests. *Machine Learning*, *45*, 5–32. https://doi.org/10.1023/A:1010933404324

Congalton, R. G., & Green, K. (2019). *Assessing the accuracy of remotely sensed data: Principles and practices* (Third edition). CRC Press.

Das, R. (2021). *Content-based image classification: Efficient machine learning using robust feature extraction techniques* (First edition). C&H\CRC Press.

Del Pozo, S., Rodríguez-Gonzálvez, P., Hernández-López, D., & Felipe-García, B. (2014). Vicarious Radiometric Calibration of a Multispectral Camera on Board an Unmanned Aerial System. *Remote Sensing*, *6*(3), 1918–1937. https://doi.org/10.3390/rs6031918

Friedman, J., Hastie, T., & Tibshirani, R. (2000). Additive logistic regression: A statistical view of boosting (With discussion and a rejoinder by the authors). *The Annals of Statistics*, *28*(2). https://doi.org/10.1214/aos/1016218223

ICOMOS ISCS. (2008). *Illustrated glossary on stone deterioration patterns* (1st Edition). Ateliers 30 Impression.

Liu, C., Szeliski, R., Kang, S. B., Zitnick, C. L., & Freeman, W. T. (2008). Automatic Estimation and Removal of Noise from a Single Image. IEEE Transactions on Pattern Analysis and Machine Intelligence, 30(2), 299–314. https://doi.org/10.1109/TPAMI.2007.1176

Mamaloukos, S. (2020). The Fortifications of Chalcis (Evripos/Negreponte/Egriboz), Greece. In L. J. García Pulido & J. Navarro Palazón (Eds.), *FORTMED2020 - Defensive Architecture of the Mediterranean, vol. XI: Proceedings of the 5th International Conference on Fortifications of the Mediterranean Coast 2020* (pp. 631–638). Universidad de Granada, Editorial Universitat Politècnica de València. https://doi.org/10.4995/FORTMED2020.2020.11331

Papadopoulos, K., & Savvatianou, V. (2014). Architectural and Structural Aspects of the Ancient Greek Temple of Apollo Epikourios. In F. M. Mazzolani & G. Altay (Eds.), *Proceedings of the 2nd International Conference on Protection of Historical Constructions* (pp. 725–730). Boğaziçi University Press.

Quinlan, J. R. (1993). *C4.5: Programs for machine learning*. Morgan Kaufmann Publishers.

Quinlan, J. R. (1996). Learning decision tree classifiers. *ACM Computing Surveys*, *28*(1), 71–72. https://doi.org/10.1145/234313.234346

Rueden, C. T., Schindelin, J., Hiner, M. C., DeZonia, B. E., Walter, A. E., Arena, E. T., & Eliceiri, K. W. (2017). ImageJ2: ImageJ for the next generation of scientific image data. *BMC Bioinformatics*, *18*(1), 529. https://doi.org/10.1186/s12859-017-1934-z

Russo, M., Carnevali, L., Russo, V., Savastano, D., & Taddia, Y. (2019). Modeling and deterioration mapping of façades in historical urban context by close-range ultra-lightweight UAVs photogrammetry. *International Journal of Architectural Heritage*, *13*(4), 549–568. https://doi.org/10.1080/15583058.2018.1440030

Sgouropoulou, C. (2021). Temple of Athena and Zeus Soter at Ancient Phigalia. ODYSSEUS Portal. http://odysseus.culture.gr/h/3/gh352.jsp?obj_id=13282

Shepard, D. (1968). A two-dimensional interpolation function for irregularly-spaced data. In R. B. Blue & A. M. Rosenberg (Eds.), *ACM '68: Proceedings of the 1968 23rd ACM national conference* (pp. 517–524). ACM. https://doi.org/10.1145/800186.810616

Tsin, Y., Ramesh, V., & Kanade, T. (2001). Statistical calibration of CCD imaging process. Proceedings Eighth IEEE International Conference on Computer Vision. ICCV 2001, 1, 480–487. https://doi.org/10.1109/ICCV.2001.937555

Urzi, C. (2004). Microbial Deterioration of Rocks and Marble Monuments of the Mediterranean Basin: A Review. Corrosion Reviews, 22(5–6), 441–458. https://doi.org/10.1515/CORRREV.2004.22.5-6.441

Verhoeven, G. (2008). Imaging the invisible using modified digital still cameras for straightforward and low-cost archaeological near-infrared photography. *Journal of Archaeological Science*, *35*(12), 3087–3100. https://doi.org/10.1016/j.jas.2008.06.012

Vikatou, O. (2021). *Temple of Apollo Epikourios*. ODYSSEUS Portal. http://odysseus.culture.gr/h/2/eh251.jsp?obj_id=1142

Webb, E. K., Robson, S., MacDonald, L., Garside, D., & Evans, R. (2018). Spectral and 3D Cultural Heritage Documentation Using a Modified Camera. *The International Archives of the Photogrammetry, Remote Sensing and Spatial Information Sciences*, *XLII–2*, 1183–1190. https://doi.org/10.5194/isprs-archives-XLII-2-1183-2018

Zhao, Y., & Zhang, Y. (2008). Comparison of decision tree methods for finding active objects. *Advances in Space Research*, *41*(12), 1955–1959. https://doi.org/10.1016/j.asr.2007.07.020

Zheng, Y., Lin, S., Kambhamettu, C., Yu, J., & Kang, S. B. (2009). Single-Image Vignetting Correction. IEEE Transactions on Pattern Analysis and Machine Intelligence, 31(12), 2243–2256. https://doi.org/10.1109/TPAMI.2008.263

5 Close-Range Inspection via Integrated Metric 3D Surveying and Multiwavelength Recording

The designing of the integrated workflow presented in this chapter has taken into account the lack of 3D approaches for inspecting and monitoring cultural heritage assets' preservation state and the potential advantages of fusing metric 3D surveying and multi-wavelength close-range data through novel approaches. Therefore, it aims to address the appropriate recording strategies, which implement passive and active close-range sensing techniques (optical, thermal, laser-based, and microwave radiation-based) and enable the fusion and the integrated visualization of multiwavelength data. In other words, this workflow combines geometric measurement and non-destructive recording for condition inspection, while paying attention to essential metric and radiometric aspects of the individual sensing methods, which facilitate integration. Parts of this chapters' contents have been previously published in Adamopoulos, Bovero et al. (2020), Adamopoulos, Colombero, et al. (2021), Adamopoulos & Rinaudo (2020a), Adamopoulos & Rinaudo (2020b), Adamopoulos, Rinaudo & Ardissono (2021), Adamopoulos, Rinaudo & Bovero (2019), Adamopoulos, Volinia et al. (2020).

The designed workflow starts by collecting spectral radiance images at the visible and near-infrared spectra, thermograms, ground-penetrating radar data, and 3D point clouds. Measuring a carefully designed network of points, radiometric data corrections, photogrammetric processing, and various data transformations allow for generating referenced multispectral orthophoto-mosaics (or surface developments) and amplitude slices. Then fusion and further processing of the final derivatives at the pixel level takes place. The general methodology is summarized in Figure 5.1. Similarly, at the final stages of integrated multiwavelength surveying, instead of 2D products registered in 3D space, full 3D integration can occur between models with infrared texture and iso-surfaces produced by ground-penetrating radar amplitudes.
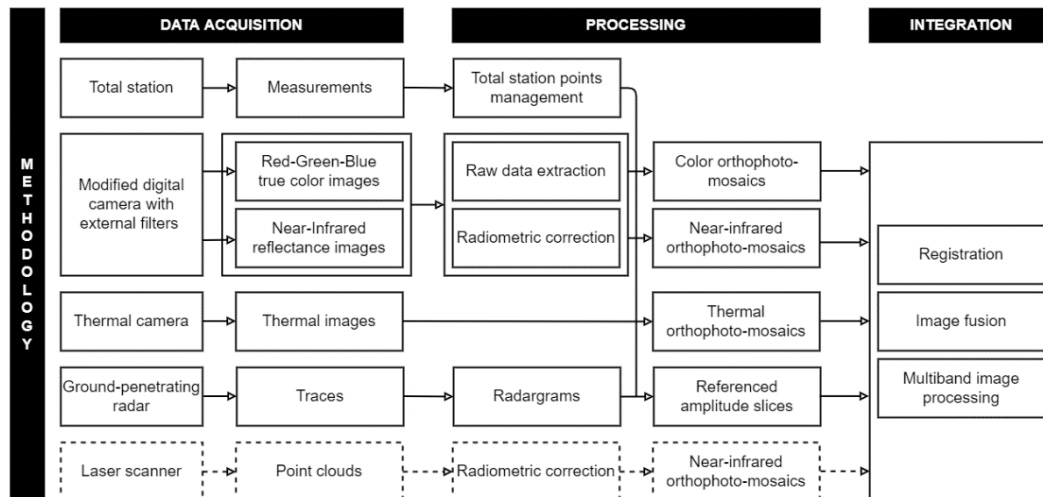
Figure 5.1. Integrated multi-sensor and multi-wavelength recording methodology.

5.1 Data Acquisition and Preparation

5.1.1 Multiband Imaging and IBM

The proposed workflow implements modified CMOS-based digital SLR cameras to capture the required high-resolution spectral radiance images at the NUV, VIS, and NIR spectra. Because orthoimage-mosaics and 3D model textures are to be produced through a standard IBM workflow, the image acquisition should follow the rules provided by the software manufacturers. General photo-shooting guidelines for cultural heritage photogrammetric applications indicate that occlusions should be avoided, and each photo should effectively use the frame size. Large overlaps are required, and every surface of the object should be depicted in at least three images. Shadows and blinks should be avoided. A network of points should be established for control and accuracy checks, and measured. Images should be saved in RAW format to maintain all the necessary radiometric characteristics and should be high-quality. Consistent illumination is required, and a standardized color chart should be used in each frame sequence. The scene SSD should be selected according to the scale requirements, and it should be at least two to three times smaller than the spatial resolution expected on the final orthoimage-mosaics and mesh textures.

Multi-view IBM can be conducted with various software (commercial, free and open-source) to obtain orthoimage mosaics and textured 3D models of the investigated historic surfaces at the NUV, VIS, and NIR spectra. The SfM/DMVR approach has been followed for all applications, although different feature description, image-matching, reconstruction, meshing, and texturing algorithms have been considered and tested. Therefore, extensive metric comparisons have been conducted to validate the selected photogrammetric software's

implementability and accuracy with beyond-visible images due to the metric nature of all experimentations.

5.1.2 Thermography and IBM

A hybrid photogrammetry-driven approach involving both color and thermal-infrared images is introduced, tackling the problems induced to thermographic 3D modeling/thermal mapping by the inherent technical characteristics of thermal-infrared sensors and the restrictions of thermographic acquisition for cultural heritage. The proposed approach employs: (a) acquisition of datasets appropriate for photogrammetric digitization purposes, (b) calibration of thermal and optical sensors, (c) image-based recording techniques, and (d) adaptive texture mapping. The implemented thermographic modeling workflow is briefly sketched in Figure 5.2.
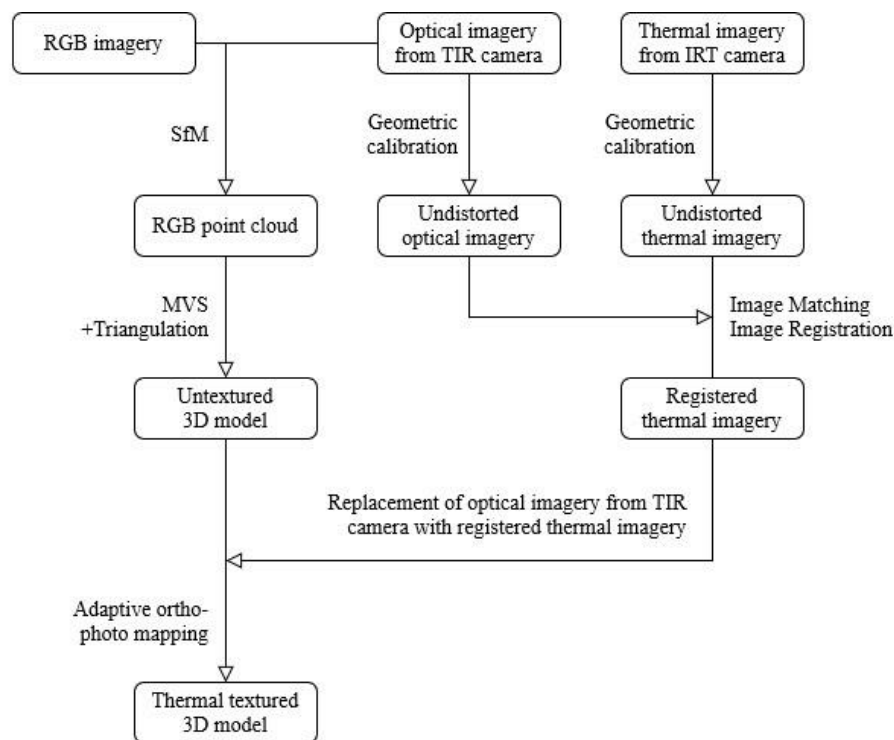
Figure 5.2. Thermographic mapping method.

The developed method employs two instruments. Acquisition employs a high-definition thermographic camera and takes advantage of the integral optoelectronic RGB and thermal sensors. As the RGB sensor's images from the thermographic camera are purposed for direct photogrammetric processing, and with the intention of acquiring high-resolution thermal textured products, a dense and robust geometry with proper overlaps is maintained during the image acquisition phase. During capturing, it is also essential to take into account that the spatial resolution of the thermal textures should match the resolution of the GPR data, which depends on the utilized equipment. The thermal image datasets are acquired in (overlapping)

strips, which consist of images captured from the same distance of the object, with a similar angle between the camera's optical axis and the plane of the object. However, the dataset's geometry still depends largely on the planarity of the façade, architectural component, or structure. Capturing additional oblique images facilitates the accurate implementation of the photogrammetric principles. The second sensor, employed for optical image acquisition, is a high-resolution RGB camera. The captured color images are used to improve the geometry of the photogrammetric sequences and acquire more accurate orientation results for the thermographic camera poses. Low-cost targets identifiable in the visible and thermal infrared spectra are placed in the scene to be used as control points with known coordinates during photogrammetric reconstruction and to facilitate RGB and TIR image registration. Images acquired with the optoelectronic (RGB) and thermal sensors of the thermographic camera are exported at the same resolution, to simplify the image registration and texturing phases at a later stage.

The thermal sensor of the thermographic camera is calibrated using a target made of materials with different reflectance at the LWIR range. The calibration, which estimates the values of intrinsic parameters, extrinsic parameters, and distortion coefficients, is computed in a two-step process: (1) solving for the parameters in a closed form, assuming lens distortion as zero, and (2) using the closed-form solution as the initial estimate of the intrinsic and extrinsic to estimate all parameters—including the distortion coefficients—with nonlinear least-squares minimization (Levenberg–Marquardt algorithm). The camera parameters are then used to undistort the thermal images, which are exported with the same resolution as the original ones. The calibration takes place before any other processing of the images, as most photogrammetric software cannot estimate the intrinsic camera parameters of the thermal sensors (self-calibration). The optical sensor of the thermographic camera is also calibrated with the same approach.

The two sets of estimated parameters about the internal geometry of the thermographic camera are used to undistort both RGB and TIR images collected with the integral sensors of the instrument. For each acquisition strip, one pair of undistorted RGB and TIR images is used to calculate the geometric relation between them, as the acquisition geometry remains unchanged throughout every strip. By manually identifying at least four common points on both images, a projective transformation can be calculated to warp the thermal image to match the system of the RGB image (2D registration). This procedure enables the accurate thermal texture mapping of the metric products by replacing the oriented optical images from the thermographic camera with the corresponding corrected thermal ones. The selected points should be on the flatter area of the object and, as much as possible, on the same plane to avoid inaccuracies in the transformation. The use of more than four points allows for the calculation of errors for the projective transform. In addition, the existence of targets easily detectable on the thermal images facilitates manual matching in case common features cannot be identified.

Each thermal image of the strip is transformed using the calculated projection parameters, and the same procedure is repeated for all acquired image strips.

An IBM 3D reconstruction pipeline is consequently followed. The geometry of the surveyed historic surface is reconstructed with an SfM/DMVR algorithmic implementation, using the dataset containing RGB images from the two optical cameras. In this way, both accurate external orientation information is obtained for the RGB sensor of the thermographic camera, and a sparse reconstruction of the scene is created. The orientation parameters of the two cameras are then optimized using points with measured coordinates. The produced 3D point cloud is then densified on a DMVR procedure, excluding the low-resolution images from the TIR instrument's optoelectronic sensor to reduce noise. Finally, the dense point cloud is meshed into a 3D model, using Delaunay triangulation. If necessary, the surface is smoothed or otherwise optimized with denoising techniques.

For the final step of the 3D temperature mapping, the high-resolution RGB images previously used to generate the dense geometry are not used. Instead, during the process of texture mapping, the RGB images from the thermographic camera are replaced with the same-resolution undistorted and geometrically corrected TIR images, maintaining the estimated orientation from the SfM phase, to apply thermal texture accurately. The texture is applied with an orthophoto adaptive algorithm so that for each part of the model's surface, only the most parallel images are used for texturing, avoiding the inclination and convergence effects. When pixel values from multiple overlapping pixels are used to texture a single triangle of the model, these values are averaged to improve the visual result of the textured product. An ortho-texture can be generated using the 3D model and the oriented thermal image dataset.

It should be highlighted that the production of the thermal orthoimage-mosaics and textures can also be performed with low-cost thermographic cameras. However, in this case, because of the very low spatial resolution the thermographic camera can acquire the thermal data should be recorded as sets of burst images to increase their spatial resolution later digitally.

5.1.3 Scanning

In the framework of the proposed workflow, scanning acts complementarily to the implemented multi-sensor approach. Scanning can either substitute image-based 3D reconstruction of the surveyed heritage asset or capture NIR reflectance data, replacing the use of a modified camera, if the laser sensor operates in the near-infrared spectrum.

The stations for terrestrial scanning of historical and ancient buildings or their remains are selected to acquire homogeneously dense point clouds (in order to avoid resampling that may eliminate necessary details), without occlusions, and

with large overlaps, which could facilitate accurate registration. Then, the scans are denoized, and the laser scanning intensities are rigorously corrected. The final point clouds can either be transformed into 3D models textured with the corrected scanning intensities, or intensity orthoimages can be produced after calculating the necessary transformation planes. Similarly, dense point clouds are acquired through structured light scanning or triangulation scanning performed in a homogeneous way for the various antiquities and historical objects. However, to the extent of the author's knowledge, there is no software accompanying a structured light or triangulation scanner that allows exporting scanning intensities. Therefore, portable scanners can be used only to digitize the geometrical shape of antiquities and historical objects, not their surface reflectance characteristics.

5.1.4 Ground-Penetrating Radar

The GPR profiles are collected along horizontal parallel profiles with the same vertical spacing between them, in order to produce homogeneous data. A wheel encoder is used to track the positioning of the antenna along the moving direction for each GPR profile acquired. Each profile's starting and ending point is measured with a total station to obtain the same reference as the photogrammetric and laser scanning data. The GPR raw data are processed to obtain radargrams and then amplitude slices in 3D space, adopting standard processing steps. The obtained radargrams can also produce 3D amplitude 'point clouds' (points iso-spaced in the three axes) that could be visualized or used to compute isosurfaces.

5.2 Data Fusion

The process of integrating the metric multiwavelength surveying results is at this stage facilitated by the relative spatial reference acquired through the measurement of an established point network, which allows their co-registration. Pseudocolored orthoimage-mosaic composites can be generated using different multispectral combinations. The true color and near-infrared mosaics are resampled to match the spatial resolution achieved at the long-wavelength infrared and millimeter ranges. The spatial reference of the mosaics is maintained while combining the different bands. Radargrams are easily co-registered with the pseudocolored orthoimage-mosaics since their relative position is known.

    The band-specific textures of 3D models require more complicated processing to be transformed into multiband textures. First, the band-specific textures (RGB, NIR, and TIR) are exported separately from the photogrammetric software. Then they can be blended together and reinserted into the photogrammetric software. However, in order to do so, the UV texture mapping of the textures for each band should be performed in the same way, meaning that every texture patch has the exact same image coordinates at the image file of every band. If this condition is

not true, using software such as Blender, each band-specific texture should be manually described in the same way for all surfaces of the object to allow integration into a multiband texture. The same process is followed if the NIR texture has been produced using laser scanning data. Due to their known relative position, iso-volumes from GPR amplitudes are easy to integrate into the multiband textured 3D models.

At the pixel level, for the multiband orthoimage-mosaic composites and multiband textures, data fusion is achieved through quantization techniques (such as principal component analysis) or wavelet decomposition, resulting in more interpretable results which can correspond to different levels of surface weathering or suspected defects.

5.3 Equipment

The implementation of the workflow described in section 5.1 included topographic instruments, digital COTS and modified SLR cameras for multispectral acquisition, photographic accessories, thermographic cameras, scanners, GPR instrumentation, and processing software. The specifications of the utilized instrumentation are presented in Tables 5.1–5.6**Table 5.6**.

Table 5.1. Digital SLR cameras.

Make and model	Canon EOS 5DS R	Canon EOS 1200D /EOS Rebel T5	Huawei P30 (Sony Exmor RS IMX600y)
Resolution	8688×5792 pixels	5184×3456 pixels	7296×5472 pixels
Sensor size	36.00×24.00 mm	22.3 x 14.9 mm	7.6×5.7 mm
Pixel pitch	4.14 μm	4.30 μm	1.01 μm
Lenses	Canon EF 24–105 mm f/4L IS USM	Canon EF-S 18–55 mm IS II	Leica 5.6 mm f/1.8 integrated

Table 5.2. Modified digital SLR cameras.

Make and model	Nikon Xnite D810	Canon EOS Rebel SL1 /EOS 100D
Resolution	7360 × 4912 pixels	5184 × 3456 pixels
Sensor size	35.9 × 24 mm	22.3 x 14.9 mm
Pixel pitch	4.88 μm	4.30 μm
Lenses	Nikon AF-S NIKKOR 24mm f/1.8G ED	Canon EF-S 18–55 mm IS II
External filters	Hoya Infrared (R72), PECA 916	LifePixel Standard Infrared, ZWB1 U-340
Modifier	MaxMax LDP	LifePixel

Table 5.3. Thermographic cameras.

Make and model	FLIR T1030sc	FLIR SC660	FLIR ONE Pro
Spectral range	7.5–14 μm	7.5–13 μm	8–14 μm
Resolution	1024 × 768 pixels	640 × 480 pixels	160 × 120 pixels
Pixel pitch	17 μm	17 μm	12 μm
FOV [1]	12°/28°/45°	12°/24°/45°	43° ± 1°
NETD [2]	< 20 mK at 30°C	< 30 mK at 30°C	< 70 mK
Accuracy	± 1%	± 2%	± 5%

Note: [1] Field-Of-View, [2] Noise Equivalent Temperature Difference (thermal sensitivity).

Table 5.4. Scanners.

Make and model	FARO Focus[3D] X 330	FARO Freestyle[3D]	STONEX F6 SR
Type	Phase shift-based laser scanner	Handheld structured-light scanner	Handheld structured-light scanner
Point density	0.009° step size	≤ 0.2 mm at 0.5 m	0.3° step size
Depth of field	0.6–330 m	0.3–0.8 m	0.25–0.5 m
Speed	up to 976,000 pts/sec	up to 88,000 pts/sec	up to 640,000 pts/sec
Ranging/depth error	± 2 mm	± 0.5 mm	± 0.09 mm
Noise level	0.3 mm at 25 m	0.4 mm at 0.5 m	0.25 mm at 0.25 m

Table 5.5. Geodetic total station.

Make and model	GeoMax Zoom30
Angle standard deviation	3″
Distance measurement accuracy on reflector	2 mm + 2 ppm
Reflectorless distance measurement accuracy	3 mm + 2 ppm

Table 5.6. Ground-penetrating radar.
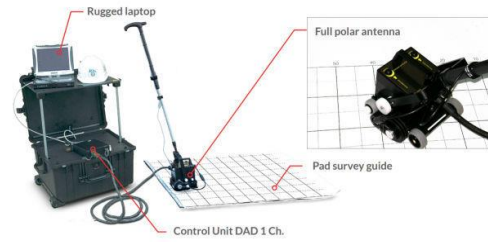
Make	IDS GeoRadar
Positioning	Survey wheel
Scan rate	127 scans/sec
Antenna unit	Aladdin
Number of channels	2
Antenna center frequency	2 GHz
Antenna polarization	Horizontal and vertical
Control unit	K2

5.4 Metric Validation

This section describes the metric evaluation performed before the implementation with case studies, which led to vital decisions about the use of specific close-range sensing techniques and processing software.

5.4.1 Historic Structures

5.4.1.1 Multispectral 3D Modeling

The object of study for this test was part of a façade at the monumental complex of the Reggia di Venaria in Turin, Italy, located in the former 18th-century stables and horse-riding school, designed by Benedetto Alfieri and restored in 2005 to host "La Venaria Reale" Conservation and Restoration Center (approx. 2.5m x 4.6m).

Due to the specific interest in testing and evaluating techniques that differed from established practices on heritage spectral imaging and modeling, the comparability of results was considered for planning the acquisition of datasets for image-based approaches with the low-cost sensors. In other words, instead of following a standard workflow for capturing the image datasets to be processed

with SfM/DMVR approach photogrammetric software, it was attempted to keep as many capturing conditions constant as possible for all sensors and spectra, for every case study. Thus, during the production of the 3D meshes, the main parameters that would vary (and therefore be compared) would only be the different wavelengths captured and different processing software. More specifically, an effort was made to keep internal and external parameters similar amongst camera sensors and spectra and constant during data acquisition, furthermore, taking into consideration scene sampling distances–spatial density of data. In all cases, custom white balance was applied, and no additional photographic equipment was used. In particular, to collect consistent data, thermal images were acquired in short periods under stable climatic conditions while maintaining the same minimum-maximum temperatures of the visualization scale. During thermal infrared photo shooting, optical images of the same scenes were also stored. All photo acquisition conditions are summarized in table 5.7. A set of 18 control and check points was measured with the GeoMax Zoom30 3", producing 5-6 mm accuracy at x, 2-3 mm at y, and 4-5 mm at z-axis.

Table 5.7. Details of image datasets for the façade at Venaria Reale.

camera	f [mm]	distance [m]	GSD [mm]	spectrum	no. images	f-stop	exposure [s]	ISO
1200D	18	1.50	0.36	VIS	55	11	1/15	200
SL1	18	1.50	0.36	full	55	11	1/15	200
SL1	18	1.50	0.36	NIR	55	11	1/5	200
SL1	18	1.50	0.36	UV	55	11	1/5	200
P30	5.6	2.00	0.35	VIS	55	1.8	1/500	200
FLIR	1.5	1.75	1.55	VIS	110	-	-	-
FLIR	-	-	-	TIR	110	-	-	-

The software employed for SfM image-based modeling included commercial solutions Agisoft Metashape Standard (AM), 3D Flow Zephyr Lite (FZ), and a pipeline combining open/ free tools: VisualSfM (VSfM), CMVS and MeshLab.

A standard semi-automatic photogrammetric procedure for large-scale heritage documentation was followed for all datasets, maintaining the same processing parameters in each software and as similar as possible between software, to be able to compare not only the quality and accuracy of produced clouds and models, but additionally algorithms used, processing times and volumes of produced data.

An overview of the processing parameters is presented in the following table (table 5.8). For the first two objects scaling was performed using multiple scales; for OBJ3, referencing was performed using 9 points with known coordinates at a local x,y,z system as control points and 9 for later check. For texture generation, a 16,384 x 16,384 resolution JPEG format was chosen in Metashape, Zephyr, and MeshLab with mosaicking blend type.

Table 5.8. SfM/DMVR processing parameters

	Agisoft Metashape	3DFlow Zephyr
PARAMETERS		
Matching & Alignment		
Key point density	high	high
Pair preselection	unordered	unordered
Key point limits	50 K	50 K
Tie points limits	accurate	accurate
Dense Matching		
Masking	no	no
Point density	high	medium
Depth filtering	moderate	moderate
Mesh Generation		
Max faces number	10 M	10 M
Interpolation	disabled	disabled

AM was able to reconstruct the scene entirely with similar results for the reprojection errors, the density of tie points and densified clouds, and the time needed for each processing step of the photogrammetric procedure of all datasets, barring for total time of P30 dataset processing. Control and check points RMSE for 3D coordinates remained below 2 mm for all spectral imagery captured by the two digital SLRs and below 4 mm for both the data captured by the Huawei P30 camera and the visible sensor of the FLIR One Pro thermal camera. All those errors were lower than the accuracy of performed topographic measurements. Although, the imagery from the latter sensor was included in the photogrammetric procedure only to be able to use the computed orientations to texture with thermal data the high-quality 3D mesh produced by the EOS 1200D VIS image dataset. This was performed without optically calibrating the IRC sensor, considering that any distortions would be insignificant on the approximately 5 cm GDS thermal images. However, the optical sensor of FLIR One Pro was calibrated with the Single Camera Calibrator App of MATLAB. FZ was also able to fully reconstruct the facade producing similar volumes for point clouds and meshes for the datasets from all sensors and spectra. However, tie point count together with reprojection errors were higher for the Huawei P30 imagery, and additionally, double the processing time was needed for the full 3D reconstruction from that dataset. In all cases, xyz RMSEs for the facade with FZ were smaller than 2.5 mm. VSfM was able to reconstruct only parts of the facade, nevertheless in great detail.

Both Agisoft Metashape and 3DFlow Zephyr produced high-to-very high-quality 3D meshes and texturing results for all sensors and spectra. Furthermore, P30 imagery produced a very low amount of noise, but for all comparisons with the SL1 VIS data, mean distances were < 1 mm for both software and RMS < 4 mm for AMP, < 6 mm for FZ, which correspond to approximately 2‰ of the smaller dimension of the reconstructed object and, additionally, are lower than the accuracy of the ground control points used for referencing the scene.

Table 5.9. Geometric comparisons (mean and RMS distances measured in mm).

1200D	**P30**	**SL1 full**	**SL1 UV**	**SL1 NIR**
AM	-0.572	0.284	-0.946	0.116
	/3.589	/2.206	/2.053	/2.190
FZ	-0.020	-0.284	0.307	0.085
	/3.882	/5.128	/4.129	/4.323

Models produced from digital SLR and mobile phone camera image datasets had similar levels of roughness, high preservation of surface details on the final mesh, and sharp textures. Moreover, on UV and NIR models of the façade, areas of high moisture content, delamination and decay were easily distinguishable. The high accuracy 3D model with the low-resolution thermal texture produced could also assist in a more abstract identification of the areas with high surface humidity.
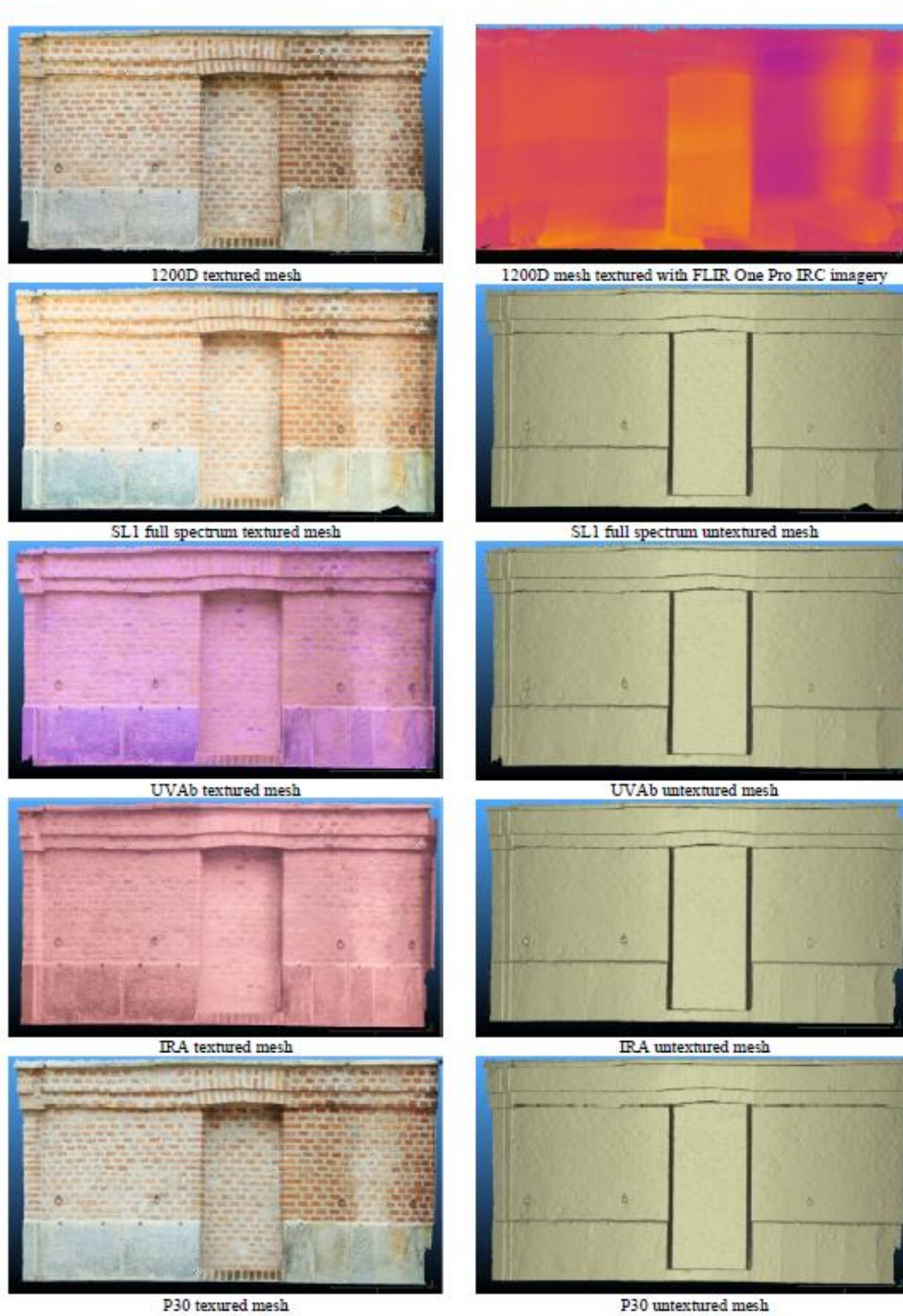
Figure 5.3. Textured 3D models of the façade at Venaria Reale.

The results produced by combining SFM/DMVR pipelines and spectral imaging (Figure 5.3) proved that combination's feasibility for historic building recording. As anticipated, conditions of data acquisition and characteristics of the case studies have an even greater effect on the implemented photogrammetric pipelines and the 3D results produced than when applying standard optical photogrammetric approaches for large-scale heritage applications. Especially, sharpness, radiometric uniformity, and overlaps of the photos are some of the

parameters that impact the quality of spectral meshes' quality. When modified to allow multiband capturing, the internal alterations of a low-cost digital SLR, mainly regarding focusing, are significant. Even though Metashape was able to reconstruct all datasets for the case study involved fully, other software did not succeed to do so (despite the use of similar algorithms by Zephyr). In conclusion, the use of the low-cost equipment implemented here proves promising, considering the very high-quality meshes and textures produced by the cellphone camera, the ability to distinguish colorings, delaminations, decay, and moisture from the digital SLR non-VIS meshes, and moisture content from the model produced with thermal textures (from FLIR One).

5.4.1.2   Thermographic 3D Modeling

The test study for this evaluation was part of the front façade at Castello del Valentino palace in Turin. The thermal imagery was densely captured with the T1030sc camera (Figure 5.4), maintaining approximately a 90% side overlap and a 70% overlap between the image strips, over a part of the main façade measuring 14 × 7.5 m^2. All thermal imagery captured for this work's purposes was recorded passively, without artificial heating, and thus captures long-infrared signatures derived from the predominating environmental conditions. RGB images were also captured from the same positions through the optoelectronic sensor of the FLIR instrument. Forty-two RGB and IRT image pairs were collected from an average distance of 11.6 m. An additional 72 RGB image dataset was captured with the SL1, resulting in a combined optical dataset of 144 images. Twenty pre-signalized and feature points were measured with the TST, scattered over the study area, with a resulting accuracy of half a centimeter at the x and y-axis, and the z-axis.

Figure 5.4. Visualization of the thermal image acquisition geometry.

The resulting total Root-Mean-Square Error (RMSE) for the control points on the reconstructed façade was 9 mm, and for the check points 7 mm. A high-resolution 3D model was produced (Figure 5.5), consisting of approximately 10 million triangles with an average edge size of 2 mm, while the spatial resolution of the thermal data was approximately 6 mm. Thus, the model was reduced to having

a dense cloud grid of 10 mm so that metric and thermal data would have compatible resolutions.

No significant problems were observed with the stitching of the thermal texture apart from the small arches' occluded cornices above the large windows and the floral decorative sculptures with the irregular geometry (Figure 5.6). The model was used for visual inspection, and it was further processed to create a one cm-resolution thermal orthophoto-mosaic, a product easily exploitable for quantitative thermal analyses and other visual analytics. Although no significant degradation was observed due to frequent restoration interventions, the plaster integration could be observed in many areas with this approach, along with the underlying structure and, in specific areas, the remaining moisture.

Figure 5.5. View of the façade's model with thermal texture.
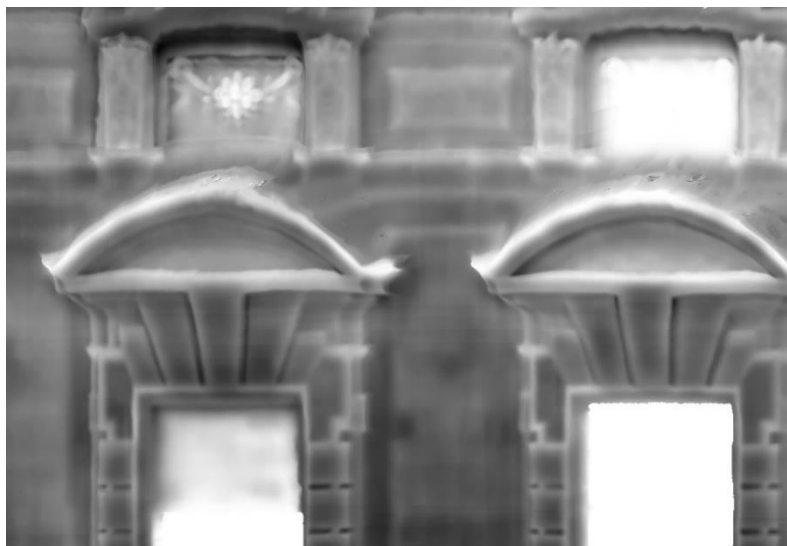
Figure 5.6. Close-up view of occluded areas with blurred thermal texture.

The workflow applied for the 3D thermographic modeling was assessed during the IRT image-correction, geometry reconstruction, and texture mapping phases in the interest of providing a detailed metric and visual evaluation for the complete methodology. In addition, a comparative analysis between the methods described in section 5.1.2 and other cost-effective techniques, which have also been adopted for thermal 3D mapping, was also carried out.

As previously discussed, during the matching phase, between RGB and IRT images, selecting at least four corresponding features is required to estimate the transformation parameters to project the thermal data into the optical imagery correctly. By including more than four features, an error of the transform was calculated, which was approximately equal to 1.5 pixels on the image plane (for all strips), meaning less than 9 mm RMSE in the transformation of the IRT images, on the surface of the architectural façade. More tests applied by measuring the difference of corresponding points in RGB-IRT image pairs, which were not included in the initial calculations of the transform, showed similar errors.

To perform metric comparisons about the façade's reconstructed geometry, the surface was additionally reconstructed according to two different scenarios. In the first scenario, the uncalibrated thermal images were used directly for the point cloud and 3D model generation inside the photogrammetric software. The second scenario concerned the use of the low-resolution RGB images, derived from the optical sensor of the FLIR T1030sc thermo-camera, as the photogrammetric block to generate the metric 3D products. As presented in table 5.10, the investigated methodology significantly improved the reconstruction density, accuracy, and surface quality. Results from the reconstruction using only the SL1 images are also presented in the same table as reference values. Figures 5.7 and 5.8 further showcase how the lower-resolution RGB images and the IRT have affected the reconstruction. The mean distance between the model produced from the SL1 images and the T1030sc RGB images was 3.2 cm, and the standard deviation was 3.3 cm. The same values regarding the distance between the model produced from the SL1 images and the T1030sc RGB images were 5.8 cm and 5.4 cm, respectively, meaning observable geometric errors on the model. The 3D model produced by thermal imagery had significant discrepancies within the areas lacking photogrammetric control points and at the edges of the façade.

Table 5.10. Comparison between photogrammetric reconstructions from different datasets

Imagery Dataset	RMSE*-Control Points (cm)	RMSE*-Check Points (cm)	Point Cloud Density (millions of points)
thermal images-FLIR T1030sc	1.0	1.8	1
optical images-FLIR T1030sc	1.8	2.8	1
optical images-FLIR T1030sc and Canon Rebel-SL1	0.9	0.7	11
optical images Canon Rebel-SL1	0.4	0.4	10

Note–*: Root-Mean-Square Error

Figure 5.7. Façade models produced by Canon Rebel-SL1 and FLIR T1030sc optical imagery (top), FLIR T1030sc optical imagery (middle), and FLIR T1030sc thermal-infrared imagery (bottom).
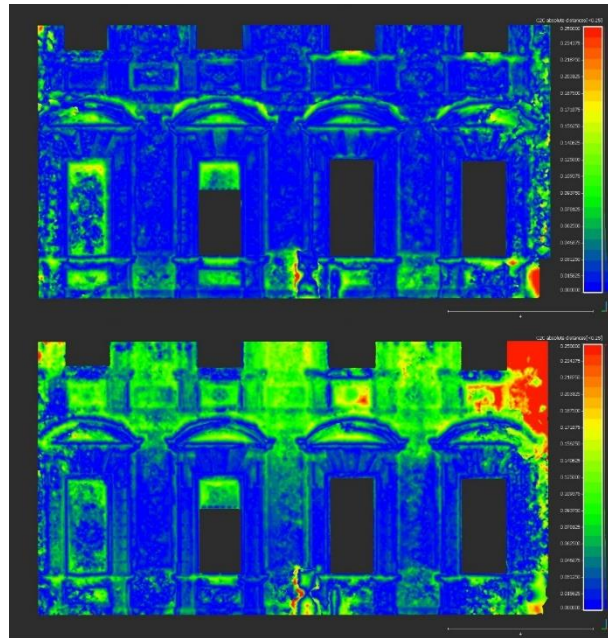
Figure 5.8. Absolute distances between reference model produced by Canon Rebel-SL1 optical imagery and FLIR T1030sc optical imagery (top), and FLIR T1030sc thermal-infrared imagery (bottom).

In order to obtain comparative results for the thermal textures of the created 3D models, the model generated by the FLIR T1030sc optical imagery was textured by replacing the RGB images with the corresponding IRT images, thus maintaining the position, orientation, and calibration parameters of the original images, without applying any additional correction. In addition to that, the 3D model generated by the FLIR T1030sc thermal imagery was textured without any intervention, applying the self-calibration and orientation parameters estimated during the sparse reconstruction phase in the photogrammetric software. The results are shown in Figure 5.8, where overlays of the thermal orthophoto-mosaics on the RGB orthophoto-mosaics are provided to visualize any spatial error between the two types of textured products. As is evident, the implementation of the integrated workflow was extraordinarily successful in this aspect. The ortho-product of directly involving the thermal imagery in the photogrammetric process resulted in remarkably similar, visually, results despite the geometric inaccuracies described above. However, the mapping result involving 3D reconstruction from the FLIR T1030sc camera's RGB sensor had evident flaws.
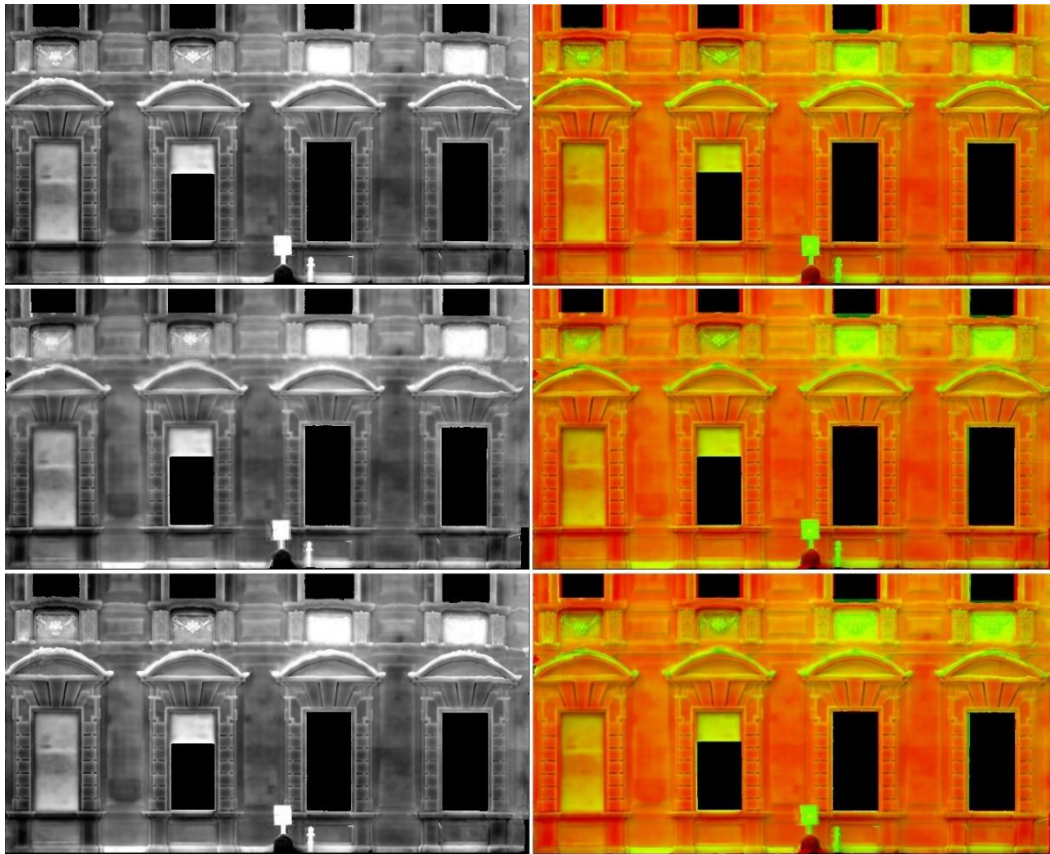
Figure 5.9. Thermal orthophoto-mosaics of the façade (left column) and overlay on RGB mosaic (right column)—produced with the proposed workflow (top), produced using imagery from both thermal and optical sensors of the thermo-camera (middle), and using only thermal imagery (bottom).

The investigated thermal 3D modeling procedure was also implemented employing the FLIR SC660 IRT camera (640×480 spatial resolution), with the intention of testing applicability with lower-cost sensors. In this instance, the matching errors on the RGB-IRT image-pairs were approximately 2 pixels (2 cm), the image-based reconstruction RMSEs combining optical imagery from the REBELl-SL1 camera were 4 mm for the control pints and 4 mm for the check points, and similarly to the previous case, there were no visible texturing problems. The apparent difference was the spatial resolution of thermal texture (1 cm), which meant that at least 2–3 cm per pixel should be shown in the final thermal orthophoto-mosaic, considering the metric accuracy. A comparison between partial thermal orthophoto-mosaics is presented with Figure 5.10, while Figure 5.11 shows the full thermal-orthophoto-mosaic produced with imagery from the FLIR T1030sc. Although similar radiometric differences could be observed, the mapping result from the lower-resolution FLIR appears more blurred, and faint traces of the texture-stitching procedure can be observed. However, the results of employing a medium-resolution camera, more common for general building inspections, showcase an essential potential of involving low-cost IRT sensors for thermographic 3D modeling.
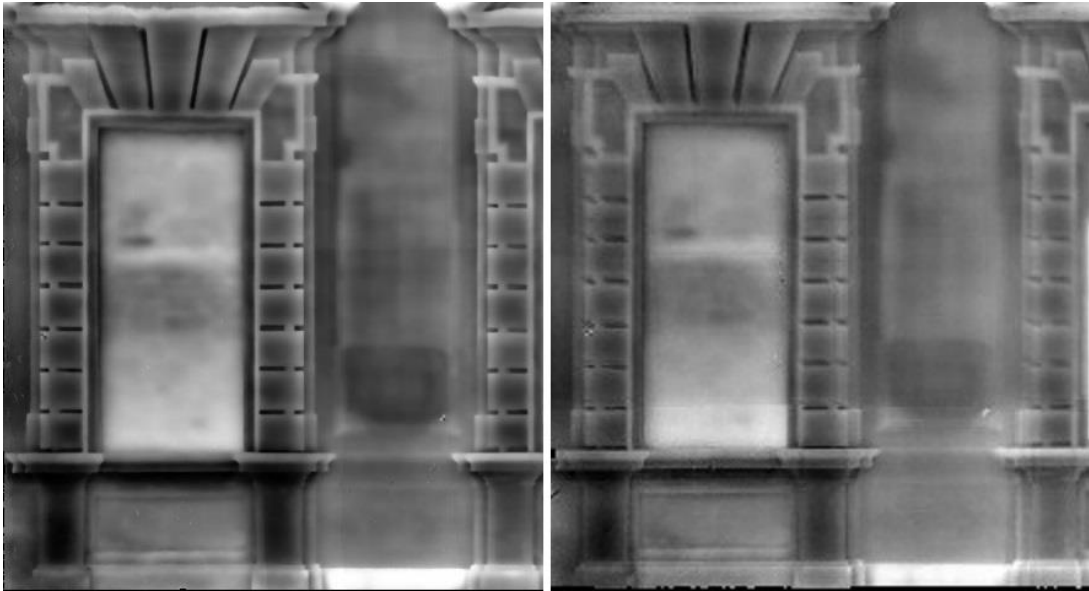
Figure 5.10. Comparison between orthophoto-mosaic for part of the façade produced with the discussed workflow using the sc1030 camera (left) and the 660SC camera (right).

Figure 5.11. Thermal orthophoto-mosaic produced with FLIR 660SC imagery.

An essential advantage of the presented workflow is that it can easily be adapted for the thermal evaluation of façades and flat architectural elements, and geometrically more complex building elements. As an example, Figure 5.12 shows the results of applying the workflow for a part of a column on the main façade of the Castle of Valentino.

Figure 5.12. View of the final 3D thermal model of a column's base, where the position of restoration materials can be observed.

Since original temperature values are maintained when mapping the 3D model or when generating the thermal orthophoto-mosaics, the temperature can be easily measured at specific points on the final textured products (on the surface of a material). By identifying the gray-intensity values and adjusting them according to the minimum and maximum temperature of the thermal reference scale, temperature values and local differences can be easily estimated (the same applies when other color palettes have been used for the thermal textures instead of grayscale). The gray intensities can be measured in any image processing software. Some image processing software (for example, ImageJ) also allows for selecting an area about which statistics can be presented regarding the color values—minimum, maximum, mean, standard deviation—which can also be translated to temperature values following the same correction procedure. Figure 5.13 illustrates the measurement of gray values, which, when corrected according to the temperature range, show a local mean temperature of 17.0 °C, local minimum temperature of 16.9 °C, and maximum temperature of 17.3 °C.
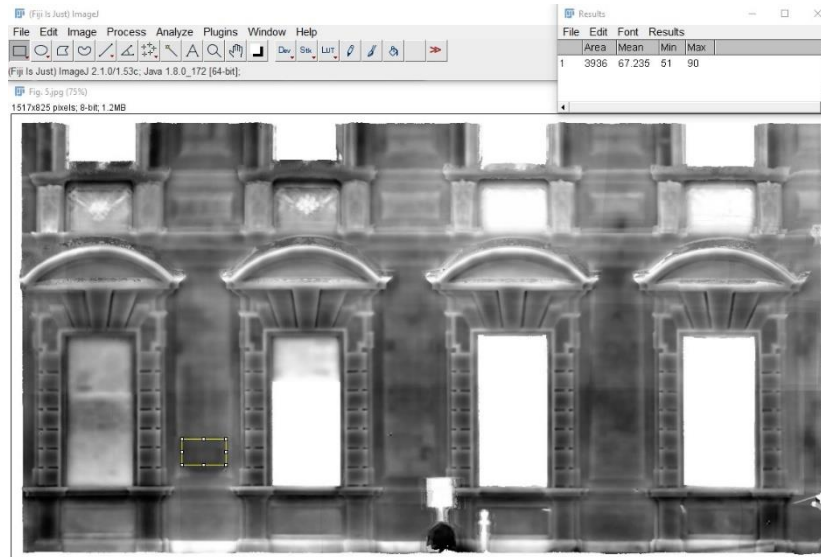
Figure 5.13. Measurement of thermal intensity values in ImageJ.

5.4.2 Historic Objects

5.4.2.1 Scanning and IBM at the visible spectrum

The test objects for this evaluation (presented with figure 5.14) were:

- a copy of Early Cycladic II Spedos-variety marble figurine, dimensions: 4cm x 4cm x 16cm
- a Roman column capital replica, dimensions: 45cm x 45cm x 45cm
- a bust of Francis Joseph I of Austria from the *Accademia Carrara di Bergamo* (Province of Bergamo, Lombardy, Italy), dimensions: 40cm x 50cm x 90cm, and
- a small 19th-century religious stone sculpture of Christ Crucified from *Castello di Casotto* (Province of Cuneo, Piedmont, Italy), dimensions: 31cm x 22cm x 5cm.

Figure 5.14. Case studies (from left to right): Cycladic figurine copy, Roman capital replica, stone bust of Francis Joseph I of Austria, and small sculpture of Christ Crucified.

5.3.2.1.1 IBM

The instrumentation used for the collection of imagery consisted of the full-frame Canon EOS 5DS R camera, the Canon EOS 1200D camera, and the Huawei P30 smartphone.

Imagery for the figurine copy and the small sculpture was acquired using a turntable; artificial targets were placed around the objects to scale the scenes. A tripod was utilized to stabilize the cameras avoiding micro-blur. Regarding the case studies of larger dimensions, images were acquired obliquely with significant overlaps; an invar scale bar was also photographed in the scene for scaling. Despite the different resolutions of the imaging sensors, it was attempted to maintain similar object sampling distances by considering the distance from the object and available focal lengths to acquire comparable data. Depth-of-Field (DoF) was calculated during acquisition, as sharpness was also considered. The characteristics of the datasets are summarized in table 5.11. The last two datasets captured only the upper part of the sculpture.

Table 5.11. Characteristics of imagery datasets.

Dataset	Object	Camera model	Mega-pixels	f [mm]	Distance [m]	No. of images	f-stop	Exposure [s]	ISO
1	figurine copy	EOS 5DS R	52	24	0.25	50	f/7.1	1/20	200
2	figurine copy	EOS 1200D	18	18	0.20	50	f/8	1/20	200
3	figurine copy	Exmor RS IMX650	40	5.6	0.25	50	f/8	1/20	200
4	capital replica	EOS 5DS R	52	35	0.88*	50	f/7.1	1/40	200
5	capital replica	EOS 1200D	18	18	0.69*	50	f/8	1/40	200
6	stone bust	EOS 1200D	18	18	0.90*	50	f/16	1/60	100
7	small sculpture	EOS 1200D	18	18	0.38	142	f/16	1/15	100
8	small sculpture	EOS 1200D	18	55	0.27	60	f/16	1/15	100
9	small sculpture	Exmor RS IMX650	40	5.6	0.12	60	f/1.8	1/50	100

Note: * signifies average values.

The photogrammetric software solutions employed for the SfM–MVS approach image-based modeling included:

- Agisoft Metashape Professional 1.5.1 (3499$)
- 3DFlow Zephyr Aerial 4.519 (4329$)
- Pix4Dmodel 4.5.3 (49$/ month)
- Autodesk ReCap Photo 19.3.1.4 (web-based; ReCap Pro 54$/ month)

- Regard3D 1.0.0. (free and open-source) which employs a K-GRraph matching algorithm and implements the Multi-View Environment for dense scene reconstruction
- a pipeline combining VisualSFM—a GPU-based bundler for SfM, CMVS for MVS dense scene reconstruction, and MeshLab for Screened Poisson Surface Reconstruction and mesh color-texturing.

The image-based processing solutions are herein referred to with the abbreviations AMP, FZA, P4D, ARP, VCM, and R3D, respectively. For the datasets' photogrammetric processing, a customized laptop was used, with a 6-core Intel i7-8750H CPU at 2.2 GHz (Max 4.1 GHz), 32 GB RAM, and NVIDIA GeForce RTX 2070 GPU.

To effectively evaluate the performance of the software implemented and the effects of utilizing different imaging sensors, similar parameters, when applicable, were selected for all the image-based modeling workflows, as summarized in table 5.12. Standard semi-automatic digitization approaches were implemented in all cases, starting with the reconstruction of a sparse cloud, then densifying it after estimating depth maps, creating a mesh with the use of triangulation algorithms, and finally texturing the generated mesh with orthophoto adaptive approaches. No manual removal of noise was performed, apart from deleting the scene and other components unconnected to the object, selected by component size.

Concerning the implemented algorithms, it should be highlighted that the free software VisualSFM utilizes scale-invariant feature transform (SIFT)-based detection and description, while Regard3D uses A-KAZE and LIOP (Local Intensity Order Patterns) for this purpose; in contrast, 3DFlow Zephyr uses a modified Difference-of-Gaussian (DoG) detector. Furthermore, both Metashape and Zephyr perform global bundle adjustment, however, VisualSFM and R3D implement Incremental SfM. Also, while all other software utilized Poisson Surface Reconstruction to generate the triangulated mesh, in FZA, an edge-preserving algorithmic approach was selected to compare results.

Masking of the background on the images was performed in all commercial software, barring RCP that does not allow the user to intervene in any processing step. In P4D, the application of annotations takes place only after an initial full scene reconstruction, if images are correctly aligned, meaning that for the case study of the capital, an extra 1:03:56 was required for the EOS 5DSR dataset, and an extra 0:37:41 was required for the EOS 1200D dataset, for the first dense cloud and textured mesh reconstruction, additionally of what is reported below.

The dense point clouds deriving from free reconstruction pipelines—where there was no option for masking unwanted areas of the imagery—were cleaned automatically using Statistical Outlier Removal (SOR) to efficiently remove noise, before mesh generation. A maximum octree depth of 13, limited surface

interpolation, and specific limits for the number of triangular faces were selected in those solutions that allowed customization of the parameters for the 3D mesh generation step. Mesh texturing was performed without color or exposure-balancing the imagery, and without averaging values from multiple images, creating single-image file textures.

Table 5.12. Processing parameters of image-based photogrammetric modeling.

Reconstruction Step	Parameter	Value
	Key point density	high (50K)
Feature detection and	Tie point density	high (50K)
matching - alignment	Pair preselection	higher matches
	Camera model fitting	refine
Dense	Point density	high
Matching	Depth filtering	moderate
Mesh	Max number of faces	5M (10M for capital replica)
Generation	Surface interpolation	limited
Texture	Texture size	8,192 x 8,192 pixels
Generation	Color balancing	disabled

For the figurine case study, only AMP and FZA were able to fully reconstruct the scene correctly from datasets 1 (EOS 5DS R), 2 (EOS 1200D), and 3 (Exmor RS IMX650). FZA required significantly more processing time, producing generally sparser results. Similar re-projection errors were observed. P4D was not successful in reconstructing the object from any dataset, and RCP results included partial reconstructions with noise and fictitious surfaces (figure 5.14). VCM pipeline entirely reconstructed the scene from dataset 1 (figurine, EOS 5DS R), but a small amount of noise remained after triangulation, affecting the final mesh, and the texturing results were problematic. Furthermore, the VCM pipeline was not able to reconstruct the object from dataset 2 (figurine, EOS 1200D) and resulted in an incomplete point cloud with a lot of noise for dataset 3 (figurine, Exmor RS IMX650; see figure 5.15). R3D resulted in dense point clouds that included a big percentage of noise for dataset 1 (figurine, EOS 5DS R) and 3 (figurine, Exmor RS IMX650; see figure 5.15), which was not possible to be removed automatically (or manually) and therefore were not exploited further to construct 3D meshes. Results from SfM–MVS photogrammetric processing are listed in table 5.13.
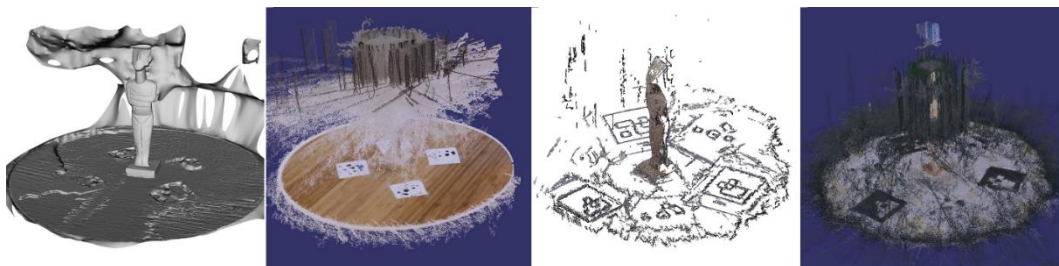
Figure 5.15. Examples of partial and noise-containing reconstructions (from left to right): dataset 1 RCP, dataset 1 R3D, dataset 3 VCM, dataset 3 R3D.

Table 5.13. Photogrammetric results, datasets 1–3.

		Dataset 1		Dataset 2		Dataset 3	
	Software	**AMP**	**FZA**	**AMP**	**FZA**	**AMP**	**FZA**
	Images Aligned	50	50	50	50	50	42
Sparse Cloud	Matching time [hh:mm:ss]	00:00:40	00:02:48	00:00:18	00:01:40	00:00:41	00:05:34
	Alignment time [hh:mm:ss]	00:00:19	00:01:11	00:00:06	00:00:20	00:00:10	00:00:34
	Tie points [1,000 points]	98	24	29	19	77	27
	Projections [1,000 points]	321	136	92	91	212	118
	Adjustment error [pixels]	0.49	0.79	0.54	0.46	0.65	0.72
	Resolution [mm/pixel]	0.05	0.05	0.06	0.06	0.04	0.04
Dense Cloud	Processing time [hh:mm:ss]	00:10:31	01:16:39	00:04:31	00:24:03	00:09:09	00:46:40
	Point count [1,000 points]	1,832	591	1,169	370	2,414	3,920
Triangle Mesh	Processing time [hh:mm:ss]	00:00:21	00:00:08	00:00:16	00:00:47	00:00:30	00:00:10
	Faces [1,000 triangles]	4,482	1,168	2,846	737	5,000	1,551
	Vertices [1,000 points]	2,246	589	1,427	369	2,514	783
Texture	Processing time [hh:mm:ss]	00:04:07	00:04:01	00:02:46	00:01:25	00:05:49	00:02:32
	Total time [hh:mm:ss]	00:15:58	01:24:47	00:07:57	00:28:15	00:16:19	00:55:30

For the capital case study, all software solutions could fully reconstruct the scene correctly (Table 5.14). Processing times were comparable between commercial software. P4D produced the densest sparse cloud results, and AMP the densest dense point cloud results. Notably, the camera auto-calibration parameters, extracted from the commercial software, were interchangeable upon changing their format.

Similarly, the object was reconstructed with all photogrammetric solutions from the obliquely acquired dataset 6 (bust; EOS 1200D). However, RCP seemingly created a few double surfaces and misaligned different planes of the object's surface. Processing times between open software and AMP were comparable, while FZA required significantly more time to process the dataset in this case. The meshes created with the open-source software had some holes at the lower and upper parts. R3D generated a very dense point cloud, but a high number of duplicate points resulted in a low-resolution mesh (Table 5.15). Texturing results were similar.

Table 5.14. Photogrammetric results, datasets 4 and 5.

		Dataset 4			Dataset 5		
	Software	**AMP**	**FZA**	**P4D**	**AMP**	**FZA**	**P4D**
	Images Aligned	50	50	50	50	50	50
	Matching time [hh:mm:ss]	00:01:05	00:10:14	0:00:51	00:01:04	00:09:23	00:00:49
	Alignment time [hh:mm:ss]	00:00:33	00:01:02	0:02:53	00:00:21	00:00:27	0:01:50
Sparse Cloud	Tie points [1,000 points]	197	78	1,262	102	52	547
	Projections [1,000 points]	535	361	2,697	258	247	1,126
	Adjustment error [pixels]	0.98	1.44	0.17	0.69	0.94	0.11
	Resolution [mm/pixel]	0.08	0.09	0.08	0.16	0.16	0.16
Dense Cloud	Processing time [hh:mm:ss]	00:23:15	01:44:35	00:11:35	00:07:51	00:31:01	00:03:15
	Point count [1,000]	43,611	2,168	12,032	10,941	1,811	3,742
	Manual denoizing	no	no	no	no	no	no
Triangle Mesh	Processing time [hh:mm:ss]	00:36:40	00:00:27	00:07:20	00:03:44	00:00:21	00:00:44
	Faces [1,000 triangles]	10,000	4,245	10,000	9,995	3,587	10,000
	Vertices [1,000 points]	7,739	2,935	7,445	5,507	2,293	6,773
Texture	Processing time [hh:mm:ss]	00:36:16	00:07:00	00:35:40	00:11:35	00:04:36	00:10:02
	Total time [hh:mm:ss]	01:37:49	02:03:18	0:58:19	00:24:35	00:45:48	00:16:40

Table 5.15. Photogrammetric results, dataset 6.

		Dataset 6				
	Software	**VCM**	**R3D**	**RCP**	**AMP**	**FZA**
	Images Aligned	50	48	50	50	50
	Matching time [hh:mm:ss]	00:02:19	00:03:36		00:00:36	00:00:59
	Alignment time [hh:mm:ss]	00:01:03	00:00:30		00:00:13	00:17:34
Sparse Cloud	Tie points [1,000 points]	23	143		59	48
	Projections [1,000 points]	75	498		156	205
	Adjustment error [pixels]	1.30	0.17		0.52	0.60
Dense Cloud	Processing time [hh:mm:ss]	00:11:39	00:23:01		00:05:37	00:22:22

	Point count [1,000 points]	1,582	11,786		9,880	2,666
	Processing time [hh:mm:ss]	00:06:05	00:01:02		00:06:31	00:02:01
Triangle Mesh	Faces [1,000 triangles]	1,451	252	1,003	5,000	3,737
	Vertices [1,000 points]	726	127	1,848	2,500	1,873
Texture	Processing time [hh:mm:ss]	00:01:52	00:00:48		00:03:10	00:03:54
	Total time [hh:mm:ss]	0:22:58	0:28:57		0:16:07	0:46:50

Table 5.16. Photogrammetric results, datasets 7–9.

		Dataset 7		Dataset 8			Dataset 9	
	Software	**AMP**	**FZA**	**AMP**	**FZA**	**VCM**	**AMP**	**FZA**
	Images Aligned	142	69	60	60	60	60	23
	Matching time [hh:mm:ss]	00:01:05	00:03:40	00:01:55	0:01:39	00:01:22	00:01:38	0:02:58
	Alignment time [hh:mm:ss]	0:00:24	00:09:05	00:01:19	00:46:48	00:01:28	00:00:55	0:28:02
Sparse Cloud	Tie points [1,000 points]	89	36	420	132	54	88	34
	Projections [1,000 points]	273	154	1,270	803	253	242	127
	Adjustment error [pixels]	0.52	0.52	0.35	0.47	1.02	1.15	1.43
	Resolution [mm/pixel]	0.09	0.09	0.02	0.02	0.02	0.02	0.2
Dense Cloud	Processing time [hh:mm:ss]	00:23:10	00:55:20	00:14:27	00:42:16	00:15:43	00:25:30	00:25:06
	Point count [1,000 points]	2,058	4,211	9,980	3,958	1,764	11,325	1,720
Triangle Mesh	Processing time [hh:mm:ss]	00:01:23	00:02:30	00:02:58	00:03:34	00:06:03	00:05:32	00:01:13
	Faces [1,000 triangles]	4,846	4,605	5,000	4,839	3,864	5,000	2,061
	Vertices [1,000 points]	2,424	2,312	2,563	2,500	1,935	2,504	1,055
Texture	Processing time [hh:mm:ss]	00:09:25	00:18:25	00:03:59	00:09:50	00:09:47	00:04:09	00:02:51
	Total time [hh:mm:ss]	0:35:27	1:29:00	0:24:38	1:44:07	0:34:23	0:37:44	1:00:10

The object in dataset 7 (small sculpture, EOS 1200D, f=18 mm) was fully digitized using AMP, while FZA produced sparser results because not all images of the scene were oriented, despite the significantly longer processing time required. All software produced dense results from dataset 8 (small sculpture, EOS 1200D, f=55 mm), fully reconstructing the scene; AMP generated the densest 3D point

cloud with the lowest reconstruction error, and FZA required the most time for processing. From dataset 9 (small sculpture, Exmor RS IMX650), the complete scene was retrievable only by using VisualSFM. Both RCP and FZA generated partial models (figure 5.16), while AMP produced a very noisy surface. Regard3D failed to generate any mesh from datasets 7–9. Results from SfM–MVS photogrammetric processing of these datasets are listed in table 5.18.
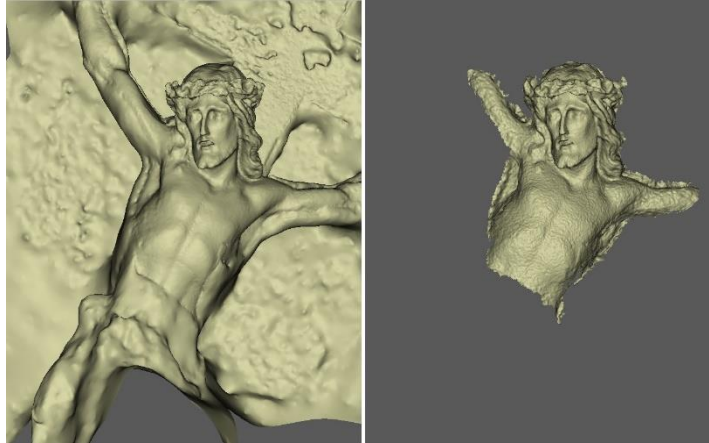
Figure 5.16. Partial meshes generated with RCP (left) and FZA (right) from dataset 9.

5.3.2.1.2 Scanning

For the objects' scanning sessions, a FARO Focus3D X 330 was used along with two portable handheld near-infrared structure light scanners: the FARO Freestyle3D, and the STONEX F6 SR, recently evaluated for the digitization of heritage objects.

Scans were performed under homogeneous light conditions in circular patterns, planned to cover the complete geometry of the objects and eliminate occlusions as much as possible. The scanning distances were approximately 0.4–1 m, translating to 0.2–0.4 mm resolution point cloud densities according to manufacturers' specifications for all scanners. The case study of the capital replica required eight separate scans to be performed to fully capture the object's 3D surface with the Focus3D X 330 and to ascertain the registration of all partial scans in one scene.

Scanned point cloud manipulation was performed with the software provided or suggested by manufacturers. Registration, denoising, and decimation were performed with Autodesk ReCap Pro 5.0.4.17 for raw scans from FARO scanners and with Mantis Vision Echo 2.3.1 for raw scans from the STONEX scanner. The 3D meshing was performed in MeshLab with similar parameters as used for the photogrammetric point clouds.

For the figurine copy case study, no model was constructed since the Focus 3D X 330 scanner did not provide results with enough density, and the handheld

scanners resulted in point clouds not correctly registered, with large amounts of noise which could not be removed either manually or automatically. For the capital replica case study FARO Focus3D X 330 and SF6 SR produced dense results, with some holes remaining in the first case due to occlusions. Freestyle3D produced a very noisy and sparse cloud. These scanning results are listed in detail in table 5.17. Scanning-based models were also produced for the stone bust after merging 8 partial overlapping surface models captured with the FS SR (14 million points), and for one side of the small sculpture (383 thousand point); all other digitization by scanning failed because partially scanned scenes could not be registered.

Table 5.17. Scanning results, capital replica.

	STONEX F6 SR	FARO Focus3D X 330	FARO Freestyle
Acquisition duration [mm:ss]	02:16	90:56	10:40
Registration duration [mm:ss]	05:08	14:35	---
Denoising duration [mm:ss]	24:15	2:26	00:02
Meshing duration [mm:ss]	01:23	04:01	01:27
Cloud points [1,000]	20,928	1,289	435
Mesh triangles [1,000]	6,350	6,488	1,951

5.3.2.1.3 Comparisons and Evaluation

The assessment of the quality of produced meshes considered completeness, preservation of the surface detail, noise, roughness, and additionally visual fidelity of texture quality for photogrammetric models. Models from the scanners had no observable noise. However, the surface produced with F6 SR was oversimplified, proving that the Mantis Echo Vision eliminated some of the surface details, despite the fact that low values for noise filtering had been selected; distances ranged below 2 mm (figure 5.17).

Figure 5.17. Scanning results. Untextured Stonex F6 SR mesh (left), untextured FARO Focus 3D X 330 mesh (center), and scalar field mapping of Hausdorff distances; maximum visualized distance 1 cm.

For the photogrammetric datasets 1, 2, and 3, AMP and FZA produced very consistent results of similar detail and roughness. The models produced from dataset 1 (EOS 5DS R, figurine copy) were of remarkably high texture quality (figure 5.18). The models from dataset 3 (Exmor RS IMS 650, figurine copy) contained an amount of noise (figure 5.19). The calculated absolute distances between all models for those datasets were smaller than 0.5 mm (one standard deviation), which was roughly 0.3% of the objects' size, with mean distances being lower than 0.3 mm (table 5.18).

For dataset 4 (capital replica, EOS 5DS R), models from AMP and VCM had more holes. Models from P4D and RCP were smoother. The other models contained a small amount of noise on flatter surfaces, and P4D seemed to oversimplify the surface details. Furthermore, the free software models had a small amount of remaining noise at the edges (figure 5.20). All commercial software produced similar textures. The calculated absolute distances between photogrammetric models for dataset 4 were smaller than 1.5 mm (one standard deviation), roughly 0.4 % of the objects' dimensions, except for the model from P4D, about which the calculated distances to other models were larger than 2 mm (one standard deviation) as displayed in table 5.19. A mapping of the geometric differences is also presented with figure 5.21.

Regarding dataset 6 (capital replica, EOS 1200D), all models contained an amount of surface noise, ranging from low to medium levels, with the VCM pipeline being the one that resulted in higher level of preservation of surface detail and lower roughness levels. P4D and R3D meshes were the noisiest (figure 5.22). Overall, texture quality between the commercial software was similar and better than of that produced by free reconstruction pipelines (figure 5.23). The calculated absolute distances between photogrammetric models (vertices of final mesh) for dataset 5 was smaller than 2.5 mm (one standard deviation—σ), roughly 0.6% of the objects' dimensions, except for the model from P4D, where higher values were observed (table 5.20).

P a g e | 179

Table 5.18. Hausdorff distances between photogrammetric models for the figurine copy case study – Datasets 1-3 (distances in mm).

	Dataset 2 AMP		Dataset 3 AMP		Dataset 1 FZA		Dataset 2 FZA		Dataset 3 FZA	
dataset 1 AMP	0.15	0.11	0.17	0.14	0.21	0.29	0.16	0.15	0.19	0.18
dataset 2 AMP			0.19	0.16	0.23	0.28	0.21	0.18	0.18	0.14
dataset 3 AMP					0.18	0.17	0.17	0.14	0.15	0.10
dataset 1 FZA							0.20	0.20	0.17	0.16
dataset 2 FZA									0.16	0.10
	Mean abs.	Std. dev	Mean abs.	Std. dev	Mean abs.	Std. dev	Mean abs.	Std. dev	Mean abs.	Std. dev

Table 5.19. Hausdorff distances between photogrammetric models for the capital replica case study – Dataset 4 (distances in mm).

	FZA		P4D		RCP		VCM		R3D	
AMP	0.66	0.45	0.75	1.30	0.76	0.59	0.69	0.54	0.80	0.57
FZA			0.80	1.50	0.72	0.78	0.72	0.71	0.79	0.68
P4D					0.95	2.14	0.94	1.06	0.96	1.07
RCP							0.80	0.67	0.82	0.64
VCM									0.60	0.59
	Mean abs.	Std. dev	Mean abs.	Std. dev	Mean abs.	Std. dev	Mean abs.	Std. dev	Mean abs.	Std. dev

Table 5.20. Hausdorff distances between photogrammetric models for the capital replica case study – Dataset 5 (distances in mm).

	FZA		P4D		RCP		VCM		R3D	
AMP	0.60	0.45	0.68	0.81	0.72	0.99	0.50	0.50	5.45	3.33
FZA			0.94	1.06	1.04	1.23	0.73	0.68	5.37	3.23
P4D					1.07	1.51	0.90	0.95	5.48	3.22
RCP							1.05	1.51	5.55	3.23
VCM									5.37	3.26
	Mean abs.	Std. dev	Mean abs.	Std. dev	Mean abs.	Std. dev	Mean abs.	Std. dev	Mean abs.	Std. dev

Figure 5.18. Textured photogrammetric meshes of the figurine copy, (from left to right) dataset 1 AMP, dataset 1 FZA, dataset 2 AMP, dataset 2 FZA, dataset 3 AMP, dataset 3 FZA.
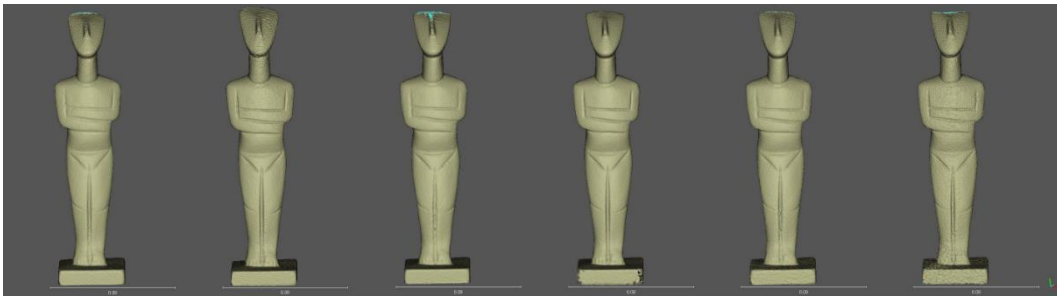
Figure 5.19. Untextured photogrammetric meshes of the figurine copy, (from left to right) dataset 1 AMP, dataset 1 FZA, dataset 2 AMP, dataset 2 FZA, dataset 3 AMP, dataset 3 FZA.

Figure 5.20. Untextured photogrammetric meshes from dataset 4, (from left to right) AMP, FZA, P4D, RCP, VCM.
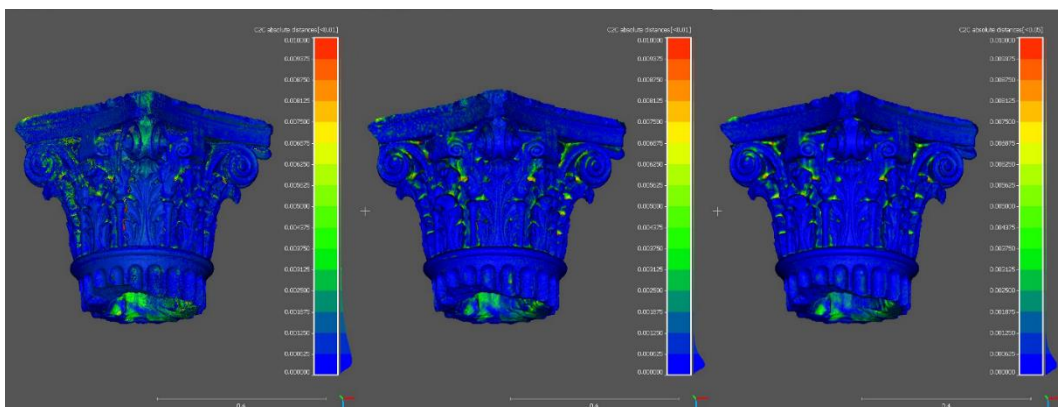
Figure 5.21. Scalar field mapping of Hausdorff distances for dataset 4 between RCP SfM–MVS mesh and: AMP mesh (left), FZA (center), and P4D mesh (right); maximum visualized distance 1 cm.

Figure 5.22. Textured photogrammetric meshes of the capital replica from dataset 5, (from left to right) AMP, VCM, R3D.

Figure 5.23. Untextured photogrammetric meshes of the capital replica from dataset 5, (from left to right, and from top to bottom): AMP, FZA, P4D, RCP, VCM, R3D.

Concerning dataset 6 (stone bust, EOS 1200D), FZA, RCP, and VCM-generated meshes were those more similar to the scanned mesh, and between them, in terms of surface detail and surface roughness (figures 5.24, 5.25). However, as mentioned above, the RCP mesh had duplicate surfaces, and the FZA-produced mesh had a few holes on the top of the head where there was a smaller overlap between images. The AMP-produced mesh was also similar to the scanned one on the flatter surfaces, but on edges and 'fabric' folds a significant amount of noise remained. The textures were similar and differentiated only because of the small surface anomalies present at the web-based and open-source software produced meshes. Calculated surface differences are presented in figure 5.26. Differences between the AMP-generated model and the other models were the smallest (table 5.21), while differences between AMP-FZA models ranged below 1.4 mm (1 σ).

Figure 5.24. Untextured meshes of the stone bust from dataset 6 (from left to right, and from top to bottom): F6 SR, AMP, FZA, RCP, VCM, R3D.
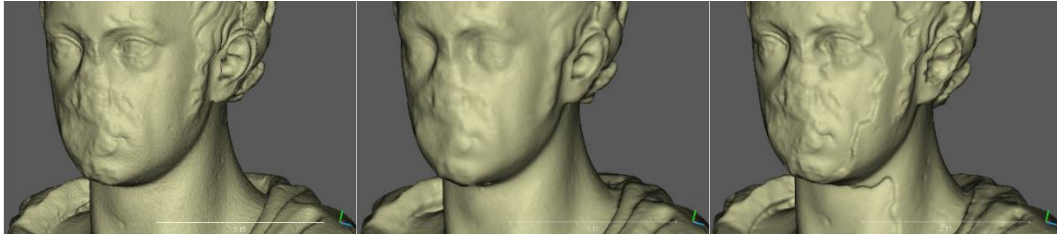
Figure 5.25. Detail from untextured photogrammetric meshes of the stone bust from dataset 6 (from left to right): F6 SR, FZA, RCP.
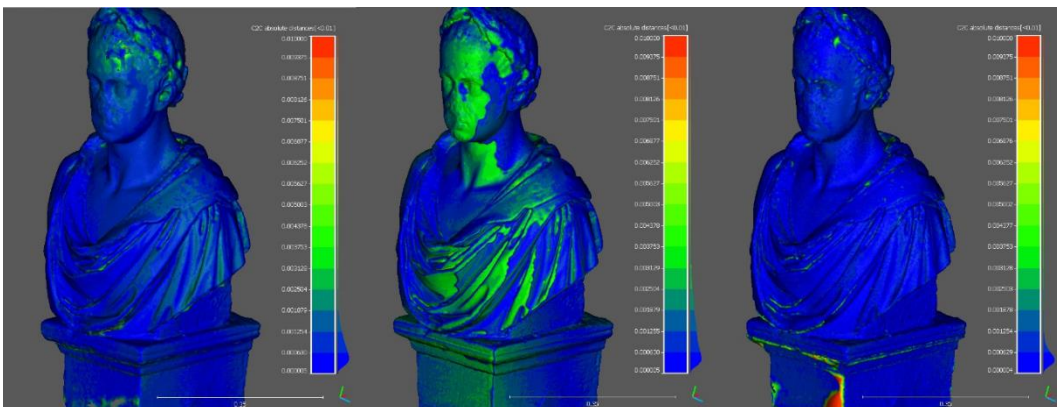
Figure 5.26. Scalar field mapping of Hausdorff distances for dataset 6 between AMP SfM–MVS mesh and: FZA mesh (left), RCP (center) and VCM mesh (right); maximum visualized distance 1 cm.

Table 5.21. Hausdorff distances between photogrammetric models for the stone bust case study – Dataset 6 (distances in mm).

	FZA		RCP		VCM		R3D	
AMP	0.82	0.58	1.28	0.89	0.69	0.82	1.03	1.31
FZA			1.21	1.31	1.00	1.15	1.11	1.37
RCP					1.44	1.19	1.68	1.5
VCM							1.21	1.36
	Mean abs.	Std. dev	Mean abs.	Std. dev	Mean abs.	Std. dev	Mean abs.	Std. dev

The only fully reconstructed mesh for dataset 7 from AMP had smoothed-out surface features. All reconstructed models from dataset 8 had similar characteristics (figure 5.27). Some double surfaces could again be observed on the surface produced with RCP. Surprisingly, the generated surface with better-preserved surface features, was the one produced from dataset 9 (small sculpture, Exmor RS IMX650) with the pipeline implementing VisualSFM, CMVS, and MeshLab (figure 5.28). The differences observed between the meshes generated from dataset 7 ranged below 1 mm (1 σ), while the differences between models from dataset 8 ranged below 0.7 mm (1 σ), which are both considerable taking into consideration that the resolutions of these datasets were 0.09 mm and 0.02 mm, respectively. Significantly the surface deviation between the dataset 9 VisualSFM model and the high-resolution Metashape model from dataset 8 was below 0.5 mm (1 σ). Some of the measured distances are presented in table 5.22.

Table 5.22. Hausdorff distances between photogrammetric models for the small sculpture case study – Datasets 7–9 (distances in mm).

	AMP-dataset 7		FZA-dataset 7		AMP-dataset 8		VCM-dataset 9	
AMP-dataset 8	0.70	1.45	0.81	1.53	0.24	0.48	0.28	0.86
	mean abs.	std. dev.	mean abs.	std. dev.	mean abs.	std. dev.	mean abs.	std. dev.
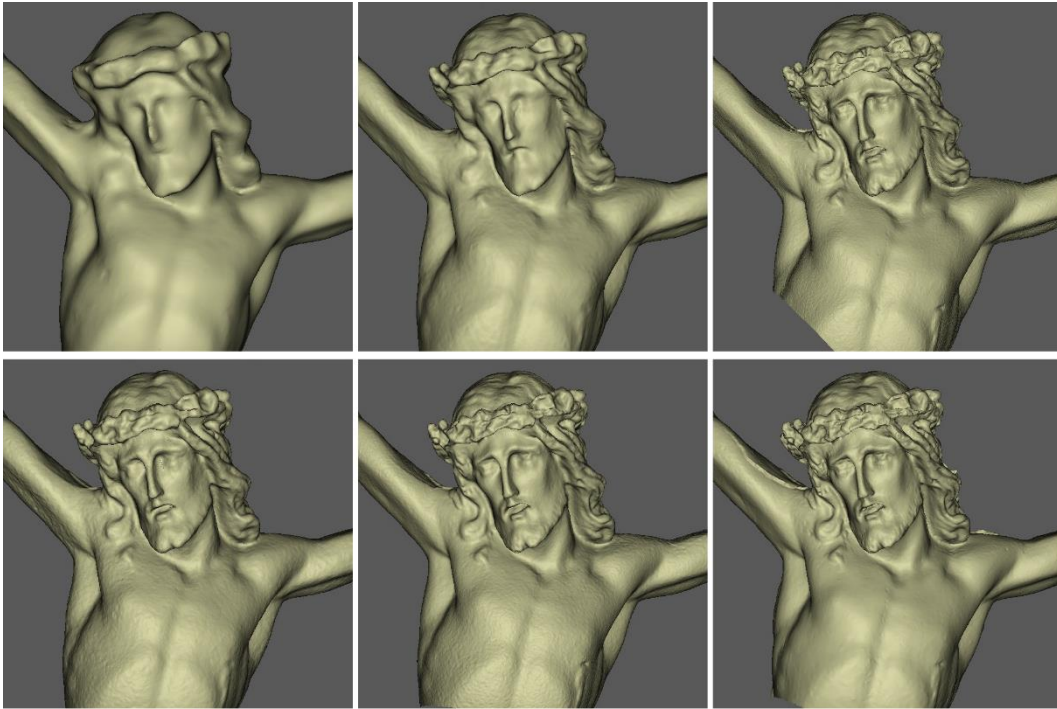
Figure 5.27. Untextured meshes of the small sculpture, (from left to right, and from top to bottom): F6 SR, AMP-dataset 7, AMP-dataset 8, FZA-dataset 7, FZA-dataset 8, and RCP-dataset 8.

Figure 5.28. VCM-produced mesh from dataset 9 (smartphone camera).

5.3.2.1.4. Further Metric Comparisons

For the capital replica case study, more geometric assessments could be performed, comparing scanning meshes, assumed as ground truth, to the photogrammetric models. Calculation of distances was performed in Cloud Compare, with the Cloud-to-Cloud distance tool on final meshes' vertices, after Fine Registration (ICP) was employed. The Hausdorff distances between scanning and photogrammetric meshes ranged below 3 mm (one standard deviation) for dataset 4, except for the P4D model, and below 3.5 mm (one standard deviation) for dataset 5, except for

the R3D model, which contained a great magnitude of noise. The results are presented in detail in tables 5.23 and 5.24. The main differences between models produced with photogrammetric and scanning techniques were observed at parts of the capital replica that occluded due to its complicated geometry.

Table 5.23. Hausdorff distances between 3D scanning and photogrammetric models from dataset 4 (distances in mm).

	AMP		FZA		P4D		RCP		VCM		R3D	
3D X	0.84	2.18	1.01	1.57	1.32	2.14	1.17	1.69	1.21	1.79	1.01	1.04
F6 SR	1.72	1.75	1.23	1.40	1.23	1.43	1.48	1.61	1.21	1.39	1.17	1.35
	Mean abs.	Std. dev	Mean abs.	Std. dev	Mean abs.	Std. dev	Mean abs.	Std. dev	Mean abs.	Std. dev	Mean abs.	Std. dev

Table 5.24. Hausdorff distances between 3D scanning and photogrammetric models from dataset 5 (distances in mm).

	AMP		FZA		P4D		RCP		VCM		R3D	
3D X	1.46	1.96	1.29	1.90	1.37	2.16	1.42	2.04	1.25	2.09	5.75	3.30
F6 SR	1.53	2.16	1.54	1.41	1.22	1.43	1.51	1.69	1.31	1.44	6.22	3.33
	Mean abs.	Std. dev	Mean abs.	Std. dev	Mean abs.	Std. dev	Mean abs.	Std. dev	Mean abs.	Std. dev	Mean abs.	Std. dev

For the stone bust, further geometric assessments could also be performed, comparing photogrammetrically produced surfaces with the scanned model. Accuracies considering as ground truth the scanned F6 SR model are presented in table 5.25 and visualized in figure 5.29. The AMP and FZA models were more metrically accurate, considering that surfaces deviated below 1.3 mm (1 σ) from the ground truth model, only 3 ‰ of the object's smallest dimension. Mean distances and their standard deviation for the models produced from non-commercial software ranged at about 1 mm.

Table 5.25. Hausdorff distances between 3D scanning and photogrammetric models from dataset 6 (distances in mm).

	AMP		FZA		RCP		VCM		R3D	
F6 SR	0.63	0.73	0.66	0.65	1.22	1.00	0.75	0.92	1.11	1.38
	Mean abs.	Std. dev	Mean abs.	Std. dev	Mean abs.	Std. dev	Mean abs.	Std. dev	Mean abs.	Std. dev
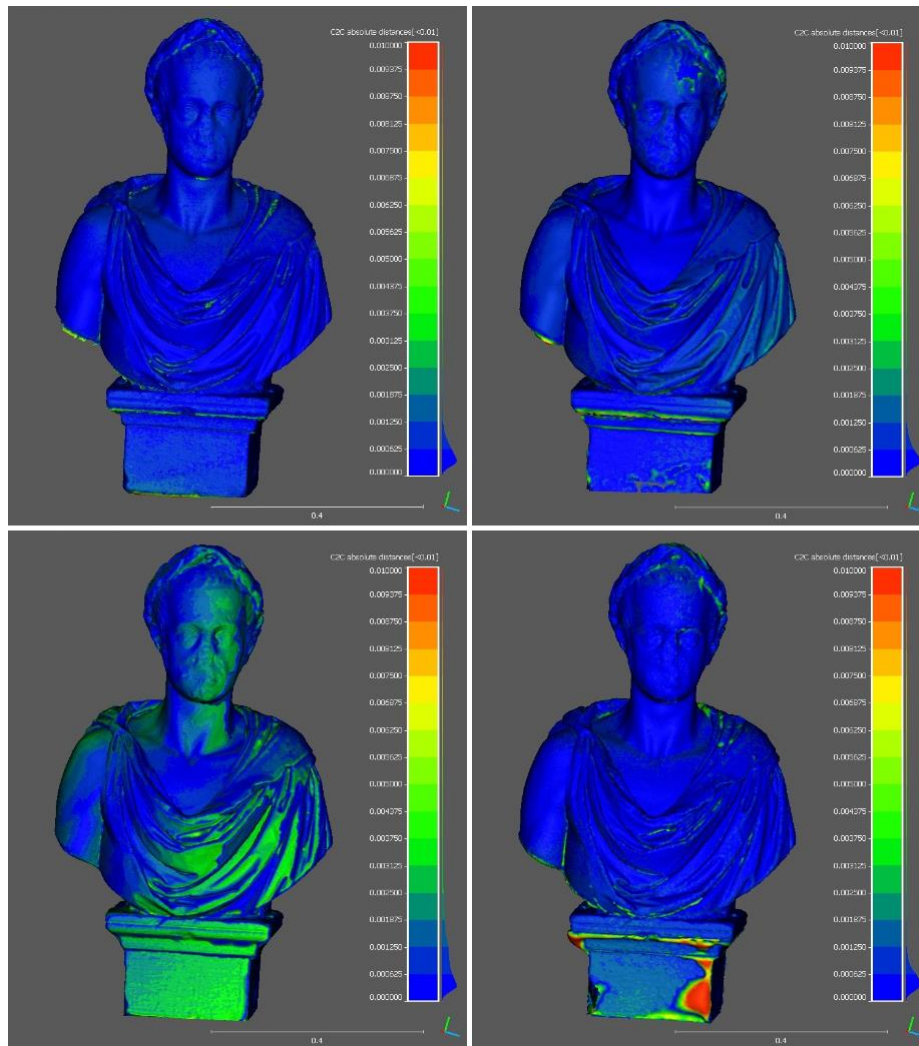
Figure 5.29. Scalar field mapping of Hausdorff distances between dataset 8 photogrammetric models and the scanned F6 SR model showing surface deviation from AMP (upper left), FZA (upper right), RCP (lower left), and VCM (lower right); maximum visualized distance 1 cm.

5.3.2.1.5. Discussion

The presented metric tests on heritage objects carried out a selective comparison of state-of-the-art SfM and MVS image-based modeling solutions of different costs and portable scanners for small-scale heritage digitization. As expected, challenges occur from the different nature of heritage objects, with geometry, surface features, and texture playing an important role on the decision-making for acquisition and processing workflows.

Photogrammetric results are affected by the type of camera sensor, sampling distance, and coverage of the object on the image space. For complex, featureless, or very small case studies, only the expensive commercial solutions appear to be able to fully reconstruct the photogrammetric scene, proving that perhaps the more cost-effective solutions are better suited for static scenes, or when the background is homogeneous and of vastly different color than the object, so that it can be recognized as background by the utilized software.

For the photogrammetric reconstruction from the datasets of the capital replica and the stone bust, almost all workflows produced similar results. However, some persistent noise problems can be attributed to oblique images and thus can be tackled by acquiring more rigid, dense, and light-consistent imagery datasets.

Although AMP, FZA, and RCP proved to be the more efficient solutions, it should be stated that RCP offers no adjustable parameters and a limitation of 100 images per project, which is an important problem for real-case heritage digitization applications. Furthermore, AMP offers only a few adjustable parameters, with no details being available on the algorithmic approaches it exploits. On the other hand, FZA allows every parameter on the digital reconstruction workflow course to be customizable. Despite default options resulting in noisy results -relative to FZA- an expert can identify how to optimize its implementation for heritage purposes. Especially the implementation of an edge-preserving meshing algorithm, that also limits the interpolation of the dense point cloud in 3DFlow Zephyr, allows the generation of high-quality surfaces, preserving detail similar to the handheld scanners. P4D, a software mainly oriented towards long-range applications and flatter geometries, did not provide satisfactory results. The main problem with the free solutions was surface noise (due to capturing conditions) which cannon easily be filtered in post-production.

Image-based methods tackled occlusions caused by complex geometries, but other problematic surfaces may require various combinations of documentation techniques. Furthermore, the textures produced from scanning techniques were not of adequate quality. Thus, meshes produced in this manner need to be textured with other methods, ranging from simple image-to-mesh registration, co-registration with photogrammetric models, and integrating sensors for multiple data acquisitions. Differences between Focus3D X 330 and Stonex F6 SR results can be attributed to the fact that the first one is oriented mainly towards architectural documentation and other construction applications.

Using a mobile phone camera for photogrammetric purposes also seemed promising, not affecting the metric properties of the results but having a visible effect on the generated noise levels. Although, despite the high resolution and quality of the mobile camera sensor, texture results were of lesser quality than textures produced from datasets of high-resolution digital SLR cameras. Thus, more experiments need to be conducted to evaluate the radiometric capacity of smartphone cameras for high fidelity texturing of heritage models. To conclude, smartphone cameras and web-based solutions provide an exciting potential for applications where metric quality is not the primary concern, such as rapid recording, dissemination for education, or promotion of cultural heritage for touristic purposes.

5.5 Experimental Results

5.5.1 Stone Sculptures

This case study combined NIR reflectance imaging performed with a modified commercial camera, image-based multi-view 3D modeling, and 3D mapping techniques. The aim was to explore a reproducible, rapid, and easily implementable method for inspecting stone sculptures. Towards this direction, NIR spectral models were produced using two algorithmic implementations, and their metric quality was evaluated. The geometric results are further discussed compared to models produced by RGB images. Then the produced high-quality NIR models are used to implement different mapping techniques based on classification and segmentation approaches, exploiting the high-resolution NIR reflectance intensities to produce different visualizations. Afterward, the 3D digital visualization results are discussed on their capacity to accurately represent the weathering levels on historical stone sculptures. Finally, aiming to evaluate the applicability of the suggested method on different scales, it is demonstrated for two case studies of different dimensions.

5.5.1.1   Materials and Methods

The suggested approach was evaluated on different scales, with two different case studies of historical stone sculptures exposed to external environmental conditions being involved. The first one was a 17th-century marble statue (approx. height of 1.75 m) from the Fountain of Hercules at the *Reggia di Venaria Reale* near Turin. The Palace of *Venaria* was one of the Residences of the Royal House of Savoy, included in the UNESCO World Heritage List in 1997. *Musei Reali Torino* owns the statue. The second case study was a small 19th-century religious stone sculpture of Christ crucified (approx. dimensions 31 cm × 22 cm) from *Castello di Casotto* (Garessio, Province of Cuneo, Piedmont) owned by *Regione Piemonte*. The *Casotto* Castle was originally a Carthusian monastery, later acquired by the Savoy and transformed into a castle and hunting lodge by Carlo Alberto (30).

Figure 5.30 Images of the case studies; statue from the Fountain of Hercules (left) and small stone sculpture of Christ Crucified (right)

The images were captured with the Canon Rebel SL1 converted camera for this experimentation. NIR image acquisition was performed with the implementation of a near-infrared-pass filter (700–1400 nm), and VIS image acquisition was performed with the implementation of a UV-NIR-cut filter. Additionally, a Canon EF-S 18–55 mm f/4–5.6 IS II zoom lens was used. The camera was mounted on a tripod during all acquisition scenarios to avoid micro-movement effects. An x·rite ColorChecker® Classic target with 24 colors was used for color correction, utilizing middle gray for visible white balancing. Post-capturing photo-editing operations were performed in Adobe Lightroom Classic. The raw NIR radiance images were radiometrically corrected and subsequently transformed into reflectance images, as described in section 4.1.2.

Multi-view image-based 3D reconstructions were conducted with Agisoft Metashape Professional (AMP) 1.5.1 and with 3DFlow Zephyr Aerial (FZA) 4.519. Both software is based on Structure-from-Motion (SfM), and Multiple-View-Stereo (MVS) approaches. AMP employs scale-invariant feature transform (SIFT)-like detection and description, then calculates approximate relative camera location and uses Global bundle adjustment to refine them, a type of MVS disparity calculation for dense reconstruction and Screened Poisson surface reconstruction. FZA employs a modified Difference-of-Gaussian (DoG) detector, a combination of Approximate Nearest Neighbor Searching, M-estimator Sample Consensus, and Geometric Robust Information Criterion for matching, then hierarchical SfM and Incremental adjustment, dense MVS reconstruction with fast visibility integration, tight disparity bounding and finally meshing with an edge-preserving algorithmic approach was selected to differentiate from AMP. To be able to compare the performance between the two different algorithmic implementations with NIR datasets, it was attempted to employ similar photogrammetric reconstruction parameters inside both software, when applicable.

Metrical comparisons and manipulation of the final textured models were performed with the open-source software Cloud Compare. Segmentation of the NIR

textured models to create 3D thematic mapping was performed in free and open-source software MeshLab. Finally, the 3D visualizations were realized in the free software Cloud Compare. All image-based processing was performed with the same laptop, with a Hexa-core Intel i7-8750H CPU at 2.2 GHz (Max 4.1 GHz), 32 GB RAM, and an NVIDIA GeForce RTX2070 GPU.

5.5.1.2   Application

The dense capturing of the images was planned according to the software manuals and considering relevant works with similar algorithmic implementations. Rigid imagery datasets were acquired for both case studies, with large overlaps (over 80%) from close ranges (Figure 5.31). The internal and external capturing parameters were maintained constant, as well as the ground sampling distances (GSD) between the NIR and VIS spectra, to increase the comparability of the final 3D models. In this way, both the metric evaluations and the assessment of SfM/DMVR-based reconstruction performance from NIR images were facilitated.
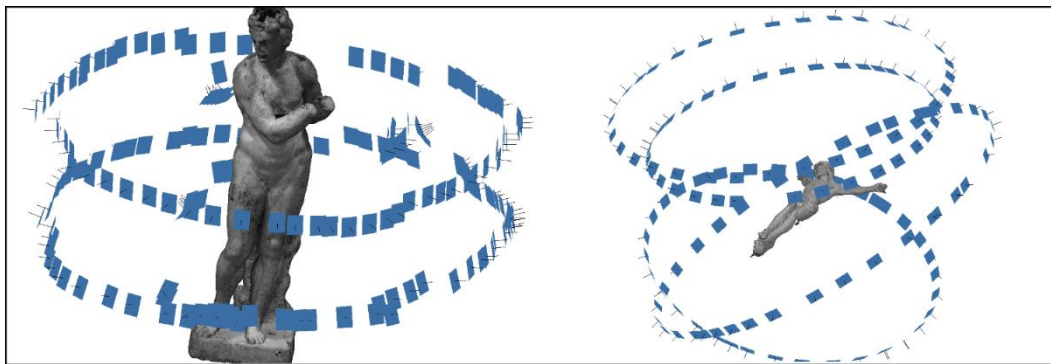
Figure 5.31. Image capturing scenarios; statue from the Fountain of Hercules (left) and small stone sculpture of Christ Crucified (right)

Low ISO values were used to prevent sensor luminance noise, simultaneously maintaining the exposure durations under the clipping limit value. The images were captured in Canon's raw image format (.cr2) to avoid the loss of valuable intensity data. In both spectra, datasets of 180 and 142 images were selected for each object. The capturing conditions used to collect the datasets are summarized in Table 5.26. It should be highlighted that artificial lighting was not used for the first case study, as it resulted in extremely variable light conditions. The image acquisition was complex due to the geometry of the sculpture and the non-uniform illumination by various light sources inside the conservation labs where it was hosted. Also, it was impossible to implement the same camera positions for VIS and NIR imaging, but a constant distance from the object was marked and maintained, and similar angles between each position were kept. For the case study of the Crist Crucified sculpture, a ring flash was used to eliminate all shadows in a more controlled environment. The images of different spectra were captured from the same positions. Additionally, for this case study, a turntable was utilized during acquisition. The

object was rotated four times to capture different but overlapping sides. Scaling for the first case study was performed using an invar scale bar of 1.000165m (±15 nm). Additionally, small paper targets were placed at the base and the body of the marble statue to assist the orientation between the 3D models. The scaling of the second case study was performed by using as reference the measured dimensions of the wooden cross (precision of measuring ±0.25 mm)

Table 5.26 Characteristics of the imagery datasets

Case study	f [mm]	Distance [cm]	GSD [mm]	Spectrum	f-stop	Exposure [s]	ISO
1	18.0	98	0.22	VIS	f/11	1/2	200
1	18.0	98	0.22	NIR	f/11	5	200
2	18.0	38	0.09	VIS	f/16	1/15	100
2	18.0	38	0.09	NIR	f/16	1/15	100

Before processing, raw VIS images of the marble statue were digitally manipulated to soften the highlights and the shadows, as this was later resulting in high surface noise on the 3D models, paying attention to not eliminating the surface features useful for image-based modeling. NIR images were exported in a single-band format. In addition to that, all the implemented images were masked accordingly in both software, to exclude the unwanted areas of each scene, and out-of-focus areas, to increase the quality of imagery, therefore reducing noise levels and processing times.

Multi-view image reconstructions with NIR and VIS imagery followed a standard semi-automatic SfM/DMVR pipeline, similar in both software despite the significant differences in algorithmic implementations. Similar reconstruction parameters were used between them, regarding volumes and quality of processing outputs (max. of 10M triangles for the meshes). The 3D models were constructed in a four-step procedure. The first step referred to the sparse reconstruction of each object, with a concurrent estimated calculation of the cameras' relative orientation, and autocalibration with SfM approaches. For this step, the chosen accuracy and density parameters were the highest available in both software. According to re-projection errors, the sparse point clouds were filtered from noise and local cluster distances with statistical filtering. For the second step, results were densified by employing MVS stereo-matching algorithms. The third step comprised of meshing the dense point clouds into triangular surfaces (Delaunay algorithm). The generated meshes were subsequently cleaned from small unconnected components and spikes. The final step involved the application of texture mapping to acquire single-file high-resolution textures from the original images. Given the high quality of original imagery, color balancing and blending between images were constrained significantly to reduce the possibility of radiometric errors. When choosing the resolution of textures, sampling distances were considered to be at least two or three times higher than the original pixel sizes. Between each stage of the reconstructions,

thorough visual checks were performed to determine quality, and then denoizing procedures were followed, identically for all the produced dense results, not to reduce comparability.

The 3D mapping was accomplished with two alternative procedures to enhance NIR modeling results toward an accurate visualization of the surface pathology. It was performed based on the hypothesis that the NIR reflectance intensities corresponded to the level of weathering since it was discovered that the natural patina of the stone was mostly invisible in the near-infrared spectrum and that the dominant deterioration pattern for both case studies was biological, while no physical damages were observable.

The first 3D mapping approach was to assume that the reflectance intensities were already a precise, detailed representation of the weathering levels. Although to increase interpretability, NIR textures were reduced to 3-bit grayscale. In this way, pseudocolored mappings of the levels of weathering were generated, which were then re-projected onto the final meshes.

For the second 3D mapping approach, after exhaustive tests to decide the optimal number of levels of deterioration that should be visualized, the 3D NIR textured models were ultimately classified according to 6 distinct classes/levels of weathering. The number of thematic mapping classes was selected to make more interpretable the distinguishably different levels of weathering between the case studies and the not so distinct levels of weathering for each case study separately. The created thematic layers corresponded to levels of surface decay ranging from low (almost healthy stone) to very high (substantial surface biodeterioration and thick deposits). In order to apply this type of mapping, intensity information was transferred from the single-image textures to the triangles of the meshes and then used the colorized mesh to perform segmentation based on the color. Subsequently, the respective 3D sub-models were colored with different hues, and the surface areas were calculated. For better visualization results, artificial lighting according to the normals of the 3D meshes was also applied.

5.5.1.3   Results and Discussion

In order to thoroughly assess the image-based modeling results, their densities, reconstruction errors, and processing durations were recorded in detail for both software. The photogrammetric results are presented in Table 5.27. In addition, the preservation of surface detail on the final 3D models and the levels of generated noise were also assessed.

Table 5.27 Image-based reconstruction results

	Statue from the fountain of Hercules				Sculpture of Crist Crucified			
	VIS AMP	NIR AMP	VIS FZA	NIR FZA	VIS AMP	NIR AMP	VIS FZA	NIR FZA
Aligned images	180	180	176	180	142	142	70	140
Matching time	00:05:16	00:04:24	02:24:36	00:51:47	00:01:05	00:01:25	00:12:11	00:07:06
Alignment time	00:05:33	00:03:39	00:18:24	00:13:52	00:00:24	00:00:34	00:00:51	00:01:00
Tie points	454,192	426,852	258,384	177,250	89,440	53,780	35,861	42,321
Point projections	1,434,286	1,365,710	1,743,280	1,192,860	273,196	139,401	154,077	207,060
Reprojection errors	0.65	0.80	1.01	1.11	0.52	0.68	0.52	0.80
Densification time	01:43:36	02:17:14	02:06:24	03:09:11	00:23:10	00:24:13	00:55:20	02:31:58
Dense cloud points	14,676,050	15,719,040	5,580,119	4,916,655	2,058,186	2,033,498	4,210,383	4,343,056
Meshing time	00:08:35	00:09:07	00:05:23	00:03:50	00:01:23	00:01:34	00:02:30	00:05:40
Mesh vertices	5,000,615	5,000,615	3,693,700	3,244,014	2,424,234	2,355,906	2,312,486	2,316,916
Mesh triangles	10,000,000	10,000,000	7,375,384	6,473,051	4,845,581	4,707,857	4,604,754	4,623,336
Texturing time	00:10:29	00:10:43	00:24:37	00:13:20	00:09:25	00:06:05	00:18:25	00:08:57
Total processing time	02:13:29	02:45:07	05:19:24	04:32:00	00:35:27	00:33:51	01:29:17	02:54:41

Geometric comparisons were performed amongst the models derived from different software and spectra, computing Hausdorff distances between the vertices of the final meshes. This task was executed in Cloud Compare with the Cloud-to-Cloud tool, after using an Iterative Closest Point (ICP) algorithm to perform fine registration. Additionally, it was decided to compare with meshes produced with a STONEX F6 SR structured light scanner, which were down-sampled to match the density of the models produced with image-based techniques.

For the case study of the marble statue from the fountain of Hercules, image-based modeling resulted in full reconstructions of the object for both VIS and NIR datasets. Point clouds from both spectra were of similar volume, although FZA produced denser results than AMP. The re-projection errors of the reconstruction were also slightly higher for FZA. Despite the fact that the use of NIR images did not seem to influence the processing times, the NIR-produced meshes contained low levels of surface noise, concentrated in the areas where shadows could not be eliminated. It should be highlighted that NIR digitization resulted in the same level of surface detail preservation as VIS digitization (see Figure 5.32). Hausdorff distances between vertices of the final meshes for VIS and NIR reconstructions showed differences of 0.72 ± 0.58 mm for AMP and 0.73 ± 0.74 mm for FZA. In both cases, the differences with the mesh produced from the F6 SR scanner were in the range of 0.8 ± 0.7 mm. Textures were of the same quality. The NIR model finally selected for 3D mapping was the one from AMP because of the lower surface noise.

Figure 5.32 Photogrammetric models, statue from the Fountain of Hercules (from left to right): AMP VIS, AMP NIR, FZA VIS, FZA NIR

For the case study of the stone sculpture of Crist Crucified, FZA was not able to reconstruct the object from all images for the VIS scenario (images from two out of four circular capturing patterns were oriented), but the problem was overcome with NIR imagery. However, this cannot be attributed to the different features visible on the NIR images, but rather to the employed software's algorithmic implementations. In this case, all the scenarios produced dense results of similar volume. Similar processing times were observed for VIS and NIR modeling, and similar to the last case study, slightly higher reconstruction errors. Furthermore, there was significant observable surface noise in both NIR models, but the level of surface detail preserved was identical to the VIS ones (see Figure 5.33). Hausdorff distances between vertices of the final meshes for VIS and NIR reconstructions showed differences of 0.39 ± 0.25 mm for AMP and 0.29 ± 0.41 mm for FZA. Textures were of the same very high quality. The NIR mesh that was finally selected to apply 3D mapping was the one from AMP because of the visibly lower surface noise. In both cases, the distances between the photogrammetric models and the meshes produced from the F6 SR scanner ranged below 0.70 mm.
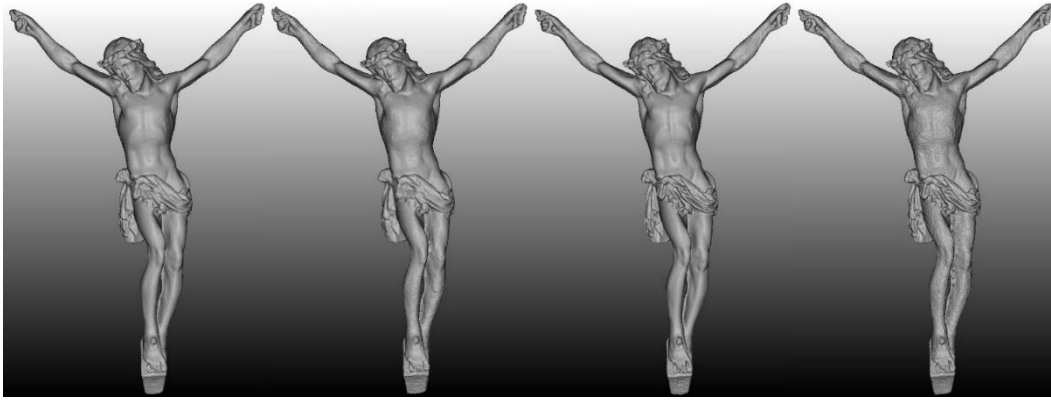
Figure 5.33 Photogrammetric models, sculpture of Crist Crucified (from left to right): AMP VIS, AMP NIR, FZA VIS, FZA NIR

As expected, the mapping results produced with the NIR models have a good correspondence with the real-life situation about the state of weathering. The suggested 3D image-based approaches are significantly more accurate than manual mapping by hand or by 2D CAD and GIS systems and allowed to map in three-dimensions details of up to sub-millimetric detail. They gave valuable first insight on the overall assessment of the surface weathering, which could not be achieved with a VIS textured model, because of the misinterpretations caused by the natural patina. The 3D segmentation performed on the models based on the NIR reflectance also allowed to record the area and percentage of each level of weathering and to compare the case studies involved (see Table 5.28).

Table 5.28 Areas of 3D surface weathering in comparison

Statue of Hercules			Sculpture of Christ	
Area (m^2)	Area (%)	Level of weathering (color)	Area (%)	Area (m^2)
0.048718	2.28	very-high (red)	0.00	0.000000
0.672628	31.41	high (orange)	0.00	0.000000
0.860497	40.19	medium-to-high (light orange)	1.15	0.003707
0.432027	20.18	medium (yellow)	5.27	0.017002
0.120743	5.64	medium-to-low (light green)	93.58	0.301840
0.006489	0.30	low (green)	0.00	0.000030

In the case of the application for the statue from the fountain of Hercules, and despite the problems created to 3D mapping by the remaining shadows in the occluded areas, the circular forms of the biodegradation patterns were easily distinguishable in both protected and unprotected areas of the surface. Notably, significant weathering is present at shallow cavities and cracks whose origin is either due to the construction techniques or because of physical damage induced over time. Extensive high levels of deterioration are evident on almost the entire surface of the statue (see Figure 5.34), as 73.88% of the surface was characterized by medium-to-high to very-high levels of deterioration according to our approach. Only 0.30 % was characterized by low levels of weathering. The observed high

levels of bio-decay can be largely attributed to the characteristics of the external environment where the marble statue was positioned. The proximity of the sculpture to a water fountain, in combination with rain and moisture, favors the action of biological agents, which was not the case for the second heritage object under study. For the first case study, the thematic 3D segmentation and visualization approach produced more comprehensive results than the direct use of the NIR reflectance values.

Fig. 5.34 Visualization of the levels of weathering for the statue of Hercules Fountain with high-resolution NIR texture (left), 3-bit NIR texture (center) and 3D thematic mapping after segmentation of the 3D model (right)

Unlike the previous example, 3D mapping after segmentation of the small sculpture of Christ Crucified showed relatively low levels of deterioration on the surface (see Figure 5.35), as 93.58% of the total surface classified as medium-to-low or low deteriorated according to our approach. This result can be supported by the fact that the object was preserved in much better surrounding conditions that statue from the Fountain of Hercules that was long exposed to high moisture conditions. Only 5.27% of the total surface was classified as medium deteriorated and 1.15% as medium-to-high; these areas were concentrated on cavities around

the hair, thorny wreath, and chest. For this case study, the visualization with the reduced NIR texture provided more comprehensive results towards the assessment of the state of preservation.
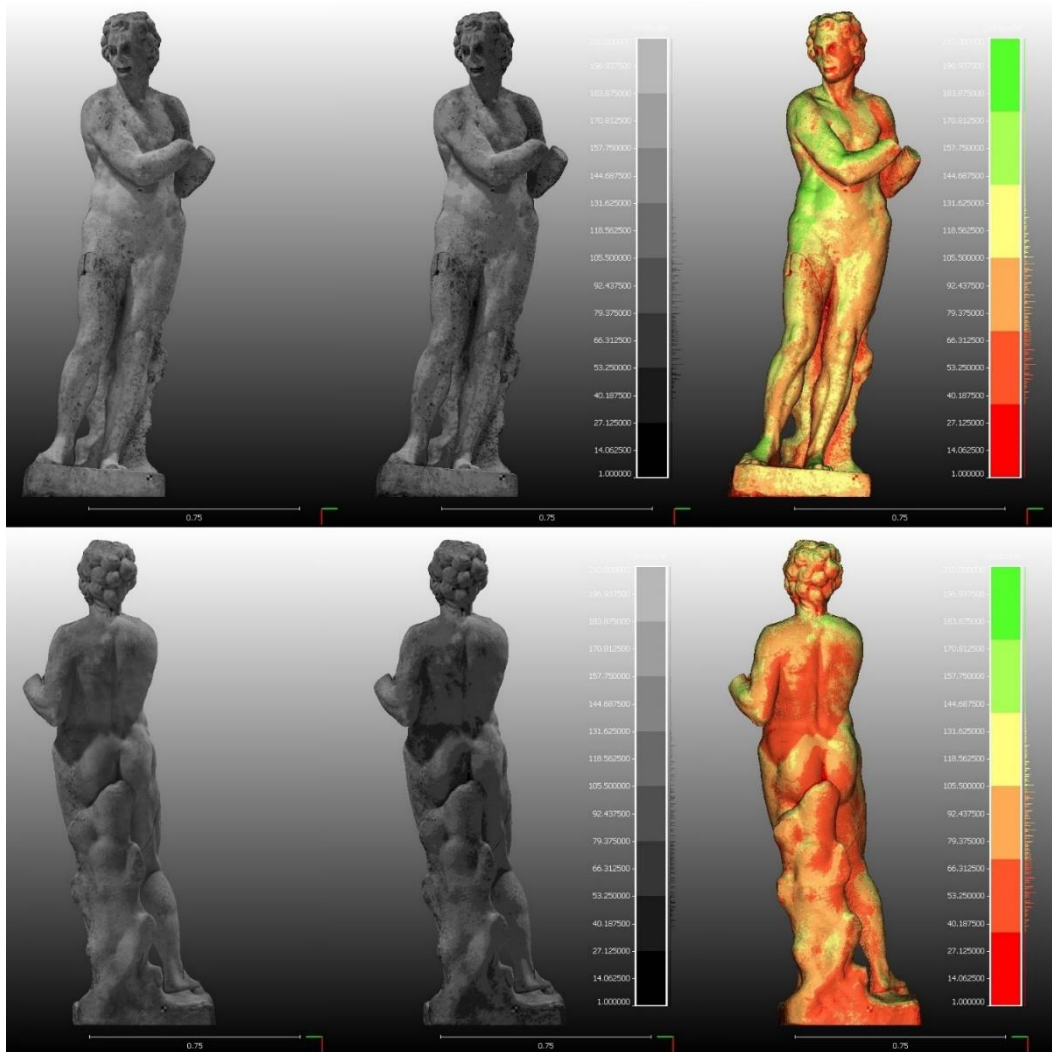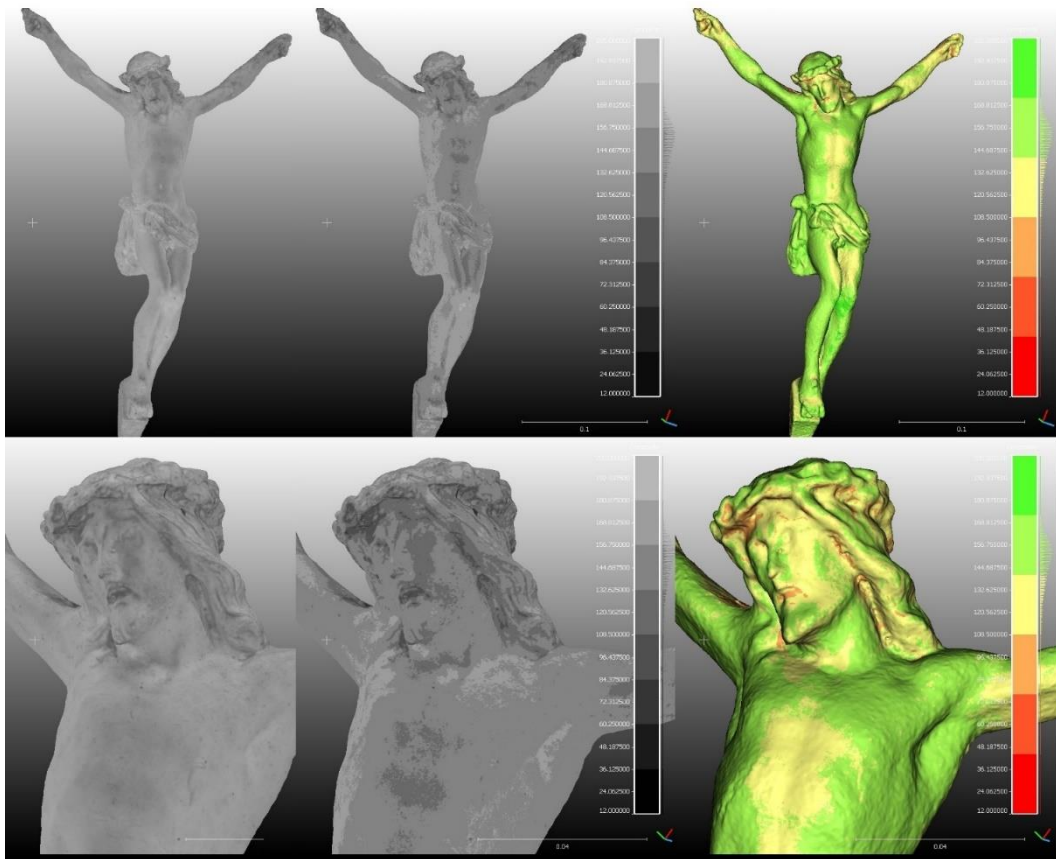

Fig. 5.35 Visualization of the levels of weathering for the sculpture of Christ Crucified with high-resolution NIR texture (left), 3-bit NIR texture (center) and 3D thematic mapping after segmentation of the 3D model (right)

5.5.2 Wooden Sculptures

This case study combined near-infrared reflectance and ultraviolet fluorescence (UVF) photography performed with modified camera sensors, IBM, and triangulation scanning. The objective was to explore the direct implementation of multiband 3D photogrammetric modeling, the optimal integration among the techniques, and the metric validity of application for objects of archaeological significance. Towards this direction, NIR and UVF 3D models of a wooden sculpture were produced, utilizing various algorithmic implementations to process the spectral image datasets. Additional experimentation with VIS reflectance datasets assisted the evaluation.

5.5.2.1   Materials and Methods

To evaluate the suggested multiband 3D modeling approach, an Egyptian wooden sculpture dating back to the New Kingdom (1550–1069 B.C.E.) was used as a case

study, which belongs to the Egyptian Museum of Turin (Inventory Number Cat. 745). The Cat. 745 statuette represents Hapy, god of the Nile flood, or a more generic fecundity figure.

Two Nikon Xnite D810 DSLR cameras were used, one unmodified for VIS imaging, and one modified with a Hoya Infrared filter (R72) suitable for detecting electromagnetic radiation in the range 780-950 nm and coupled with a PECA 916 filter for UVF.

For color and NIR imaging, the lighting was produced with 2 Ianiro Varibeam Halogen 800W lamps positioned left and right of the object (looking at it) with an of 30 ° with respect to the surface. Image datasets could not include the same orientations because different cameras were used for VIS and NIR. An x·rite ColorChecker® Classic with 24 colors was used as a color and scale reference. The camera was fixed on a customized metallic structure to ensure stabilization. A remote controller was used for focusing to reduce micro-movements and micro-blur effect during capturing. The ISO was set to 100 to minimize noise, exposure to 1.6 sec, and f-number to f/16 for the needed DoF. The resulting VIS DoF was 0.44 m, and thus the focusing area was placed on the main body of the statue for the vertical images and for the horizontal close-ups on the closest plane. The DoF for the NIR images was significantly smaller while keeping the same capturing distance, and images were topically not as sharp as VIS images. The white circle area was an effect of the lenses used, and therefore image coverage of the object was chosen to avoid overlapping of the white circle on NIR images with the object. Images were exported in 100% quality JPEG format at original dimensions. From each dataset, a final selection of 100 images was made.

The UV lighting was realized with 2 Labino® UV spot lamps with UV light MPXL and UV FLOODLIGHT with the following characteristics: emission peak at 365 nm wavelength, approximate distribution angle of 3.5°, and irradiation 4500 μW/cm2 at 38 cm away from the surface. The UV light was induced in a room with no visible light leaks. The camera was again fixed on a customized metallic structure to ensure stabilization. For every image, after the turntable was turned a fixed number of degrees and the automatic focusing was performed, the visible light sources were turned off, and the statue was "painted" by UV light by moving the UV sources in order to cover entirely the side of the object captured by the camera, as the statue's dimensions did not allow it to be fully illuminated at all times. ISO was set to 100 to minimize noise, exposure to 10 sec, and f-number to f/16 for the needed DoF. Images were exported in 100% quality JPEG format at original dimensions. In Adobe Lightroom, the temperature was pushed to 15000 °K to avoid remaining leaks of the blue spectrum.
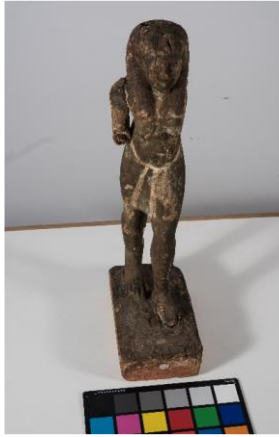
visible reflectance image, Nikon D800E

Near infrared reflectance image, Nikon D810 + Hoya R72 filter

Ultraviolet fluorescence image, Nikon D810 + PECA 916 filter

Figure 5.36. Images of the wooden statuette.

Multi-view image reconstructions with VIS, NIR, and UVF images followed a standard semi-automatic SfM/DMVR pipeline. Agisoft Metashape Pro (AMP), 3DFlow Zephyr Aerial (FZA), Autodesk Recap Photo (ARP), and a workflow combining VSfM, CMVS, and MeshLab (VCM)

5.5.2.2 Application

Tables 5.29–5.32 report on the photogrammetric application. A dataset that included both VIS and NIR images was also considered to check if the reconstruction would improve.

Table 5.29. Image-based modeling with visible reflectance images.

	VSfM+CMVS+MeshLab	Agisoft Metashape Pro	3DFlow Zephyr Aerial	Autodesk Recap Photo
PARAMETERS				
Matching+Alignment				
Keypoint density		high	high	
Pair preselection		generic	circular	
Key point limit		50,000	high	
Tie point density		5,000	5,000	
Camera model fitting		adaptive	adaptive	
Dense Matching				
Masks/Annotations		yes	yes	
Point density		high	high	
Depth filtering		moderate	default	
Mesh Generation				
Max number of faces		5,000,000	5,000,000	
Interpolation		disabled		
Texture Generation				
Max octree depth	14	-	14	
Texture size	8,192	8,192	8,192	
Color balancing	enabled	enabled	default	
RESULTS				
Sparse Cloud				
Images Aligned	100/100	100/100	100/100	100/100
Matching time	0:01:21	0:06:19	0:03:02	
Alignment time	0:01:01	0:00:05	0:12:29	
Tie points	26,978	41,416	64,784	
Projections	129,007	197,154	433,168	
Repr. error [pixels]		0.542	0.873	
Ground-res [mm/pix]		0.093	0.094	
Dense Cloud				
Processing time	0:25:17	0:40:39	01:25:54	
Point count	3,917,997	8,718,541	2,813,797	605,118
Mesh				
Processing time		00:02:42	00:00:38	
Face count		4,940,090	5,582,910	1,117,071
Quality		high	very high	high
Texture				
Processing time		00:14:46	00:13:21	
Quality		very high	very high	very high
Total processing time	0:27:39	1:04:31	1:55:24	04:05:00

Table 5.30. Image-based modeling with near-infrared reflectance images.

	VSfM+CMVS+MeshLab	Agisoft Metashape Pro	3DFlow Zephyr Aerial	Autodesk Recap Photo
PARAMETERS				
Matching+Alignment				
Keypoint density		high	high	
Pair preselection		generic	circular	
Key point limit		50,000	high	
Tie point density		5,000	5,000	
Camera model fitting		adaptive	adaptive	
Dense Matching				
Masks/Annotations		yes	yes	
Point density		high	high	
Depth filtering		moderate	default	
Mesh Generation				
Max number of faces		5,000,000	5,000,000	
Interpolation		disabled		
Texture Generation				
Max octree depth	14	-	14	
Texture size	8,192	8,192	8,192	
Color balancing	enabled	enabled	default	
RESULTS				
Sparse Cloud				
Images Aligned	100/100	100/100	99/100	100/100
Matching time	0:01:13	0:05:50	0:03:24	
Alignment time	0:01:01	0:00:12	0:12:27	
Tie points	21,760	63,440	71,321	
Projections	111,397	295,319	478,838	
repr. error [pixels]		0.630	0.843	
Ground-res [mm/pix]		0.097	0.097	
Dense Cloud				
Processing time	0:26:39	0:46:43	01:21:00	
Point count	3,758,790	7,995,464	2,053,831	504,853
Mesh				
Processing time		00:04:30	00:00:26	
Face count		5,000,000	4,065,162	925,900
Quality		high	high	high
Texture				
Processing time		00:31:02	00:09:24	
Quality		very high	very high	very high
Total processing time	0:28:53	1:28:17	1:46:41	3:00:00

Table 5.31. Image-based modeling with visible and near-infrared reflectance images.

	VSfM+CMVS+MeshLab	Agisoft Metashape Pro	3DFlow Zephyr Aerial	Autodesk Recap Photo
PARAMETERS				
Matching+Alignment				
Keypoint density		high	high	
Pair preselection		generic	circular	
Key point limit		50,000	high	
Tie point density		5,000	5,000	
Camera model fitting		adaptive	adaptive	
Dense Matching				
Masks/Annotations		yes	yes	
Point density		high	high	
Depth filtering		moderate	default	
Mesh Generation				
Max number of faces		5,000,000	5,000,000	
Interpolation		disabled		
Texture Generation				
Max octree depth	14	-	14	
Texture size	8,192	8,192	8,192	
Color balancing	enabled	enabled	default	
RESULTS				
Sparse Cloud				
Images Aligned	100/100 (50+50)	100/100 (50+50)	94/100 (50+44)	100/100 (50+50)
Matching time	0:01:07	0:03:55	0:03:04	
Alignment time	0:00:55	0:00:10	0:13:44	
Tie points	22,456	79,490	76,327	
Projections	87,157	271,061	337,515	
repr. error [pixels]		0.593	0.881	
Ground-res [mm/pix]		0.098	0.096	
Dense Cloud				
Processing time	0:33:50	0:37:58	01:24:47	
Point count	3,990,793	8,433,079	2,503,588	586,196
Mesh				
Processing time		0:02:43	00:00:34	
Face count		4,984,640	4,988,565	1,076,754
Quality		high	high	high
Texture				
Processing time		0:48:01	00:08:26	
Quality		very high	very high	very high
Total processing time	0:35:52	1:32:47	1:50:35	3:35:00

Table 5.32. Image-based modeling with ultraviolet fluorescence images.

	VSfM+CMVS+MeshLab	Agisoft Metashape Pro	3DFlow Zephyr Aerial	Autodesk Recap Photo
PARAMETERS				
Matching+Alignment				
Keypoint density		high	high	
Pair preselection		generic	circular	
Key point limit		50,000	high	
Tie point density		5,000	5,000	
Camera model fitting		adaptive	adaptive	
Dense Matching				
Masks/Annotations		yes	yes	
Point density		high	high	
Depth filtering		moderate	default	
Mesh Generation				
Max number of faces		5,000,000	5,000,000	
Interpolation		disabled		
Texture Generation				
Max octree depth	14	-	14	
Texture size	8,192	8,192	8,192	
Color balancing	enabled	enabled	default	
RESULTS				
Sparse Cloud				
Images Aligned	40/40	40/40	31/40	40/40
Matching time	0:00:12	0:00:30	0:01:04	
Alignment time	0:00:32	0:00:03	0:13:51	
Tie points	8,032	55,617	27,071	
Projections	23,660	151,632	109,758	
RMS repr. error		0.575	0.790	
Ground-res [mm/pix]		0.099	0.097	
Dense Cloud				
Processing time	0:10:55	0:05:43	00:27:57	
Point count	1,641,267	7,723,984	2,470,189	566,730
Mesh				
Processing time		00:02:40	00:00:20	
Face count		5,120,180	493,907	1,024,035
Quality		high	medium	high
Texture				
Processing time		00:05:38	00:06:25	
Quality		high	high	high
Total process. time	0:11:39	0:14:34	0:49:37	0:50:00

5.5.2.3 Results and Discussion

All three commercial software produced similar results in terms of visual fidelity, with FZA producing slightly higher surface detail. The software produced very different volumes of results with relatively comparable total processing times. All meshes and textures produced were high-resolution, and even the UVF 3D model was efficiently similar to the others, despite the availability of a much smaller dataset. Point clouds produced with CMVS could not be cleaned from noize.

Mean distances between software remained ≤0.25 mm and ≤0.75 mm RMS, except for RMS of the Hausdorff distances for the UVF spectral meshes (Table 5.32), proving the difficulty of the contemporary SfM/DMVR-approach based software to directly 3D reconstruct scenes from ultraviolet images comparing to true color images.

Table 5.33. Mean/RMS Hausdorff distances [mm] between photogrammetric meshes—comparison of reconstruction with different software.

	VCM-AMP	VCM-FZA	VCM-ARP	AMP-FZA	AMP-ARP	FZA-ARP
UVF	0.07/1.02	0.19/1.34	0.25/1.22	0.10/0.71	0.20/1.54	0.16/1.64
VIS	0.00/0.30	0.01/0.31	0.04/0.45	0.01/0.37	0.02/0.28	0.05/0.30
VIS&NIR	0.02/0.36	0.06/0.54	0.05/0.63	0.01/0.37	0.03/0.36	0.03/0.35
NIR	0.07/0.62	0.14/0.66	0.25/0.69	0.03/0.37	0.02/0.40	0.08/0.30

Mean distances between datasets remained ≤0.30 mm and ≤0.60 mm RMS highlighting how similar the results from direct 3D modeling from UV, VIS, and NIR spectra can be with optimal photo-acquisition conditions (Table 5.34). The highest distances were observed for the free VSfM-CMVS-Meshlab processing pipeline because not all noise could be removed.

Table 5.34. Mean/RMS Hausdorff distances [mm] between photogrammetric meshes—comparison of reconstruction from different datasets.

	VIS-VIS&NIR	VIS-NIR	UVF-VIS	UVF-NIR
VCM	0.27/0.24	0.24/0.37	0.25/0.25	0.27/0.51
AMP	0.05/0.22	0.08/0.28	0.05/0.58	0.01/0.60
FZA	0.05/0.20	0.03/0.30	0.02/0.48	0.00/0.36
ARP	0.01/0.21	0.01/0.23	0.02/0.27	0.01/0.29

Scanning of the wooden statuette was performed with two scanners implementing different technologies:

a. Handheld scanner STONEX F6

›   Measurement method: structured infrared light

› XY point density: 5 mrad (2.5 mm at min distance)

› Distance Range: 0.5-4.0 m, Scan Range: 0.5-7.0 m

› Accuracy XYZ: ±0.1%-0.2% (approximately 1mm at 0.5 m distance), Precision: Up to 0.5 mm at a range of ≤1 m

› Acquisition duration: 4 mins (1,005 frames)

› Workflow performed in Mantis Vision – Echo software after recording: (1) Sequential Registration and Global registration; (2) Noise removal: Moving Least Squares (r = 40) + Statistical Outlier Removal (outlier coeff = 4); (3)Spawn mesh

The final mesh was produced in Geomagic Wrap after the removal of unwanted parts. The mesh had 10,300 triangles (not including the bottom of the base). No extra post-processing was required to remove noise or fill holes.

b. Non-contact digitizer VIVID 9i - Konica Minolta

› Measurement method: triangulation

› Light-Receiver lens: MIDDLE: Focal distance f = 14 mm

› Distance Range: 0.5-2.5 m, Scan Range: 0.5-1.0 m

› Accuracy XYZ: ± 0.20 mm at 1 m distance, Precision (Z, σ): 0.048 mm

› Acquisition duration: approximately 1.5 hrs

Four individual scans were performed, 2 with the statuette standing and 2 in a horizontal position. Each scan consisted of up to 15 separate scenes that were oriented inside the sub-scans' projects upon acquisition, using three manually selected common points with each time the previous scene was captured. This pre-registration was executed inside the 'Polygon Editing Tool' software accompanying the scanner. For every scene, the scanner was repositioned, and auto-focusing was implemented again. After each scan was completed, the mesh results were exported for each scene separately in a .vvd file format. The final mesh produced in Geomagic Wrap after the manual alignment and global registration of the separate scenes, removal of duplicate faces, and closing of the holes, had 1,790 thousand triangles. The distance between the produced point clouds from structured-light and triangulation scanning was mean 0.64 mm and RMS 0.90 mm.

Considering as ground truth the mesh produced by the VIVID 9i triangulation scanner, as more precise and more accurate than the handheld laser scanner model, metric assessments were performed to ascertain the validity of direct 3D modeling with the multi-spectral data on the Egyptian statuette, by carrying out Hausdorff distance tests between the 3D models (Table 5.35).

Table 5.35. Mean/RMS Hausdorff distances [mm] between spectral photogrammetric models and Konica Minolta mesh.

	AMP	FZA	ARP	
VIS	0.03/0.36	0.02/0.34	0.05/0.40	VIS
VIS-NIR	0.01/0.43	0.02/0.30	0.06/0.50	VIS-NIR
NIR	0.07/0.40	0.03/0.40	0.07/0.50	NIR
UV	0.07/0.48	0.03/0.30	0.03/0.61	UV

In all cases, more than 95% of the sampled vertices and faces were closer than 0.6 mm from the ground truth model, where 0.6 was the expected accuracy, meaning 2-3 times the 0.2 mm accuracy of the VIVID 9i. Conclusively, all spectral and multi-spectral datasets were deemed sufficient for the direct modeling approach. Figures 5.37–5.39 present comparisons between the photogrammetric models.
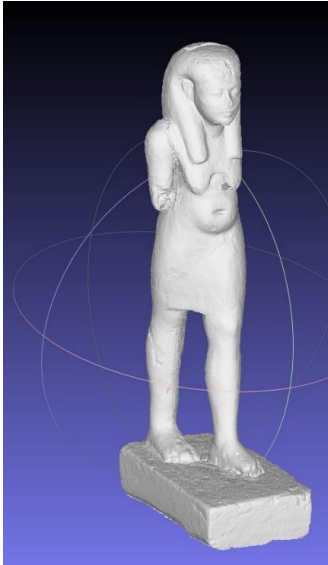
statuette 3D mesh produced from Visible spectrum images with AMP – front side

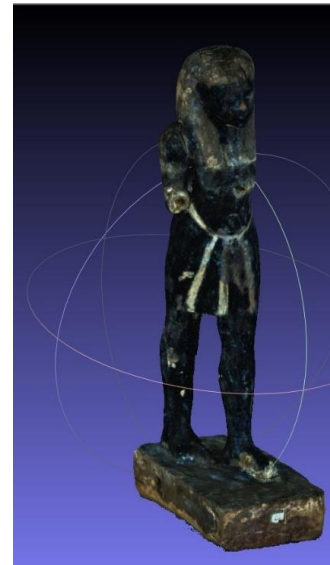*statuette 3D mesh produced from Near-Infrared spectrum images with AMP – front side*
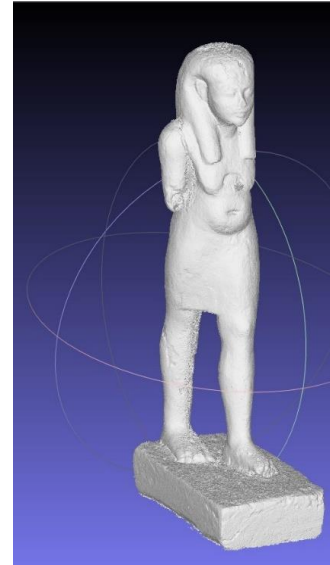
statuette 3D mesh produced from Ultra-Violet spectrum images with AMP – front side
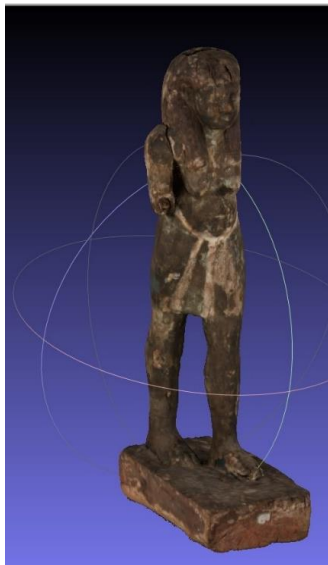
statuette 3D textured mesh produced from Visible spectrum images with AMP – front side
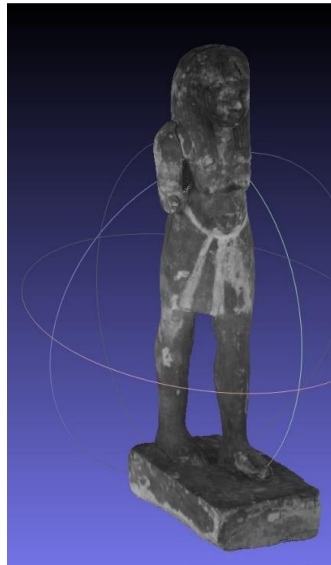
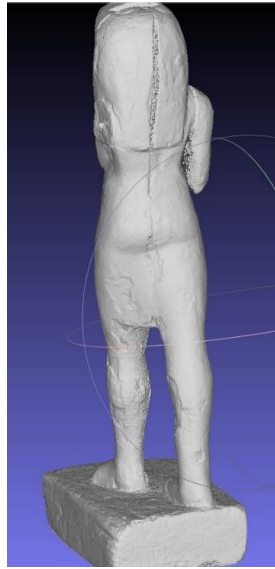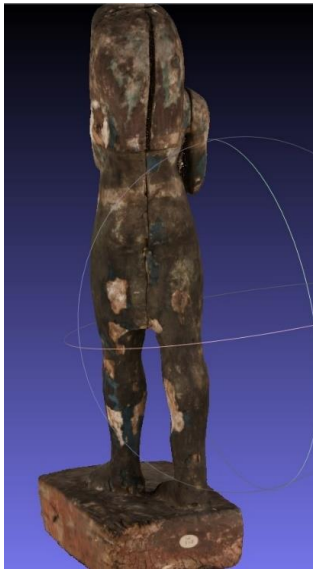*statuette 3D textured mesh produced from Near-Infrared spectrum images with AMP – front side*

statuette 3D textured mesh produced from Ultra-Violet spectrum images with AMP – front side

Figure 5.37. Comparison of color, near-infrared reflectance, and ultraviolet fluorescence models for the Egyptian statuette—front side.

statuette 3D mesh produced from Visible spectrum images with AMP – back side

statuette 3D mesh produced from Near-Infrared spectrum images with AMP – back side
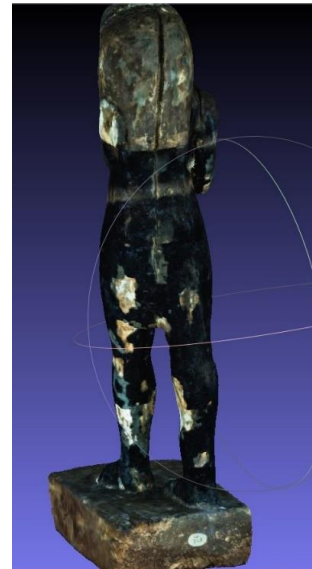
statuette 3D mesh produced from Ultra-Violet spectrum images with AMP – back side

statuette 3D textured mesh produced from Visible spectrum images with AMP – back side
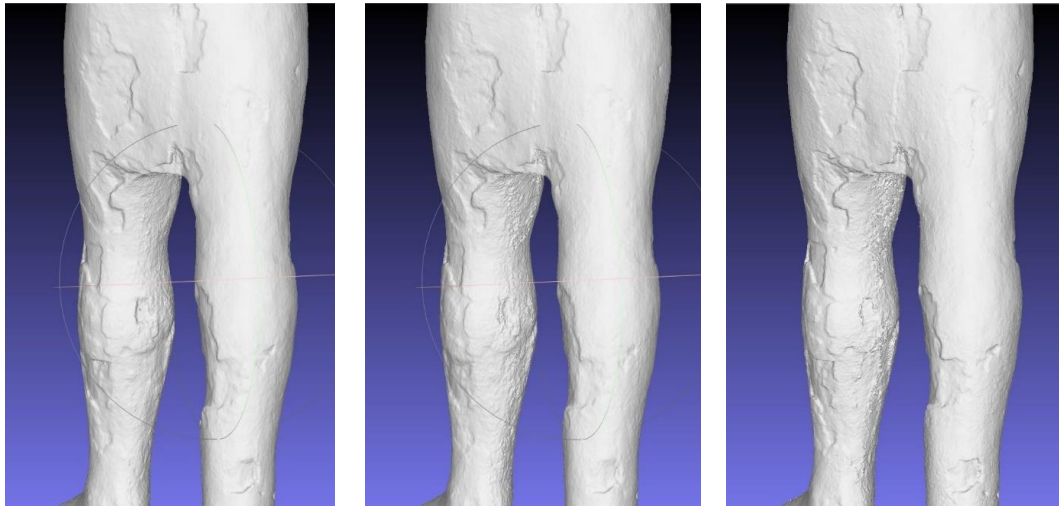
statuette 3D textured mesh produced from Near-Infrared spectrum images with AMP – back side

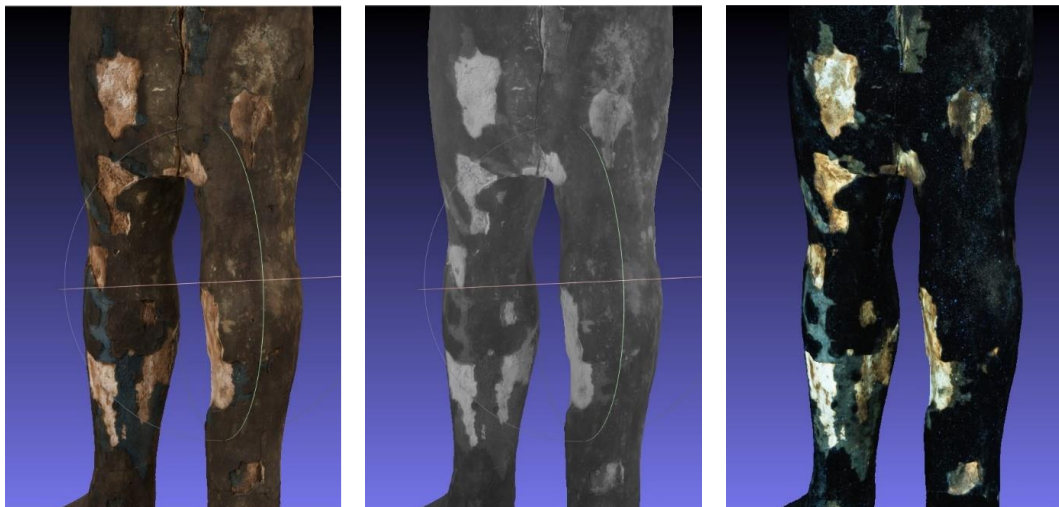*statuette 3D textured mesh produced from Ultra-Violet spectrum images with AMP – back side*

Figure 5.38. Comparison of color, near-infrared reflectance, and ultraviolet fluorescence models for the Egyptian statuette—back side.

statuette 3D mesh produced from Visible spectrum images with AMP – detail

statuette 3D mesh produced from Near-Infrared spectrum images with AMP – detail

statuette 3D mesh produced from Ultra-Violet spectrum images with AMP – detail

statuette 3D textured mesh produced from Visible spectrum images with AMP – detail

statuette 3D textured mesh produced from Near-Infrared spectrum images with AMP – detail

statuette 3D textured mesh produced from Ultra-Violet spectrum images with AMP – detail

Figure 5.39. Comparison of color, near-infrared reflectance, and ultraviolet fluorescence models for the Egyptian statuette—back side detail.

In the context of this case study, the conclusion was that the only useful level of integration for similar archaeological objects would be the fast generation of a 3D mesh via triangulation scanning, and the production of different texture files through photogrammetric processing from reflectance and fluorescence images at various spectra.

5.5.3 Castello Del Valentino

The *Castello del Valentino* is a suburban mansion and riverside royal residence already existing in the sixteenth century when it was bought by Emanuele Filiberto di Savoia. It belongs to the site "Residences of Royal House of Savoy", inscribed in the UNESCO World Heritage List in 1997. The castle is located on the left bank of river Po in Turin (Piedmont region, Italy). The castle has been subjected to numerous extensions, alterations, transformations, and restoration works throughout the last centuries. The overall condition of the front (west) façade (figure 5.40) is visibly better conserved compared with the riverside (east) façade (figure 5.41), where several altered surfaces are visible predominantly in the lower parts of the façade, which can be partly attributed to the effects of moisture.
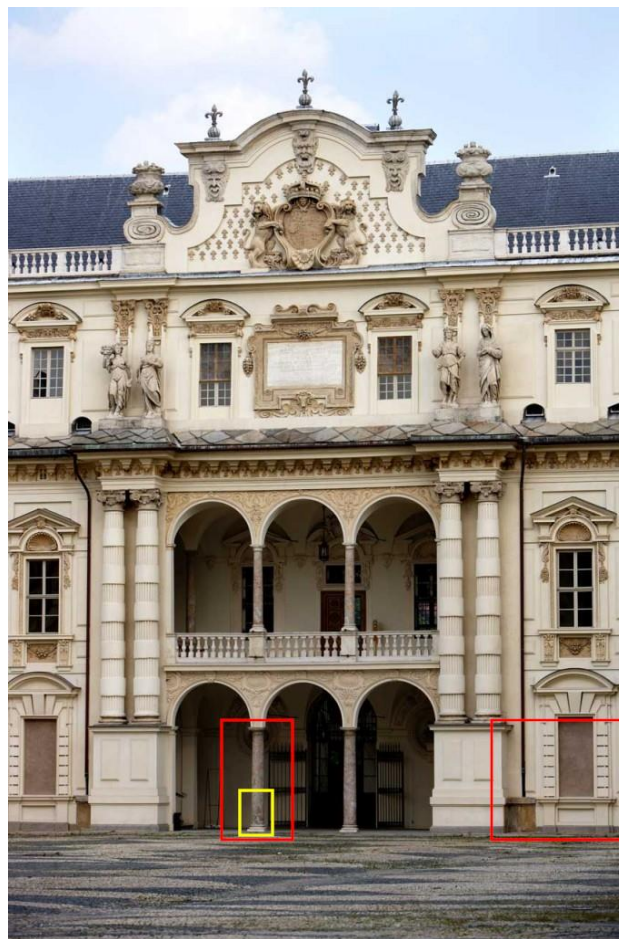

Figure 5.40. *Castello del Valentino* main (west) façade (modified from https://castellodelvalentino.polito.it). The preliminary surveys are indicated in red, and the detailed surveys in yellow color.

Figure 5.41. *Castello del Valentino* riverside (east) façade. The preliminary surveys are indicated in red and the detailed surveys in yellow color.

5.5.3.1 Materials and Methods

As explained earlier in this chapter**,** the integrated documentation considers the acquisition of multidisciplinary data collected with a multi-sensor and multiwavelength approach. The recorded data are summarized in Figure **5.42.**
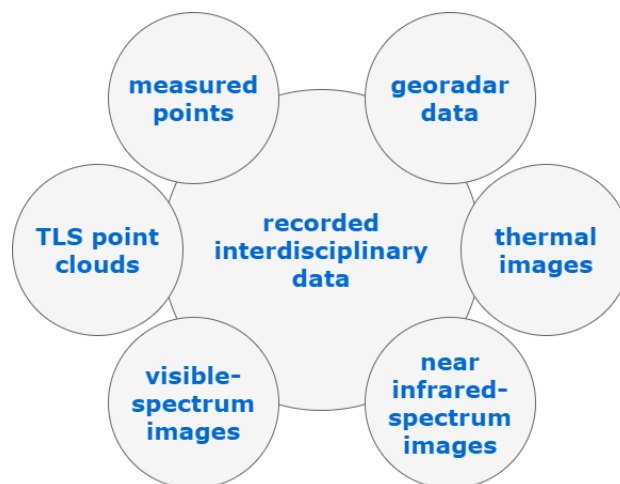

Figure 5.42. Scheme of recorded data.

Topographic measurements were performed with the GeoMax Zoom PRO 3″ reflectorless total station. The TLS surveys were carried out with the FARO Focus3D X 330 phase-shift scanner. The camera used for VIS and NIR reflectance imaging was the Canon EOS Rebel SL1. A Canon EF-S 18–55 mm f/3.5–5.6 IS II lens was used to acquire all the optical images by attaching two external VIS and NIR-pass filters. The camera used for TIR imaging was the FLIR T1030sc. The system utilized for the ground-penetrating radar surveys was composed of an Aladdin 2-GHz IDS antenna box and an IDS K2 control unit.

5.5.3.2   Preliminary Surveys

The first phase of the surveys involved TLS range data acquisitions at the lower areas of the riverside façade and the main part of the east façade. The stations were placed to acquire homogeneously dense point clouds without occlusions, and thus two scans were performed on the east façade and six on the west, with large overlaps, which could facilitate accurate registration. The scans were used to generate general plans and low-resolution models of architectural surfaces after registering, denoising, and subsampling the 3D point clouds. Furthermore, the near-infrared scanning intensities were corrected and exploited to create rapidly and cost-efficiently a representation of weathering stages (figure 5.43), since the majority of the observed surface deterioration patterns belonged to a single typology—grey biogenic crusts.

The second phase referred to the preliminary recording of many architectural elements by multiband imaging. VIS and NIR images were collected as parallel as possible to the surfaces of interest—avoiding any large deformation—and from consistent positions. Each element was captured in a single image frame for this scenario, retaining homogeneous spatial resolution for all the acquired imagery at approximately 5 mm. Image quality was validated by calculating background noise and vignetting levels—systematic errors caused by camera electronics. Uncompressed raw image data were exported with the RawDigger software, and visible-spectrum images were color-balanced.
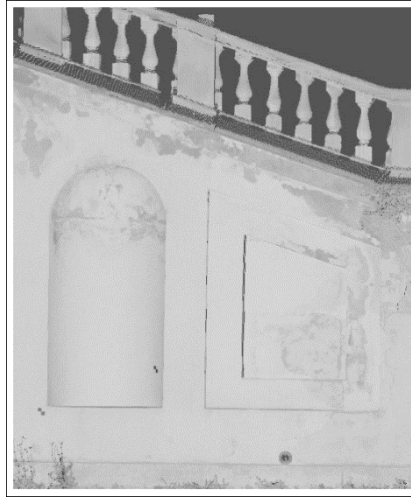
Figure 5.43. View of point-cloud pseudocolored with architectural surfaces' weathering indices (lower riverside façade)

Thermal-infrared images for preliminary recording were also collected as parallel as possible to the surfaces of interest, with approximately half the spatial resolution of the optical images, but capturing multiple images for every recorded element. Therefore, after applying the same temperature scales on the thermograms (ThermaCAM software), higher resolution TIR images were generated (same spatial resolution with optical imagery), by interpolating information from each quadruplet of images acquired at the same position.

All images were subsequently undistorted (utilizing parameters calculated by calibrating the involved sensors), then rectified by picking points that were either measured directly with the total station or indirectly by TLS, and finally merged with the HyperCube software to create multiband images. The multiband imaging data were analyzed by data reduction, decomposition, and compression methods to create 2D image visualizations that could be more easily interpretable. Figure 5.44 shows the results of one of the preliminarily surveyed areas on the main façade, where slight plaster detachments and a few surface cracks are visible through the elaboration of the multiband composites. Figure 5.45 shows another surveyed area on the riverside façade where extensive detachments, cracking, and biogenic crusts can be observed.
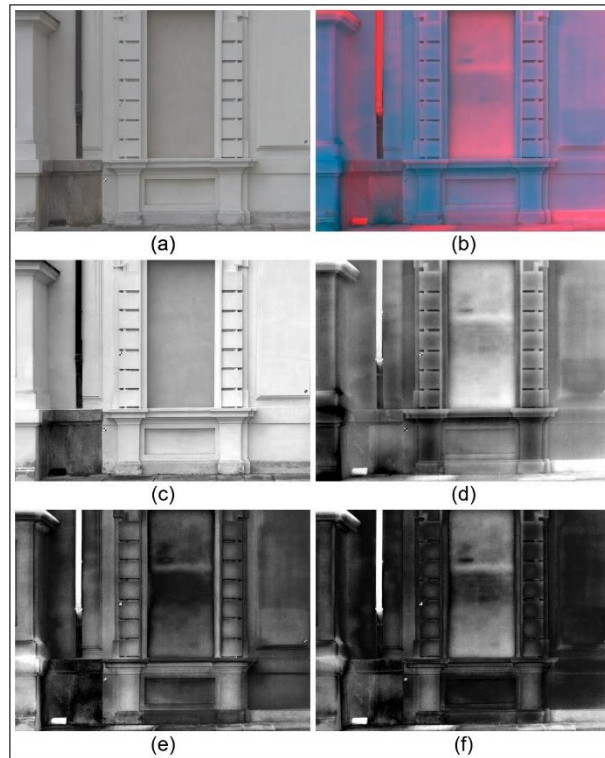
Figure 5.44. Castello del Valentino west façade multiband results: (a) cropped VIS image; (b) TIR-NIR-red false-color composite; (c,d) principal component analysis–first and second component; (e,f) Fourier transform.

Figure 5.45. Castello del Valentino riverside façade multiband results: (a) cropped VIS image; (b) TIR-NIR-red false-color composite; (c,d) principal component analysis–first and second component; (e) Fourier transform; (f) quantized image.

Wide-scale representations and 2D preliminary surveys led to identifying areas of interest for in-depth investigations by integrating higher resolution data and the elaborated GPR measurements. These two areas presented significant radiometric anomalies in the multiband analysis results (Figure 5.46).

Figure 5.46. East façade (left), and main façade left column (right) anomalies were observed by thermographic imaging and principal component analysis of the multiband data (first components).

5.5.3.3 Detailed Surveys

The areas identified to conduct further integrated documentation campaigns were a 0.6×3.8 m^2 planar surface on the lower riverside façade and the main façade's left column.

Imagery for photogrammetric processing was densely collected (> 80% bidirectional overlap) for both the planar and cylindrical geometries. For this scenario, a VIS and NIR spatial resolution of at most 1.5 mm was achieved to produce high-resolution mesh textures and orthophotos. Thermal images for high-resolution mesh texturing and ortho-mosaic production were also rigidly collected from a close range to match the optical imagery's spatial resolution as possible. The distances of photo shooting also considered the spatial resolution of the ground-penetrating radar. A standard semi-automated methodology based on structure-from-motion (SfM) and multi-view stereo (MVS) algorithms was followed in Agisoft Metashape with the EOS Rebel SL1 photos, using as reference measured coordinates of placed targets or points picked from the point clouds, achieving similar accuracy of approximately 5 mm for both spectra and surveyed areas. To tackle the problems of 3D modeling with the low-resolution thermal images, the hybrid photogrammetry-driven approach involving both optical and TIR images from the T1030sc was employed. The resulting accuracy was similar to that of the

high-resolution image datasets while maintaining a low noise level on the point clouds and models.

The GPR profiles were collected along horizontal profiles with a vertical spacing of 5 cm. In addition, the profiles followed a circular pattern for the column. A wheel encoder was used to track the positioning of the antenna along the moving direction for each GPR profile that was acquired. Each profile's starting and ending points were also measured with the total station to obtain the same reference as the photogrammetric data. The GPR data were processed with the ReflexW software, adopting standard processing steps. The obtained radargrams produced 3D amplitude 'point clouds' that could then be visualized and were also used for computing isosurfaces of specific amplitude values

The multi-sensor results were integrated using the orthoimage-mosaics of visible, NIR, and TIR spectra to create pseudo-colored ortho-visualizations, which could be processed with the same approaches as the preliminary surveys, but also had spatial reference. This elaboration allowed the relative referencing between radar data (parallel and perpendicular to recorded surfaces), range information, and the other image-based derivatives (Figures 5.47, 5.48). Additionally, the cylindrical surface of the column could be developed—after calculating the average diameter from the TLS point cloud—to create a planar result, instead of using only ortho-projections of every side of the column (Figure 5.49). This type of visualization made interpreting the results easier by facilitating better integration of photogrammetric and GPR data.
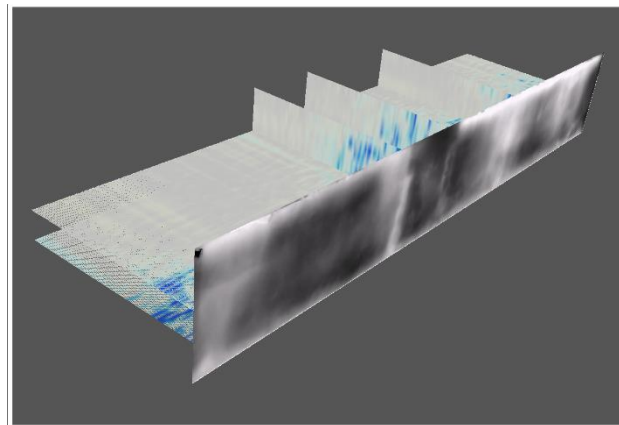

Figure 5.47. Registering of a thermal orthophoto-mosaic and GPR slices with CloudCompare.
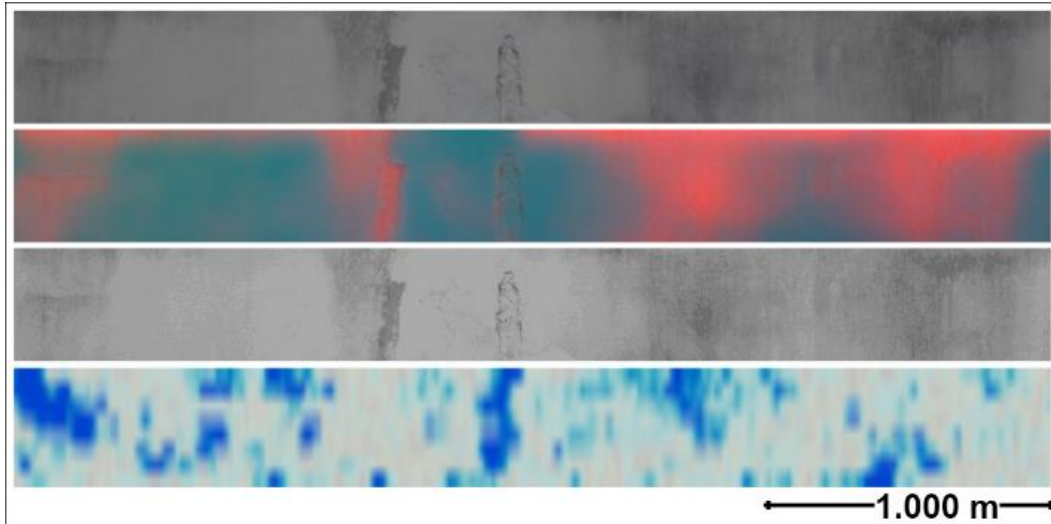
Figure 5.48. Interdisciplinary interpretation of multiband results (from top to bottom): orthophoto-mosaic, false color TIR-NIR-red composite photo-mosaic, map of surface alterations, and GPR slice parallel to the wall at 6 cm depth (riverside façade).
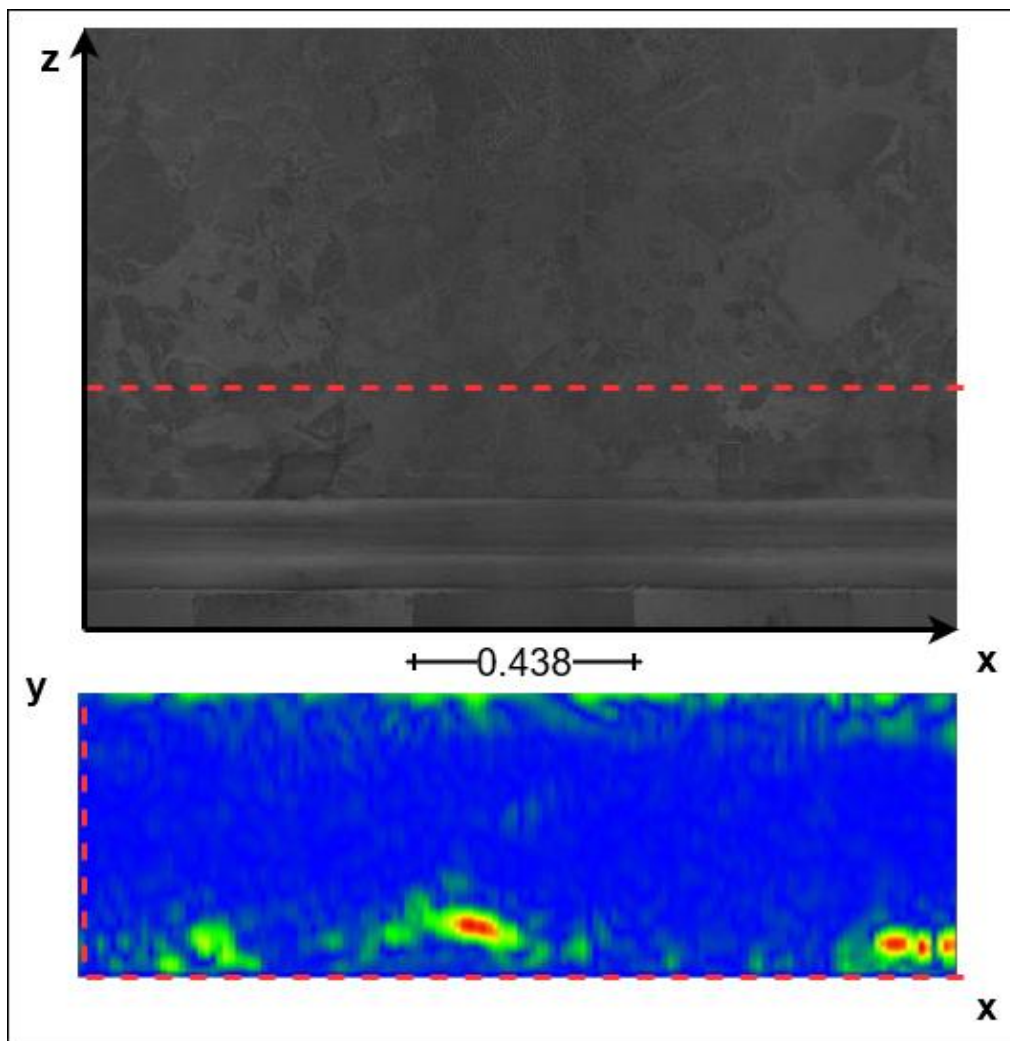

Figure 5.49. NIR developed photogrammetry-produced orthophoto of the lower left column and GPR slice of the column at h = 0.619 m from the floor (main façade).

A significant correlation was observed for the riverside façade between material loss, higher GPR reflection amplitudes, and surface thermal minima, which could be interpreted as high moisture content from water that had permeated the damaged structure's surface layers (Figures 5.50–5.54). The pixel-level fusion of the thermal orthoimage-mosaic and a GPR rarargram (by averaging the two images) was essential in identifying the potential concentrations of moisture.
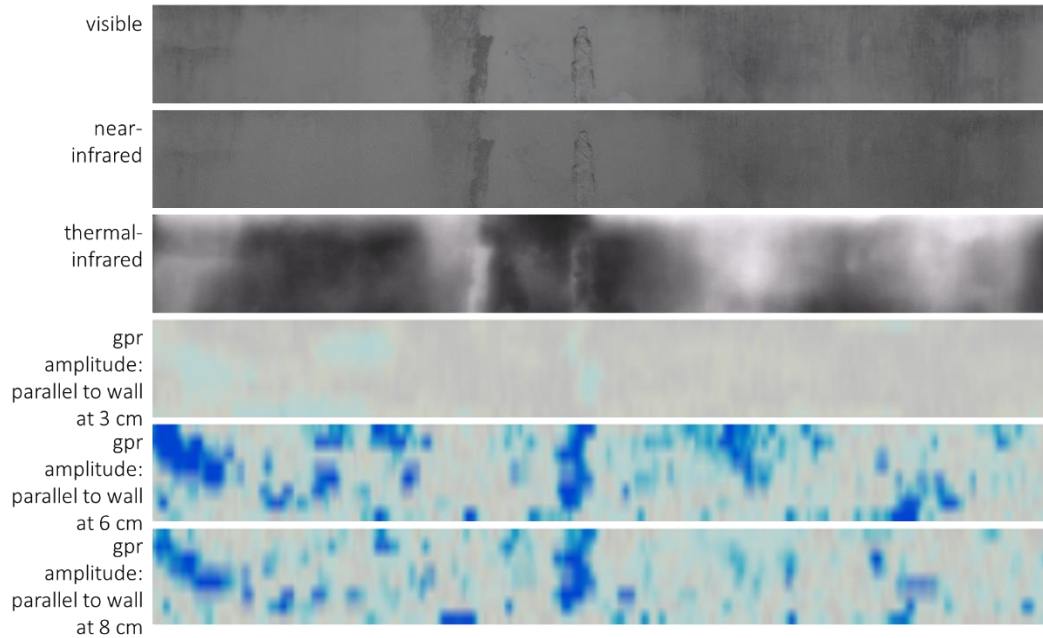

Figure 5.50. Multi-wavelength referenced orthoimage-mosaics and parallel radargrams, façade.

Figure 5.51. Multi-wavelength referenced orthoimage-mosaics and horizontal perpendicular radargrams, façade.

Figure 5.52. Processing of multi-wavelength results, identification of defects, and correlation with radargram, façade.
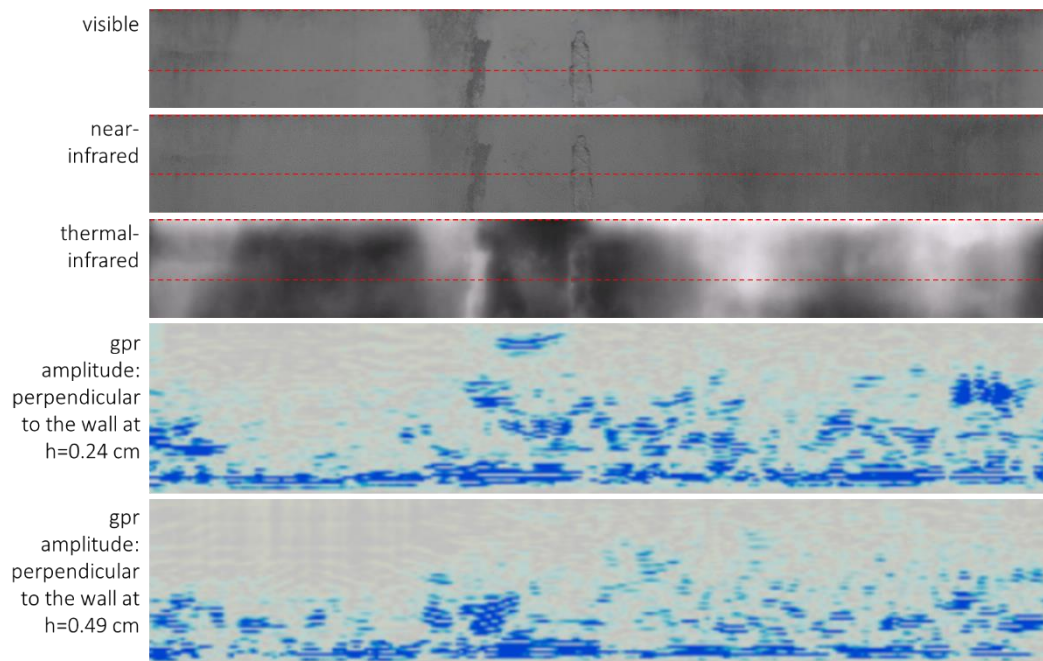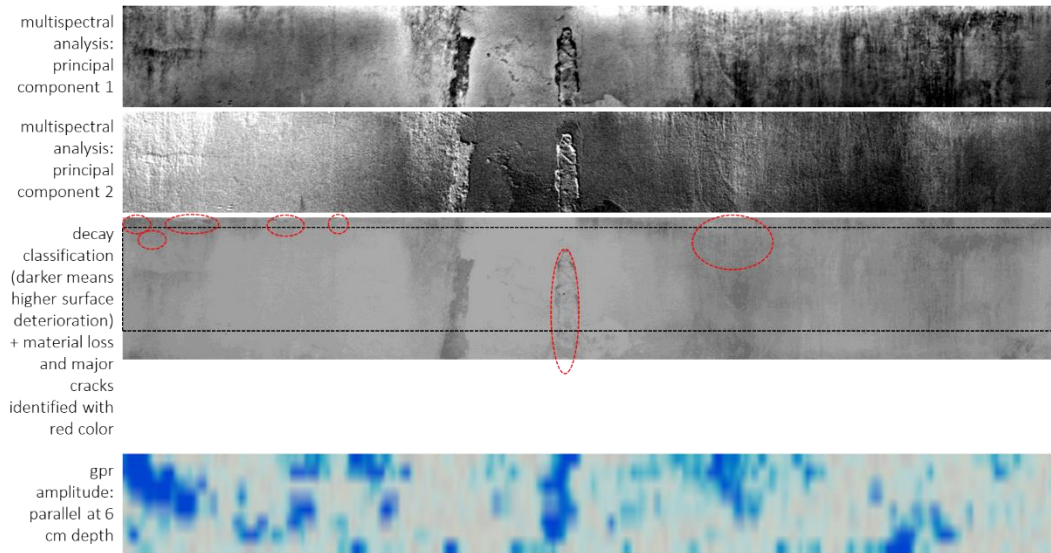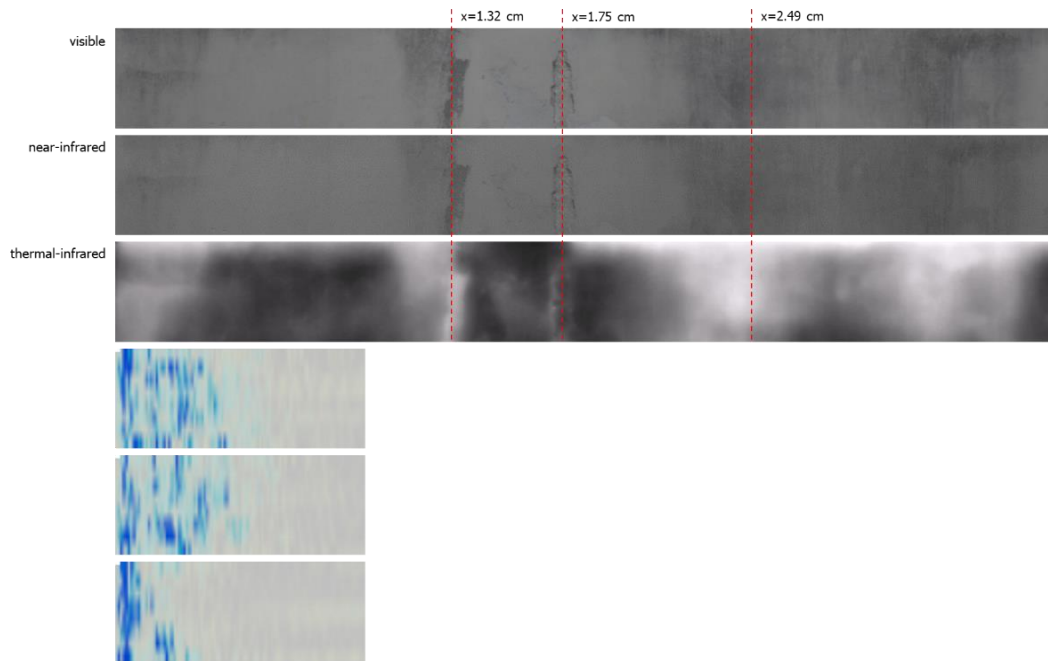

Figure 5.53. Multi-wavelength referenced orthoimage-mosaics and vertical perpendicular radargrams, façade.

Figure 5.54. Fusion of thermal infrared orthoimage-mosaic and radargram at 6cm depth, façade.

Regarding the column, the anomalies detected by on-site inspection, multiband imagery elaboration, and locating extreme amplitude values overlapped, which led to the assumption that the identified volumes with heterogeneous radiometric characteristics corresponded to replacement material (mortar) originating from previous interventions (Figure 5.56 and Figure 5.57).
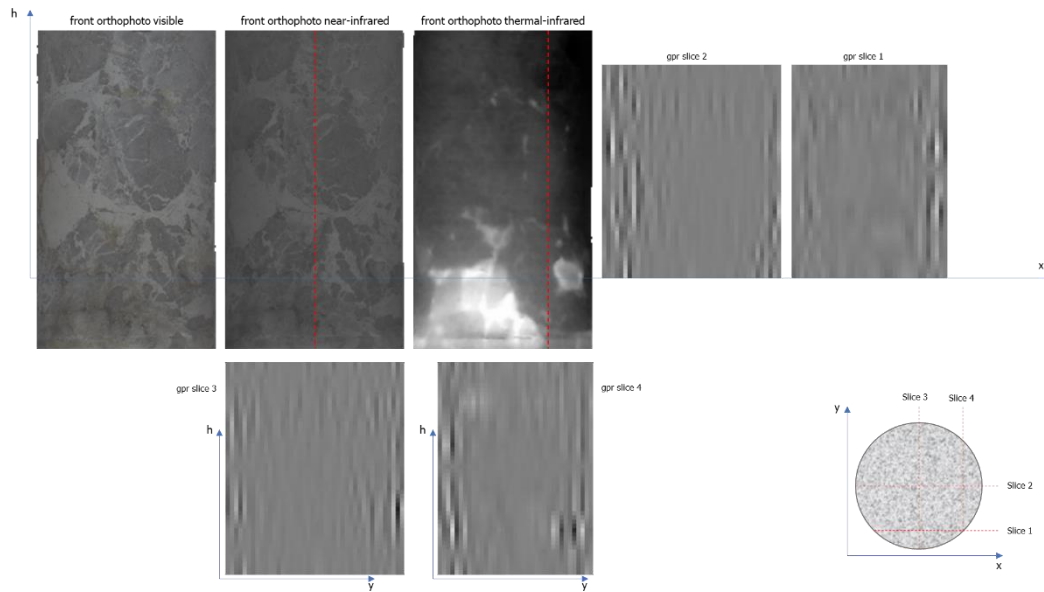

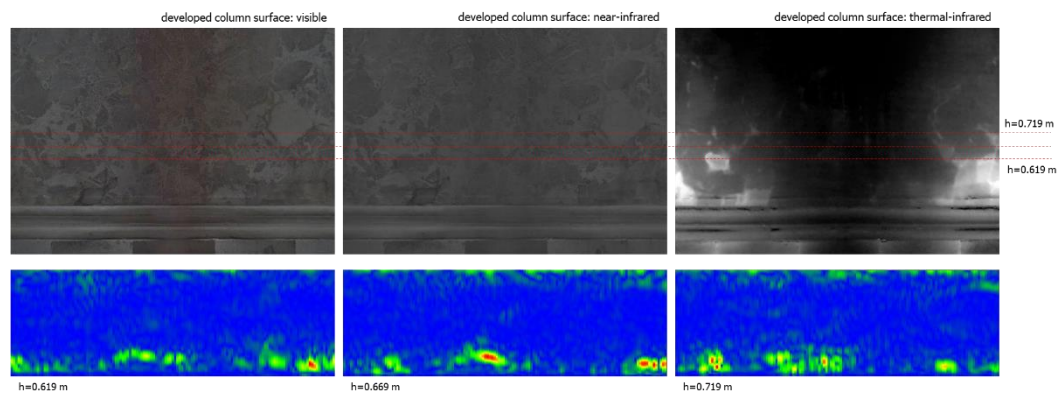**Figure 5.55.** Multi-wavelength referenced orthoimage-mosaics and radargrams, front column.

Figure 5.56. Multi-wavelength developed orthoimage-mosaics and developed radargrams, front column.

6 Conclusions

6.1 Semi-Automatic Mapping of Deterioration with Multispectral Data for Building Facades

The novel methodology proposed for the automatic classification of damage on built cultural heritage used photographic equipment for multispectral data acquisition and supervised machine learning-based image segmentation to map deterioration patterns. It was confirmed that including near-infrared reflectance intensities in the employed methods improved the classification of alterations on the historic façades. This conclusion agrees with the relevant work conducted with terrestrial LiDAR instrumentation and unsupervised segmentation algorithms.

The segmentation of multispectral composites (synthesized with visible and near-infrared reflectance images), with classifiers combining random trees and ensemble learning, performed particularly well even where a high number of surface patterns were present. However, the coexistence of different overlapping categories of biogenic colonization complicated the mapping procedure significantly. It should be highlighted that the accuracy evaluation considered some level of bias since the manually produced reference thematic maps cannot consider the overlapping surface patterns.

The proposed methodology has the limitation that it can map only the pathologies that have been previously recognized through visual inspection (or analytical techniques) because regions of interest have to be annotated to train the intelligent algorithms. However, a crucial advantage is that it produces easily interpretable mapping results, contrary to unsupervised methods where each mapped pattern class has to be a posteriori assigned to a deterioration category. Furthermore, there is a clear advantage over deep learning-based methods that require large image datasets for rapid monitoring purposes of monumental heritage structures. The direct outlook of the proposed framework is the combination with 3D recording technologies to enhance the capability of detecting the geo-metrical altering (material loss) of the historic structures and their building elements.

6.2 Combination of Semi-Automatic Mapping and GIS for the Archaeological Sites of Peloponnese

The development of an appropriate methodology for the implementation of close-range sensing technologies and FOSS GIS for stone degradation mapping has been outlined and tested on weathered ancient remains. Affordable, accessible instrumentation is employed, which adds to the practicality and flexibility of the methodology. However, implementing low-cost sensor technology implies that the collected data should be thoroughly checked and comprehensively corrected. The quality verification of the base maps used for mapping purposes is essential to the accuracy of results purposed for thematic visualization and spatial analysis.

Multiband reflectance imaging demonstrates a necessary non-destructive approach to enriching the thematic mapping process. The plethora of degradation forms, as showcased, presents distinct reflectance characteristics when imaged at different ranges of the electromagnetic spectrum. Mainly, stone patterns caused by biogenic factors present a unique spectral footprint in the infrared range. Thus, involving infrared images for the detection and mapping of degradation enhances the identification capacity for surface patterns such as vegetation, moss, and various biogenic crusts. Nevertheless, when mapping stone that presents less complex surface characteristics, the combination of images captured at multiple spectra may not be necessary, speeding up the mapping process. The application performed at the Temple of Apollo Epikourios presents such a case, where only images captured in the near-infrared spectrum were used as base maps since they maximized the reflectance contrast among observable degradation characteristics and minimized the contract between original and restoration materials that should not be distinguished. Furthermore, for this case study, a single-image approach could be followed due to the narrow extent of the investigated areas.

Photogrammetric techniques, applied for the generation of high-resolution orthoimage-mosaics from image datasets, are essential for producing the background for mapping extensive stone surfaces. Their application proved useful when large multiband datasets needed to be integrated to produce base maps in a cost-effective way. Spectral orthoimage-mosaics can more easily be fused together than individual photos. Additionally, the prospect of involving metric data introduces a spatial reference to the thematic maps, which allows for subsequent spatial analyses to be performed.

Processing rectified images and orthoimage-mosaics for extraction of the degraded stone surface features (pattern recognition) has often been performed manually. In the developed methodology, unsupervised clustering-based

segmentation has been performed, which speeds up the process but requires the interpretation of the different patterns after they have been segmented on the images. Implementation at the Temple of Athena and Dios Sotiros, and the archaeological site of Lepreum showed that this method is very effective when a large number of degradation forms are present but underperforms when there is overlap between different weathering damages. Additionally, this method of extracting surface patterns cannot detect at the same time features induced by material loss. The combined use of accurate range/depth data and multiband data should be researched in this direction. The proposed methodology also offers a more simplistic alternative for cases of stone monuments where there is an absence of extensive biodegradation, based mainly on image histogram manipulation and edge detection.

Transferring the thematic data extracted from rectified images and multiband ortho-mosaics to a GIS environment offers many advantages. This work presented that the visualization of thematic degradation results becomes more effective through a spatial information management environment and also that damage index maps and statistical results can be easily extracted through the heritage GIS implementation. This approach helps with the weathering interpretation and subsequently can assist conservation measures. The damage categories can be qualitatively and/or quantitatively defined. The potential availability of descriptive and qualitative information from other on-site investigation techniques and historical documentation can enhance the results.

6.3 Two-Dimensional Decay Mapping of Ancient Stelae

The integrated multispectral approach allows the detailed 2D mapping of degradation caused by weathering on stelae and other stone antiquities. Forms of degradation are identified by visual inspection and then automatically annotated through a supervised machine learning-based approach, applied to images combining spatially and radiometrically corrected data collected at the visible and near-infrared spectrum. The methodology employs affordable equipment and few processing steps that do not require particular training or specialist software. This process speeds up the documentation steps that are usually conducted manually before conservation treatment of the stone surfaces and facilitates decisions regarding the required cleaning techniques. The proposed method can potentially assist in the identification of areas for sampling and, subsequently, the in-depth investigations through laboratory testing. An interesting perspective would be integrating with other mapping and non-destructive on-site monitoring techniques. The designed methodology is very adaptable, as it performed well for different case studies of stone stelae that presented dissimilar surface pathology. For practical

reasons, some of the steps followed in this work may be skipped. If, for example, the camera sensor cannot be geometrically or radiometrically calibrated, the proposed approach can still produce degradation maps useful for conservation purposes. Including NIR images in the approach proved to increase the accuracy of the results for some cases, especially when biodeterioration was present; however, including only the true color images still provided high-accuracy results. Therefore, an unmodified camera can also be used to provide the necessary input for ML-based segmentation.

To conclude, a critical issue observed in this work stems from the complexity of the mapped surfaces. Overlapping of degradation forms can cause some misclassifications, while more easily definable deterioration patterns can produce higher accuracy results. The subjective visual identification between less and more degraded surfaces that present the same pathology can also affect the approach's performance. Features caused by material loss cannot be easily detected if they are not the cause of other degradation patterns (such as moss caused by concentrated moisture in the created cavities), and thus combining 3D approaches could be helpful in that direction.

6.4 Three-Dimensional Modeling and Decay Mapping of Historical Objects

Through the case studies of stone and wooden statues, novel approaches for multiband texture generation and 3D mapping were demonstrated, combining contemporary image-based 3D reconstruction software, near-infrared and ultraviolet imaging from modified cameras, and 3D mapping techniques. High-resolution 3D models of sculptures with different dimensions from beyond-visible imagery were constructed and proved their metric validity by performing extensive comparisons with models from visible imagery. Then the capacity of the most detailed band-specific models to evaluate the state of preservation of the historical surfaces proving the feasibility of the combined approach, was evaluated. The suggested decay mapping method has the advantages of being low-cost, rapid, easy to implement, and adjustable for different cases of heritage applications, compared to traditional methods for manual decay mapping. It has the additional advantage of combining the thematic information produced with the three-dimensional topology of the object, making possible accurate measurements and planning further scientific investigations and conservation interventions. The investigated method cannot replace extensive diagnostical investigations but can support them in order to reduce time and costs.

Regarding the metric aspect of the study, it should be underlined that Metashape Professional generally provided less noisy meshes from the near-infrared and ultraviolet datasets than 3DFlow Zephyr Aerial and resulted in slightly

smaller statistical reconstruction errors. Although results from both software were practically identical for conservation studies of a millimeter accuracy, even considering the metric results produced with visible imagery. As for the 3D mapping results, it was observed that reducing the information on the near-infrared textures gave a significant boost in the observation of different levels of weathering. Even more, carefully selecting the number of the levels of decay that should be visualized for an accurate representation of the pathology, and segmenting the models according to near-infrared reflectance to produce thematic 3D mapping results, enhanced the ability to interpret the deterioration patterns and enabled measurement for each segmented part of the surface.

6.5 Multi-Sensor Data 3D Integration at the Castello del Valentino

The combination of metric data with multi-wavelength results derived by laser scanning, imaging, thermography, and GPR surveys enhances the richness of recorded information for historical architecture and adds to data validity, integrated processing, and facilitates interdisciplinary interpretation. These non-destructive methods are complementary and can produce documentation content for vastly different typologies of building elements. However, as they operate at different wavelengths, they also collect data at different depths and possess distinct spatial characteristics. Thus, defining the parameters of acquisition in detail, such as spatial resolution, accuracy, and metric implications of their fusion, is crucial to reassure the quality of their integration, which can assist further diagnostic steps and conservation-related decisions.

Knowledge of heritage building surfaces' defects and previous interventions is of paramount importance for diagnosis, and the first step to achieving it is interdisciplinary documentation. In this study, the documentation workflow started from collecting high-accuracy topographic measurements, point clouds, images, and thermograms. By methodically capturing, correcting, and rectifying imagery and artificially enhancing the spatial resolution of the close-range thermograms, multiband image composites were created to perform preliminary investigations of various buildings' elements. Their 2D elaboration helped the documentation of weathering, cracks, and healthy surfaces, the localization of previously restored parts, and the identification of areas of interest for more detailed surveys. Additionally, TLS data exploitation produced visualizations of the façades' geometry and weathering indices in a rapid way.

To conduct detailed documentation surveys, densely captured image datasets were processed through SfM/DMVR-based photogrammetric approaches creating multiband high-resolution orthomosaics and textured models. These were enhanced by radargrams, grid data, and isosurfaces of amplitude values from GPR

measurements. Although the accuracy and resolution of GPR may have been of double to triple values compared to the other close-range sensing techniques, the significance of providing depth information in a non-destructive way became apparent. The fusion of all involved techniques gave a clearer picture of the nature of surface thermal anomalies, the effect of surface weathering, and the 3D volume of restoration materials. However, it should be mentioned that integrated processing of the heterogeneous data will require downscaling of the photogrammetric results to match the GPR properties and is a point of the authors' future research.

The major challenge faced in order to guarantee the integrability of the multisource data was ensuring that during acquisition, their metric parameters and relative position were known. Since sufficient surface features cannot always be identified in thermograms, placing special reflective targets proved essential for thermographic recording. Regarding the GPR measurements, having already established a grid of the antenna's movements with known position parameters helped the registration with other data. A crucial advantage of cross-examining the multiband data was that certain misinterpretations were avoided. For example, it could be determined whether certain reflectance anomalies in the infrared spectrum were caused by dark crusts or moisture concentration.

It should be highlighted that the approach that integrated multiband orthomosaics/developments and GPR slices parallel to the investigated surfaces proves the most promising. This approach not only allows for the straightforward integration between the spatially referenced heterogeneous measurements but can potentially provide an easier transition to semantic annotations and conservation-oriented building information modeling.

6.6 General Outlooks and Perspectives

The novel aspects of this dissertation can be briefly summarized as follows:

- ✓ introduction of established photographic and NDT methods into innovative methodologies for heritage inspection
- ✓ recording of accurate qualitative spectral data without multi-lidar approaches, or expensive multispectral sensors
- ✓ production of accurate approaches for decay mapping through multi-wavelength recording, data integration, and learning-based segmentation algorithms
- ✓ evaluation of metric 3D modeling with reflectance and fluorescence images
- ✓ registration/co-referencing and pixel-level integration of optical, thermal orthophoto-mosaics, and radargrams
- ✓ implementation of multidisciplinary documentation workflows having full knowledge of the metric and radiometric properties of all data and metadata

- ✓ identification of the optimal level of integration between geomatics and close-range sensing techniques for cultural heritage.

Finally, some perspectives for future research have been identified:

- ✓ integration of close-range inspection via integrated metric 3D surveying and multiwavelength recording into Heritage Building Information Modeling (HBIM) for architectural monuments and historical infrastructure
- ✓ integration of the proposed workflows with other techniques for archaeological objects (X-ray fluorescence, ultrasonic pulse velocity testing, Surface roughness measurement)
- ✓ application of the evaluated methods in order to identify areas of interest for sampling and minor destructive testing techniques
- ✓ the aerial perspective–implementation with sensors mounted on drones.

Publications

Adamopoulos, E. (2021). Learning-based classification of multispectral images for deterioration mapping of historic structures. *Journal of Building Pathology and Rehabilitation*, *6*(1), 41. https://doi.org/10.1007/s41024-021-00136-z

Adamopoulos, E., Bovero, A., & Rinaudo, F. (2020). Image-based metric heritage modeling in the near-infrared spectrum. *Heritage Science*, *8*(1), 53. https://doi.org/10.1186/s40494-020-00397-w

Adamopoulos, E., Colombero, C., Comina, C., Rinaudo, F., Volinia, M., Girotto, M., & Ardissono, L. (2021). Integrating Multiband Photogrammetry, Scanning, and GPR for Built Heritage Surveys: The façades of Castello del Valentino. *ISPRS Annals of the Photogrammetry, Remote Sensing and Spatial Information Sciences*, *VIII-M-1–2021*, 1–8. https://doi.org/10.5194/isprs-annals-VIII-M-1-2021-1-2021

Adamopoulos, E., Patrucco, G., Volinia, M., Girotto, M., Rinaudo, F., Tonolo, F. G., & Spanò, A. (2021). 3D Thermal Mapping of Architectural Heritage: Up-To-Date Workflows for the Production of Three-Dimensional Thermographic Models for Built Heritage NDT. In M. Ioannides, E. Fink, L. Cantoni, & E. Champion (Eds.), *Digital Heritage. Progress in Cultural Heritage: Documentation, Preservation, and Protection* (Vol. 12642, pp. 26–37). Springer International Publishing. https://doi.org/10.1007/978-3-030-73043-7_3

Adamopoulos, E., & Rinaudo, F. (2019). 3D Interpretation and fusion of multidisciplinary data for heritage science: A review. *ISPRS - International Archives of the Photogrammetry, Remote Sensing and Spatial Information Sciences*, *XLII-2/W15*, 17–24. https://doi.org/10.5194/isprs-archives-XLII-2-W15-17-2019

Adamopoulos, E., & Rinaudo, F. (2020a). Enhancing Image-Based Multiscale Heritage Recording with Near-Infrared Data. *ISPRS International Journal of Geo-Information*, *9*(4), 269. https://doi.org/10.3390/ijgi9040269

Adamopoulos, E., & Rinaudo, F. (2020b). Near-infrared modeling and enhanced visualization, as a novel approach for 3D decay mapping of stone sculptures. *Archaeological and Anthropological Sciences*, *12*(7), 138. https://doi.org/10.1007/s12520-020-01110-5

Adamopoulos, E., & Rinaudo, F. (2020c). UAS-Based Archaeological Remote Sensing: Review, Meta-Analysis and State-of-the-Art. *Drones*, *4*(3), 46. https://doi.org/10.3390/drones4030046

Adamopoulos, E., & Rinaudo, F. (2021a). Documenting the State of Preservation of Historical Stone Sculptures in Three Dimensions with Digital Tools. In A. Del Bimbo, R. Cucchiara, S. Sclaroff, G. M. Farinella, T. Mei, M. Bertini, H. J. Escalante, & R. Vezzani (Eds.), *Pattern Recognition. ICPR International Workshops and Challenges* (Vol. 12663, pp. 666–673). Springer International Publishing. https://doi.org/10.1007/978-3-030-68796-0_48

Adamopoulos, E., & Rinaudo, F. (2021b). Combining Multiband Imaging, Photogrammetric Techniques, and FOSS GIS for Affordable Degradation Mapping of Stone Monuments. *Buildings*, *11*(7), 304. https://doi.org/10.3390/buildings11070304

Adamopoulos, E., & Rinaudo, F. (2021c). Close-Range Sensing and Data Fusion for Built Heritage Inspection and Monitoring—A Review. *Remote Sensing*, *13*(19), 3936. https://doi.org/10.3390/rs13193936

Adamopoulos, E., Rinaudo, F., & Adamopoulou, D. (2021). Automatizing Degradation Mapping of Ancient Stelae by Dual-Band Imaging and Machine Learning-Based Classification. *ISPRS Annals of the Photogrammetry, Remote Sensing and Spatial Information Sciences*, *VIII-M-1–2021*, 9–16. https://doi.org/10.5194/isprs-annals-VIII-M-1-2021-9-2021

Adamopoulos, E., Rinaudo, F., & Ardissono, L. (2021). A Critical Comparison of 3D Digitization Techniques for Heritage Objects. *ISPRS International Journal of Geo-Information*, *10*(1), 10. https://doi.org/10.3390/ijgi10010010

Adamopoulos, E., Rinaudo, F., & Bovero, A. (2019). First Assessments on Heritage Science Oriented Image-Based Modeling Using Low-Cost Modified and Mobile Cameras. *ISPRS - International Archives of the Photogrammetry, Remote Sensing and Spatial Information Sciences*, *XLII-2/W17*, 23–30. https://doi.org/10.5194/isprs-archives-XLII-2-W17-23-2019

Adamopoulos, E., Volinia, M., Girotto, M., & Rinaudo, F. (2020). Three-Dimensional Thermal Mapping from IRT Images for Rapid Architectural Heritage NDT. *Buildings*, *10*(10), 187. https://doi.org/10.3390/buildings10100187